WETDECK SLAMMING OF HIGH-SPEED CATAMARANS WITH A CENTRE BOW

By

James R. Whelan, B.E. (Hons)

Submitted in fulfilment of the requirements
for the degree of
Doctor of Philosophy

University of Tasmania

July 2004

Statement of Originality

This thesis contains no material which has been accepted for the award of any other degree or diploma in any tertiary institution. To the best of my knowledge and belief, this thesis contains no material previously published or written by another person, except when due reference is made in the text.

This thesis is not to be made available for loan or copying for three years following the date this statement was signed. Following that time the thesis may be made available for loan and limited copying in accordance with the *Copyright Act 1968*.

James R. Whelan
30/07/2004

Abstract

The influence of a centre bow on the severe wetdeck slamming behaviour for a range of hull forms based on an INCAT fast catamaran ferry has been studied with full-scale trials, experimental drop tests and computationally. Particular attention was paid to the effect centre bow geometry has on the severity of slam events.

Full-scale trial data from a 96m INCAT vessel was analysed. The influence of vessel Froude number, wave height, relative centre bow impact velocity, relative centre bow submergence and instantaneous wave height on the slamming behaviour of the vessel was identified. Severe slams were found to be caused by wetdeck slamming. The average relative motion between the centre bow and the instantaneous water surface during slamming was calculated and this was used for scaling of the experimental drop tests.

Two-dimensional drop tests were used to experimentally investigate the behaviour of seven realistic bow geometries for catamarans with centre bow, and two vee wedge geometries. Drop tests were made under gravity with varied drop heights and mass into a long thin tank of calm water. Acceleration and surface pressure measurements and high-speed photography flow visualisation were used to detail model behaviour. The most significant observations were that the highest point in the arch should be located as far outboard as possible to minimise peak acceleration and that models with large centre bows experience peak acceleration at a lower relative initial water surface penetration depth than models with small centre bows. The trapped air in the top of the arch was also found to be important in attenuating peak acceleration.

Two theoretical models were developed to model the drop tests; a one-dimensional added mass theory and a two-dimensional volume of fluid method. The added mass theory was based on von Karman's impact theory coupled with a potential flow model to account for the upwash of water during entry and a compressible air model to describe the effect of trapped air in the arch between the hulls. This theory was found to capture the trends displayed in the drop test experiments adequately. The volume of fluid method modelled the drop tests by solution of the Euler equations on a rectangular grid. The model was validated against the broken dam problem, the run up of a Laitone wave and the wedge entry problem.

Acknowledgments

I would like to thank Prof. M. R. Davis and Dr. D. S. Holloway for their supervision and support throughout this project. I am indebted to Mr. T. Roberts for his guidance and wealth of practical advice. The assistance of Mr. P Seward and the technical staff of the University of Tasmania's School of Engineering was also invaluable.

Financial support for this project was provided through an Australian Postgraduate Award scholarship with supplementary support provided by INCAT Pty Ltd and the Australian Research Council.

The friendship and brainstorming sessions with other postgraduate students (especially Vince Anderson) is gratefully acknowledged. I would also like to thank Alison Hoban for her invaluable Japanese translation skills and Alison Greenhill for her contribution. The support of Stephen, Elizabeth and Adam Walker is also greatly appreciated. Finally, I would like to thank my mother and father.

Contents

List of Figures

List of Tables

Nomenclature

Chapters 1-4

a_C	Constant acceleration for ogee geometry calculation
A_V	Cross sectional area of hull section
A_S	Air spring cross sectional area
B	Vertical distance from keel of demi-hull to wetdeck
C_F	Force coefficient
C_P	Pressure coefficient
C_1	Distance from the centre line of a hull section to the intersection of the water surface and hull section centre bow.
C_2	Distance from the centre line of a hull section to the intersection of the water surface and the inside of the demi-hull of the hull section.
C_3	Distance from the centre line of a hull section to the intersection of the water surface and the outside of the demi-hull of the hull section.
t	Time
C_S	Time coefficient for slam definition
C_t	Isentropic coefficient constant.
n_g	Number of stress gauges in system 2 on vessel 050.
F	Forces
Fr	Froude number
F_B	Buoyancy force
F_G	Gravity force
F_F	Frictional force
F_S	Air column spring force
F_m	Forces acting on the hull section
g	Acceleration due to gravity
$h_{59}(t)$	Vertical displacement of frame 59
h_B	Vertical distance from the calm water level to the keel of the centre bow at frame 59
H_S	Slam wave height
H	Vertical distance from the undisturbed water surface to the top of the arch when the drop test model is released
H^*	Normalised drop test height

$h_w(t)$	Instantaneous wave height
$h(x)$	Function used to describe the geometry of hull sections
I_m	Impulse experienced by hull section during arch closure
k	Time step index counter
L_V	Full-scale vessel loaded water line length
L_m	Linear momentum in the vertical direction
L_{TSK}	Distance from the stern of INCAT vessel 050 to the TSK wave meter mounting
L_{59}	Distance from the stern of INCAT vessel 050 to frame 59
L	Beam of experimental drop test model
L_d	Vertical linear momentum of deficit added mass
p	Pressure
P_a	Standard atmospheric air pressure
S	Length of wetted portion of a hull section
T_a	Standard atmospheric air temperature
Re	Reynolds number
R	Gas constant
r_{ij}	Distance from control point to source or image source
m_m	Drop test model mass
m_d	Deficit added mass
m_{air}	Mass of air in air column spring
m^*	Mass number
m_a	Added mass
$\hat{n}$	Unit normal vector
V_v	Vessel forward speed
V_C	Velocity of drop test model at instant of first contact with water
V	Scaling velocity for drop tests
V_h	Far field velocity
t^*	Dimensionless time
We	Weber number
w	Width of drop test model
w_{1_i}	i th panel length calculation constant
W_t	Width of drop test tank
x	Horizontal spatial co-ordinate
$\vec{x}_{s_i}$	Source point location
$\vec{x}_{c_i}$	Control point location

y	Vertical spatial co-ordinate
y_S	Length of air column
y_d	Displacement of deficit added mass
$\Delta h(t)$	Relative distance between instantaneous water surface and centre bow keel during a full-scale slam event
Δt_C	Time scale for arch closure process
Δt	Discrete time step
ΔS	Panel length
$\forall$	Volume of drop test model beneath the highest point in the arch
ρ	Density of water
χ	Transverse distance from model centre line to the highest point in the arch
μ	Viscosity of water
σ_s	Surface tension of water
σ_{Al}	Yield stress of Aluminium
σ_J	Potential basis function source strength
σ	Stress
$\sigma^{\dagger}$	Slam global stress
σ_{min}	Minimum stress
σ_{max}	Maximum stress
$\sigma^{\dagger}_{9.10}(t)$	Time dependent slam global stress
$\forall_{air}$	Volume of air in air column spring
γ	Ratio of specific heat capacities
$\eta(x,t)$	Free surface height
ϕ	Potential function
ϕ_{ij}	Basis potential function
ϖ	Desingularisation constant
η_1	Upwash of water adjacent to the centre bow
η_2	Upwash of water adjacent to the inside of the demi-hull
Ψ	Parameter used in boundary element generation

subscripts

cb	Centre bow
wd	Wetdeck
dh	Demi-hull
fs	Full-scale

m	Model
min	Minimum value
max	Maximum value
o	Denotes instant of onset of the arch closure process

Chapter 5

$\vec{a}$	Body acceleration
A	Grid cell average porosity.
F	Scalar variable representing the fraction of fluid in a cell.
$\vec{g}$	Gravity vector
H	Porosity.
L	Wall porosity for one grid cell boundary.
$\hat{n}$	Unit normal vector associated with hull boundary segment (into fluid).
p	Pressure divided by the density of water
P	Pressure
R	A small region of computational domain.
S_l	Boundary segment of a small region R.
S	Boundary of a small region of computational domain.
S_C	Intermediate variable used to solve pressure field.
t	Time
$\hat{t}$	Unit tangential vector associated with hull boundary segment.
$\vec{u}$	Velocity vector
$\vec{u}_n$	Normal velocity vector.
$\vec{u}_t$	Tangential velocity vector.
V	Constant inflow velocity.
x	Horizontal spatial co-ordinate.
y	Vertical spatial co-ordinate.
Δx	Spatial discretisation in the x-direction.
Δy	Spatial discretisation in the y-direction.
Δt	Temporal discretisation.
$\eta_{1,2,3,4}$	Irregular star leg lengths.
ς	Intermediate variable used to calculate velocity field
ξ	Intermediate variable used to calculate velocity field
ρ	Density of water
ω_{h}	Over relaxation parameter for hull boundary cells.
ω_{f}	Over relaxation parameter for surface and full cells

1. Introduction and Review

The problem addressed in this thesis is the effect of bow form on the slamming of high speed wave piercing catamarans with a centre bow such as those constructed by INCAT Tasmania Pty Ltd. This chapter provides a general introduction to ship slamming and identifies the geometric characteristics of the INCAT centre bow. The unique problems associated with the slamming of INCAT type vessels are identified. The research undertaken to investigate these problems is outlined. The research consisted of four major elements. These were the analysis of full-scale trial data, experimental scale model tests, the development of an added mass theory and the development of a volume of fluid method. These research topics are placed in context with respect to previously published work.

1.1. Introduction

Recent trends in high speed sea transportation have been to construct larger and lighter weight vessels such as those constructed as INCAT Tasmania Pty Ltd (Thomas et al 2001). To enable efficient structural design understanding the sea loads acting on these vessels is essential (Bertram 2000). One of the principal sea loads is due to slamming and the slamming loads have been found to be important in the structural design of high speed vessels (Faltinsen 1996). A standard catamaran form has two demi-hulls connected by a flat cross structure or wetdeck (Figure 1.1.1). One particular feature of the INCAT catamaran is the presence of a centre bow attached to the wetdeck between the demi-hulls (Figure 1.1.2). The effect that the centre bow has on the slamming behaviour of the vessel is examined in this thesis.

Figure 1.1.1 Standard catamaran form with a flat wetdeck.

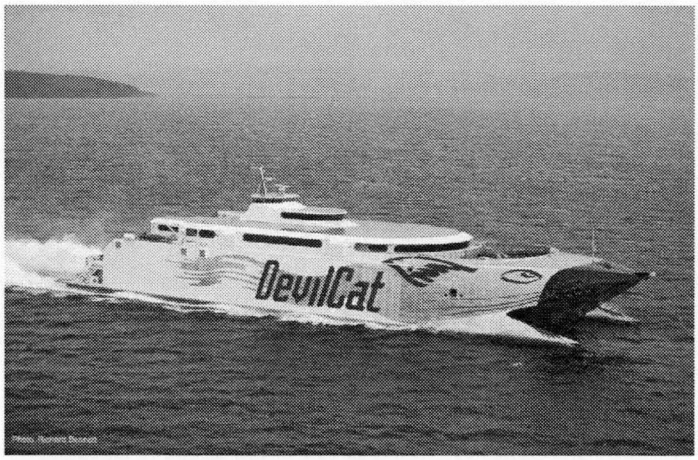

Figure 1.1.2 INCAT catamaran with a centre bow.

Slamming occurs in rough seas when the relative motions between the water surface and the ship causes violent impact to occur (Bertram 2000). Slamming is a complex physical phenomenon. Faltinsen (1996) compiled a list of the factors effecting the slamming problem. These factors are: (1) the compressibility of water; (2) formation of air pockets and bubbles at the interface between the water and the structure; (3) cavitation; (4) flow separation; (5) hydroelasticity; (6) structural form; (7) impact velocity; (8) ship accelerations; (9) forward speed of the ship; (10) relative angle between the water surface and the structure. The particular methods used to investigate these effects are discussed where applicable to the slamming of an INCAT vessel.

Four principal forms of slamming have been classified, these being bottom, bow flare, breaking wave and wetdeck slamming (Korobkin 1996, Bertram 2000). Bottom slamming occurs when the keel of a vessel emerges from the water surface and then impacts the water surface during re-entry. Bow flare slamming occurs when the bow of a vessel penetrates sufficiently deeply that the bow flare impacts with the water. Breaking wave slamming results from the impact of a breaking wave slamming results from the impact of a breaking wave with the ship structure. Finally wetdeck slamming results from the impact of the water surface with the cross structure (or wetdeck) between the hulls of a multi-hull vessel. Wetdeck slamming is a particular problem for catamarans. It has been noted that "the problem of slamming of the cross-structure of a catamaran or twin hull ship is a serious concern for the designer" (Giannotti 1975). Giannotti (1975) also observed that " the most critical portion of a catamaran for hydrodynamic impact occurrence is undoubtedly the bottom of the cross structure."

Ship slamming including wetdeck slamming may potentially cause damage to the ship structure. Such damage includes damage to the local panelling and the buckling of the ship frames. Damage of this nature has been experienced by an INCAT vessel as a result of a severe slam event (Figure 1.1.3). Damage has also been experienced by other high speed catamarans (Figure 1.1.4). In addition slamming induces a dynamic whipping response in the vessel structure (Thomas et al 2001). This whipping response may accelerate fatigue failures of the hull (Bertram 2000). The ship motions are effected by slamming. Also the slamming may cause the ship master to reduce speed (Faltinsen 1996). This impinges on the commercial operation of vessels. For these reasons understanding the effects and loads induced by slamming is important during vessel design.

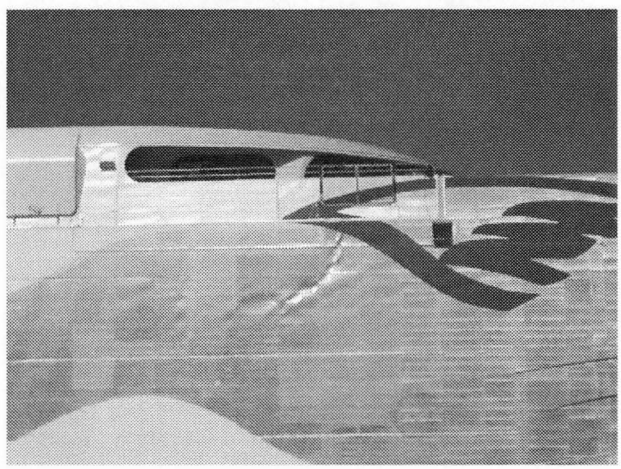

Figure 1.1.3 Damage inflicted upon an INCAT vessel due to a slam event.

Figure 1.1.4 Damage due to slamming on a standard catamaran form.

A standard catamaran will experience all four principal forms of slamming. That is bottom and bow flare slamming on the demi-hulls, breaking wave slamming and also wetdeck slamming. The slamming behaviour of INCAT vessels will differ from standard catamaran slamming due to the presence of the centre bow. The centre bow will experience bottom slamming as it initially enters the water, which of course does not occur for standard catamarans. The centre bow may also effect the nature of a wetdeck slam should one occur. It is this interaction which is of interest and this thesis examines the role of the INCAT centre bow on the slamming performance of an INCAT vessel.

1.2. Full-scale Slam Trials

The slamming behaviour of vessels in different sea ways has been investigated by sea trials of full-scale vessels. This section presents a review of full-scale trials that have been previously carried out. The review of trials has been organised into three parts: displacement mono-hulls, planing mono-hulls and catamaran trials. The gaps in knowledge that are addressed by the full-scale trials presented in this thesis are then identified.

1.2.1. Displacement mono-hulls trials

The slamming of displacement mono-hulls has been extensively investigated with full-scale trials. These trials are of interest when investigating the slamming of INCAT catamarans as these catamarans experience slamming on their demi-hulls. Also the initial entry of the centre bow shows some similarity to the entry of a mono-hull. Mono-hulls do not of course experience wetdeck slamming which is particular to catamaran vessels.

The slamming of cargo vessels during operations has been reported on in several studies. The slamming of two cargoliners (LWL 136m and 146.15m), an ore carrier (LWL 218m) and a container ship (LWL 218m) was reported on by Aertssen (1979). Structural strains, vertical and lateral accelerations, pitching, rolling, torsional motions, wave height and wind conditions were all measured. Hull surface pressures were also taken on the bow of one of the cargoliners and the ore carrier. The frequency and severity of the slamming experienced was examined. Aertssen observed that the frequency of slamming depends on four principal factors; the sea state, vessel speed, vessel draught and finally how conservative the captain is with respect to slamming. A description of a typical slam was also presented by Aertssen which was "slamming in the light-loaded condition of a fast cargo ship is the most conspicuous result of violent pitching and heaving in waves. When the

ship's bottom hits the water and the relative velocity is large, a sudden deceleration follows, the impact pressure on the plating is large, exciting important local vibrations and a shudder over the whole ship length."

The catastrophic damage suffered as a consequence of slamming by the bulk carrier Onomichi-maru (LxBxD = 216.4x37.7x17.3) was discussed Yamamoto et al (1983). The paper concluded "The disaster was caused by the buckling of the upper deck due to whipping after slamming impact in an unhappy superposition of a regular swell and an irregular swell." Damage sustained by a number of other large mono-hulls was also discussed.

The bow flare slamming of a container ship operating in the North Pacific Ocean during winter was examined by Vulovich, Hirayama, Toki and Mizuno (1989). Deck stresses, hull impact pressures, sea state, ship motions and vessel acceleration readings were made. Measurements of slamming experienced are presented. Vulovich et al (1989) noted that the "characteristic of longitudinal stresses in the foredeck were found to be quite different from those in the midship half length. Foredeck stresses vary directly with the impulsive forces on the bow flare, while those in the midship portion respond mainly in the form of whipping vibrations."

Methods of making full-scale measurements on ships were discussed by Brown, Clarke, Dow and Jones (1991) who also comment on theoretical prediction techniques for wave induced loads on ships. Brown et al comment that the "extreme wave induced loads remain one of the main uncertainties affecting reliability of ship structures." Furthermore it is noted that, "because of the complexity of the slamming process, influenced by air entrapment, by irregularity of both water surface and structure and the local elastic response, these forces are usually estimated empirically using the results of drop tests on representative ship sections."

The results of full-scale trials on the ARIES, a high speed 146m mono-hull with a maximum speed of 40knots were presented by Grossi and Dogliani (2000) and Iaccarino, Monti and Sebastiani (2000). Ship motion, wave, hull strain and hull surface pressures were measured. Grossi and Dogliani (2000) present some results for the maximum hull surface impact pressure measured. The range of impact pressures measured in the array of pressure gauges ranged from 15kPa to 55kPa and these values were generally less than the pressures obtained from the RINA simplified rule formula for impact pressure (1999). Iaccarino et al (2000) also presents some slam results for the vessel ARIES. Some example pressure against time records were presented for several slam events. Results for peak pressure against heave acceleration, peak pressure against bow acceleration and peak pressure against

maximum vertical velocity at the location of the relevant pressure gauge were plotted. For both the heave and bow accelerations and also for the maximum vertical velocity, the maximum pressures recorded were found to increase with each of these three parameters which indicates that there was a correlation between ship motions and slam severity.

Trials involving military displacement mono-hulls were discussed by Bishop, Clarke and Price (1983) who report on the full-scale trials of LEANDER and TRIBAL class frigates and compare slam bending moment response results with predictions. The relationships between sea state, vessel speed and bending moment transient response to slamming are also commented on. The Stavovy and Chuang (1976) impact theory was used to model the slamming and the underlying sea loads were calculated using a linear strip theory. Good agreement between theory and over the range of conditions tested was found. Hay, Bourne, Engle and Rubel (1994) conducted extensive sea trials on a United States Navy cruiser of the CG 47 class. Extensive ship motions, vessel strain and sea state data was recorded. Slamming and vessel whipping was investigated. Bending moment distributions for longitudinal, vertical and lateral bending due to ordinary wave loads, whipping loads and combined whipping and ordinary wave load results were presented. It was noted that dynamic forces such as slam induced whipping caused substantial bending moments which in some cases were found to exceed design limits based on static design load rules.

1.2.2. Planing mono-hull trials

A number of sea trials examining the slamming of planing mono-hulls have been published. These trials, like the trials of the displacement mono-hulls, are of interest when examining catamaran slamming because the demi-hulls and centre bow of the catamaran may slam in a similar manner to a planing mono-hull vessel. Also an examination of these trials allows the state of the art of ship slamming trials to be identified.

The slamming performance of planing military attack vessels has been investigated with full-scale sea trials. Trials with a 75ft aluminium mono-hull torpedo boat that had been instrumented with pressure gauges, strain gauges and accelerometers were conducted by Heller and Jasper (1961). The vessel was tested at high speed in rough sea states. Results for vessel performance during slam events are presented and it was noted that the load due to slamming pressures is skewed towards the bow of the vessel. The results of this investigation were used to develop a structural design procedure for planning craft. A report on the structural design of an aluminium missile boat upon which some sea trials were conducted to examine seakeeping and slamming whipping behaviour of the vessel was presented by Olkinuora et al (1991). Strain, acceleration, engine revolutions, pitch, roll and vessel

speed were measured. The relative distance between bow and water surface was also measured. Unfortunately detailed results were not published. The paper concluded that, "the wave impacts (slams) are the most important loads." A small high-speed naval craft (Length 9.5m) which had been instrumented with strain gauges, pressure transducers and a six degree of freedom accelerometer was tested by Rósen and Garme (1999). Vessel speed and sea state measurements were also made. Trials took place in the Baltic Sea. The pressure results obtained indicate that the pressure pulse experienced by the vessel during a slam was very local in nature. The highest peak pressure recorded was 370kPa when the vessel was travelling at 35knots. It was also found that the peak pressures were higher at higher speed and when operating in bow seas.

The full-scale trials of fast patrol vessels investigating slamming have previously been conducted. Aksu, Suhbrier and Temarel (1991) report on full-scale trials of a fast patrol vessel operating at speed in heavy seas. Some bow and stern acceleration results and some keel and deck strains in the midship section of the vessel were presented. Sea state measurements were also made. The results of the full-scale trials were compared with a hydroelastic theory with satisfactory agreement being obtained. A 40m long high-speed patrol vessel was tested by Takemoto, Miyamoto, Hashizume, Oka and Ohsawa (1993). Ship motions, sea conditions, hull stresses and pressure on a bottom panel and a side panel were also measured. Numerous slam events were encountered and some results are presented. The impact pressure on the bottom of the vessel was found to increase with bow acceleration. Results were compared with results from numerical simulation and model tests in a towing tank and good agreement was found. An aluminium fast patrol vessel was studied with full-scale trials by Kannari et al (1998). During the trials some slam events were recorded in heavy seas. Full-scale results were compared with linear strip theory and significant errors are identified.

The slamming of a mono-hull coastal rescue craft with an overall length of 19.6m was examined with full-scale trials by Hayman, Haug and Valsgård (1991). The behaviour, under slam loading of one of the bottom panels of the vessel was investigated using strain gauges and an accelerometer attached to the centre of the panel, two other accelerometers were attached to the keel and a bulkhead near the instrumented panel. Accelerations near the LCG were also measured. Relative water surface measurements were not made. Empirical relations between shear strain in the panel and global vertical acceleration at the LCG were given. However only a few very severe slam events were recorded and thus it was concluded that additional research is required to provide good statistical slam data.

The slamming of the semi-displacement vessel SEAHAWK II was examined by Takahashi and Kaneko (1983) during full-scale trials. Results were compared with three-dimensional model tests of

an elastic backbone model. It was found that time histories of the wave bending moments measured in the model test compared well with those measured on the full-scale vessel.

Talvia and Wiefelsputt (1991) conducted tests on a 1/5 scale self propelled model of a 35m SAR vessel at a Froude number of 1.9 in natural sea conditions. 14 hull pressure readings, bow and stern accelerations and 28 strain gauge measurements were made. Sea wave data was taken with a free floating wave buoy. The hull pressures measured during slamming were compared with DNV rules for high-speed light craft, the theory of Stavovy and Chuang (1976) and the theory of Wagner (1932). It was found that the theory of Wagner (1932) underestimated the pressures experienced by the hull, where as the DNV rules and theory of Stavovy and Chuang (1976) over estimated these pressures. The vibrations induced in the hull structure due to slamming were also investigated.

1.2.3. Catamaran trials

The behaviour of full-scale catamarans, not constructed by INCAT, under slamming loads have previously been investigated by a number of investigators. Cook (1998) conducted trials of on an 8m research catamaran. Some very limited slam event results are presented. The slam loads were observed to be of substantially higher magnitude than the underlying wave load. The slam loads were of shorter duration than the underlying wave loads. Haugen and Faltinsen (1999) undertook full-scale measurements of the wetdeck slamming of a 30m catamaran. Extensive strain measurements of the wetdeck, wetdeck panel deflections, ship motions, accelerations and sea state measurements were made. The importance of the relative impact velocity between the wetdeck and the water surface was identified. Large vertical accelerations with substantial whipping motions were observed during wetdeck slam events. A description of a wetdeck slam event was made and the factors influencing it were identified. Factors mentioned include wetdeck dead rise angle, forward speed, sea surface motion, and ship roll and pitch. Some example wetdeck slam results were given. The full-scale results were compared with a hydroelastic theoretical model and it was found that wetdeck slamming may occur even "when the vessel operates in sea states well below the operational limits given by the DNV rules." It was also found that for wetdeck slamming it was the normal velocity between the wetdeck and water surface which was the most significant for determining the maximum induced stresses. Steinman, Fach and Menon (1999) conducted full-scale experiments on an 86m Austal high speed catamaran during a delivery voyage from Perth, Western Australia to Istanbul, Turkey. Wave, motion and hull strain measurements were recorded. A number of slam events were encountered and some example results are presented. It was observed that the structural stress responses resulting from a slam event consisted of an initial response followed by a backlash stress, which may be larger than the initial stress response, a local mounting structural response and then a global modal response. The extent of each of these responses was dependent on the location relative to the location of the slam

impact. No results for the relative motion between the water surface and wetdeck were given for the slam events.

A number of full-scale investigations of INCAT vessels have been undertaken. As previously noted, INCAT vessels have a substantial centre bow which may have an effect on the wetdeck slamming of the INCAT vessels as compared with a catamaran with a flat wetdeck. Watson, Davis and Roberts (1997) examined the vessel motions of 81m and 86m Incat wave piecer catamarans. The emphasis of the paper was ship motion measurements in regular seas, however a brief discussion of slamming experienced during trials was made. Roberts, Watson and Davis (1997) recorded data during sea trials and a delivery voyage of an 81m INCAT wave piecer catamaran. A significant number of slam events were experienced and an analysis of these events was undertaken. Results for acceleration at the LCG against maximum wave height and maximum stress against wave height were given. It was found that the maximum stress was highest in a 2m sea even though the vessel operated in waves with height of up to 10m. This was attributed to the operator reducing speed in adverse conditions. The vertical acceleration at the LCG was found to increase only slowly with wave height and speed reduction by the operator also influenced this trend. The relative severity between regular wave loads and slamming loads was investigated and the large slamming loads were found to be significantly larger than the regular wave loads. The fatigue life of the vessel, including the effect of slamming, was also investigated. Yakimoff (1997) used a finite element model and full-scale trials of an 81m INCAT wave piecer to examine the impact of slamming on the fatigue life. It was found that 66% of the fatigue damage suffered by the vessel was due to slamming and the subsequent dynamic response. Roberts and Yakimoff (1998) developed global design loads for an 86m INCAT wave piecer catamaran using finite element models and full-scale data collected on a delivery voyage from Sydney Australia to Portland Britain. Of particular interest in this study were the transient loads induced by the slamming of the centre bow and wetdeck. Thomas, Davis, Whelan and Roberts (2001) examined the slamming response of a 96m INCAT vessel during commercial operations in the Cook Strait New Zealand. Structural strains, ship motions and sea state data was recorded. A definition of a slam was developed based on the time rate change of the strain transients. The relationships between maximum slam stress and significant wave height, slam occurrence frequency, slam Froude number and vessel Froude number were determined from the data records. The whipping response of the vessel to slamming was also examined. During the trials a severe slam event occurred which caused damage to the vessel. A design slam load case of 15,700kN was calculated using the structural finite element program NASTRAN that induced similar stresses in the vessel structure as were recorded during the severe slam event. Calculations of the vessel bending moment and shear force experienced during the severe slam event were compared with the DNV sag rule moment. Both the bending moment and the shear stress exceeded the DNV sag rule predictions. Thomas et al (2003) reported on the sea trials of an INCAT 86m catamaran. The data collected in the trials was analysed in a similar manner as presented in Thomas et al (2001) and the trends shown for the 86m vessel were generally similar to those displayed by the 96m vessel.

1.2.4. Full-scale trials summary

A review of the published literature involving full-scale slamming studies has been presented. Trials involving displacement mono-hulls, planning mono-hulls and catamarans are described. A number of main conclusions come out of this review. The state of the art of full-scale trials is to carry out strain gauge structural measurements combined with ship motion, sea state and hull surface pressure readings. Hull surface pressure readings, however, are problematic due to the highly localised nature of the transient pressures and thus difficult to measure. It was also found that slamming represents the greatest loading event that a vessel experiences during operations. The slamming loads were generally found to be centred in the forward portion of the vessel and that the stresses induced by slamming in this portion of the vessel had the form of a sharp spike followed by vibratory structural whipping. The stress induced by the slamming in the vessel structure is greatly influenced by the relative location of the slam load. Further from the location of the slam load the stress response is more dominated by the vibratory whipping response of the vessel rather than the initial stress spike. The severity of a slam is influenced by the relative velocity between the water surface and the ship keel or wetdeck. The greater the relative velocity the more severe the slam event. It has also been noted by numerous authors that slamming occurrence and severity is greatly influenced by the action of the vessel operator.

The full-scale trials results presented in this thesis are intended to provide additional full-scale catamaran slamming data for a high speed catamaran. Also, the relative motion between the instantaneous water surface and the wetdeck is examined in detail. A function is developed which describes this relative motion based on the full-scale results for the slam events. No previous detailed relative motion profiles describing the entry of the wetdeck during water entry as a function of time have been identified in the literature and this lack of data is addressed by this thesis.

1.3. Experimental Investigations of Slamming

A review of previous drop test experimentation and other salient experimentation investigating water entry is presented in this section. Drop tests of two and three-dimensional models into water are the principal experimental method of investigating the water entry process. Models are dropped into a body of water and the behaviour of the model during the entry process is measured. The model geometries for which previous experimentation has been published are rigid vee wedges, elastic vee wedges, rigid three-dimensional wedges with forward speed, rigid and elastic flat plates, cylinder models, a range of realistic hull forms, cones, spheres, highly elastic models and parabolic panels. Also for historical completeness the experimental impact of flying boat float hulls is also briefly

examined. Each of the drop test model geometries is considered in turn so as to allow an understanding of the development of drop test experimentation and the current state of the art to be illustrated. The originality of the drop tests involving catamaran with centre bow cross-section to be presented in this thesis is established and their significance in the context of previous drop test experimentation is identified.

1.3.1. Wedges

The impact of two-dimensional rigid vee wedges on water has been investigated extensively with experimental drop tests. The deadrise angles of the vee wedges in this review are stated as the angle between a horizontal and the underside of the vee wedge. This is consistent with the convention of von Karman (1929). Kreps (1943) drop tested 5.66°, 23° and 30° wedges and a disc. Kreps (1943) also conducted experiments with slotted 5.66° wedges, the size of the slots were varied from 2.4%, 10% and 33% of the wedge plan area. A disc with an aperture was also drop tested, the disc diameter was 120mm and the aperture diameter was 26.4mm. Bisplinghoff and Doherty (1952) tested 10°, 20°, 30°, 40° and 50° rigid vee wedges. Accelerations were recorded and high-speed photography was used to investigate the deformation of the free surface during impact. Bisplinghoff and Doherty (1952) unfortunately gave no information about the masses of the models tested. These tests were used to validate the theories of Kreps (1943), Wagner (1932), Sydow (1938), Mayo (1945), von Karman (1929) and a theory developed by Bisplinghoff and Doherty (1952). Each of these six theories were added mass theories and it was found that the added mass calculated by Kreps (1943) was greater than the added masses determined from experiment. The theory of von Karman (1929) calculated added masses which were slightly too low for all deadrise angles greater than 10°. The other four theories produced trends for the added mass, as a function of deadrise angle, which over estimated the added mass for deadrise angles less than 15° but under estimated the added mass for deadrise angles greater than 35°. These theories are discussed further in section 1.4.1. Borg (1957) experimentally investigated the unsymmetrical entry of a 45° rigid vee wedge and the symmetrical entry of an 80° rigid vee wedge. High-speed photography results recording the shape of the free surface are presented. The results of the drop tests were compared with a theory developed by Borg (1957) which used an exact relaxation solution for the flow field and incorporated an approximate closed form analytic solution for the free surface shape. Good agreement was found between the experimental and theoretical shape of the free surface. Greenhow (1987) experimentally examined the symmetrical high-speed entry of 60°, 81° and 45° rigid vee wedges. Results for the complete penetration of the free surface (that is the top of the wedge has submerged beneath the initial water surface) and for the separation of the jet from the wedge face were presented. Greenhow compared the experimental results with calculations based on the Cauchy's theorem method of Vinje and Brevig (1980) and there was good agreement.

The effect of trapped air during the entry of a vee wedge was examined experimentally by Chuang (1967). Chuang (1967) conducted a series of experiments with rigid 1°, 3°, 6°, 10°, 15° vee wedges and a rigid flat bottom model. Surface pressure and acceleration data was recorded. Photographs were taken during model impact to investigate the role of trapped air. The electrical resistance between two electrically isolated probes of thin copper sheet metal attached to the flat bottom model was also used to investigate the role of the trapped air during the slam event. It was found that models with a dead rise angle of 3° and higher did not experience significant air entrapment. The effect of the air entrapment was to reduce the maximum impact pressure experienced by the wedges as a function of dead rise angle. The wedges with dead rise angles of 3° experienced the highest pressures compared with wedges of any other dead rise angle. This indicates that the trapped air reduces impact pressures experienced by vee wedges and it is the case that the least amount of air is trapped when the wedge has a dead rise angle of 3°. The flat plate model experienced lower peak pressures than either the 1° or 3° vee wedge models. The result of this investigation was to provide a set of experimental data for estimating the maximum impact pressure due to rigid body slamming of wedges. These tests also identified that air trapped between the vee wedge and the water played a significant role in the impact process.

The effect of non-rigid panels on the vee wedge entry problem was experimentally examined by Hayman et al (1991). Hayman et al (1991) examined the behaviour of two non-rigid 30° vee wedge models during impact with water at tilt angles of 0° to 25°. One of the models was constructed from GRP sandwich material and the second model was constructed from stiffened aluminium. The models had a beam of 2.0m and a width of 1.5m and weighed 1350kg. Design was based on the 1985 DNV rules for high-speed light craft. Vertical and transverse accelerations were recorded as too were 8 surface pressure readings and numerous strain gauge measurements. The dynamics of the panels was investigated and the influence that the pressure spike experienced by wedges during impact had on local strain was examined. It was found that no conclusive statement of the effect of model elasticity on peak pressure could be made. Hayman et al (1991) also discusses the difficulties involved in measuring surface pressures and the importance of the selection of adequate pressure transducers and data acquisition rate was identified. This is because the peak spikes experienced were of very short duration.

Experiments involving the impact with water of three-dimensional rigid vee wedges with forward speed have been reported on by Stavovy and Chuang (1976) and Radev and Beukelman (1992). Stavovy and Chuang (1976) tested three 6ft long by 16in wide models. One model had a flat bottom, one a bottom with a 10° dead rise angle and one with a bottom with a dead rise angle of 0° at the stern and 20° at the bow. Models were tested at a range of forward speeds and with trim angles of 0° and 6°. Tests were made into calm water. It was found that peak pressure initially increases with impact

angle until a maximum was obtained at approximately 3°. The peak pressure then began to decrease. There was substantial scatter in the peak pressure results. The flat bottom model generally experienced the highest peak pressure. The experimental results were compared with a theory based on the Wagner (1932) impact theory and the Chuang (1969) cone impact theory. The theory agreed moderately well with experiment. The impact pressure due to the normal velocity component of the relative impact velocity was found to be approximately 100 times greater than the planing pressure due to the tangential component of the relative water surface velocity. Hence Stavovy and Chuang concluded that it was the relative normal velocity which was the most significant in determining the peak pressure experienced during impact. Radev and Beukelman (1992) experimentally examined the peak pressures and rise time of pressure experienced by 4 three-dimensional rigid metal wedges with dead rise angles of 0.0°, 0.5°, 1.0° and 10.0°. The wedges underwent a forced oscillating vertical motion and impacted calm water at forward speed. Several trim angles were tested. Radev found "the well known relation that the peak values of the slamming pressures are proportional to the squared value of the vertical speed." Moreover it was noted, "a very strong influence could be established with respect to the forward speed." It was found that as the trim angle increased the effect of the forward speed on the peak pressure also increased. This is of course consistent with the trend noted by Stavovy and Chuang (1976) with regard to the relationship between the relative normal velocity and the peak slamming pressure. Clearly the entry of vee wedges has been investigated comprehensively.

1.3.2. Flat plates

Drop tests have been used to experimentally investigate the impact of effectively rigid flat plates on water. Chuang (1966) drop tested effectively rigid two-dimensional flat plates impacting onto calm water. The pile up of water and the resulting trapped air was recorded with a high speed 16mm camera and surface pressure readings were also made. It was found that the peak pressure experienced by the plate was significantly less than the acoustic pressure limit ($\rho c V_o$) which limits the maximum pressure that a body experiences during water impact based on the compressibility of the water and the resulting propagation of the shock wave. Thus it was concluded that the trapped air layer had a significant influence on the behaviour of a flat plate during water impact. This was examined by measuring the pile up of water. Verhagen (1967) also drop tested effectively rigid two-dimensional flat plates onto calm water and made pressure and acceleration measurements. Verhagen observed that the pressure readings were initially zero at the start of the entry process and then increased to a maximum in a sharp spike. Following the maximum the pressure rapidly decreases until a minimum, which was negative and approximately a third of the peak pressure. The peak pressure then returned to zero and some minor oscillations were apparent. The results of these experiments were compared with a two part theory which combined the effects of the compressible trapped air layer and the added mass associated with the plate once contact with the water had occurred (discussed in section 1.4.4.2) and good agreement was found. Lewison and Maclean (1968)

drop tested two-dimensional flat plates and examined the surface pressure distribution along the centre line and at various transverse locations. Lewison and Maclean's (1968) model was 8ft by 10ft and had a clearance of $1/8^{th}$ inch between model side and tank wall. This was found to be a good approximation of a two-dimensional drop test. It was found that the pressure distribution was essentially constant along the centre line. In the transverse direction the pressure was lower at the sides of the model and higher in the centre. Smith, Stansby and Wright (1998) examined the impact of a horizontal flat plate with longitudinal side plates at forward speed onto wave crests. The three plates tested by Smith et al (1998) were 1150mm long and had widths of 225, 410 and 565mm and mass of 57, 75, 93 and 111kg. It was observed that the peak acceleration of the plate was reduced by 20% if the plate was initially wet and this effect was attributed to surface tension and/or surface roughness. The experimental results were use to develop empirical relationships between relative velocity, slamming coefficient and wave steepness. It was found that when creating non-dimensional coefficients it was the relative velocity between the wave and the flat plate that needed to be used to achieve the best collapse of normalised data.

The effect of varying the amount of trapped air beneath a flat plate was examined by Lewison (1970) who tested two-dimensional flat plates with small flanges attached to the sides of the plate to increase the amount of trapped air. The plate dimensions were 10ft by 7ft 9inches and the attached flanges were set at three different heights, 0.0, 1.5 and 3.0inches. It was found that the presence of the flanges significantly reduced the peak pressure experienced at the centre of the plate and that the larger flanges, and thus the greater the amount of trapped air, the more substantial the reduction in peak pressure. The results were compared with both a one-dimensional and a two-dimensional theory. The two-dimensional theory calculated significantly more accurate results than the one-dimensional theory. It was also found "that peak pressure increases linearly with drop test height, and therefore with the square of impact velocity, within the range investigated." These experiments confirmed the significance of the trapped air layer.

The slam loading of wetdeck panels has been previously examined. An elastic three beam flat plate model was tested by Haugen, Faltinsen and Aarsnes (1997). This model was designed to represent the plating, including longitudinal stiffeners, of a wetdeck of a catamaran. The plate model was impacted with five different regular waves and with calm water. The plate was tested at zero pitch angle and zero forward speed and also with a pitch angle of 5.8° at a forward speed of 3.5m/s. Vertical drop speeds varied from 1.0m/s to 3.2m/s. Pressure, acceleration, displacement, strain, wave profile and wetted surface measurements were made. It was found that "when the impact loads became high, local hydroelastic effects are important". It was also found that the normal relative velocity between the water surface and plate had a more significant effect on the loading experienced by the plate than merely the vertical impact velocity alone. The results were compared with an improved theory of

Kvålsvold (1994) and good agreement was found. Slamming tests of two essentially full-scale wetdeck panels of a surface effect ship were made by Katsaounis and Samuelides (1999). One of the panels was constructed out of 12mm aluminium plate with stiffeners and the other model was of sandwich construction with a 140mm balsa core and a skin of 21 CFRP layers supported on a steel frame. Drop tests were made onto calm and disturbed (sinusoidal waves with a wavelength of 1.5m and height of 0.07m) water surfaces. Pressure, strain and acceleration measurements were taken. It was found that the strain was linearly proportional to the pressure experienced during this impact. It was also found that the "slams on the disturbed water surface were significantly different from those of the calm water impact. The recorded maximum pressures were either greater than the calm impact results (impacts on wave crests), or lower than them (impacts on wave valleys)." This observation once again illustrates the significance of the trapped air layer or cushion. It was observed that the cushion of trapped air between the models and the water surface had "a higher elasticity than the structural elasticity" of either model. The usefulness of drop test results for full-scale design was considered and it was noted that additional results concerning the amount of trapped air and the impulse experienced by the panels was required. Dambra, Hoogeland and Vredeveldt (2000) drop tested flat elastic steel panels onto calm water at 0° and 2°angles of impact. Pressure and acceleration data were recorded. Considerable scatter was found in both the pressure and acceleration data. The drop test at 2° experienced higher peak pressures than the test at 0° and this observation is consistent with trends observed for wedges by Chuang (1967) and is attributed to the venting of the air layer and thus to reduction of the air cushion effect.

1.3.3. Cylinders

Some experimental work has been conducted to investigate the impact of circular cylinders on water surfaces. Faltinsen, Kjaerland, Nøttveit and Vinje (1977) impacted, at constant speed, rigid two-dimensional circular cylinders with calm water. Three cylinders with diameters 0.350, 0.275 and 0.200m were tested. Force, stress and water surface deformations were investigated. It was found that the force experienced by the cylinder as it penetrated the water surface was initially high and then reduced to a minimum before increasing again to a second maximum. The results were compared with an added mass theory with satisfactory agreement. Sarpkaya (1978) investigated the impact of a sinusoidally oscillating free surface, located so that the cylinder bottom was initially in contact with the mean water level, on both smooth and rough cylinders. Force measurements were recorded. The forces experienced by the cylinders were in two parts: a slam load and a drag load. The change in cylinder surface roughness had virtually no effect on the slam coefficient. However the drag coefficient increased. Millar (1978) examined the wave slamming loads on rigid horizontal circular cylinders. Millar compared his experimental results with a theory based on the added mass theory of von Karman (1929). Theoretical results compared well with experiments and were similar to those of Sarpkaya (1978). Shibue, Ito and Nakayama (1994) conducted drop test experiments with two-dimensional cylinders onto calm water. Two cylinders of radius 312mm were tested. One cylinder

had a wall thickness of 5.1mm and was made of mild steel, the other model was made of aluminium with 1.0mm wall thickness. The dynamic deformation of the models was found to influence the loading experienced by the models. However the two models were tested with different mass per unit lengths and hence the results were not conclusive.

1.3.4. Varied model geometries

A number of drop tests involving varied geometries have also been conducted. The geometries tested have included a cone, a sphere, a flat plate and a wedge with attached elastomeric layers and a paraboloidal panel. Cones were drop tested by Chuang and Milne (1971) to investigate three-dimensional effects of slamming. Cones with dead rise angles of 1°, 3°, 6°, 10° and 15° and a circular flat plate were tested. Surface pressure, acceleration and air entrapment were measured. It was found that cones trap less air than wedges with the same dead rise angle. Generally the maximum pressure experienced by a cone was found to be less than for a corresponding wedge except for the case of a 1° dead rise angle. Moghisi and Squire (1981) drop tested spheres into mixtures of water and Golden Syrup at various temperatures. The viscous forces experienced by the sphere during impact were quantified and found to be significant in these tests due to the high viscosity of the fluid used. Ando (1989) investigated the cushioning effect of an elastomeric layer attached to the bottom of a flat plate during a drop test onto calm water. The peak acceleration was found to be a strong function of the elasticity of the elastomeric layer. It was shown that "an elastomeric layer of optimal modulus of elasticity could significantly reduce the slamming forces on flat bottoms falling vertically on a water surface." Ando (1989) also examined the effect on the peak acceleration of a 10° wedge with elastomeric layers attached. It was found that the elastomeric layers increased the peak accelerations experienced by the wedge. This was attributed to the cambering of the wedge surface. Wraith, Brown, Joubert and Yan (1993) discussed the design of a drop test facility. Wraith et al (1993) also developed a dimensional analysis for model scaling for the drop testing of paraboloidal panels with two radii of curvature. Brown, Wraith and Joubert (1999) conducted drop tests of paraboloidal panels with two radii of curvature. Pressure and acceleration data were recorded. The experimental results were compared with an added mass theory and good agreement was found. It was found that the effect of hull curvature was not strong. It was also commented that for application to actual ship problems it is the relative curvature between hull and water surface that is significant. The effect of model mass was examined and this was found to have a small effect on peak pressure, although a greater effect on acceleration was observed.

1.3.5. Realistic hull sections

Realistic hull sections have been tested by a number of experimenters. Two inflatable Mariner ship sections were drop tested by Chuang (1969). It was found that the inflatable fabric hull sections (hull

sections which were highly elastic) experienced considerably lower pressures than those experienced by a rigid body of the same shape. This indicates that the elasticity of a drop test model has a significant influence on it performance during drop testing. A 1/15 scale model of a three dimensional bow form was drop tested from various heights and a several impact angles by Hagiwara and Yuhara (1976). Maximum impulsive pressure results were compared with those obtained for a 1/3 scale model of the same bow form. It was found that the relative face area of pressure transducers used in testing had a significant impact on the peak pressures that were measured. This was attributed to the averaging effect of pressure transducer face area, which was not scaled with model scale. Yamamoto et al (1985) conducted drop tests of a two-dimensional realistic bow flare section. This work was done as part of an investigation of the sinking of a container ship in the North Pacific Ocean. Drop tests were conducted both symmetrically and at a number of inclination angles. Pressure and velocity measurements were made and these were compared with the theories of von Karman (1929), Wagner (1932) and Chuang (1970). Zhu and Faulkner (1994), Zhu and Faulkner (1994a) and Zhu and Faulkner (1995) conducted three-dimensional drop tests of a SWATH like model to investigate the wetdeck slamming of twin hull vessels. Dynamic effects of the model panels and the air cushioning effect were found to be significant. Pressure, strain and acceleration data was recorded. The pressure transients presented all displayed a very sharp pressure spike, and the corresponding strain spikes were equally sharp. These results were similar to the simple two-dimensional wedge entry process. Zhao, Faltinsen and Aarsnes (1997) undertook drop tests of a 30° wedge model and a realistic bow flare cross section model. Pressure, wetted surface, vertical force, vertical drop velocity and vertical acceleration data was collected. These results were compared with two theories, a modified Wagner (1932) theory and a fully non-linear numerical simulation. The significance of separation during the entry of a drop test model was noted. Separation was identified in both the theory and the experiment as having a significant influence on the behaviour of the hull section during entry.

An investigation of the hydro-elastic effects of bow flare slamming on a fast mono-hull was conducted by Kapsenberg and Brizzolara (1999) using a three-dimensional elastic free running scale model. The tests were conducted at scale speeds of 40kts in bow quartering seas. The pressures induced by the slamming were measured in two ways. The first was by use of traditional high resonance frequency pressure gauges with small diameter sensitive area. The second method of measuring pressure was square sensors based on the scaled actual properties and dimensions of the full-scale ship panels. The sensors were constructed in this manner so that the local slam loads on a particular full-scale ship panel could be investigated. The strain induced in the square sensor panels due to slamming loads were used to determine the slam pressures. The resonance frequency of the senor panels was varied from 200 to 600rad/s and it was found that this had very little effect on the slam pressures measured. The deformation of the sensor panels was measured using an accelerometer and it was found that the rise time of pressure spike was an order of magnitude higher than the deformation velocity than the panel indicating a quasi-static situation for the fluid-structure interaction. It was also found that the rise time for the pressure spike measured by the traditional pressure gauge was significantly higher than that measured by the sensor panel. This effect was attributed to the averaging of the pressure spike over the greater area of the panel sensor. Kapsenberg

and Brizzolara (1999) suggested that the lower pressures measured by the panel sensors compared with the smaller traditional sensors are a more appropriate measure of the pressures experienced by ship panels and thus have more practical meaning for the designer.

1.3.6. Flying boat float tests

The systematic investigation of slamming was initially undertaken by von Karman (1929), work which was motivated by the impact of flying boat floats on water. The landing of flying boats on water displays many similarities with the slamming of ship hulls and for this reason a brief summary of the testing involving flying boats is presented. The National Advisory Committee for Aeronautics (NACA) conducted a number of drop tests and full-scale trials of flying boat floats to investigate this type of water impact event. Thompson (1930) conducted full-scale trials of a Curtiss H-16 flying boat. The global accelerations and surface pressure distribution were measured during landing, planing and plowing. Batterson (1944) drop tested a flying boat float model with forward speed at a range of masses and trim angles into initially calm water. Relationships between resultant velocity, model mass, flight angle, trim angle and impact normal accelerations were measured. Miller and Merten (1952) conducted experimental drop tests at forward speed of a rigid prismatic float connected to a rigid upper mass by an elastic structure. This mass-spring-mass model was used to investigate structural flexibility and hydrodynamic loads. The elasticity of the model reduced accelerations at the centre of gravity by 6% to 25%. Mayo (1952) reports on the impact of a flying boat landing on the front of a wave. Milwitzky (1952) presented a summary of experimental drop tests of model flying boat floats conducted by NACA.

1.3.7. Experimental slamming summary

A review of the published literature involving model drop tests has been presented. Experiments examining inelastic and elastic vee wedges and flat plates have been identified as too have experiments involving cylinders, cones, spheres and highly elastic models, parabolic panels, flying boat floats and realistic hull sections. The state of the art of drop tests has been found to record model acceleration, surface pressures, and water surface deformation during the entry process. For elastic models strain measurements are also made. It has been found that the loads on the models are due principally to hydrodynamic effects, except in those cases when a significant amount of air became trapped between the model and the water surface. In these cases (for example flat plate impact), the compression of the air has a significant influence on the water entry process. During the entry of an inelastic catamaran cross section model a significant amount of air may become trapped. This effect, along with the effect of geometric form is the principal attention of experiments presented in this thesis. No published results of drop tests of this double arch catamaran geometry have been found and it is this deficiency in experimental results that this project addresses.

1.4. Theoretical Analysis of Slamming

A review of the theoretical approaches and methods used to investigate slamming is presented in this section. The review is organised in terms of the types of problems examined. The problems of wedge water entry, cylinder entry, flat plate impact, the impact of spheres, cones and curved panels are each examined in turn. Methods used to investigate the impact of arbitrary shaped bodies and realistic hull forms are then presented. The application of slam theories to the full ship problem is then examined.

1.4.1. Wedge water entry

The water entry of a wedge has been investigated extensively. The wedge entry problem shows substantial similarity to practical ship slamming problems and is also amenable to analysis due to its simple geometry. One approach to examine the wedge entry problem is to consider the transfer of momentum between the wedge and the fluid by considering the added mass associated with the wedge. Other approaches to the water entry problem of a wedge are self similarity based solutions, analytic and quasi-analytic solutions and asymptotic expansion based solutions. Each of these types of solutions are reviewed.

Added mass theory has been applied to the problem of the water entry of wedges. The impact of wedges was examined first by von Karman (1929). This work was motivated by the problem of the impact of flying boat floats on water. The added mass was calculated from the velocity potential solution for a flat plate impacting with water. Von Karman (1929) also considered flat plate impact with water and this was done by examining the pressure acting on the flat plate which was found to be a function of the ratio of the impact velocity and the velocity of sound in water. The effects of the elasticity of the plate were identified as being significant but were not examined quantitatively. Wagner (1932) extended the von Karman (1929) analysis for the wedge entry problem by including the effects of the upwash of water around the wedge during impact. The pressure distribution over the wedge surface was also calculated from the velocity potential solution for the flow about the flat plate. A graphical solution for wedge water entry problem free surface shape was developed by Pierson (1950) who determined the shape of the free surface by an iterative method based on continuity, dynamic similarity and irrotational potential flow. The potential function was solved over the flow field using Cauchy's theorem and graphical integration was used to calculate the pressure and force acting on the wedge surface. Pierson (1951) used the theory developed in Pierson (1950) to calculate the added mass of a wedge entering water. Pierson solved for the added mass by graphical integration of the potential distribution over the wedge surface and free surface. This added mass was compared with those of von Karman (1929), Wagner (1932), Kreps (1943), Sydow (1938), Mayo (1945) and

Monaghan (1949) for deadrise angles between 10° and 60°. Generally good agreement was observed between this theory and those of Kreps (1943), Sydow (1938), Mayo (1945) and Monaghan (1949). An added mass theory was also used by Bisplinghoff and Doherty (1952) to model vee wedge water entry. In this theory the added mass was calculated from the kinetic energy of flow about a wedge that was found from the velocity potential solution for an expanding prism. An approximate correction of the deformation of the free surface was also applied. The theory was compared with the theories of von Karman (1929), Wagner (1932), Kreps (1943), Sydow (1938) and Mayo (1945). Reasonable agreement was observed between this theory and those of Sydow (1938) and Mayo (1945). Fabula (1957) examined the entry of rigid two dimensional bodies into water including wedge geometries. The approach adopted was an added mass approach. The added mass was calculated from the flow about an ellipse fitted to have the same width and penetration as the body impacting with the water. No account of the elevation of the free surface was made (as was the case in the theories Wagner (1932) or Bisplinghoff and Doherty (1952) for example). The theory was found to give good results for wedges and also elliptical cylinders. Payne (1981) reviews added mass theories for the wedge entry problem and concluded that the approach of von Karman (1929) was adequate and simple. Payne includes the force component acting on the wedge due to the spray sheets. This was done by estimating the volume of fluid in the spray sheets from Bisplinghoff and Doherty (1952) approximate free surface elevation expression and then applying continuity to determine the amount of fluid in the jets. A modest improvement is seen as a result of this improvement. Payne also used the method of Taylor (1930) as a second method to calculate the added mass and some improvement was seen compared with test data.

The water entry of a wedge shows self similarity and this property has been used by several researchers to investigate the wedge entry problem. Garabedian (1953) considered the oblique water entry of a wedge using a self similar solution and complex theory. A conformal mapping approach was used. Mackie (1969) used the property of self-similar flow theory and complex variable theory to solve the wedge entry problem. The convex nature of the free surface was examined as too was the angle formed by the jet with the wedge underside. The theory was not compared with experimental results. Some contributions to problems involving similarity of flows including a free surface were presented by Dobrovol'skaya (1969) for flow about wedges. The formulation was based on the Wagner (1932) function that allowed the problem to be reduced to a singular integral equation. The method developed can be used to solve problems where the flow region is bounded by a free surface and uniformly moving (or fixed) rectilinear impermeable boundaries. Johnston and Mackie (1973) used Lagrangian coordinates and the concept of self similarity to solve the constant velocity wedge entry problem. The results of the analysis for the contact angle between the water surface and the wedge side are compared with the solution of Dobrovol'skaya (1969) and some significant differences are observed.

An exact relaxation solution for an unsymmetrical wedge entry problem and also a closed form analytical solution for the approximate shape of the free surface streamline for a thin wedge was presented by Borg (1957). An approximate solution for a blunt-nosed wedge impact was also presented. Results were compared with experimental results for the wedge entry problem. Free surface profile results show good agreement with theory. Borg (1959) presented an approximate solution for the pressures and forces acting on a small deadrise angle wedge. Closed form analytical expressions are given for the maximum pressure and also the total vertical force. The results were not compared with experiments or other theories

A linearised theory for the systemic wedge entry problem and also the entry of a thin wedge and for cone entry was presented by Mackie (1962). Analytic expressions for the free surface are determined. A justification of using a linearised free surface approximation was presented. Results of the analysis were not compared with other theories or experiments. Pinsent (1966) like Mackie (1962) presented a linearised solution for the wedge entry problem. The fluid however was assumed compressible and the wedge was assumed to enter at significant Mach number and thus this approach is of limited interest for ship slamming. It was found however that deformation of the free surface reduced as the Mach number increased and also the presence of the free surface acted so as to lower the pressure differences arising from compressibility.

A quasi analytic solution to the constant velocity wedge entry problem using numeric conformal mapping approach was presented by Hughes (1972). An example calculation was presented for a wedge with a 45° deadrise angle. Results for the pressure distribution over the wedge surface were presented and compared with an analytic solution with good agreement. A sensitivity analysis of the parameters, which describe the wedge entry problem, was also carried out and the solution procedure was found to be robust.

The approach of Vinje and Brevig (1980) based on Cauchy's theorem was used by Greenhow (1987) to model the entry of a wedge into calm water. Special attention was applied to the intersection between the free surface and the body surface. The effects of the detail of the jet flow and its separation from the wedge surface were examined. Results were in qualitative agreement with experiment.

Extensions of the theory of Armand and Cointe (1987) for cylinder entry to the wedge entry problem have been developed by Howison, Ockendon and Wilson (1991) and Faltinsen (2002). Howison et al (1991) conducted an analysis of the wedge entry problem for small deadrise angles and extended the

asymptotic expansion solution method of Cointe and Armand (1987) to non-self similar motion. Air cushioning and liquid-liquid impact were also considered, as too was a generalised three-dimensional impact problem. Theoretical pressures against time histories are compared against some experimental results with reasonable agreement being obtained. Faltinsen (2002) developed a matched asymptotic expansion for the water entry of a wedge with a finite deadrise angle based on the theory of Armand and Cointe (1987). The results of the analysis are compared with the similarity solutions of Dobrovol'skaya (1969) and the results of Wagner (1932) amongst others. It was observed that the theory produces good results.

1.4.2. Three-dimensional prismatic wedges

The impact of three-dimensional prismatic wedges has been the focus of three studies. The impact of a prismatic float connected to a rigid upper mass by a spring was considered by Mayo (1952). The hydrodynamic impact loads were calculated using the added mass theory of Mayo (1945) in which the added mass associated with a section of the prismatic float was calculated from the potential solution for a triangular prism. It was found that the two mass system (1 mode) was not an adequate model for the landing of a flying boat floats in which the higher modes were found to have a significant effect. Schnitzer (1953) presented a solution for loads on prismatic bodies. A two-dimensional added mass calculation was used with a correction for three-dimensional effects. The added mass of each section was calculated from the solution for a prismatic vee-section. The theory was used to predict the behaviour of chime-immersed flying boat floats during water landings and fair agreement was observed compared with experiments. The impact of a three-dimensional vee wedge prism was modelled by Beukelman (1980) using a two-dimensional strip approach. The average slam pressure experienced by sections of the prism during forced heave and pitch in calm water was calculated. The slam pressure experienced by a section was calculated by considering the damping force, buoyancy force and the rate of change of added mass of the section. The added mass for each hull section was calculated the using the Frank close fit method (Frank and Salvesen 1970). The effect of forward speed was examined and it was found that the theory agreed well with experiments involving a segmented model.

1.4.3. Cylinder water entry

The water entry of a cylinder has been examined by a number of researchers. This water entry problem shows a number of similarities to the slamming of a ship section and is for this reason of interest. Two general approaches to the cylinder entry problem have been used: added mass formulations and theories based on asymptotic expansions to solve for the velocity potential.

Added mass theories have been used to model the water entry of circular cylinders. An added mass theory for the slamming of a circular cylinder in the splash zone of a wave was presented by Kaplan and Silbert (1976). The load on the cylinder was calculated from the sum of the buoyancy force and the impact force. The impact force was calculated from added mass theory in which the added mass of a segment of partially submerged circular cylinder was obtained from the Taylor (1930) added mass result obtained from a conformal mapping solution. The results of the analysis were used to conduct a statistical analysis of the impact loads on a horizontal platform member and thus allowed an estimate of fatigue life and also the maximum loads to be made. An added mass theory presented by Sarpkaya (1978) also utilised the Taylor (1930) added mass expression to model the impact of a cylinder on a sinusoidal oscillating free surface. Drag forces were also included in the calculation. The theory was used to determine slamming force coefficients. Wave slamming loads on horizontal circular cylinders were investigated by Millar (1978). Slam, buoyancy and drag loads resulting from the wave actions were considered. The slam loads were calculated from the von Karman added mass method with a modification to account for the infinite acceleration that is calculated when the von Karman (1929) added mass approach is used for the initial stage of the entry process of a cylinder. The modification assumed that the rise time for the slam force could be calculated by considering the motion of a shock wave propagating in the water. Furthermore it was assumed that the flow field behind the shock was that given by the incompressible flow solution. From this analysis it was shown that the rise time for peak force was of the order of the time taken for the shock to travel about 1/5 of a cylinder diameter. If the Taylor (1930) added mass expression is used (for example Kaplan and Silbert (1976)) then the acoustic modification is not required as the Taylor (1930) added mass expression is differentiable regardless of the cylinder penetration depth and thus the infinite acceleration does not arise. Despite this good agreement with experiment was found. A summary of added mass expressions for cylinder water impact, water exit and cylinders near solid boundaries was presented by Greenhow and Yanbao (1987). They use these added mass expression to examine the slamming of cylinders and to examine the effect of the upwash of the water surface.

An asymptotic expansion was used by Armand and Cointe (1987) and also Vorus (1996) to solve for the impact of a cylinder on water. Armand and Cointe (1987) match an inner domain solution at infinity and the outer domain solution near the singularity (jet region) so that they have the same behaviour. The impact force was then calculated. As a first approximation a first order impact force was found from an integration of the first order outer solution. The first order solution for the slamming force coefficient was found to be 2π, which corresponds to the Wagner (1932) result. A more accurate, second order impact theory was also calculated. In this more sophisticated calculation the second order outer problem was solved for using a second order Taylor expansion of the boundary condition which yields a total impact coefficient of 2π less a second order correction term. Cointe (1989) extends the theory of Armand and Cointe (1987) to model the impact of a spilling breaker on a cylindrical marine structure. Vorus (1996) makes use of a uniform first-order geometric linearity, (that is the cylinder is modelled as a flat plate expanding on the undisturbed free surface). This

assumption has been used extensively in the Wagner (1932) class of asymptotic solutions of which this theory is an example. The flow along the section surface was modelled with a spray root offset and the free surface flow was calculated from the dynamic boundary condition. The theoretical formulation was solved numerically and the theory was applied to cylinder, wedge and generalised geometric forms with good results.

The effect of elasticity in the cylinder impact problem was studied by Faltinsen, Kjaerland Nøttveit and Vinje (1977) who presented a solution for the impact with water of both elastic and inelastic horizontal cylinders of finite length. The forces acting on the cylinder were assumed to be a hydrostatic force and a force due to the variation of the added mass associated with the cylinder. The added mass of a section of the cylinder was calculated from the potential function with $\phi = 0$ on the mean free surface. The potential function was solved numerically by distributing sources and dipoles over the average wetted body surface. The elasticity of the cylinder in the longitudinal direction was included in the theory by considering the cylinder as a slender beam, fixed at both ends that deflected as it entered the water. The cross section of the cylinder was assumed not to vary. The velocity of a cylinder section due to its deflection as a function of length along the cylinder was combined with the constant entry velocity and it was this velocity, and corresponding displacement value that was used to calculate the forces acting on a section of cylinder. The theory was for constant velocity entry processes. The theoretical results were compared with experiment and found to under estimate the stresses experienced by the cylinder.

1.4.4. Flat Plate Impact

The impact of a flat plate on water has received considerable study. This has been motivated by the need to understand the loads experienced by hull panelling during slamming. This section considers firstly the deformation of the free surface caused by the venting of the air from beneath the plate as it approaches the water surface. Secondly the theories dealing with the forces experienced by inelastic plates when they come into contact with water are considered. Finally the role of elasticity in flat plate impact is considered.

1.4.4.1. Venting of air during flat plate impact

The effect of the trapped compressible air layer between a rigid flat plate and an initially flat water surface was examined by Johnson (1968). Two models were presented. In the first model the water surface was assumed not to deform and in the second model the water surface was assumed to deform in a manner described by the solution of Wehausen and Laitone (1960). The air was modelled as a

two dimensional inviscid compressible flow and these equations were solved numerically. The equations describing air flow were solved using Saucer's method of near characteristics (Saucer 1962,1963). It was found that the assumption to neglect the deformation of the free surface was such that the theoretical results did not match experimental results very well. When the free surface was allowed to deform, the solution used to model this deformation was found to be inappropriate. This was because it did not model the deformation of the free surface near the edge of the plate adequately and this was a critical region in determining how the trapped air vents into the surrounding environment

The cushioning effect of air during the initial stages of water impact of an inelastic flat plate was also examined by Lewison and Maclean (1968). Three different air flow models were used in this study: a simple one-dimensional theory, an improved one-dimensional theory and a two-dimensional theory air flow model. The deformation of the water surface resulting from the increased surface pressure was solved using a Cauchy theorem. The simple one-dimensional air flow model neglected the sideways movement of the air, and thus calculated a pressure that acted over the entire plate surface. The modified one-dimensional theory assumed that the average pressure on the plate was some fixed proportion of the centre line pressure. In the two-dimensional theory the air flow vented from the edge of the plate was calculated both as a function of time and distance from the centre line of the plate. The experiment and theoretical pressure against time records show good agreement for the two-dimensional air model, but not quite as good for the two one-dimensional models.

The problem of the deformation of the free surface caused by an increase in air pressure as a flat plate or low deadrise angle wedge falls toward an initially calm water surface was examined by Falch (1989). The water motion was solved for using a boundary element method and the compression of the air layer between the body and the water was modelled with a one-dimensional theory. The simulation terminated when the water and the body came into contact. The compressible air was modelled as either isentropic or isothermal depending on the simulation. Results for the impact of a flat plate and two wedges of deadrise angles 0.5° and 1.5° were presented. It was found that the pressure distribution induced was strongly effected by the deadrise angle.

1.4.4.2. Flat plate impact theories incorporating water contact

Once contact is made between an inelastic flat plate and the water the direct hydrodynamic interaction between the flat plate and water needs to be incorporated into the impact theory, this is in addition to the interaction between the water surface and the compressible trapped air layer. Four solutions have

been presented to this problem. Each of these solutions makes use of the von Karman (1929) added mass theory and models the trapped air as an effective spring.

A semi-empirical theory investigating the role of the trapped air layer during flat plate impact with water was presented by Chuang (1966). The theory equates the impulse experienced by a von Karman (1929) added mass term of width equal to that of the flat plate with the impulse produced by the pressure force acting on the flat plate due to the compression of the trapped air layer. The time variation of the pressure in the trapped air layer was determined empirically.

A more comprehensive flat plate water impact theory was developed by Verhagen (1967) who used a two stage theory to model the process. The first part of the theory modelled the deformation of the free surface caused by the venting of the air between the plate and the water surface. It was found that the effect of the air layer between the fluid and the plate and the deformation of the free surface needed to be taken into account to adequately model the impact process. Verhagen modelled the air flow as a time varying one-dimensional compressible isentropic flow. The deformation of the free surface resulting from the increased air pressure was calculated by assuming that the fluid flow was a potential flow. The free surface condition was linearised and the solution was found using the method of Wehausen and Laitone (1960). The air pressure distribution at the edge of the plate resulting from the air venting into the surrounding atmosphere was assumed to reduce from the elevated value to atmospheric pressure in a linear manner over a length proportional to the distance of the plate above the undisturbed water surface. Once the plate came into contact with the deformed water surface and the air ceased venting from beneath the plate a second theory was used to model the impact. This part of impact was modelled using an added mass theory. The trapped air layer was modelled as an isentropic, compressible spring between the plate and an added mass term equal to the von Karman (1929) added mass. Conservation of momentum was then used to formulate equations for the pressure and hence force experienced by the plate.

A two stage impact theory was used by Koehler and Kettleborough (1977) to consider the impact of a flat plate and wedges with small deadrise angle with water. This theory shows a number of similarities with the theory of Verhagen (1967). During the initial approach of the section towards the water the trapped air between the section and the fluid surface was modelled using a one-dimensional theorem derived from the continuity equation and a momentum equation. The water surface was allowed to deform due to the variation of the surface air pressure. The water flow field was solved numerically by solving the Navier-Stokes equations on a rectangular grid. The shear forces at the air/water interface were calculated from boundary layer relations. Once contact occurred between the water surface and the section a second theoretical model is used which was similar to that of Verhagen

(1967) was used to model this stage of the entry. It was found that a slight variation 0.25° creates a substantial change in the pressure distribution and the magnitude of the pressure experienced by the underside of the section.

A two stage theory to model the impact of a flat plate on water was also presented by Gallagher and McGregor (1985) who used the method developed in Gallagher (1983) to model a number of slamming simulations. Gallagher (1983) developed a finite difference, time marching solution for the water entry problem. The solution allows for the calculation of the pressure transients acting on the body as it enters the water. This pressure field was calculated in three stages: an acoustic pressure, a hydrodynamic pressure and a hydrostatic pressure. These three pressure fields were then combined using the principal of superposition. The accuracy of the scheme was enhanced by ensuring conservation of energy using a variational energy algorithm. Gallagher and McGregor (1985) considered the impact of a flat plate. The force acting on the plate was modelled as a two stage process. The initial entry up until contact of the water with the plate, including the effects of the trapped compressible air layer was modelled with the finite difference code. Once contact with the water had been made a second theory was used. This theory was one in which the trapped air was modelled as a spring, at one end of which was the plate mass and at the other end was an added mass equal to the von Karman (1929) added mass. This theory was also used to model the impact of a wedge and a cylinder on water.

1.4.4.3. Elastic flat plate impact

The impact of elastic flat plates on a water surface has been the subject of a number of studies. The hydroelastic slamming of wetdeck panels was investigated by Kvålsvold and Faltinsen (1993,1995). The hydrodynamic loads were calculated from the velocity potential which was solved using an asymptotic method valid for small local angles. The motions of the panel during impact were calculated from a frequency domain ship motion program. The deformation of the plate was modelled by considering it as a Timoshenko beam and solving for the dry normal modes. It was found that the local hydroelastic effects of the wetdeck structure can significantly reduce the hydrodynamic impact loads on the wetdeck. Faltinsen (1997) presented an analysis for the impact of an elastic beam on water. The impact problem was modelled as a two stage process. Firstly an initial structural inertia phase was considered and then a subsequent free vibration phase was modelled. The effect of forward speed was included in the analysis. It was found that the stresses induced in the plate were linearly proportional to the impact velocity. The stresses were not sensitive to the radius of the wave nor the where the wave initially impacted on the plate. Korobkin (1996a) presented an acoustic approximation for the slamming of a slightly elastic flat plate colliding with an ideal weakly compressible liquid. Korobkin (1998) examined the impact of a compressible liquid on an elastic plate. The effect of air on the impact process was investigated. It was found that the analysis did not

reveal any great advantage of utilising the air cushioning effect. Dambra, Hoogeland and Vredeveldt (2000) considered the full-scale slamming of ship panels using the finite element code MSC.Dytran. The air cushion effect was accounted for in the model. The fluid-structure interaction was modelled using a general coupling algorithm. This algorithm combined an Eulerian mesh for the fluid with a Lagrangian mesh for the structure. When these two meshes come into contact the interaction was accounted for by forces that caused a distortion of the Lagrangian and Eulerian meshes. Simulations were conducted for a strengthened aluminium plate impacting calm water at 0° and 2°. Results were compared with experiment and agreement was observed.

An approximate method to estimate the dishing of flat panels due to slamming pressure loads was developed by Jones (1973). The pressure loads were approximated by a triangular pressure pulse. The maximum pressure obtained during the pressure pulse was calculated using the method of Ochi (1971). The period of the pressure pulse was calculated by considering the natural frequency of a fully clamped plate and also a simply supported rectangular plate. The dynamic behaviour of the plate was examined. The results of this analysis were compared with the experimental results of Clevenger and Melberg (1963) and agreement was found.

The effect of attaching a highly elastomeric layer to a rigid flat plate was considered by Ando (1989). The transfer of momentum between the plate and the water during impact was modelled using an added mass theory based on von Karman (1929) added mass theory. The elastomeric layer and also the trapped air bubble were modelled as a spring. The amount of trapped air was found empirically and it was assumed to compress isothermally. There was good agreement between theory and experiment. The optimum properties of the elastomeric layer were also determined so that the flat plate would experience minimum peak acceleration.

1.4.5. Sphere, cone and curved panel impact

Several theories examining the impact of spheres on water have been presented. An added mass theory was developed by Trilling (1950) to model the impact of an arbitrary shaped three-dimensional body, impacting at an arbitrary angle onto water. The approach adopted was to approximate the entry of an arbitrary shaped body by an ellipsoid of identical depth of penetration, length and submerged volume. The potential function for the flow about the ellipsoid was then solved using a linear boundary condition on the free surface and neglecting the splash. The theory was used to model the entry of a sphere impacting at 45° and results compared favourably with experiments. The added mass approach was also used by Moghisi and Squire (1981) to model the impact of a sphere on a viscous fluid. The added mass was calculated from the theory of Shiffman and Spencer (1945a,b).

Good agreement was observed between experiments and the theory. The oblique water entry problem of a rigid sphere into an ideal incompressible fluid was studied analytically by Miloh (1991). The solution method was to develop analytical asymptotic expressions for the horizontal and also the vertical added mass coefficients by considering the motion of the fluid resulting from an impulsively started partially submerged sphere. The free surface was assumed flat and equipotential and thus the time dependent vertical and horizontal added masses were calculated. Results were compared with a numerical exact solution and good agreement was observed. A solution for the impact of a half-sphere floating on a liquid surface and also the water impact of the body with small deadrise angle was presented by Korobkin (1995). The acoustic effects were included in the analysis.

A general expression for the pressure distribution on a cone penetrating a water surface was developed by Chuang (1969a). This analysis was similar to that of Wagner (1932) for the vee wedge entry problem. The flow about a cone was idealised as a flow about a flat circular disc. The stream function was found for this flow regime from which the water behaviour for the flow about the cone was determined. The pile-up of water around the cone was also calculated from the stream function by integrating the vertical velocity in time on the undisturbed water surface. The unsteady hydrodynamic impact pressure distribution was found from the Bernoulli equation. The theoretical results were compared with the two dimensional wedge solution.

The water entry of panels curved in two axis was examined by Brown, Wraith and Joubert (1999) using a generalised von Karman (1929) analysis. The expression for the added mass was based on the added mass half circle of von Karman (1929) but was generalised for the three dimensional problem to have the form of a half ellipsoid with minor and major axis related to the curvature of the panel. Acceleration and average pressure results compared well with theory.

The impact of rigid blunt and pointed bodies with an ideal compressible fluid was examined by Korobkin and Pukhnachov (1988) using an acoustic approximation. Korobkin (1992) extended the theory of Korobkin and Pukhnachov (1988) to include the effects of the deformation of the body during impact.

1.4.6. Arbitrary geometry

The impact of arbitrary shaped bodies and in particular realistic hull sections are considered in this section. The design theories of Stavovy and Chuang (1976) and also Ochi and Motter (1971) are

presented. Theories based on boundary element methods are then considered and finally finite difference based schemes are identified.

Stavovy and Chuang (1976) and also Ochi and Motter (1971) both presented design methods for calculating the slam loads on vessels of arbitrary geometry. Both of these two theories have been incorporated into a number of subsequent ship slamming calculation theories developed by other researchers. The theory of Stavovy and Chuang (1976) is an analytic method of calculating the slamming pressure distribution on high speed vessels. The approach used was to calculate the relative normal velocity between the water surface (including waves) and small panels of the vessel hull. The normal relative velocity component was then used to calculate the slam pressure based on Wagner (1932) wedge impact theory, Chuang cone theory (1969a) and also experimental drop tests. The planing pressures could also be calculated from the tangential relative velocity component. The theory agreed well with experiment. Ochi and Motter (1971) developed a semi-empirical method to estimate slamming characteristics for ship design. Experimental results for the maximum slamming pressures experienced by 15 hull forms were used to determine an estimation method for the maximum pressure experienced by an arbitrary hull form. This was done by applying a conformal mapping scheme to the geometry of the arbitrary hull form and then a regression analysis to calculate a maximum pressure coefficient. The regression analysis was based solely on the geometry of the hull section.

A number of theories for the impact of arbitrary shaped sections have been based on boundary element solutions for the velocity potential. The entry of both rigid and non-rigid bodies of circular or wedge cross section impacting with water were examined by Geers (1982) using a boundary element method for the fluid flow part of the problem. Results were presented for the impact of a rigid vee wedge and also a rigid cylinder. The use of this boundary element method, combined with a finite element method for the impact of non-rigid impacts was discussed and the use of a transformation matrix between the fluid and the structure was developed, although no results were given. A non-linear boundary element method to solve for the water entry of two-dimensional bodies of arbitrary cross section was presented by Zhao and Faltinsen (1993). The theory includes the formation of jets at the intersection between the free surface and the body. The theory was compared with a similarity solution result for a wedge and also a simple asymptotic based on the Wagner (1932) theory. A numerical study of flare slamming was presented by Wang, Troesch and Maskew (1996) for two different mixed Eulerian-Lagrangian schemes. The first numerical scheme presented was one in which the potential function was solved using a desingularised source boundary element method. The second method used to solve the potential function was a source and doublet singularity distribution. In this method both the source and doublet singularities were directly distributed over the boundary surfaces of the fluid domain. Both these methods were to be robust and accurate time stepping schemes for non-linear free surface problems. The results of the study were compared with

experiments with good results. Chihua and Yousheng (1997) present a non-linear boundary element method to calculate the bow flare slamming. Simple sources are used as the basis function. Instabilities on the free surface due to the time stepping are damped by a cubic spline re-gridding process and special attention is given to the free surface/hull surface interface. Numerical examples are presented for the wedge entry problem and also for a realistic hull section. The solution for the wedge entry example was compared with the solution of Zhao and Faltinsen (1993) and good agreement was observed. The study of bow flare hull section found that the maximum pressure on the flare part of the section was greater than the maximum pressure on the keel of the hull. A two-dimensional, asymmetric theory for impact problems is presented for sections of arbitrary geometry by Xu, Troesch and Vorus (1998). The formulation is based on the method of discrete vortices as used by Vorus (1996). The theory is in two parts one for the case of when separation does not occur and the second for when separation occurs from one side of the section. The effect of the jet flow due to asymmetry was also examined. Zhao, Faltinsen and Aarsnes (1997) extended the non-linear boundary element method developed by to Zhao and Faltinsen (1993) to include the effects of separation from knuckles or fixed separation points. This improved theory was compared with an improved Wagner (1932) solution and also an experimental drop test with good agreement. Separation was found to significantly influence the forces experienced by the section during entry.

Finite difference schemes to solve either the Euler or Navier-Stokes equations have been applied to the entry of a range of two-dimensional body geometries. Arai and Tasaki (1987) use a finite difference scheme on a rectangular grid to solve the unsteady Euler equations and thus the water entry of a wedge with a knuckle. Arai, Cheng and Inoue (1994) solve for the entry of an arbitrary shaped body impacting water using a body fitted coordinate finite difference scheme and the fractional volume of fluid method. This combination of schemes was found to give good results in particular the interface between the free surface and the body surface was handled very well. Results were presented for 30° and 45° wedge entry, cylinder entry and a realistic hull section entry. Results were found to be adequate. Arai, Cheng and Inoue (1995) use the body fitted coordinate system they previously developed in Arai, Cheng and Inoue (1994) to optimise the profile of horizontal members in the splash zone of offshore structures. The von Karman (1929) approach was used to find that a section of parabolic form experiences the minimum force during constant velocity impact. The finite difference scheme was then used to simulate the symmetrical and unsymmetrical impact of two parabolic sections. It was found that these forms experienced a lower maximum force than the cylinder section for inclination angles less then 30°. Arai, Cheng, Inoue and Miyauchi (1995) considered the impact of catamaran cross section with water using the theory developed by Arai, Cheng and Inoue (1994). This theory was also used by Arai, Cheng, Inoue, Miyauchi and Ishikawa (1995) to optimise mono-hull bow sections in terms of slamming characteristics. Varyani, Gatiganti and Gerigk (1998, 2000) used a finite difference scheme to calculate the slamming pressure coefficient for mono-hull forms and catamaran wetdecks by numerically solving the Euler equations on a rectangular grid. The theory predicted the forces experienced during the entry process adequately

including the effects of separation. Some example calculations were given for wedges with knuckles and the separation was clearly evident.

1.4.7. Slam loads on vessels

The development of theoretical methods to calculate slam loads on full-scale vessels operating in realistic seas has received much attention. This group of problems requires the solution of both the ship motions (and hence the underlying wave loads) as well as the slam loads. The response of the vessel structure is also of interest. The approach adopted by numerous researchers to solve this problem is to firstly use a ship motions program to calculate underlying wave loads and to detect when a slam event has occurred. A secondary procedure is then used to solve for the slam load. The slam load theories that are used can be broadly classified into four categories (i) added mass theories, (ii) asymptotic expansion theories, (iii) the Stavovy and Chuang (1976) impact theory and (iv) the slam theory of Ochi and Motter (1971). Each of these approaches to solving the full-scale ship slamming problem is discussed. A fully three-dimensional full-scale slam theory is also examined. A number of theories that deal specifically with the wetdeck slamming of catamarans have also been developed and these are reviewed.

Full-scale ship slamming theories incorporating two-dimensional added mass theories to model the slam event have been presented by several researchers. Yamamoto, Fugino, Fukasawa and Ohtsubo (1979) developed a ship motion strip theory in which the effects of ship slamming were included. The slam loads were calculated from the rate of change of the added mass associated with the section during re-entry. This theory was used to calculate the structural response of the ship (modelled as a free-free beam). The results of the analysis were compared with model tests and found to be adequate. Soares (1989) used a linear strip theory to calculate ship motions and hence relative motions between the instantaneous water surface and the ship hull during slamming. A two-dimensional added mass theory was used to calculate the slam load. The added mass for each hull section was calculated using the Frank close-fit method (Frank 1967). The effects of forward speed were included in the calculation by considering the change in added mass as the fluid moves from one ship section to the next. The ship motion program was used to determine when a strip of the ship experiences a slam event and also the relative motion between the water surface and the ship hull. The vibration response of the vessel was then solved for with a two-dimensional Timosheko beam formulation. Some example calculations were presented for a Mariner hull and the vibratory response of the hull girder was determined. Rassinot and Mansour (1995) examined the hydrodynamic loads on a ship due to slamming. A strip theory approach was used for these calculations, and the effects of forward speed were also examined. The ship was represented as a non-uniform free-free beam. The slam loads on the ship were calculated from an added mass approach that assumed conservation of energy, rather than conservation of momentum, which is the more wide spread method. The slam

loads were calculated approximately by considering the impact of a circular cylinder and also a sphere instead of the exact hull section geometry. The response of a Mariner hull (modelled as a non-uniform free-free beam) to slam loading was then examined. The slam loads were decoupled from the wave loads. It was found that this approach allowed calculation of the hull response (bending moment) during impact, but the vibrations following impact were not modelled adequately. Rosen and Garme (1999) considered the slamming of a planing vessel with a v-shaped bottom using a two-dimensional, time domain strip theory. Slamming loads were included in the theory using a two-dimensional added mass calculation. The added mass of the hull section as it entered the water surface was determined from the potential function for the fluid flow. The potential function was solved numerically by distributing sources and vortices along the hull surface and the water line at the level of the spray root. The potential function was given a value of zero along a line parallel to the undisturbed instantaneous free surface, but elevated to the level of the spray root, thus satisfying approximately the dynamic free surface boundary condition. The no through flow boundary condition was satisfied on the hull boundary. The pile up of the free surface was estimated from the Pierson splash up hypothesis (Payne 1994). The theory estimated the slamming force adequately so long as separation did not occur from the hull surface. Non-linear hydrodynamic loads and dynamic responses of a ship in waves were calculated by Weem et al (1998) using the LAMP computer program. LAMP is a time domain simulation for ship motions, wave loads and structural response. The ship motions calculated with a boundary element method in which the body boundary condition is satisfied exactly on that portion of the hull beneath the incident wave free surface, and the free surface boundary condition is satisfied by linearization about the incident wave surface. The slam loads are calculated by using the calculated ship motions to identify when a slam occurs and then using a two-dimensional calculations to determine the slam loads. In this theory the ship motions were decoupled from the slam loads, this is of course a modelling approximation as the slam loads do influence the ship motions. The two-dimensional slam loads were calculated using either a generalised Wagner approach or empirical methods. A number of numerical examples are presented for an AEGIS cruiser in storm waves and for a conceptual "wave piercer" ship geometry.

Matched asymptotic expansions have been used to model ship slamming by Watanabe (1987) and Magee and Fontaine (1998). Watanabe (1987) calculated the pressure distribution due to slamming on the three-dimensional flat bottom of a ship in waves. This was done by a matched asymptotic expansion. The outer region of the flow solution was that for a three-dimensional flat plate and the inner region of the flow was that for two-dimensional planing flow. These two solutions were matched asymptotically to make the problem determinate and thus a composite solution for the entire region was calculated. The theory was found to give good results when the correct ship motions were used in the calculation procedure. However when incorrect ship motions were used the results were poor. The slamming behaviour of a ship was studied by Magee and Fontaine (1998) with a ship motion program that incorporated a matched asymptotic slamming procedure. The ship motions were calculated using a six degree of freedom large wave amplitude sea keeping computer program. The

slamming was modelled in a secondary procedure using a strip theory in which the slam of the ship keel was modelled as flat plate of expanding width. A jet solution was introduced at the edge of the plate to account for the singularity at this point. The slam loads were then included in the full ship motion calculations. It was found that when the slam loads were coupled with the ship motion calculations the local, mean and maximum slamming pressures were reduced compared with an uncoupled calculation.

The method of calculating the pressure distribution over an arbitrary shaped body developed by Stavovy and Chuang (1976) has been incorporated in a number of full ship motion theories to allow the calculation of slamming pressures on vessels. A non-linear strip theory for heave and pitch motions in regular head seas of large amplitude was developed by Børresen and Tellsgård (1980). The slam loads were included in this theory by using the empirical results of Chuang (1967), upon which the theory of Stavovy and Chuang (1976) was partially based. The slam forces were found to increase the loads experienced by the hull tested when compared with the loads experienced by the hull due to the underlying sea loads alone and also to caused the response of the hull to be non-linear. Belik, Bishop and Price (1987) examined bottom and flare slamming and structural response of a vessel. The bottom slamming was modelled using an impact theory for pressures and also a momentum theory for loads. The impact theory calculated a maximum pressure acting on a hull section and then assumed that this pressure varies in time according an assumed function. The maximum pressure was calculated from the theory of Stavovy and Chuang (1976). The force acting on each hull section was then calculated by integrating the pressure for each hull section. The momentum theory was based on the two-dimensional added mass theory for each section. The added mass was calculated from the sectional added mass in terms of the infinite frequency of oscillation added mass. The impact theory was found to be most significant during the early stages of the re-entry of a hull section and the momentum theory forces dominated the later stages of the re-entry process. The ship motions were solved in the frequency domain and these were used to calculate the bottom and bow flare slamming motions. This work was used to examine the effect of hull form on bottom and bow flare slamming. A two-dimensional hydroelastic theory and also a three-dimensional hydroelastic theory was developed by Aksu, Price and Temarel (1991) and was used to examine the effects of slamming on a slender and a non-slender flexible hull. The slamming loads experienced by both hulls were calculated by first calculating the ship motions in an irregular sea way and then using these calculated ship motions to determine when a slam occurred. The slam loads were thus calculated using the Stavovy and Chuang (1976) impact theory. The slam load was applied to the hull structure at an assumed location (0.125 ship lengths from the bow). Both the two and three-dimensional theories worked well for the slender body, but not for the non-slender body.

The quasi-empirical two-dimensional slam theory developed by Ochi and Motter (1971) has been incorporated into several full ship motion programs to investigate slamming. Ochi and Motter (1973)

used the theory developed in Ochi and Motter (1971) to enable the calculation of the frequency and severity of slam impacts, ship speed limits to avoid slamming damage, slam forces and the main hull girder response to impact. The analysis was applied to a Mariner hull geometry operating in the North Atlantic Ocean and also a winter route in the North Pacific Ocean. The problem of the combination of low frequency wave induced bending and high frequency slam induced stresses was examined by Hansen (1994). The ship motions were calculated by linear wave theory and the slam loads are calculated separately by the method of Ochi and Motter (1971). The slam load was applied to the forward section of the mono-hull. A probabilistic analysis of frequency and severity of slamming was also developed

The impact of a generic ship structure impacting a wave profile was modelled by Marco (2002) using the three dimensional finite element code LS-DYNA. The air, water and ship structure were all included in the model using eulerian and lagrangian procedures. A generic example of a ship structure impacting with a wave profile was used as an example to demonstrate the application of these non-linear dynamic finite element methods.

The wetdeck slamming of catamarans, on the scale of the full-scale ship rather than at the scale of panels, has been the focus of a number of studies. Giannotti (1975) presented a method to calculate the slam loads on the cross structure of a catamaran. The slam load was calculated using empirical relations developed by Smiley (1951) and also Chuang and Milne (1971) who both conducted drop tests of two-dimensional wedges and three dimensional cones with various angles. Wetdeck pressure and load histories were developed. A probabilistic approach, using a ship motions program, was then used to calculate the number of impacts per unit time. Results were compared with model tests and full-scale trials with good agreement. The wetdeck slamming of a surface effect ship was examined by Kaplan (1987). The slam load was calculated using an added mass theory. The added mass was considered to be a half circle with radius of the instantaneous longitudinal wetted length of the wetdeck during a slam and width equal to the beam of the wetdeck. This approach to calculating the impact forces avoids the infinite impact forces that occur when a strip theory or sectional approach is used to calculate the added mass for the wetdeck impact. Results were compared with experimental model tests. It found that there were some definite differences in the magnitude and time scale of the slam loads between theory and experiment. Also there were substantial vibratory effects in the experimental results that were not evident in the theory and this was attributed to the fact that the theory was for rigid bodies only. The problem of a wave impact on the bow end of a catamaran wetdeck was considered by Korobkin (1995). The wetdeck was modelled as an Euler beam and the Wagner (1932) approach for the hydrodynamics was used. It was found that the interaction of the beam deflection and the liquid flow may lead to higher hydrodynamic pressure than a rigid beam. Okland, Moan and Aarsnes (1998) presented a numerical method for calculating the structural loads on twin hull vessels exposed to severe wetdeck slamming. The response of the vessel from a

harmonic regular sea was calculated from the summation of linearised velocity potential for the incident wave, diffraction wave and radiation velocity potential. The slamming loads were calculated by considering the a longitudinal section of the wetdeck and calculating the velocity potential for this section as it enters the water surface. Green's second identity was used to solve for the velocity potential (Kvålsvold 1994). The free surface deformation was neglected and the free surface boundary condition of $\phi=0$ was applied on the undisturbed free surface. The results were compared with the slamming loads experienced by a segmented catamaran model. Good agreement between the predicted and the measured force is observed.

The probability of slamming has also been investigated using ship motion programs. For example Wu, Tulin and Fontaine (2000) used a two and a half dimensional ship motion code to calculate the probability of fore foot emergence (and hence slamming) of the bow of a frigate. They noted that this might be a useful tool in early stage design to assess the likelihood and severity of slam events.

1.4.8. Summary of theoretical investigations of slamming

A review of the theoretical investigation of water entry problems has been presented. The water entry of two-dimensional wedges, three-dimensional prismatic wedges, cylinder entry, flat plate impact, sphere, cone and curved panel impact have all been examined. The entry of bodies of arbitrary geometry have also been considered. Methods of calculating of slam loads on full-scale vessels by incorporating slamming theories into ship motion programs were then examined. Based on this review two principal conclusions are drawn with respect to the most promising theoretical approaches to investigate the slamming of catamaran with centre bow cross sections. Firstly an added mass based theory is likely to provide a robust method of investigating the forces acting on a section of this geometric form. This is because added mass theories have been used with reasonable success to model a diverse range of water entry problems. Secondly, a very general and flexible approach to model water entry problems is the class of solutions based on finite difference numerical solutions. This approach captures such effects as separation and highly non-linear free surface deformation. Also the deformation of the free surface due to variations in air pressure can be included in finite difference solution formulations. Indeed Bertram (2000) commented "real progress (in slamming analysis) is likely to be achieved with field methods like FEM (finite element method), FDM (finite difference method), or FVM (finite volume method). For this reason a finite difference numerical solution approach to slamming analysis was considered to be a promising method of investigating the detail of the water entry problem.

1.5. Summary

This chapter considered what ship slamming is and the consequences that slamming has for ship design. Three methods of investigating slamming were considered: (a) full-scale ship trials, (b) experimental scale model tests and (c) theoretical approaches to slamming. The novelty and relevance of the work to be presented in this thesis was established. It was shown that there was only a limited amount of published data for full-scale catamaran slamming and in particular detailed relative motion results between the wetdeck and the instantaneous water surface during slamming were not available. It was also demonstrated that experimental drop tests of scale catamaran with centre bow cross section models had not previously been conducted and this thesis addresses this lack of knowledge. Finally a review of theoretical models investigating slamming was undertaken. This was used to identify that an added mass theory would be a suitable way of modelling the water entry of catamaran with centre bow section to allow a gross understanding of the entry event to be developed. It was also observed that a flexible and generally applicable theoretical approach to model the detail of water entry is the numerical finite difference class of solutions to solve for the unsteady water entry problem. Thus a finite difference theory was shown to provide a suitable solution procedure to examine the water entry problem.

2. Full-Scale Trial Results

2.1. Overview

This chapter presents results from full-scale trials conducted on Incat vessel 050 whilst on operations in the Cook Strait, New Zealand during 1999 and early 2000. Details of the vessel, instrumentation and data acquisition system used in the trials are described. A method to identify and quantify severe slam events is developed and the relative motion between the water surface and the vessel centre bow is calculated for each severe slam event. The effects of vessel Froude number, wave height, relative centre bow impact velocity, relative centre bow submergence, longitudinal location of slam load and instantaneous wave height on slam severity are analysed.

Thomas, Davis, Whelan and Roberts (2001) also conducted an analysis of the data collected during this series of trials of vessel 050. The analysis presented in this section focuses more on aspects of slam occurrence relating to the location of the slam event and the velocity of entry of the centre bow into the water during the slam.

2.2. Vessel and Trial Details

Full-scale trials were conducted on INCAT vessel 050. Vessel 050 is a high-speed, wave piercing aluminium passenger ferry. Major hull specifications are listed in Table 2.2.1. A general arrangement diagram is shown in Figure 2.2.3. The full-scale trials were undertaken during commercial operation in the Cook Strait, New Zealand. The vessel serviced a route between Picton and Wellington in a journey of approximately 1hour and 40 minutes see Figure 2.2.1. Two return crossings were made each day. Trials were conducted from April 1999 to January 2000.

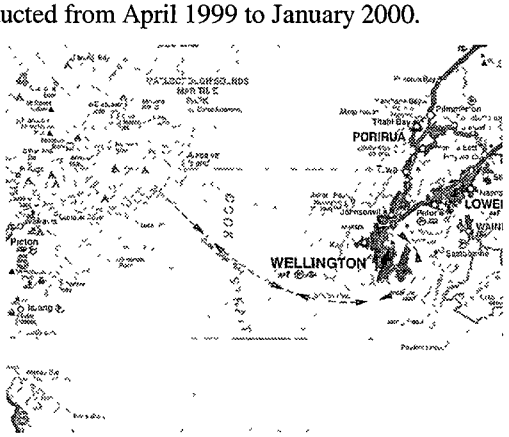

Figure 2.2.1: Location of full-scale trials. (Picture courtesy of G. A. Thomas)

A data acquisition system was fitted to the vessel to allow the measurement of stress at various locations, ship motions and sea-state. The data acquisition system was set up in two separate systems.

System 1 was located in the bow of the vessel and was designed to investigate local slam loading on the centre bow and forward wetdeck. Readings from 8 strain gauges and a radar based wave height meter supplied by TSK were recorded. The strain gauges were located as shown in Figure 2.2.3. The TSK meter was located on the ship centre line slightly forward of frame 70. Frame numbers are shown in Figure 2.2.3. A DaqBook controlled by a lap top computer recorded data at 100Hz. The system was activated when a particular strain gauge reading exceeded a preset strain value. 18 seconds of data was recorded, the first 6 seconds of which preceded the trigger event. The 6 seconds of data was recovered from the DaqBook buffer and allowed the vessel behaviour immediately prior to the trigger event to be recorded.

System 2 was located in the electronics room and was designed to study global ship loading. The TSK meter was used to measure instantaneous absolute wave height at slightly forward of frame 70, bow vertical displacement, running significant wave height and relative wave height. Heave, sway and surge accelerations were measured at the loaded centre of gravity. Ship speed was measured using the vessel's on-board global positioning system. Data from 8 strain gauges was recorded and the gauges were located as shown in Figure 2.2.3 and Appendix I. Data was recorded using a DaqBook controlled by a personal computer. Sampling was undertaken at a frequency of 20Hz for 90 seconds. The system was triggered when the heave acceleration exceeded a pre-determined value, which was independent of the trigger condition for system 1. The recorded data included 10 seconds of data from just prior the trigger event, this data was recovered from the buffer of the DaqBook.

The trials were conducted in collaboration with a New Zealand ferry operator and INCAT's research and development staff. Commercial limitations meant that it was not possible to measure some aspects of vessel performance which were considered by INCAT and New Zealand ferry operator staff to be of secondary importance or impractical to measure. As a consequence of these limitations vessel angular accelerations were not measured, however vertical ship displacement at frame 70 was measured which mitigates to some extent the lack of pitch data. The limited number of strain gauges fitted to the vessel meant that only one of the two hulls of the vessel was instrumented so that any asymmetry in the slam events measured could not be identified in these parts of the structure. During operations the cargo and fuel load carried by the vessel varied depending on economic demand and refuelling schedule respectively. No records of the cargo and fuel load carried by the vessel when a slam event occurred were made, with the exception of the slam event that caused damage (Figure 2.2.2) and was investigated by Thomas et al (2001). Variation in the vessel mass may create a variation in the vessel's response to sea conditions and behaviour during slamming. In particular the height of the wetdeck above the still water level will be less for a more heavily laden vessel and this will influence the frequency of slamming for a given sea state. The effect of vessel loading was therefore not able to be examined in the current full-scale trials. Also encountered sea direction data was not recorded as the vessel was undertaking commercial operations and the crew were otherwise engaged. The sea direction influences the slamming behaviour of the vessel (Rósen and Garme (1999)) and this could not be quantified in the current study. Despite these limitations the trials data

was of value in understanding the behaviour of a high-speed catamaran undertaking normal commercial operations.

Specification	Dimension
Length overall	96.00m
Length waterline	86.00m
Beam overall	26.00m
Demi-hull beam	3.70m
Deadweight	800tonnes
Speed, fully loaded condition	38+ knots
Main engines	Four CAT 3618 marine diesel engines. 7200kW each @ 1050rpm
Propulsion	4 Lips 150 D water jets

Table 2.2.1 Vessel 050 major specifications.

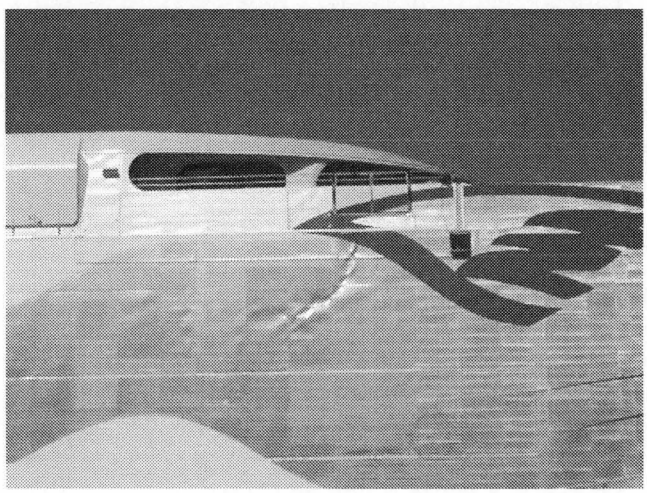

Figure 2.2.2 Slam damage suffered by vessel 050 during operations in the Cook Strait New Zealand.

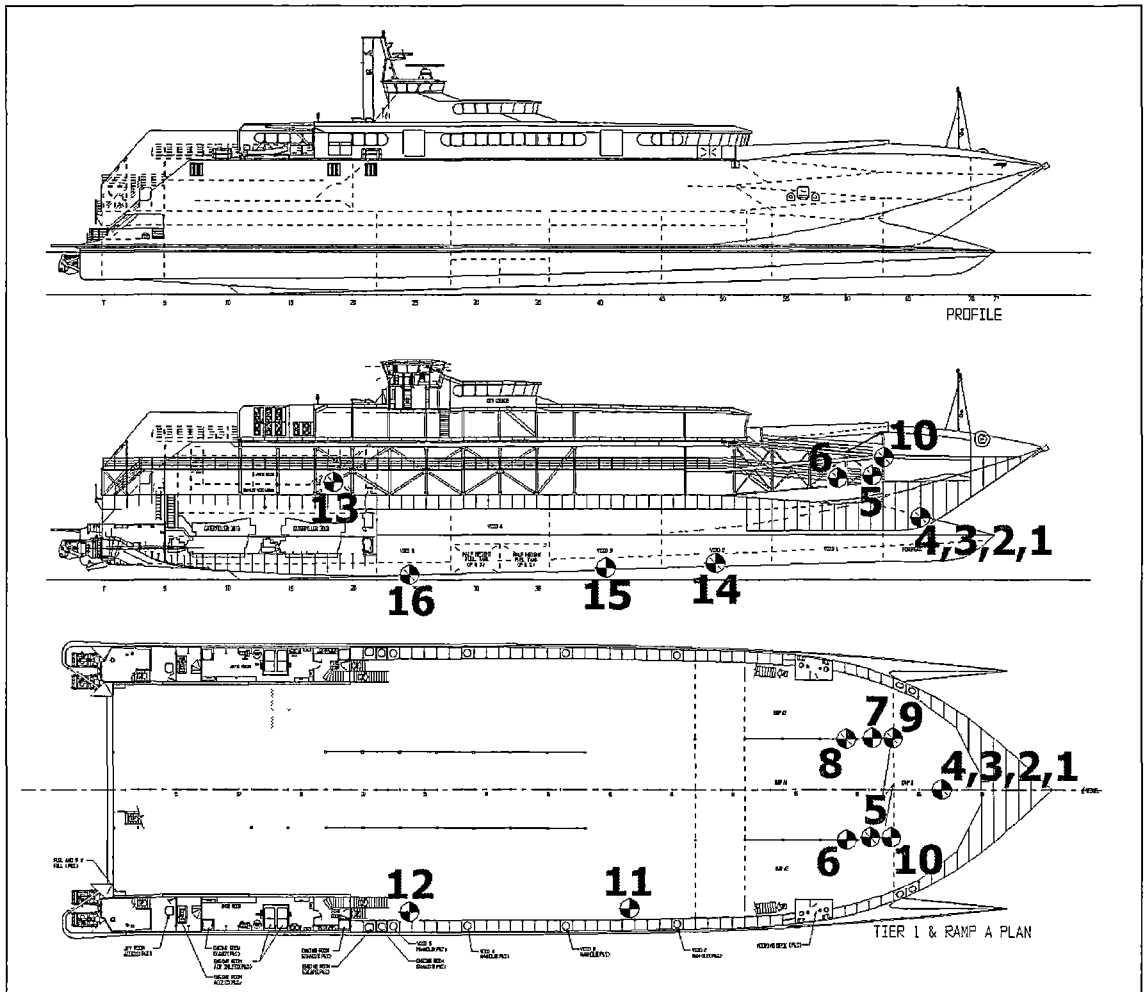

SYSTEM 1		SYSTEM 2	
No.	Location	No.	Location
1	Top rider at frame 69 on CL	9	Port lower steel post at frame 63
2	Top rider at frame 67 on CL	10	Stb. lower steel post at frame 63
3	Top rider at frame 66 on CL	11	Stb. portal x-brace at frame 41
4	Top rider at frame 65 on CL	12	Stb. portal x-brace at frame 23
5	Stb. fwd diagonal at frame 62	13	X-brace vehicle deck
6	Stb. aft diagonal at frame 59	14	Stb. hull keel at frame 49.5
7	Port fwd diagonal at frame 62	15	Stb. hull keel at frame 40.5
8	Port aft diagonal at frame 59	16	Stb. hull keel at frame 24.5

Figure 2.2.3 Strain gauge locations. (Picture courtesy of G. A. Thomas)

Off sets for the gauges	x [m]	y [m]	z [m]
Gauge 1	0.0	82.8	0.5
Gauge 2	0.0	80.4	0.5
Gauge 3	0.0	79.2	0.5
Gauge 4	0.0	78.0	0.5
Gauge 5	4.9	74.4	6.8
Gauge 6	4.9	70.8	6.8
Gauge 7	-4.9	74.4	6.8
Gauge 8	-4.9	70.8	6.8
Gauge 9	4.9	75.6	6.8
Gauge 10	-4.9	75.6	6.8
Gauge 11	9.0	49.2	10.7
Gauge 12	9.0	27.6	10.7
Gauge 13	4.5	21.8	6.4
Gauge 14	11.3	59.4	-2.1
Gauge 15	11.3	48.6	-2.1
Gauge 16	11.3	29.4	-2.1

Table 2.2.2 Offsets for locations of strain gauges.

2.3. Slam Records

The sea trials of vessel 050 were conducted for 10 months. During this period the vessel spent approximately 2,000 hours at sea under commercial operating conditions. Approximately 1,200 20 second data records (6.7 hours of data) were recorded on instrumentation system 1 and 1,800 90 second data records (45 hours of data) were recorded on instrumentation system 2. There were approximately 400 more system 2 data records than system 1 records because system 1 failed towards the end of the trials. Although trigger conditions for system 1 and system 2 were not identical there was generally one system 1 data record for each system 2 data record. The 1,800 system 2 data records were scanned for slam events using the criteria detailed in section 2.4. In all 38 slam events were found in the system 2 data records. Slam events were also found on system 1 and these could be correlated with those found in the system 2 data based upon the instantaneous wave height data and the time that the files were created.

An example slam event is shown in

Figure 2.3.1 so that those features that characterise a slam event may be illustrated. The data records presented are 12 seconds of data that has been extracted directly from the complete 20 seconds of data for the system 1 records or 90 seconds of data for the system 2 data record. Outside this 12 second window only the underlying wave loads are present. The underlying wave load is of course not the principle object of this study, however the general form of the underlying wave loads experienced by the vessel can be observed in Figure 2.4.2 for four slam events and three strain gauge records.

The stress histories experienced on all strain gauges, the three linear accelerations at the loaded centre of gravity and the instantaneous wave height are presented in

Figure 2.3.1 for an example slam event. The stress records on the strain gauges located in the centre bow of the vessel (gauges 1 to 4) are plotted in the upper left graph of

Figure 2.3.1. These gauges all experience a clearly defined, sharp stress spike followed by a second stress spike which is in the opposite direction to the first stress spike and of a reduced magnitude (snap back). Structural whipping is also apparent and this is observed to be of a higher frequency than the underlying wave load. The stress histories for gauges 5 to 8 are shown in the upper right graph in

Figure 2.3.1. These gauges are fitted on the diagonal bracing that is in the region 5m aft of the jaws of the bow. The stress record on these gauges show similar features to those observed on gauges 1 to 4. That is, there is a significant stress spike of duration 0.2s followed by a snap back of reduced magnitude. This is then followed by some whipping that is of a higher frequency than the underlying sea loads. The stress records for the strain gauges 9 to 16 that are distributed throughout the main structure of the vessel (Figure 2.2.3) are shown in the middle two graphs of

Figure 2.3.1. A stress peak, which is less sharp than those recorded on gauges located nearer to the vessel bow (gauges 1 to 8), is observed on all strain gauges. The peak stress recorded on gauges 16 and 13 located at the aft of the vessel occur as much as 0.21s after the peak stress measured in the stress gauges located in the bow of the vessel (gauges 1 to 4). The linear acceleration on all three axis are shown in the lower left graph of

Figure 2.3.1. The Z axis (vertical) acceleration displays an underlying wave acceleration overlaid upon which is a slam acceleration which is of the same frequency as the structural whipping. The surge and sway accelerations are also shown and these display an underlying wave acceleration and a slam induced whipping acceleration. The bottom right graph shows the instantaneous encountered wave height recorded by the TSK meter located at frame 70 (84m from the transom). The slam event is seen to coincide with a rising wave surface whose crest occurs at 6.5s. Steinman, Fach and Menon (1999) observed a similar structural slamming response in an 86m Austal high-speed catamaran ferry during a delivery voyage.

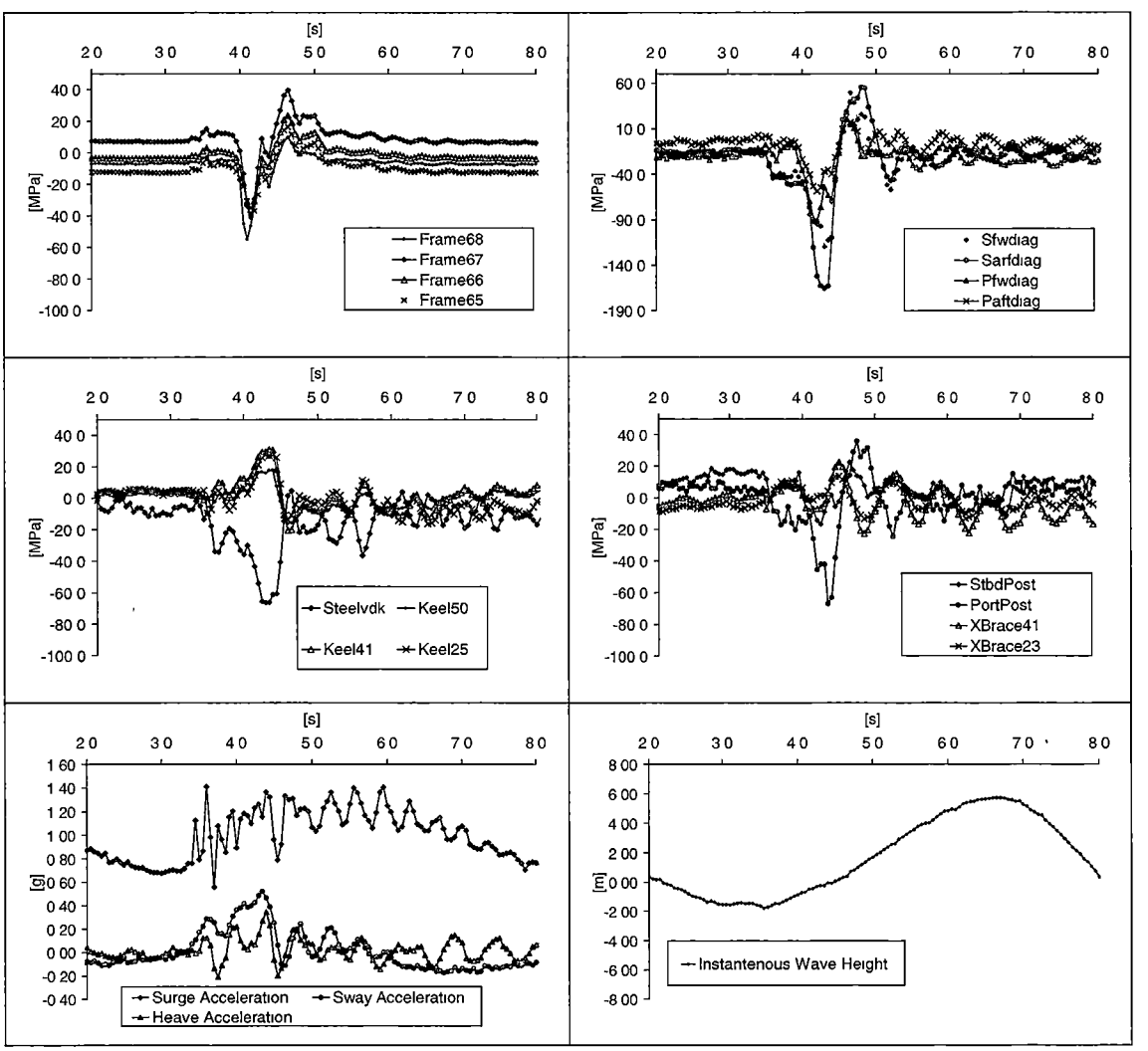

Figure 2.3.1 Example slam result. Recorded on 9/9/1999 at 7:45am.

2.4. Slam Event Classification

A definition of a slam event was developed so slam events could be identified from the data records. Thomas et al (2001) suggested that a suitable criterion to identify a slam event was

$$\left.\frac{d\sigma}{dt}\right|_{\text{prior to the peak}} > \frac{0.1\times\sigma_{Al}}{C_s}, C_s = 1.0\text{s} \qquad (2\text{-}1)$$

for a strain gauge time record that had been high pass filtered at 0.6Hz. This criterion identifies all high rate of change loading events. However as noted by Thomas (2003) "The small slam events which predominate the slam peak stress distribution appear to have little or no influence on the fatigue life (of the vessel)." Nor do the small slam events cause structural damage to the vessel due to the ultimate strength of the vessel being exceeded. Aertssen (1979) suggested that an absolute stress criterion was a suitable method of identifying when slamming occurred. Aertssen (1979) stated "Even a small shock on the hull induces whipping stresses, but not every shock may be called a slam. Only when the captain is so strongly impressed by the shock that he feels as if the ship were struck by a body and that consequently he thinks about reducing speed, is that shock called a slam." Bishop, Clarke and Price (1983) comment concerning the definition of a 'significant slam' and state that a 'significant slam' is said to occur when "the impact force or pressure exceeds a prescribed value." Thus a criterion based solely upon the magnitude or severity of the stress experienced by the vessel is proposed to identify slam events. The severity of a slam event is quantified by defining, slam global stress

$$\sigma^* = \frac{\left(\sum_{t=1}^{t=n_g} \max\left(-\sigma_{min}, \sigma_{max}\right)_t^2 \Big/ n_g\right)^{1/2}}{\sigma_{Al}}, \sigma_{Al} = 100\text{MPa} \qquad (2\text{-}2)$$

The values of σ_{min} and σ_{max} are based on the minimum and maximum stress levels measured within a 10s data record window on the strain gauges in system 2. The strain records were shifted so that the long term average was zero. This was done so that the dynamic wave loads and the slam loads (if present) were decoupled from the static load in the structure due to the cargo load and vessel structural mass and the consequent hydrostatic buoyancy forces. Stress records were not high pass filtered to remove underlying wave load as the phasing between the ordinary wave induced response cycles and the impulsive slam load affects the severity of the response of the ship structure (Hay, Bourne, Engle and Rubel (1994)). The regular swell loads can act to either mitigate or exaggerate the effect of the slam load as a result of phasing. Slam global stress provides a global measure of slam severity that is a more robust basis for comparing two slam events than strain results from a single gauge. Results from a single strain gauge are susceptible to the local loading effects of each particular slam event. The criterion to identify a slam was set to be

$$\sigma^* > 0.2 \qquad (2\text{-}3)$$

The cut off criteria of $\sigma^{*} > 0.2$ used to define a slam event is of course in part arbitrary, however the justification of this particular cut off criteria is as follows. The σ^{*} values for all of the potential slam event records collected in January 2000 are presented in Figure 2.4.1 by way of example. It is evident that the vast majority (90%) of these data records display σ^{*} less than 0.2 and only a few records (10%) have σ^{*} greater than 0.2 and for these records σ^{*} is substantially greater than 0.2. In Figure 2.4.1 four particular data records are identified (records A, B, C and D) and the stress records for three of the strain gauges are presented in Figure 2.4.2 for each of the four data records. In record A ($\sigma^{*} = 0.43$) a substantial loading event is observed and this loading event is considered to be a slam event. In record B ($\sigma^{*} = 0.26$) a loading event similar but of reduced magnitude to that seen in record A is observed. In record C ($\sigma^{*} = 0.19$) no loading event that is substantially greater than the underlying wave load is evident. A loading event, which is termed a minor slam, is apparent. This minor slam displays the whipping response of a slam event however the gross loading associated with this minor slam event is not large compared with the underlying wave loads nor the slam events observed for example in records A and B. Only the underlying wave load is apparent in Record D ($\sigma^{*} = 0.12$).

Clearly the decision to consider the minor slam evident in record C not to be a significant slam event is of course arbitrary. However slams which are unlikely to cause global structural damage, that is slam events in which the loading experienced is of the same order of the underlying wave loads, are of less interest than those slam events which may cause global structural damage such as that seen in Figure 2.2.2. The underlying wave loads do not of course generally cause global structural damage. Minor slamming such as in record C may or may not cause local damage such as panel dishing due to local pressure effects such as those discussed by Rósen and Garme (1999). However these effects are less significant than global structural damage. Slam loading events below the 0.2 threshold are also expected to have a small impact on the fatigue life of the vessel. The effect of slamming events on the fatigue life of the vessel is difficult to quantify and the work of Thomas (2003) on Incat hull 042 (an 86m Incat vessel of similar design to vessel 050) was used as a guide. Thomas found loading cycles with a stress range of less than 11.7MPa had virtually no impact on the fatigue life of the vessel for the loading regime considered. Loading cycles with a stress range less than 11.7MPa are similar to those observed in minor slam seen in record C.

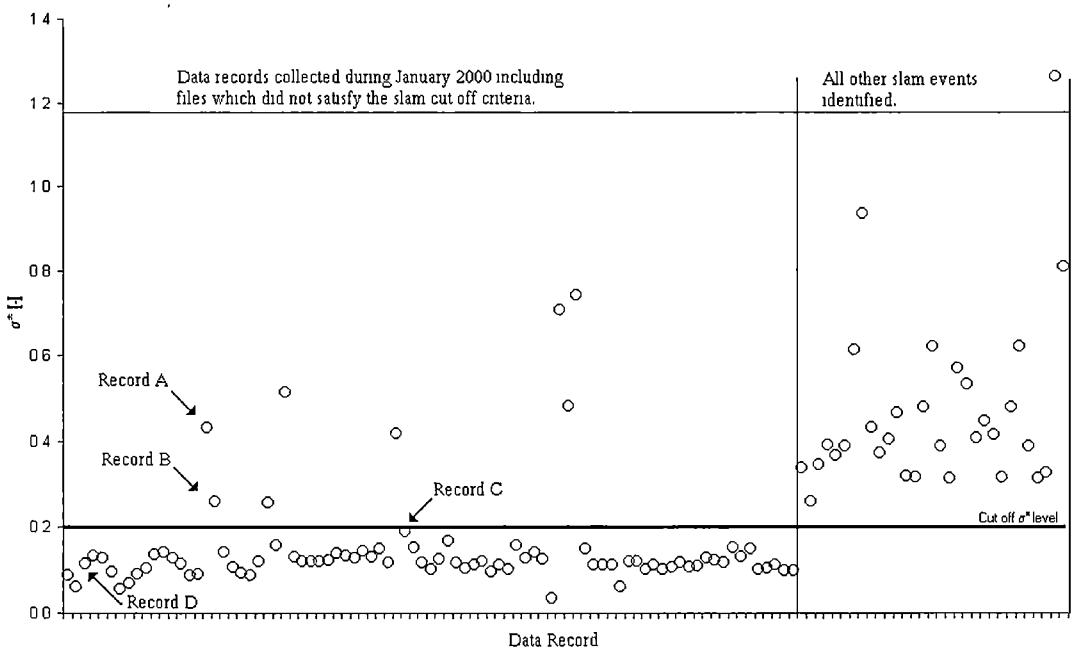

Figure 2.4.1 Slam global stress results for all data records collected in January 2000 and slam global stress results for all other data records identified as containing a slam event.

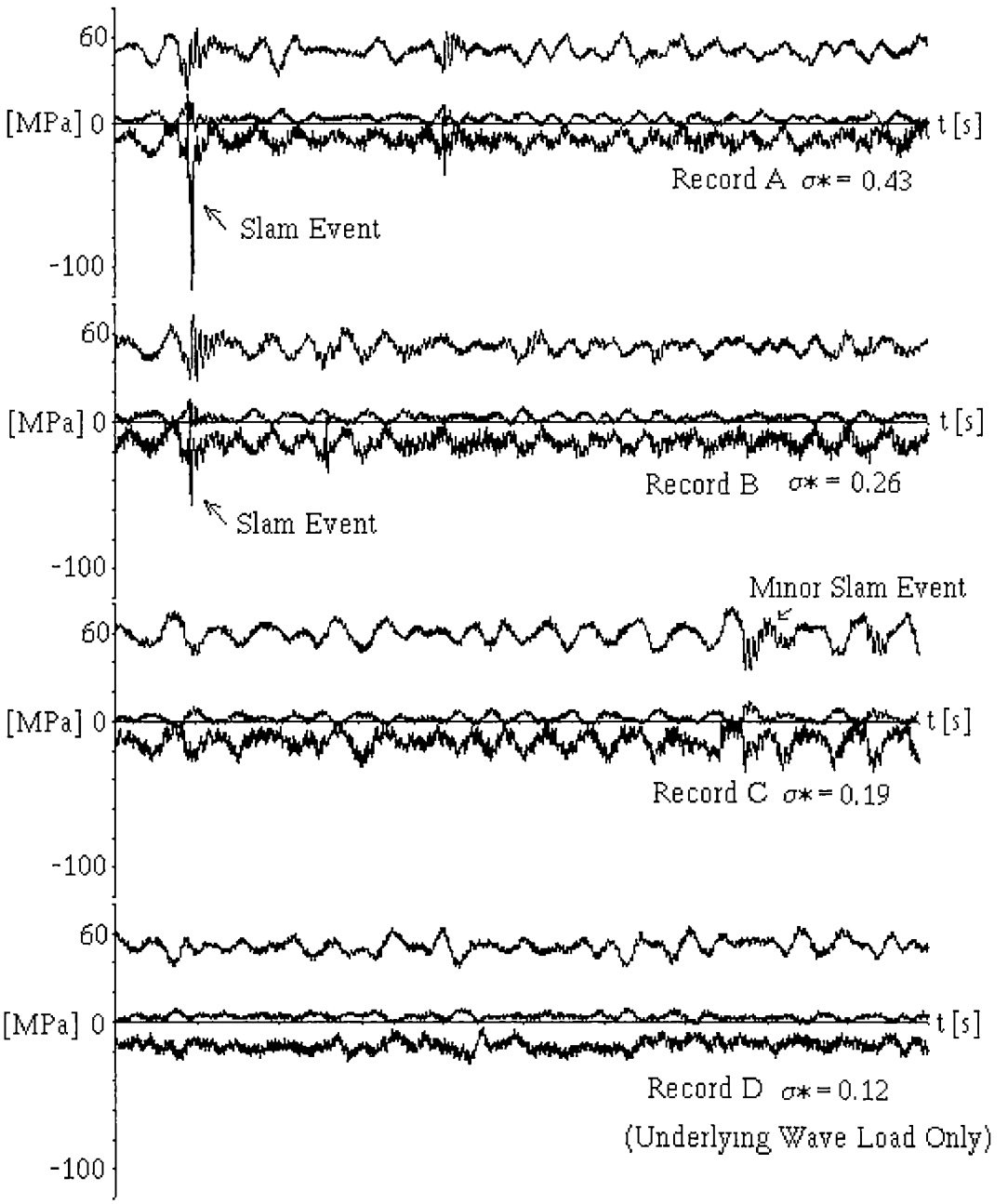

Figure 2.4.2 Particular stress records for four data records collected during January 2000. For each record the upper stress transient is for gauge 11, the middle record gauge 14 and the lower record gauge 10. 90 seconds of data is shown.

The behaviour of the vessel during slamming was quantified, in addition to the slam global stress, with the time dependent global stress, slam wave height and vessel Froude number.

A time dependent measure of the global loading response experienced by the vessel was developed based upon the root mean square of the stress levels in gauges 9 and 10 in system 2. These two gauges were selected, as they were located close to the centre of slamming and systemically in the vessel structure and thus the time dependant slam global stress is thus defined,

$$\sigma^{r}_{9,10}(t) = \frac{\left(\left(\sigma(t)_9 + \sigma(t)_{10}\right)/2\right)^{1/2}}{\sigma_{Al}}, \quad \sigma_{Al} = 100\text{MPa}. \tag{2-4}$$

A time dependent measure of the slam induced stress was developed so that the relative timing between the instantaneous wave height, vessel vertical position and the peak loading could be quantified.

A measure of wave height was defined based upon the instantaneous wave trough depth prior, and wave crest height following the slam event. It was found that all slams recorded during the trials occurred as a result of impact into the front of the encountered wave and thus there were no difficulties identifying which wave trough and wave crest were associated with each slam event. The slam wave height is thus

$$H_S = h_{w\,crest} - h_{w\,trough} \tag{2-5}$$

This wave height measure was used because the characteristics of the wave upon which the slam occurred were of particular interest in this study.

The vessel Froude number is defined based on the vessel water line length,

$$Fr = V_V / \sqrt{g L_V} \tag{2-6}$$

2.5. Relative Slam Entry Motion

The loading experienced by a ship hull during slamming is a strong function of the relative motion between the water surface and the ship hull (Bertram (2000), Arai (1995)). In this section a method to quantify this relative motion is developed and applied to each slam event identified in the trial data. An average entry relative motion is then calculated for a typical slam event.

Incat vessel 050 has suffered damage to the wetdeck at the top of the arch, slightly aft of the jaws of the bows, in the vicinity of frame 59 (Roberts (2003)), see Figure 2.2.3 and Figure 2.2.2. It was thus considered that the relative motion between the instantaneous water surface and the vessel hull in the

damage zone (ie frame 59, 70.8m from the transom) was a suitable location at which to consider the relative slam entry motion. The relative slam entry motion was calculated by determining the relative vertical distance between the keel of the centre bow at frame 59 and the instantaneous water surface during a slam event. The slam entry motion is then approximated with a parabola so that comparison between different slam events can be made and a typical slam entry motion profile developed.

The relative vertical distance between the foot of the centre bow at frame 59 and the instantaneous water surface $\Delta h(t)$ was calculated using the formula

$$\Delta h(t) = h_{59}(t) + h_B - h_w(t - (L_{TSK} - L_{59})/V_V) \qquad (2\text{-}7)$$

where;

- $h_{59}(t)$ is the vertical displacement of frame 59. $h_{59}(t) = 0.0$ when the vessel is at rest in calm water. The vertical ship displacement was measured by a TSK meter located at frame 70 (13.2m forward of frame 59). It is assumed that the vertical ship displacement at frame 59 and frame 70 are the same. This assumption neglects some of the effects of the pitch motion of the vessel and the error that this assumption introduces is discussed in detail at the end of this section.
- h_B is the vertical distance between the centre bow foot and the still water level. This height varies depending upon the cargo and fuel loads carried by the vessel. A value of 0.2m was used in these calculations.
- $h_w(t-(L_{TSK}-L_{59})/V_V)$ is the instantaneous wave height at frame 59. During the trials the instantaneous wave height was measured by a TSK meter located at frame 70. The instantaneous wave height at frame 59 was thus estimated from the instantaneous wave height at frame 70 and this was done by assuming that the water surface profile did not change as the vessel moved through it. Hence the instantaneous wave height was simply shifted from frame 70 to frame 59 by adjusting the time base by the time interval ($(L_{TSK}-L_{59})/V_V$) taken for the vessel to traverse the distance between frame 70 and frame 59. This assumption introduces some error as the change in shape of the encountered wave and its propagation is neglected. The influence of the demi-hulls on the water surface is also neglected, as too is the effect on the water surface of the centre bow.

An example calculation of the relative slam entry motion is presented for a particular slam event. The slam event is first identified based on the slam global stress criteria presented in section 2.4. The data record is then examined and the slam event is identified and this has been done and the stress records for all strain gauges in instrumentation system 2 are graphed in the uppermost plot of Figure 2.5.1. For this particular record the slam event occurred at approximately 5 seconds as noted in Figure 2.5.1. The vessel speed is then extracted from the data record and this is used to calculate the time shift ($(L_{TSK}-L_{59})/V_V$) required to calculate $h_w(t)$ at frame 59. The vertical displacement of frame 59 ($h_{59}(t)$) and the instantaneous wave height at frame 59 ($h_w(t)$) are then found from the data records and these two results have been graphed in the middle plot of Figure 2.5.1. That part of the $h_{59}(t)$

and $h_w(t)$ which occurred during the slam event is indicated in Figure 2.5.1. The slam relative entry motion is then calculated using the equation for $\Delta h(t)$ and this is done in the lower most plot in Figure 2.5.1. That portion of the of the $\Delta h(t)$ result that coincided with the slam event is identified as indicated in Figure 2.5.1. It is this portion of the $\Delta h(t)$ record that is of particular interest and it is extracted from the rest of the $\Delta h(t)$ record.

The temporal bounds required to define that portion of the $\Delta h(t)$ record, which describes the relative motion during the slam event, are set in the following manner. The slam $\Delta h(t)$ record is considered to commence when $\Delta h(t) = 0.0$, corresponding to initial contact of the centre bow keel with the instantaneous water surface. The slam $\Delta h(t)$ is considered to terminate slightly after $\Delta h(t)$ has obtained a minium.

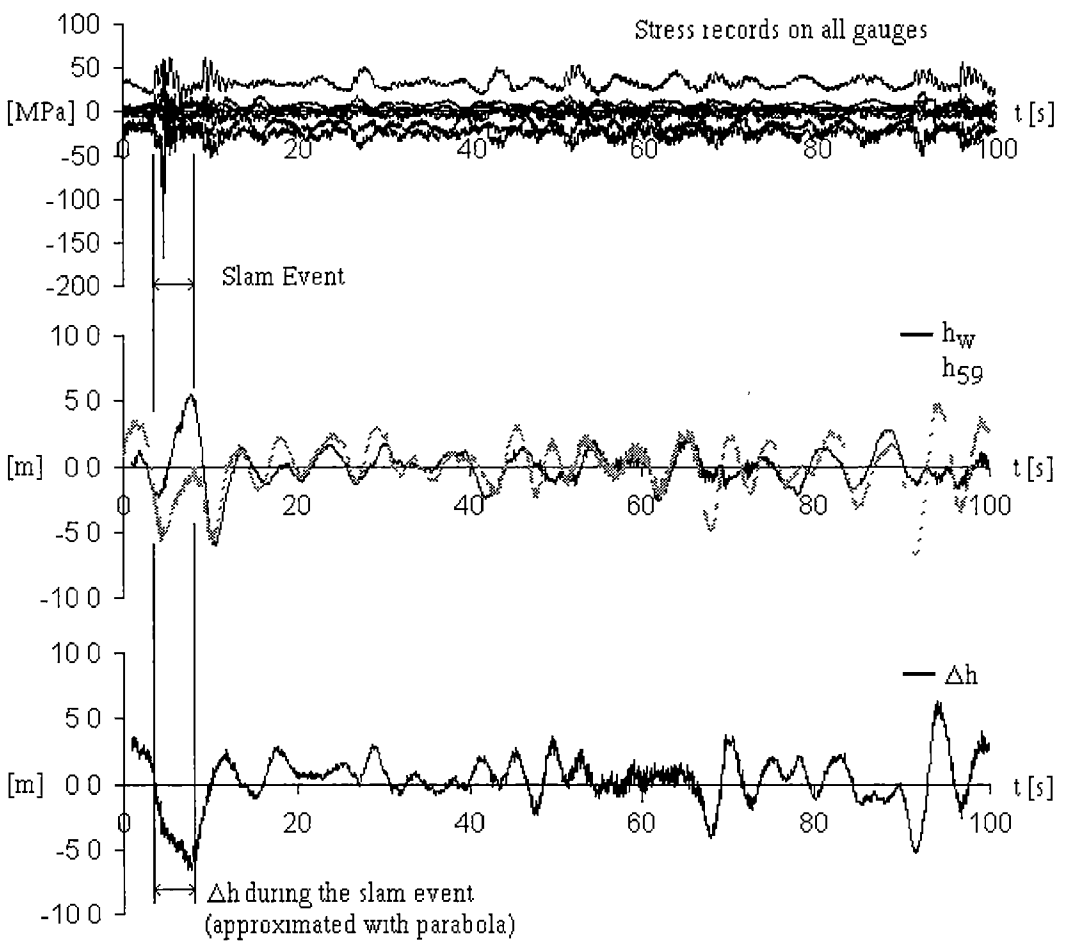

Figure 2.5.1 Example relative motion calculation.

The relative entry motion during the slam event is then approximated with a parabola using a least squares method and this is shown in Figure 2.5.2 for the example slam event. The time base is shifted

so that t = 0.0s coincides with the initial impact of the centre bow keel with the instantaneous water surface ($\Delta h(t) = 0.0$). For some slam events the noise in the $h_{59}(t)$ and $h_w(t)$ records was such that this time shift could only be implemented approximately and hence some error is introduced.

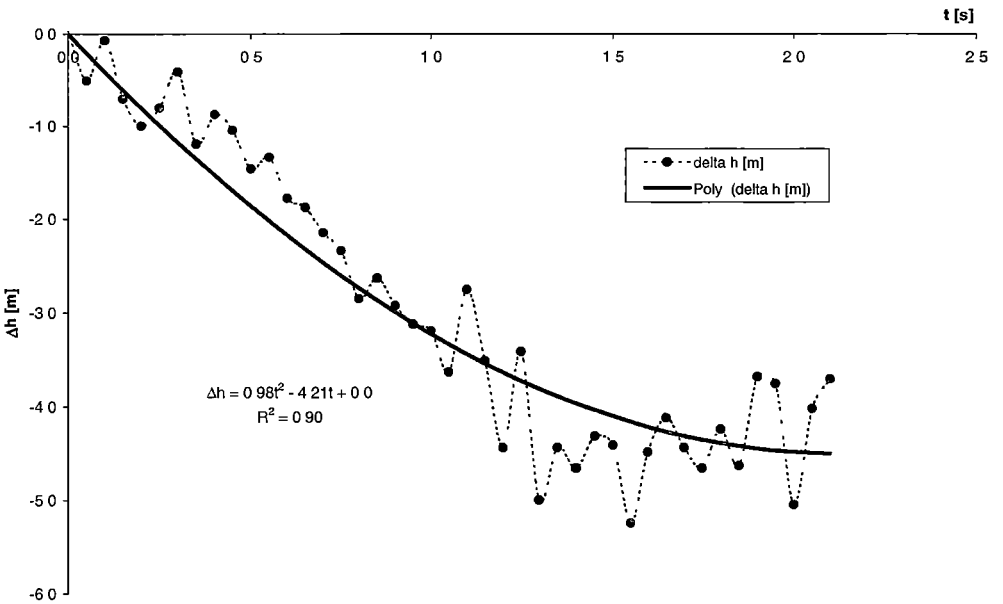

Figure 2.5.2 Example of fitting a parabola to $\Delta h(t)$ data for a slam.

The approximation of the relative entry motion during a slam event with a parabola was repeated for each of the slam events identified and the results from this procedure are plotted in Figure 2.5.3. The average parabolic approximation to $\Delta h(t)$ was found and it is also plotted in Figure 2.5.3. The equation of the average slam entry profile is

$$\begin{aligned} &\Delta h(t) \cong at^2 + bt + c \\ &a = 3.12 \pm 1.65 \\ &b = -6.83 \pm 2.12 \\ &c = 0.07 \pm 0.30 \end{aligned} \qquad (2\text{-}8)$$

The average correlation coefficient was 0.91, which indicates that a parabola was not an inaccurate approximation to $\Delta h(t)$.

In Figure 2.5.3 the entry profiles for all the slam events analysed are plotted. As can be seen the penetration of frame 59 into the instantaneous water surface occurs with a significant range of relative motion profiles. 13 of the 33 slam events analysed are seen not to pass through the origin of the graph. This is because the noise in the data records was in some cases sufficiently large that it was impossible to identify precisely when the centre bow keel initially impacted the water surface. Also in some slam events the centre bow keel was initially in contact with the water surface when the slam

event entry commenced. However, given the significant range in slam entry profiles the error resulting from not all slam entry profiles passing precisely through the origin was considered not to have a significant impact on the calculation of the typical entry profile. This is due to the averaging that occurs during the calculation of this typical slam entry profile.

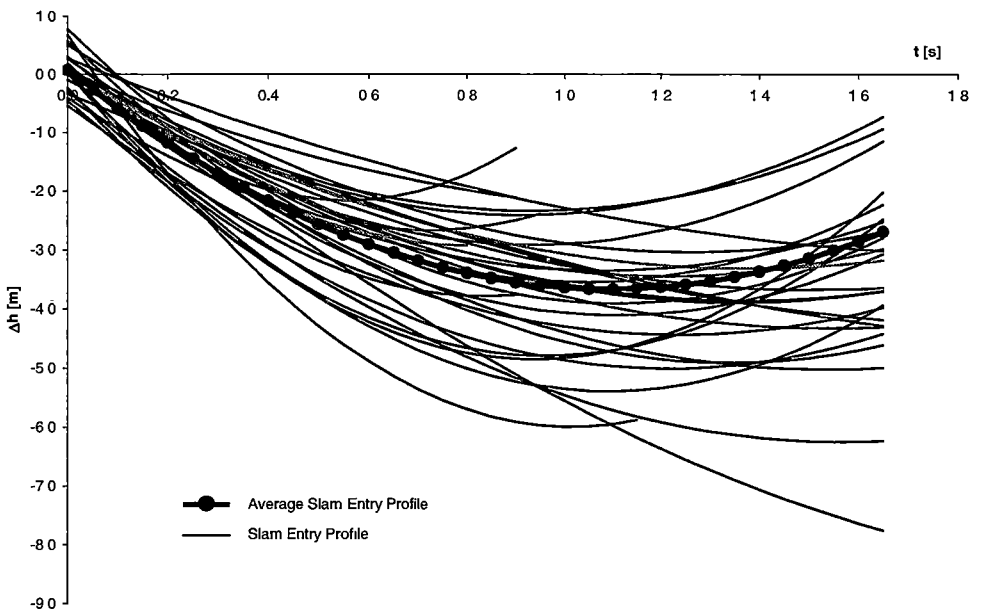

Figure 2.5.3 Slam entry motions for all slam events and the average slam entry profile

The procedure used to calculate $\Delta h(t)$ introduces three sources of error. Firstly clearance between the water surface and the centre bow keel varies depending upon the cargo loading condition of the vessel. This error has been estimated by calculating the change in vessel draught between an unloaded and load state. This was found to introduce an error of ±0.1m. Secondly an error is introduced by assuming that the vertical displacement of frame 59 is the same as the vertical displacement of frame 70 where the TSK meter is located. This assumption results in some of the pitch motion of the vessel being neglected. The error that this introduced was quantified by calculating the displacement of frame 59 by interpolating between the vertical displacement of the loaded centre of gravity and the TSK meter. The vertical displacement of the loaded centre of gravity was calculated by integrating the vertical acceleration records for this location for a particular slam record. The numerical drift that integrating digital acceleration data introduces was accounted for by ensuring that the average velocity and average displacement experienced by the vessel during the 90seconds of the data record were both zero. It was found that the vertical motion of frame 59 and the vertical motion of the TSK meter were in phase and varied by at most ±0.4m. The final source of error comes from the calculation $h_w(t)$ at frame 59. This calculation requires that the instantaneous water surface is temporally shifted as discussed above. The instantaneous water surface of course evolves in time as it is formed due to the combination waves of various frequencies travelling in

different directions. The errors associated with changes in the instantaneous water surface are difficult to quantify and it has been assumed that an error of ±0.2m is caused by variation in the water surface. These three error components can be combined by calculating the root mean square and thus a total error of ±0.46m is obtained. This is approximately 10% of the maximum $\Delta h(t)$ value obtained during the typical slam entry and is considered acceptable.

2.6. Slam Results

The relationship between the vessel Froude number (Fr) and the slam wave height (Hs) is shown in Figure 2.6.1. A linear least squares fit to the data reveals that vessel Froude number reduces with increasing slam wave height. This trend is attributed to the tendency of the operator to modify vessel operations depending on sea conditions. No slam events were identified for Froude numbers less than 0.24. This is attributed to the necessity of the vessel operator to run the vessel in an economic manner, which thus requires operation at commercial speeds. Also in the event that the sea state was too extreme the vessel operation was cancelled due to regularity requirements or operator management policy. This of course limits the upper bound of slam wave heights that are encountered by the vessel. These features illustrate that the data collected during commercial trials is significantly influenced by the operator's management policy and hence attitude with respect to risk of damage that may be sustained in service. This effect has been commented on previously by Aertssen (1979) who stated "that slamming frequency is a function of the captain's daring". Also, Haugen and Faltinsen (1999) observed that ship masters moderate the operation of their ships to reduce slamming and Roberts, Watson and Davis (1997) noted full-scale trial results are "derived from an operator envelope where speed is reduced in adverse conditions." It can be noted that the slam data obtained was all at relatively low Froude low speed, the design cruise speed of 38kts corresponds to a Froude number of 0.67.

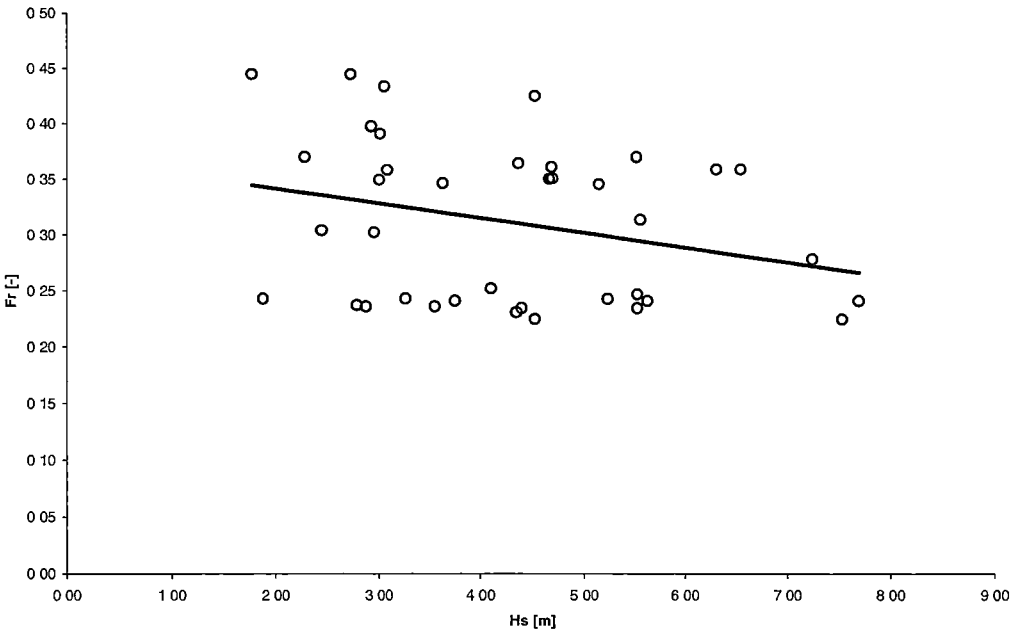

Figure 2.6.1 Vessel Froude number against slam wave height.

The relationship between the slam global stress and the slam wave height is shown in Figure 2.6.2. A linear trend line was fitted to the data using a least squares fit and it is evident that as the slam wave height increases so too does the slam global stress. The trend in slam global stress and slam wave height must be considered in the context of the trend of the reduction of vessel Froude number with slam wave height identified in Figure 2.6.1. Despite the vessel travelling at lower Froude numbers, at higher slam wave heights the vessel still experiences higher global slam stresses during slamming. This indicates that the effect of slam height on slam global stress is particularly significant.

The distance between the wetdeck and the still water surface for vessel 050 at frame 59 (tunnel height) in a loaded state is approximately 2.80m. Slamming commences at a slam wave height of 1.73m and thus it would appear that for slamming to occur the slam wave height must exceed 61% of tunnel height.

The relationship between slam event occurrence frequency and slam wave height is shown in Figure 2.6.3. This figure reveals that slamming becomes frequent once the slam wave height becomes comparable to or exceeds the tunnel height. This is in the slam wave height range 2.5m to 3.0m for which 18% of all slams occur. 15% of all slams occur in slam wave height range of 6.0m to 8.0m whereas 67% of slams occurred in the range of slam wave heights 2.5m to 5.0m. However, this does not conclusively indicate that slamming is necessarily less likely on larger waves since the histogram presented in Figure 2.6.3 may be influenced by the sea spectrum that is encountered.

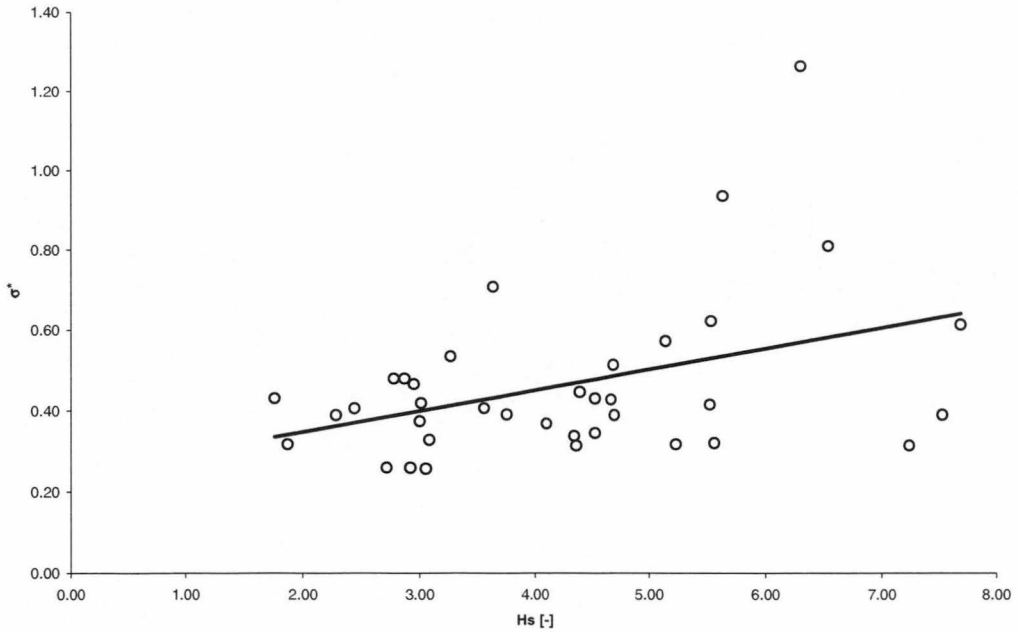

Figure 2.6.2 Slam global stress against slam wave height.

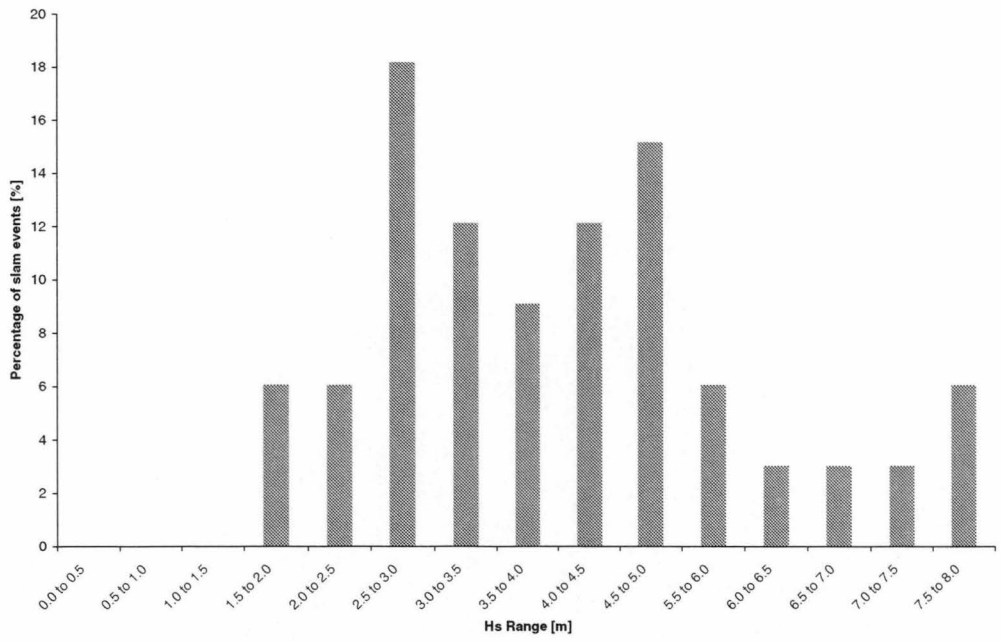

Figure 2.6.3 Histogram for percentage of slam events which occurred for different slam wave heights.

The relationship between slam global stress and vessel Froude number is shown in Figure 2.6.4. The trend of slam global stress with Froude number is not simple. A linear least squares fit to the data displays a reduction in slam global stress with vessel Froude number. However a parabolic least square fit to this data displays an initial increase of slam global stress with vessel Froude number before a maximum is obtained at Froude number 0.3 and then a reduction of slam global stress with Froude number is observed. The slam events that display the highest and the third highest slam global stress both occur at approximately Froude number 0.36 which is generally in the middle of the range of Froude numbers over which slamming occurs (0.22 to 0.45). It was identified earlier that the operator reduces vessel Froude number with increasing slam wave height (Figure 2.6.1) and that the slam global stress increases with slam wave height (Figure 2.6.2). Thus the most severe slamming occurs when the operator does not reduce speed sufficiently for the slam wave height which is encountered. This is illustrated by the most extreme slam event identified (σ^*=1.26, Hs=6.30m, Fr=0.36). This slam event displays a mid range Froude number but a high slam wave height and thus a very high slam global stress.

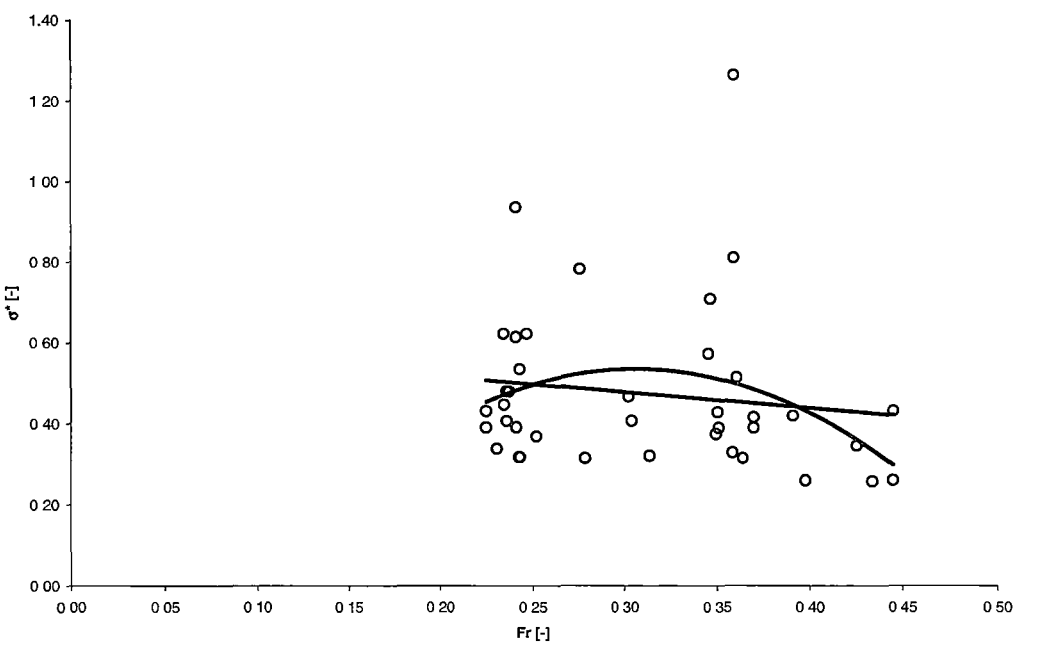

Figure 2.6.4 Slam global stress against vessel Froude number.

Figure 2.6.5 shows the relationship between the slam global stress and the relative velocity between the instantaneous water surface at frame 59 and the keel of the centre bow when the centre bow initially impacts the water surface. This velocity is calculated from the parabolic approximation to $\Delta h(t)$ for each slam event. A least squares linear fit to the data displays a reduction in slam global stress with increasing relative velocity. However the lower bound of the results, which is determined by drawing a straight line through the lower most data points, displays an increase in slam global stress with relative velocity.

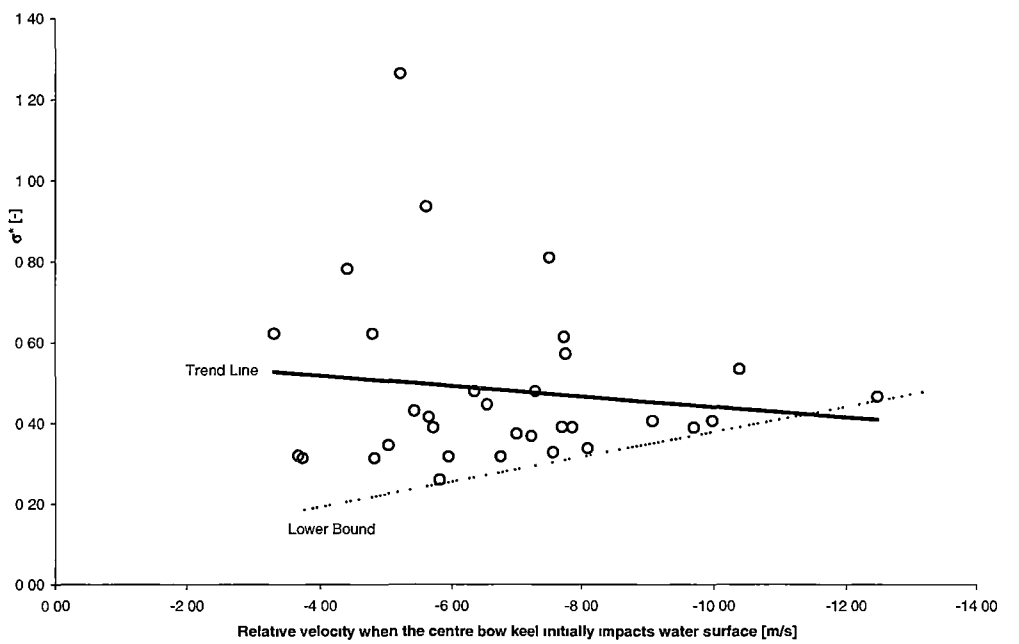

Figure 2.6.5 Slam Global stress against relative velocity when centre bow keel impacts instantaneous water surface.

Figure 2.6.6 shows the relationship between the slam global stress and the relative velocity when the instantaneous water surface initially impacts the wetdeck. This data set was processed in precisely the same way as the data set for the relative velocity of impact between the centre bow keel and the instantaneous water surface. The same trends are shown in Figure 2.6.6 as are displayed in Figure 2.6.5. Two data points are shown each with a relative impact velocity of 0.0m/s, since during both of these slam events the wetdeck did not impact the water surface.

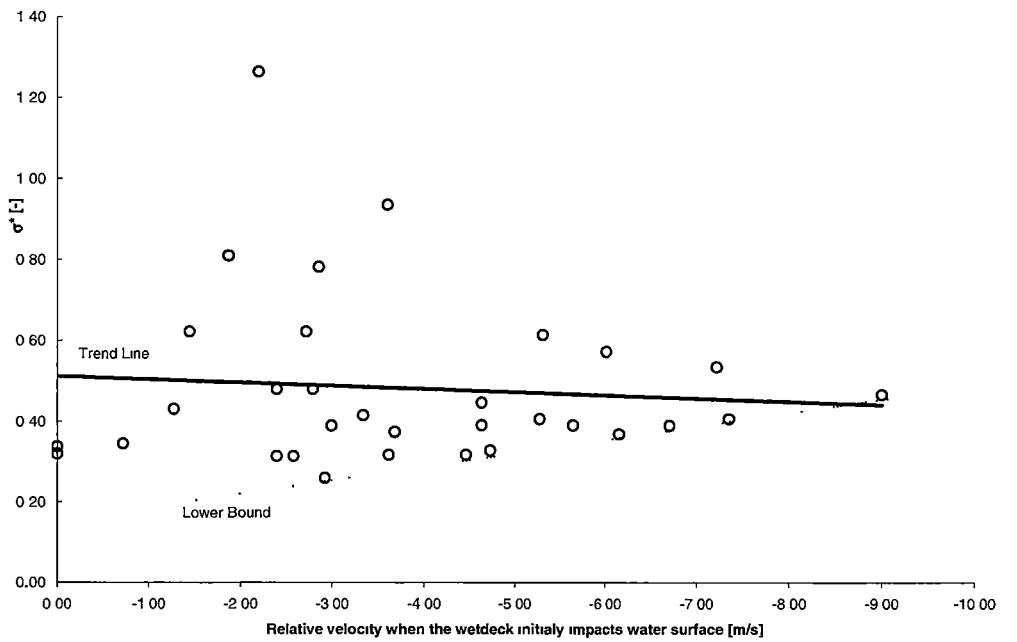

Figure 2.6.6 Slam global stress against the relative velocity between the instantaneous water surface and the wetdeck when the wetdeck initially impacts the water surface.

Both Figure 2.6.5 and Figure 2.6.6 indicate a reduction of scatter in the slam global stress as the relative velocity increases. It would appear that a larger relative entry velocity leads to a more clearly defined slam event. This might be expected since the overall penetration of the wave by the bow or wetdeck would be greater in such cases and the effect of irregularities or variations in the form of the water surface would be relatively smaller.

Figure 2.6.7 is a plot of slam global stress against maximum Δh (the penetration of the foot of the centre bow beneath the instantaneous water surface at frame 59). This graph indicates that the wetdeck impacts with the instantaneous water surface for all but two severe slam events. For these two slam events the minimum wetdeck and water surface clearance is 0.1m and 0.27m. Given the accuracy of the calculation of Δh it is possible that wetdeck slams did occur for these two slam events. Figure 2.6.7 also indicates that the wetdeck submerges as much as 4.1m below the instantaneous water surface at frame 59. However since deformation of the water surface due to vessel-water interaction occurs once wetdeck impact has occurred, the penetration distance as calculated here does not necessarily indicate a clearly defined parameter of the slam entry. It should however be seen rather as an indication of the severity of the event in terms of potential for relative penetration rather than actual penetration. Once again, we see that events with larger slam penetration leads to reduced scatter of the global slam stress and indicates a more clearly defined slam process.

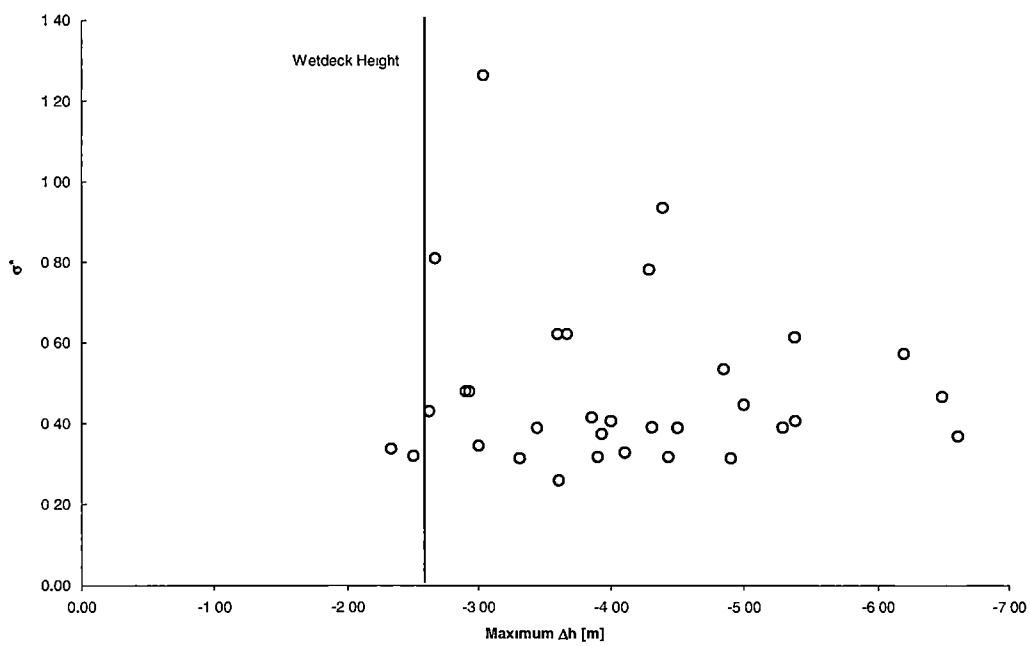

Figure 2.6.7 Slam global stress against maximum relative instantaneous water surface penetration of the centre bow keel.

The relationship between the penetration of the instantaneous water surface by the centre bow keel at the time corresponding to peak time dependent slam global stress and slam global stress is shown in Figure 2.6.8. The submergence of the centre bow relative to the instantaneous water surface profile required for impact of the wetdeck with the instantaneous water surface profile (-2.60m) is also plotted on this graph. The majority (68%) of slam events experience peak time dependent slam global stress after the wetdeck has become submerged. Of the slam events that experience peak time dependent slam global stress when the wetdeck is not submerged 80% of these slam events are ones in which the peak time dependent slam global stress occurs after $\Delta h(t)$ has obtained a minimum. For these events it is case that the wetdeck impacted the instantaneous water surface prior to the peak time dependent slam global stress being obtained. The two slam events identified in Figure 2.6.7 in which wetdeck submergence did not occur are two slam events in which peak time dependent slam global stress occurs before maximum penetration was reached. The time interval between peak time dependent slam global stress and minimum $\Delta h(t)$ is shown in Figure 2.6.9. Whilst there is some scatter, we see that an average maximum submergence occurs at the same time as maximum global slam stress.

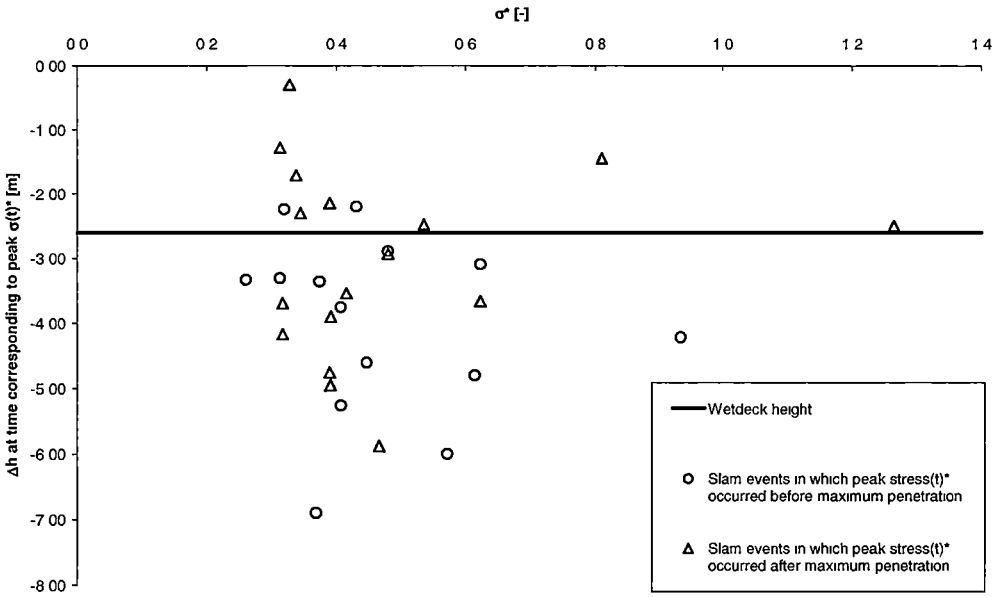

Figure 2.6.8 $\Delta h(t)$ at the time corresponding to peak time dependent slam global stress against slam global slam stress.

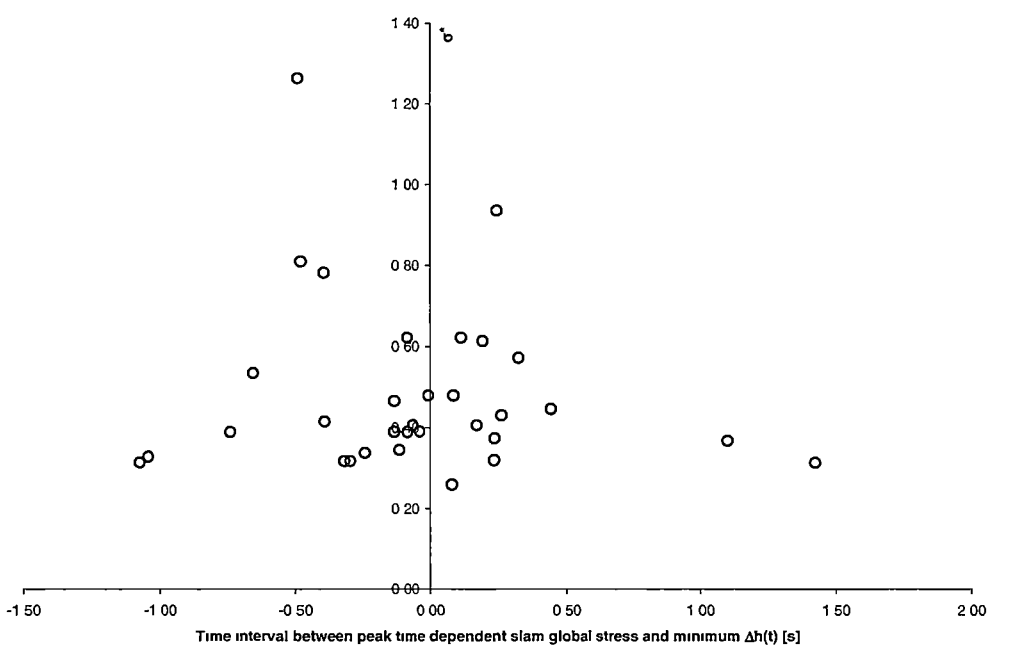

Figure 2.6.9 The time interval between peak time dependent global stress and minium submergence of centre bow. (Positive time refers to when minimum submergence occurs after maximum time dependent peak stress.)

The relationship between the time dependent slam global stress and the slam wave height is shown in Figure 2.6.10. It was found that the 81% of the slams occurred onto the lower half of the front of the encountered wave and that the more severe slams occurred on this portion of the wave. A linear least square trend line displays a reduction in slam global stress with higher location of impact on the wave face. The three most severe slam events occurred on the lower 10% of the wave face. The confluence of the trough of a wave and a catamaran wetdeck is likely to lead to a more severe slam than the confluence of a wave crest and a catamaran wetdeck due to the similarity of the longitudinal wetdeck geometry and wave trough profile.

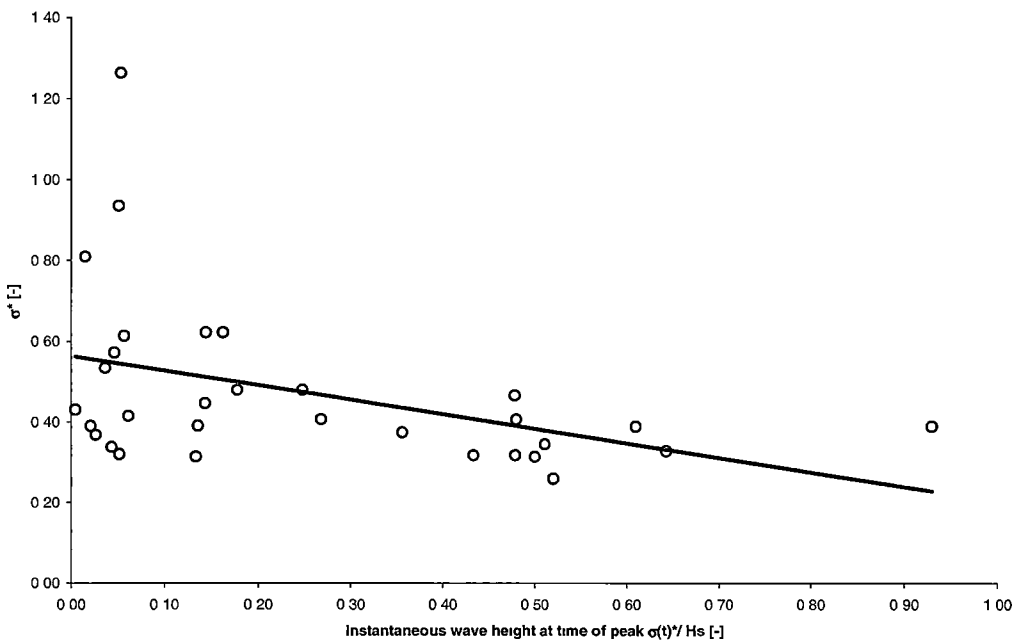

Figure 2.6.10 Instantaneous wave height at time of maximum time dependent slam global stress divided by the slam wave height against slam global stress. All slam events occurred on the front of the waves.

The longitudinal location of the slam event is examined in Figure 2.6.11 by comparing the number of vessel lengths travelled between the time when the instantaneous water surface impacts the wetdeck at frame 59 and the peak time dependent slam global stress. It was found that 62% of slam events occurred within ±0.025 vessel lengths of frame 59 and that 78% occurred within ±0.05 vessel lengths of frame 59. These findings confirm that slamming is centred on frame 59. It also indicates that the mechanism of slamming is indeed principally wetdeck slamming as the wetdeck extends some 0.07 vessel lengths forward of frame 59 and in all but 2 slam events the vessel experienced relative motions sufficient for the wetdeck to come into contact with the instantaneous water surface.

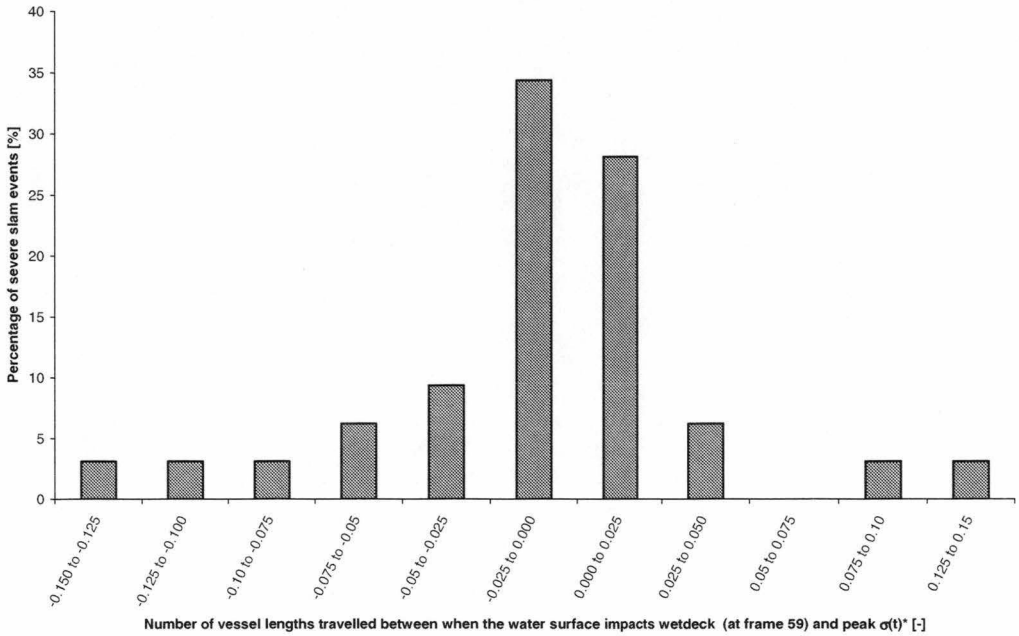

Figure 2.6.11 Histogram for the number of vessel lengths travelled between the time the water surface impacts the wetdeck (at frame 59) and peak time dependent slam global stress.

2.7. Summary

In this chapter the slamming experienced by INCAT vessel 050 during commercial operations in the Cook Strait New Zealand was examined. Vessel structural stress records, vessel motion and the encountered water surface data were collected. A definition of a slam event based solely on the magnitude of the loading experienced by the vessel was developed. This allowed slam events to be identified and their severity quantified. 38 severe slam events were identified from 10 months of trial data. The sea conditions during slamming were quantified by a wave height measure, the slam wave height, which was the peak to trough height of the waves upon which slamming occurred.

An example of the data records obtained for a typical slam event was presented. It was observed that slamming produced a high rate of change stress response in the vessel structure and that the peak stresses induced in the structure by the slam significantly exceeded the stresses causes by the underlying wave loads. The relative motion between instantaneous water surface and the vessel centre bow during slamming was calculated from the data records, and the form of this relative motion was approximately parabolic in form. A typical slam entry motion profile was developed, and this motion profile is used in Chapter 3 for the scaling of experimental scale models.

The effect of a number of parameters on the slamming behaviour of vessel 050 was examined. It was found the vessel Froude number during slamming reduced with the slam wave height and the slam global stress increased with slam wave height. It was found that the slams with the highest slam global stress occurred when the slam wave height was relatively high and the vessel Froude number was in the mid range of Froude numbers. It was also found that slamming occurred principally when the wetdeck came into contact with the trough of the encountered wave and that the slam load was centred approximately 6.0m aft of the jaws of the bow at frame 59.

3. Experimental Methods and Results

3.1. Overview

An experimental program was undertaken to gain insight into the slamming of a catamaran with a centre bow and to provide validation for the computational part of this project. Operational experience with INCAT wave piercer catamarans fitted with a centre bow has shown that occasional severe wetdeck and bow slam events can give rise to transient loads in excess of 1000 tonnes (Thomas et al 2001) and can lead to appreciable structural damage. Drop tests have been carried out previously by other investigators (Chapter 1), a particular focus of the present work is the double arch profile which is a characteristic feature of Incat wave piercer vessels. The experimental program entailed the drop testing of essentially of two-dimensional scale models into initially still water. This chapter details the equipment and techniques used in the experimental drop tests and the results obtained. A dimensional analysis of slamming is conducted and the results used in conjunction with full-scale trials data (Chapter 2), to develop a method for model scaling. The drop test facility is described, as too are the geometries of nine 1/40-scale models. The instrumentation and data acquisition system used to measure transient pressure and acceleration data is specified. Flow visualisation and data processing techniques are also described. The experimental results obtained during the test program are presented, including flow visualisation results, pressure, acceleration and velocity time records and peak pressure and acceleration values. Velocity and surface penetration at the moment of peak acceleration are also presented. The effect of the clearance between model side and tank wall is investigated, as too is the importance of the relative volume of the centre bow and the location of the highest point in the arch.

It was found that the cross section geometry greatly influenced the acceleration and pressure transients experienced by the models during water impact. For example the peak accelerations experienced by the models for a given normalised drop height varied by one order of magnitude. It was also found that the arch models with a centre bow which had the top of their arch located furthermost from the model centre line experienced the lowest peak accelerations.

It is recognised at the outset that there are significant limitations inherent in using two-dimensional scale model drop tests to represent a full-scale slam event. However it is considered that a two-dimensional drop test will provide basic insight into the transient entry process and the manner in which different bow profiles respond. The full-scale slam event is of course a three-dimensional process. The forward speed of the vessel, the variation of vessel geometry along the vessel length and the shape of the encountered water surface will lead to a significant departure from a two-dimensional model test. However, for slender hull forms at high-speed the effects associated with these flow and geometric features will be less significant than those effects associated with the transverse variation of

model geometry. Other factors, which will influence a full-scale slam event, include the time-wise vertical movement of the bow relative to the water surface and the underlying similarity parameters, such as the effective Reynolds and Weber numbers, and normalised drop height (which is equivalent to the effective Froude number). The normalised drop height is maintained at scale for similarity and thus the Reynolds and Weber numbers at model scale will not be identical to those at full-scale. This is an appropriate basis for scaling because the inertial forces are significantly larger than the viscous and surface tension forces.

3.2. Model Scaling

A full-scale ship slam is an extremely complex event. It is a three-dimensional, transient, two fluid, free surface, compressible, fluid structure interaction flow problem with implications for ship motion, structural design and fatigue life amongst other factors. This type of event is quite difficult to model and thus a simpler, but similar event needs to be considered. Consequently it was decided to conduct essentially two-dimensional drop tests of scale models of varying cross section into still water. This approach will capture many of the essential features of a true slam event whilst being practicable and well defined.

The general layout of a catamaran with a centre bow cross section model impacting a calm water surface in a long thin tank is shown in Figure 3.2.1.

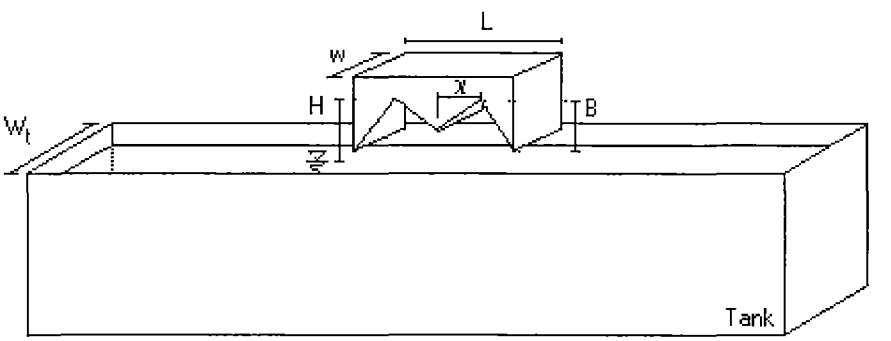

Figure 3.2.1 Schematic drop test diagram for scaling.

Neglecting viscosity and surface tension the section entry process is described by the variables m_m/w (model mass divided by model width), L (beam), ρ (fluid density), V (scaling velocity) and g (gravity). $V = \sqrt{2gH}$ is the velocity the model will obtain if it falls under gravity through a height H (the distance from the undisturbed water surface to the top of the arch when the model is released). These five variables maybe combined into two dimensionless groups by application of the Buckingham pi theorem, thus the normalised drop height

$$H^* = \sqrt{\frac{2H}{L}} \qquad (3\text{-}1)$$

and mass number

$$m^* = \frac{m_m}{\rho w L^2} \qquad (3\text{-}2)$$

are obtained. The normalised drop height is equivalent to an effective Froude number for the entry process. However we are modelling the entry of a hull section which is constrained in the full-scale case by its connection to the remainder of the vessel which is significantly different from the entry of a free falling hull cross section model. To allow scaling between these two inherently dissimilar events we set out to ensure that the velocity as a function of time matches that of the relative velocity between the instantaneous water surface and the vessel wetdeck at frame 59. This is done by matching the entry velocity profile at two instants during the entry process. The velocity profile for the full-scale vessel was found in chapter 2 for an average slam event to be $\Delta h(t) = 3.12t^2 - 6.83t + 0.07$. Taking the velocity at the instant (t_{wd}) that the wetdeck impacts the water surface as a required parameter, the section velocity is $\Delta\dot{h}(t_{\text{wd}}) = -3.65\text{ms}^{-1}$. Further the velocity at which the demi-hull keel would impact the nominal water surface level is found at $t_{\text{dh}} = -0.30s$, and the section velocity at this instant is $\Delta\dot{h}(t_{\text{dh}}) = -8.72\text{ms}^{-1}$.

It should be noted that in the full-scale trial observations the keel of the demi-hulls does not necessarily move above the water surface. However the two points on the actual motion profile when the demi-hull keel and the wetdeck impact the water surface are used as reference points to model the overall entry process. This is because the test models were necessarily dropped with the demi-hull keel above the initial water surface level so as to achieve the required conditions.

In order to translate the requirement to model the time variation of vertical velocity into a requirement for the mass number use is made of the von Karman (1929) momentum analysis for which the added mass (m_a) of the section is that of a submerged half circle of diameter L. By equating the initial momentum at t_{dh} (as the demi-hull keels impacts the water) with the momentum at t_{wd} (when the wetdeck reaches the water surface) and neglecting the effects of gravity, we thus obtain the required model mass as m_m, where

$$\Delta\dot{h}(t_{\text{dh}})m_m = \Delta\dot{h}(t_{\text{wd}})(m_m + m_a) \qquad (3\text{-}3)$$

that is,

$$m_m = \frac{m_a}{\left(\frac{\Delta\dot{h}(t_{\text{dh}})}{\Delta\dot{h}(t_{\text{wd}})} - 1\right)}. \qquad (3\text{-}4)$$

Noting that $m_a = \frac{\pi \rho w L_{fs}^2}{8}$ and dividing both sides by $\rho w L_{fs}^2$ (noting that suffix fs denotes full-scale and suffix m denotes model scale)

$$\frac{m_m}{\rho w L_{fs}^2} = \frac{\pi/8}{\left(\frac{\Delta \dot{h}(t_{dh})}{\Delta \dot{h}(t_{wd})} - 1\right)} \tag{3-5}$$

Since $\frac{\Delta \dot{h}(t_{dh})}{\Delta \dot{h}(t_{wd})} = \frac{8.72}{3.65}$, then we have

$$m^* = \frac{m_m}{\rho w L_{fs}^2} 0.284 . \tag{3-6}$$

Finally it is required that the normalised drop height, which must meet the requirement of Froude scaling, is matched at full-scale and model scale. This gives

$$\sqrt{2H_{fs}/L_{fs}} = \sqrt{2H_m/L_m} . \tag{3-7}$$

The beam of vessel 050 at frame 59 (lateral position about which slamming was centred as discussed in chapter 2) is $L_{fs} = 23.8\text{m}$ and $H_{fs} = B_{fs} + \frac{\Delta \dot{h}(t_{dh})^2}{2g}$, where $B_{fs} = 5.1\text{m}$ is the distance from the demi-hull keels to the wetdeck and $\frac{\Delta \dot{h}(t_{dh})^2}{2g}$ is the drop height required to obtain $\Delta \dot{h}(t_{dh})$ due to free fall. Thus

$$H_{fs}^* = \sqrt{\frac{2H_{fs}}{L_{fs}}} = 0.87 \tag{3-8}$$

Thus a suitable normalised drop height (0.87) and mass number (0.284) have been identified for scaling from full-scale trials results to drop test model scale.

The justification for neglecting surface tension and viscosity was as follows. The forces associated with these two fluid properties are not significant since the Reynolds number ($\text{Re} = \rho VL/\mu = 263 \times 10^6$) at full-scale is large, indicating that viscous effects are small compared with the inertial effects. At model scale the Reynolds number ($\text{Re} = 0.85 \times 10^6$) is 309 times smaller than at full-scale but is still large in absolute terms. Similarly the Weber number at full-scale ($\text{We} = \rho V^2 L/\sigma = 57.4 \times 10^6$) is significantly larger than 1 indicating the surface tension effects are small compared with the inertial effects. At model scale the Weber number ($\text{We} = 0.027 \times 10^6$) is 2126 times smaller than at full-scale but remains large in absolute terms.

Examination of the full-scale trial results (Chapter 2) reveals that severe slamming occurs over a significant range of relative motions. The average relative motion was used in this section to develop suitable scaling values. However the scatter in the full-scale relative motion results indicate that drop testing over a range of normalised drop heights and mass numbers is necessary to fully encompass experimentally the measured full-scale scatter. The range of normalised drop heights required for testing is shown in Figure 3.2.2 and this range was fully encompassed in the experimental program as indicated in this figure. The range of mass numbers required for testing is shown in Figure 3.2.3. Only two mass numbers were tested, however these two mass numbers were representative of the range of mass numbers calculated from full-scale data.

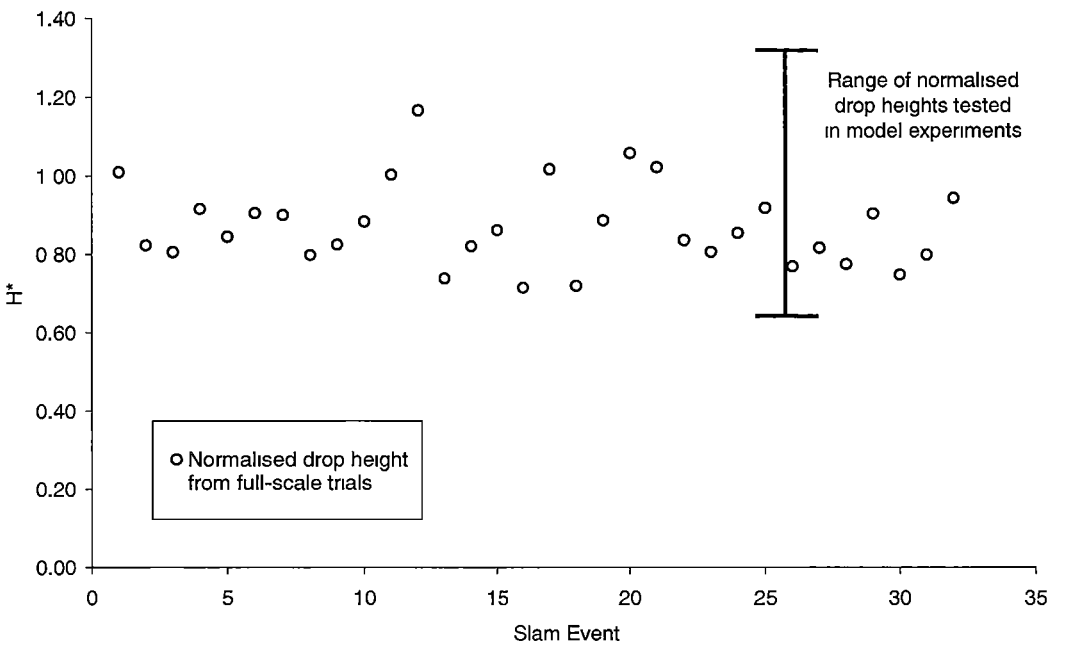

Figure 3.2.2 Normalised drop heights calculated from full-scale slam events data.

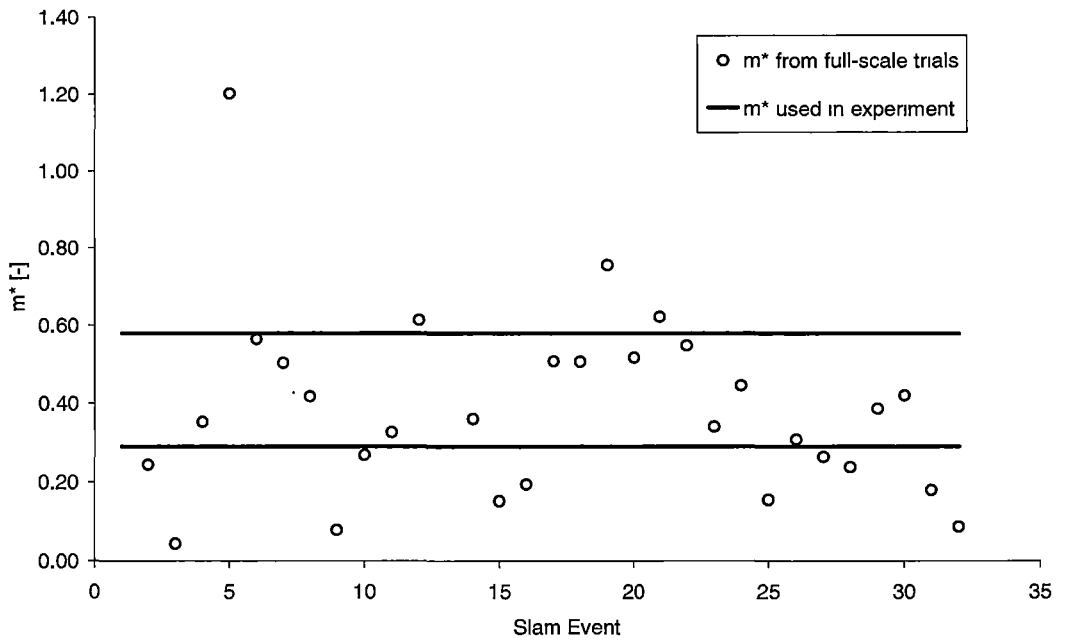

Figure 3.2.3 Mass numbers calculated from full-scale slam events and the mass numbers used in experiment.

Despite the rational selection of normalised drop height and mass number as required for scaling, the entry motion profile of the drop test models may vary significantly from the relative motions experienced by the full-scale three-dimensional ship. This is principally due to the inherent dissimilarity of the two events. The model tests are essentially the free fall of an isolated mass whereas a full-scale ship slam is the impact of a hull section, forced by the motion of the ship as a whole, into the encountered wave profile. Thus the value of drop tests in modelling full-scale ship slams is limited. Model tests involving forced motions would ensure a better similarity of relative motions, however tests of this nature were considered too complex for the current study.

During the drop test experiments vertical acceleration ($\ddot{y}$), pressure (p) and time (t) measurements were made. These variables can be made non-dimensional as shown in Table 3.2.1. This was done so that scaling may be undertaken between model and full-scale.

Dimensionless Coefficients	Formula
Force Coefficient (C_F)	$\frac{m_m \ddot{y}}{\rho w L V^2}$
Pressure Coefficient (C_p)	$\frac{p}{\rho V^2}$
Dimensionless time (t^*)	$\frac{tV}{L}$

Table 3.2.1 Dimensionless Coefficients.

This introduces the question of the most appropriate performance indicator of a bow profile. If strength of the local plating is the dominant issue, then clearly the peak pressure is of concern. If deformation of the bow structure, such as has occurred in some severe full-scale slam events, is the dominant issue then it is the maximum force which is of concern. If it is the transmission of energy into the whipping and the global motion of the ship as a whole that is the issue, then it is the total impulse of the bow force transient that is of concern. Since deformation of the bow structure has been the main problem caused by the slam events, the focus of the present work is on the force. Whilst the pressure data obtained here also gives some information relating to the strength required of the hull plating, it seems likely that the maximum hull pressures in full-scale slam events may be more sensitive to three dimensional effects. These issues are discussed further is section 3.6.

3.3. Drop Test Facility

The drop test facility Figure 3.3.1 consisted of a tank (300mm by 1200mm by 2400mm), tower, centre post and adjustable bearings. The model was attached to the bottom of the centre post. The model could be attached so that it impacted the water symmetrically or asymmetrically (roll of 2.5°, 5.0°, 7.5° or 10.0°). The centre post was restrained in all degrees of freedom except vertical translation by two sets of bearings mounted 600mm apart in the tower. The centre post was made of 100mm square aluminium box section in which many holes had been drilled to remove as much mass as possible whilst maintaining the desired rigidity. The bearings were adjusted to ensure the centre post and model fell freely, without vibration and in the required direction. The centre post and model were raised by a simple pulley mechanism to the required height. Repeatability of this process was ensured by the use of a height gauge fitted to the top of the tower. The model and centre post was released with a quick release shackle triggered with a cord. Additional mass could be attached to the centre post and model by bolting it to the top or bottom cross bar of the centre post. The model and centre post, when dropped, were stopped firstly by impact with the water in the tank and then finally by padded shock absorbers. Drops could be carried out from 0mm to 800mm depending upon model size. Spray and splash from drop tests were contained within the tank by a spray shield.

The depth of water in the tank and the tank length were selected such that fluid-wall interaction effects were small compared to the model-fluid interaction effects. The tank was filled with water to a depth of 1.000m. The water depth used was comparable with the water depths used in previous drop tests of models of a similar scale and was selected on that basis. For example Zhu and Faulkner (1994a) used a water depth of 0.750m for model 0.2m wide, 0.3m long and 0.2m tall and Smith, Stansby and Wright (1998) used a water depth of 1.0m to test a 1.150m by 0.565m flat plate model with side plates. Chuang and Milne (1971) used a water depth of 2.44m for various wedge models 0.508 long by 0.673m wide, this water depth was relatively deeper than the current experiments. The tank length was designed by estimating the blocking effect that the walls of the tank caused. This was done by considering the volume of fluid elevated above the initial water surface level during the impact of a 15° wedge into an infinite expanse of fluid by use of the Wagner (1932) expression for the water

surface elevation. The volume of elevated fluid outside a notational tank wall was then calculated. It was assumed that the elevated fluid outside the notational tank would cause the initial water surface inside the notational tank to rise by some amount over the time of the impact event so that continuity was satisfied. Thus the blocking effect of the tank walls could be estimated by considering the average velocity of the initial water surface due to the wall blocking effect and it was found that this velocity was less than 1% of a typical model velocity for a tank length of 2400mm. This was considered acceptable. The effects of surface gravity waves were also found not to create wall interaction problems over a typical time scale of a drop test. The effects of acoustic waves during drop tests were considered, however it was not feasible to build a tank large enough to ensure that no reflected waves returned to the model during the test. The author is unaware of any experimental drop test work that has successfully measured the effect of acoustic waves during slamming.

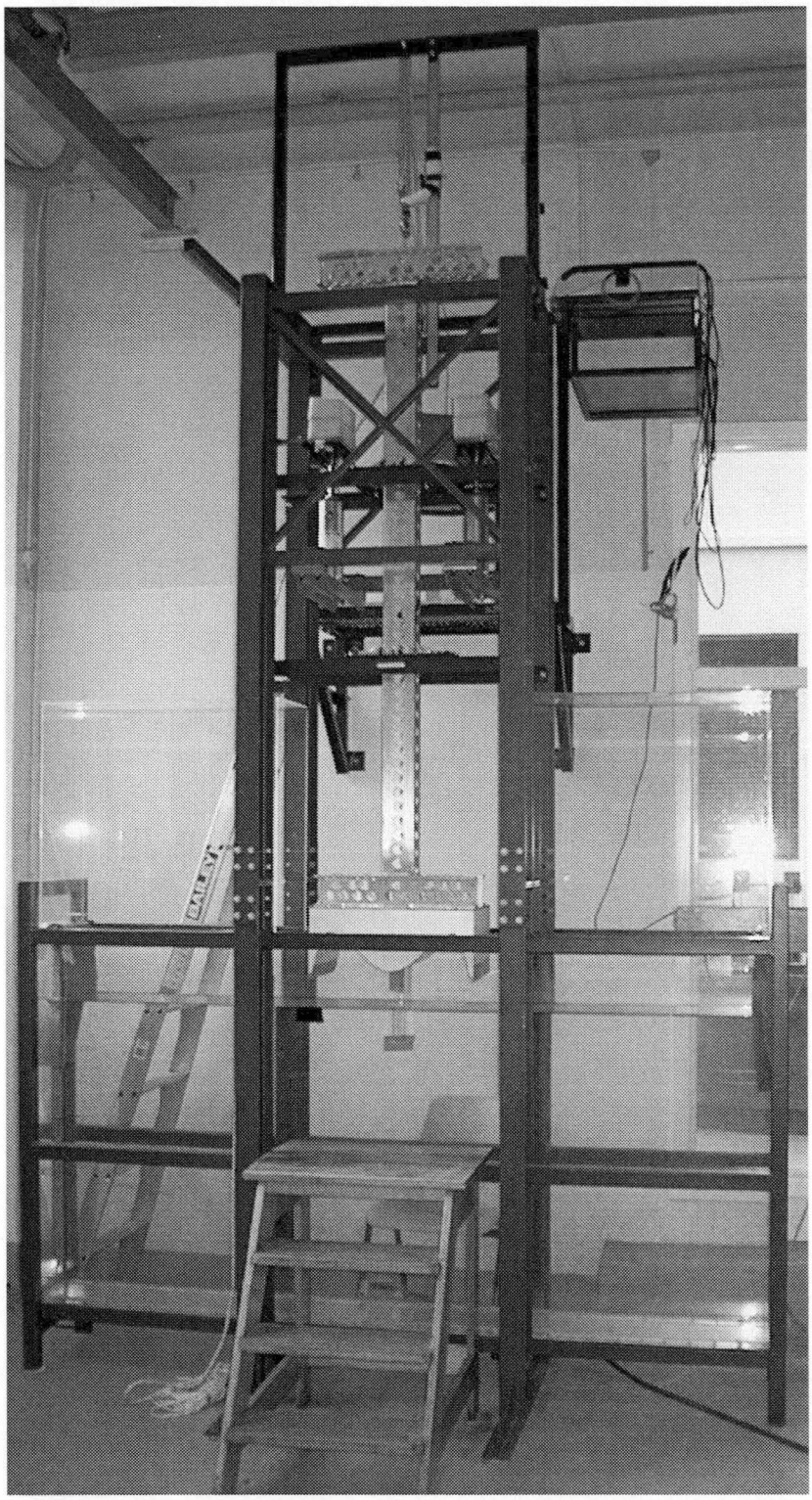

Figure 3.3.1 Drop test facility

3.4. Instrumentation

The experimentation program required the measurement of the vertical linear acceleration of the models and surface pressure on the models as they impacted with initially calm water. Flow visualisation of the impact was also required. This was achieved using two pressure transducers, an

accelerometer and a high-speed digital camera. Signal conditioning and data acquisition was done with a DC amplifier, low pass filter, analogue signal conditioner, analogue to digital converter and a lap top computer (see Figure 3.4.1).

An Endevco model 7290A-30 variable capacitance accelerometer was used to measure the vertical acceleration of the models, its key characteristics were

Range	+/- 30g
Sensitivity	66 +/- 4 mV/g
Frequency Response (5%)	0 to 1500 Hz.

This accelerometer satisfies the range and frequency requirements of the experiment, and responds at 0Hz, which enabled measurement of the initial free fall motion of the model, hence the initial impact velocity. The accelerometer was attached to the centre post.

The selection of pressure transducers for scale model drop tests can be problematic because the face diameter of the pressure transducer can significantly influence the measured peak pressures. This occurs because the pressure transducer measures the average instantaneous pressure over the face of the instrument rather than the peak instantaneous pressure at an infinitesimal point. If the face diameter of the pressure transducer is too large compared with the size of the model and maximum characteristic relative flow velocity and time scale of any pressure spikes then inaccurate results may be obtained (Hagiwara and Yuhara (1976)). Similarly if pressure panels such as those used by Kapsenberg and Brizzolara (1999) were used to measure the pressure transients then similar averaging effects would be observed as these panels are necessarily large compared with model scale. Thus the pressure transducer selected was a piezoresistive Endevco model 8510B-500, the key characteristics of which were:

Range	+/- 0-3,447 kPa
Sensitivity	4.1 kPa/mV
Face Diameter	3.8 mm
Diaphragm resonance frequency	500 kHz
Linearity	0.25% Full Scale Output

This model of pressure transducer was used successfully by Zhu and Faulkner (1994a) during drop test experimentation of three-dimensional SWATH like models, of a similar size to the models used in the current experimental program.

Pressure transducers were fitted to the models with threaded aluminium plugs that were permanently attached to the model. The transducer mountings were designed so that the sensor face was flush with the model surface. If the transducers were fitted so that the transducer face was below the model surface then air could be trapped between the transducer face and the water producing spurious results. Alternatively if the pressure transducer protruded beyond the model surface then spurious results would be obtained also. Two pressure transducers were used and these were successively positioned in a range of locations in the model until all desired pressure readings had been made.

The accelerometer and the two pressure transducers were connected to an Endevco model 136 three-channel DC differential voltage amplifier. This amplifier has a 200 kHz bandwidth, a gain range of 0 to 1000 and can provide four selectable excitation voltages. A 4-pole Butterworth low-pass filter is built in that can be set to 2kHz, 4kHz or 10kHz. A DBK54 analogue signal conditioning unit attached to a DaqBook112 analogue conversion module was used to convert the analogue signals to digital signals. Data was recorded using a lap top computer running a DaisyLab program at a sample rate of 7042Hz. Low-pass filtering at 4kHz, 10kHz and no filtering was tested and no significant difference was observed in the data obtained and thus no filtering was used during the experiments. Results were post processed using Excel and Visual Basic.

A Kodak high-speed digital camera with a maximum resolution of 512×240 pixels and a maximum frame speed of 500Hz was used for flow visualisation. The camera was positioned so that the lens was at the same height as the initial water surface. This position was selected to minimise parallax error caused by the different refractive indexes of water, Perspex and air. The focal length was 5.8m. Images were processed using WinAnalyse software to calculate model motions by tracking visual targets attached to the model. This method of measuring the model motion was not successful because the resolution was too low and too noisy. When the displacement record was differentiated to find velocity and acceleration records the results obtained were extremely noisy due to numeric errors associated with the differentiation algorithm.

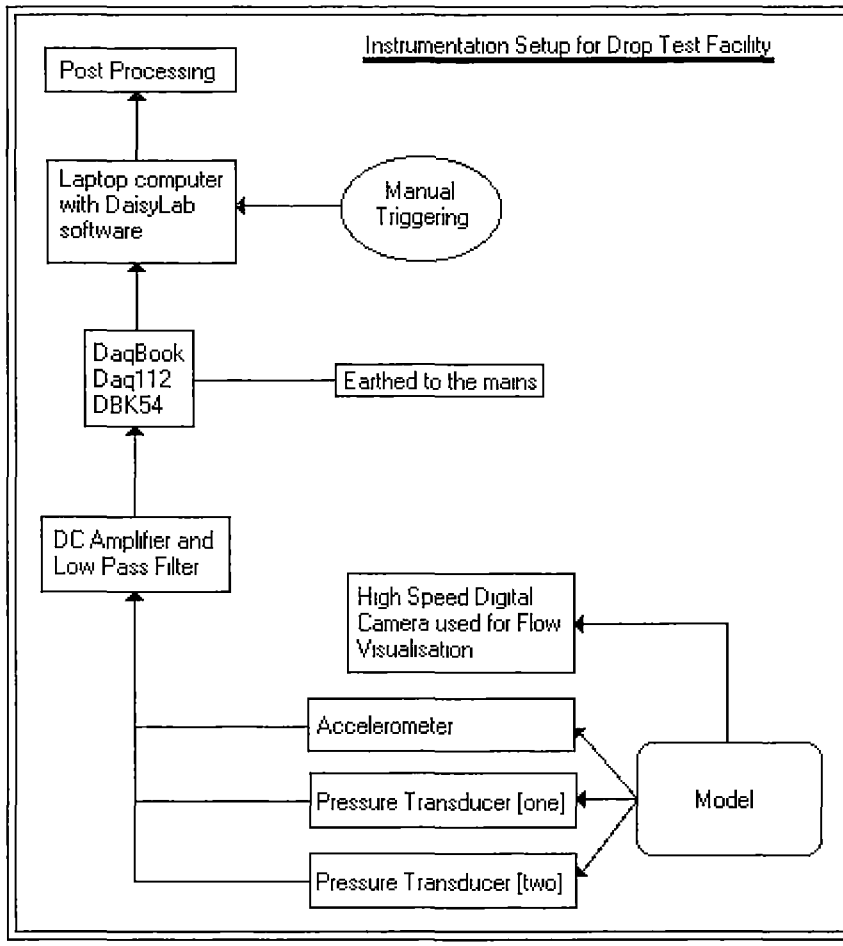

Figure 3.4.1 Instrumentation overview

3.5. Models

Nine models were constructed with a range of cross sections (Figure 3.5.1) so that the geometrical features that influence slamming performance under drop test conditions could be investigated. The cross section of INCAT vessel 050 at frame 59 was the basis for the design envelope of the model geometries. The models were hollow to allow a wide range of mass numbers to be tested and to allow pressure transducers to be fitted. A 3mm aluminium plate lid with a rubber gasket was used to seal the models to stop them filling with water. All models were designed to be effectively rigid.

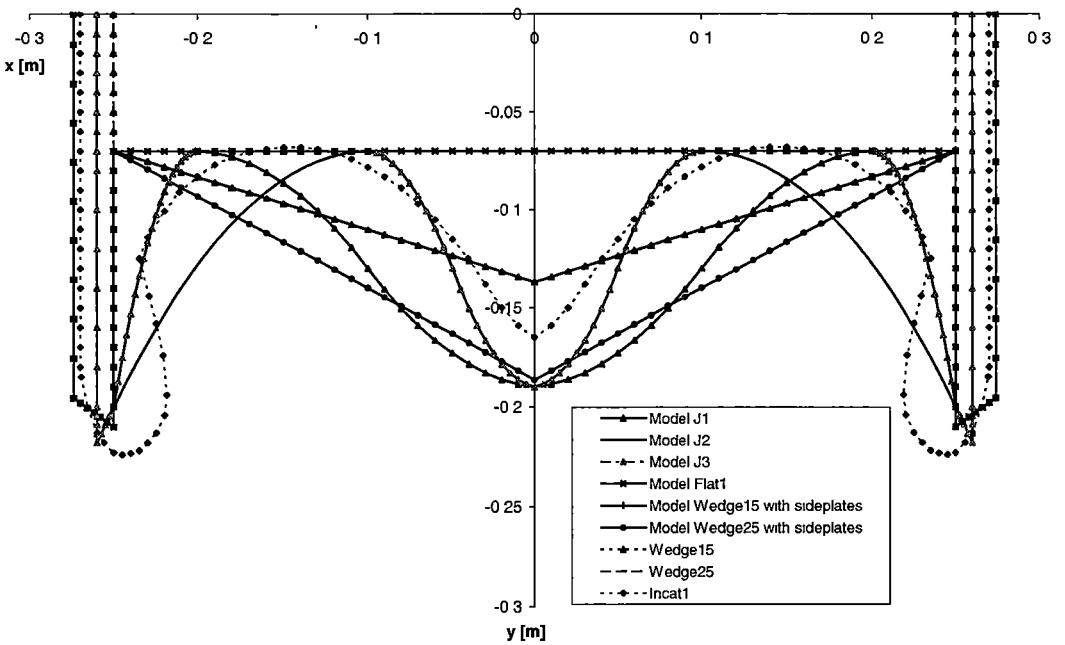

Figure 3.5.1 Geometry of all models

Some of the gross geometric characteristics of the models can be quantified by three geometric parameters which are listed Table 3.5.1. The normalised wall clearance is the ratio of the clearance between the model side and the tank wall to the tank width. All models except where explicitly stated had a normalised wall clearance of 0.033. The area ratio is the volume of the model beneath the top of the arch ($\forall$) divided by the product of the model beam, height and width. The location of the highest point in the arch (for arch models with centre bow) is the ratio of the distance of the highest point in the arch from the centre line of the model to half the model width.

Geometric Parameter	Definition
Normalised Wall Clearance	$\frac{W_t - w}{W_t}$
Area Ratio	$\frac{\forall}{LBw}$
Highest Point in Arch	$\frac{2\chi}{L}$

Table 3.5.1 Geometric model parameter definition.

Two wedge models with dead rise angles of 25° and 15° were constructed. Both these models had knuckles (Figure 3.5.3 and Figure 3.5.4). These two cross sections were selected to allow comparison of the experimental results obtained from the drop test facility with previous results of other researchers. This allowed a check on the adequacy of the experimental results. The 25° and 15° wedge models have cross sections similar to a notional mono-hull vessel, thus results obtained will be of value for comparison with catamaran cross sections. The wedge models were constructed of folded 3mm aluminium plate.

Two additional models were created by attaching sideplates to the 25° and 15° wedge models to approximate the demi-hulls of a catamaran (Figure 3.5.5 and Figure 3.5.6). These two models had the highest point in the arch located far from the centre line of the model, and a wedge shaped centre bow. The 25° wedge with sideplates represented a cross section with an area ratio (Table 3.5.1) greater than the corresponding INCAT vessel 050 cross section, used as a reference hull. The 15° wedge model with sideplates had a centre bow with an area ratio similar to that of INCAT vessel 050. The sideplates were made from timber (painted aluminium grey for aesthetic reasons).

Model J1 (Figure 3.5.7) was developed to represent a cross section with a voluminous curved centre bow and the highest point in the arch displaced significantly from the centre line of the model. Model J2 (Figure 3.5.8) has a fine, curved centre bow with the highest point in the arch located close to the centre line of the model. Significant volume was placed at the top of the demi-hull of model J2. Model J3 has the same fine curved centre bow as model J2 and same demi-hull shape as model J1, joined at the top of the arch with a large flat wetdeck (Figure 3.5.9). This model was designed to examine how the combination of a fine centre bow, fine demi-hulls and a flat wetdeck influenced slamming during drop tests. Models J1 and J2 were CNC milled from fibreboard and then finished with water proof paint. Model J3 was made with a foam core and fibreglass exterior.

Model Flat1 was a flat plate model with sideplates attached (Figure 3.5.11). This model was designed to represent a catamaran cross section that did not have a centre bow and to act as a basis for

comparison so as to assess the effect of a centre bow on slamming performance during drop tests. The model was constructed from 5mm aluminium plate with sideplates made from timber.

Model Incat1 was based on a cross section of INCAT vessel 050 (Figure 3.5.10). This model was used to allow comparison of the current INCAT centre bow geometry with alternative centre bow geometries. This model was constructed with a foam core and a fibreglass surface.

The demi-hulls on the model cross sections were finer than the demi-hulls of INCAT vessel 050. The data collected during the full-scale trails of INCAT vessel 050 (Chapter 2) indicated that severe slamming occurred primarily due to wetdeck slamming. Thus bottom slamming on the demi-hulls was considered unimportant and no attempt was made to model it.

Pressure transducer mountings were fitted to the models as described in Section 3.4 and the location of these mountings are given in Table 3.5.2 and Figure 3.5.3 to Figure 3.5.11.

A series of four 15° wedge models with sideplates were constructed with normalised wall clearances of 0.033, 0.100, 0.170 and 0.270 to investigate the effect of the gap between model end and tank wall on slamming performance during drop tests. Pressure tappings were only fitted to the models with a normalised model width of 0.033. The 15° wedge with sideplates geometry was selected to investigated the effect of normalised wall clearance because it had a catamaran-like geometry and wedge models were not difficult to manufacture.

A generic spline was developed to allow geometric specification of all models except model Incat1. The definition of the spline for each model is given in Figure 3.5.2 and Table 3.5.2. Table 3.5.2 also contains the area ratios and the location of highest point in the arch for each model.

Examination of the geometry of the models constructed reveals that the models vary in beam (L) by as much as ±4%. This has implications for the accuracy of comparisons of dimensional accelerations and dimensional pressure values between models for a particular mass number and normalised drop height. That is, a larger model may experience higher acceleration than a smaller model for a particular mass number and normalised drop height, however in non-dimensional terms these accelerations may be of the same relative magnitude. It is possible to quantify the relative difference in relative magnitudes of dimensional and non-dimensional acceleration and dimensional and non-dimensional pressure by comparing the scaling of two geometrically similar models with beams L_1 and L_2 and their behaviour at a particular normalised drop height and mass number. The mass number is

$$m^* = {m_m}/{\rho w L^2} \tag{3-9}$$

thus

$$m_m = \rho w L^2 m^* . \tag{3-10}$$

The normalised drop height is

$$H^* = \sqrt{2H/L} \tag{3-11}$$

and thus the scaling velocity value equals

$$V = \sqrt{gLH^*} . \tag{3-12}$$

The force coefficient is

$$C_F = m_m \ddot{y} / \rho w L V^2 . \tag{3-13}$$

Substituting the m_m and V values into the force coefficient expression

$$C_F = \ddot{y} \rho w L^2 m^* / \rho w L g L H^{*2} = \frac{m^*}{gH^{*2}} \ddot{y} \tag{3-14}$$

The effect of a change in model beam (L) can now be assessed by considering the ratio of the force coefficients for the two models C_{F1}/C_{F2} and noting that mass number and normalised drop height are constant for the two models, thus

$$\ddot{y}_1 / \ddot{y}_2 = C_{F1} / C_{F2} \tag{3-15}$$

Hence acceleration values may be compared in either dimensional or non-dimensional form with no relative change in relative magnitude.

Considering the effect of changing the model beam on the relative magnitudes of the dimensional and non-dimensional pressure values for two geometrically similar models of different beams at the some particular mass number and normalised drop height, the pressure coefficient is

$$C_p = p / \rho V^2 . \tag{3-16}$$

Substituting the expression for V from above

$$C_p = p / \rho g L H^{*2} . \tag{3-17}$$

The effect of a change in L can now be assessed by considering the ratio of the pressure coefficients of the two models C_{p1}/C_{p2} and once again noting that normalised drop height is constant for each of the models, thus

$$p_1 / p_2 = Cp_1 L_1 / Cp_2 L_2 \cdot \quad (3\text{-}18)$$

Hence the relative magnitudes of the dimensional and non-dimensional pressure values vary linearly with changes in model beam. The model geometries vary in beam by less than ±4% and thus the relative magnitude of the dimensional and non-dimensional pressure values for the models will also vary by ±4%. This variance was considered to be small and that comparative conclusions would be unchanged if they were based on the dimensional or non-dimensional pressure values. Thus dimensional pressure results are presented in this chapter.

Domain	Range	Constraints
$0 = x_1 \le x < x_2$	$f_1(x) = a_1 x + b_1$	$f_1(x_1) = y_1$ $f_1(x_2) = y_2$
$x_2 \le x < x_3$	$f_2(x) = a_2 x^2 + b_2 x + c_2$	$f_2(x_2) = y_2$ $f_2(x_3) = y_3$ $f_2'(x_3) = \tan(\theta)$
$x_3 \le x < x_4$	$f_3(x) = a_3 (x_4 - x)^{b_3}$	$f_3'(x_3) = \tan(\theta)$ $f_3(x_3) = y_3$
$x_4 \le x < x_5$	$f_4(x) = 0$	$f_4(x_4) = y_4 = 0$ $f_4(x_5) = y_5 = 0$
$x_5 \le x < x_6$	$f_5(x) = a_5 (x - x_5)^2$	$f_5(x_6) = y_6$
$x_6 \le x < x_7$	$f_6(x) = a_6 x + b_6$	$f_6(x_6) = y_6$ $f_6(x_7) = y_7$
$x_7 \le x \le x_8$	$f_7(x) = a_7 x + b_7$	$f_7(x_7) = y_7$ $f_7(x_8) = y_8 = 0$
θ	$\tan^{-1}\left(\frac{-2(y_2 - y_3)}{(x_3 - x_2)}\right) < \theta \le 180^o$	$Tan(\theta - 180))$ is the slope of the spline at (x_3, y_3). A restraint is applied to θ so that the spline is monotonic decreasing in the domain $x_2 \le x \le x_4$.

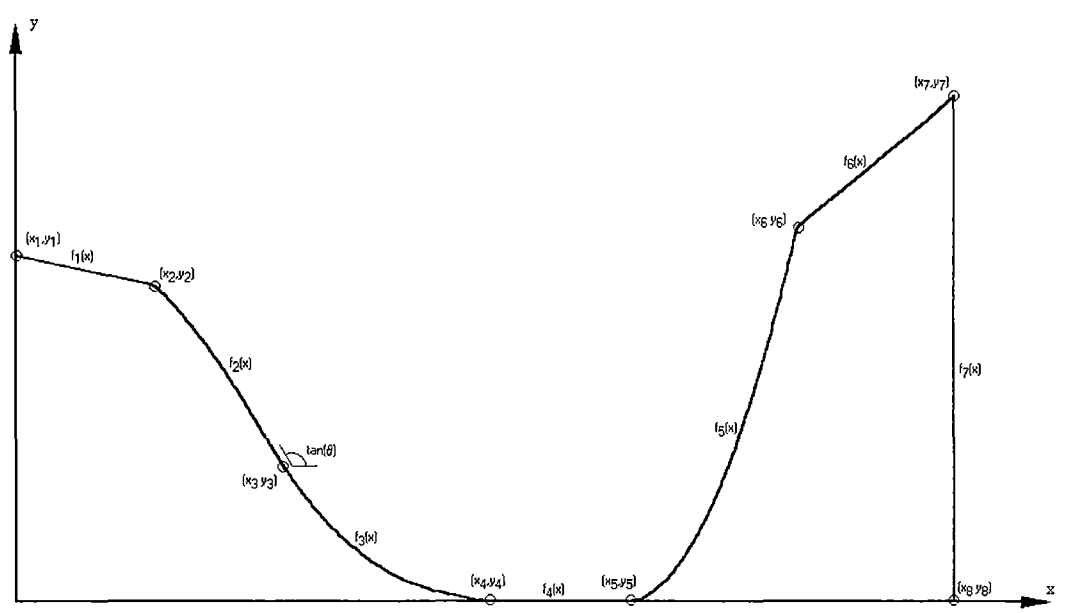

Figure 3.5.2 Spline definition of model

Spline Knots for all Models											
			Wedge15 wtth sideplates	Wedge25 with sideplates	Wedge15	Wedge25	Model J1	Model J2	Model J3	Flat1	Incat1
	x1	[m]	0.000	0.000	0 000	0.000	0.000	0.000	0.000	0.000	
	y1	[m]	0.067	0.117	0.067	0 117	0.120	0.120	0.120	0.000	
	x2	[m]	0.250	0.250	0.250	0.250	0.000	0.000	0.000	0 000	
	y2	[m]	0.000	0 000	0 000	0.000	0 120	0.120	0 120	0 250	
	x3	[m]	xxx	xxx	xxx	xxx	0.100	0.050	0.050	xxx	
	y3	[m]	xxx	xxx	xxx	xxx	0.060	0.060	0.060	xxx	
	theta	[deg]	xxx	xxx	xxx	xxx	131.7	114.0	114.0	xxx	
	x4	[m]	xxx	xxx	xxx	xxx	0.200	0.100	0.100	xxx	
	y4	[m]	xxx	xxx	xxx	xxx	0.000	0.000	0.000	xxx	
	x5	[m]	0.250	0.250	xxx	xxx	0 200	0.100	0.200	0 250	
	y5	[m]	0.000	0.000	xxx	xxx	0.000	0.000	0.000	0.000	
	x6	[m]	0.250	0.250	xxx	xxx	0.250	0.250	0.250	0.250	
	y6	[m]	0.140	0.140	xxx	xxx	0.130	0.130	0.130	0.140	
	x7	[m]	0.274	0.274	xxx	xxx	0.260	0.260	0.260	0.274	
	y7	[m]	0.126	0.126	xxx	xxx	0.148	0.148	0.148	0 126	
	x8	[m]	0.274	0.274	xxx	xxx	0.261	0.261	0.261	0 274	
	y8	[m]	0.000	0.000	xxx	xxx	0 000	0.000	0.000	0.000	
Model Properties											
Area Ratio		[-]	0.303	0.467	xxx	xxx	0.404	0 361	0 249	0 083	0.291
Highest Point In Arch		[-]	0.912	0.912	xxx	xxx	0.769	0 384	0 000	0 000	0.547
Location of Pressure Transducers											
P1	Px1	[m]	0.017	0.014	0.017	0.014	0.000	0.000	0.000		0.020
	Py1	[m]	0.062	0.110	0 062	0.110	0.120	0 120	0.120		0.082
P2	Px2	[m]	0.097	0.096	0 097	0.096	0.067	0.033	0.033		0.054
	Py2	[m]	0.041	0.071	0 041	0.071	0 092	0 092	0.092		0 043
P3	Px3	[m]	0.217	0.159	0.217	0.159	0.133	0.067	0.067		0.149
	Py3	[m]	0.009	0.042	0 009	0.042	0.028	0.031	0.031		0 000
P4	Px4	[m]		0 209		0.209	0.200	0.100	0.150		0.198
	Py4	[m]		0.019		0.019	0.000	0.000	0.000		0.012
P5	Px5	[m]						0.175			
	Py5	[m]						0.032			

Table 3.5.2 Spline knots and location of pressure transducers

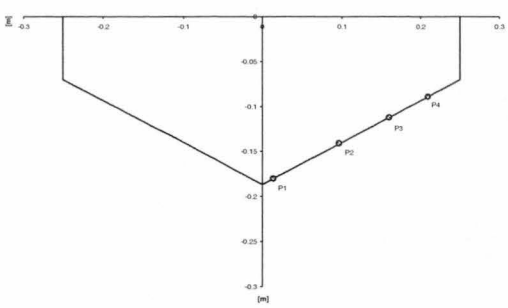

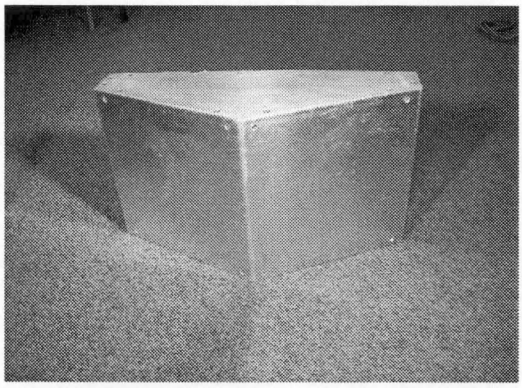

Figure 3.5.3 Wedge25. Cross-section and location of pressure transducers.

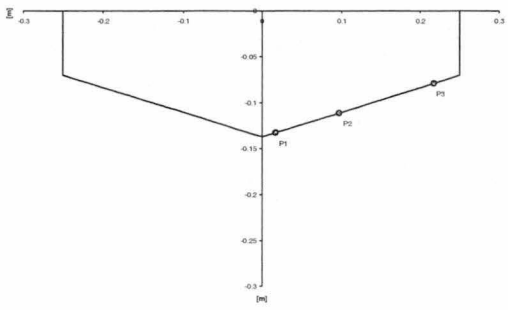

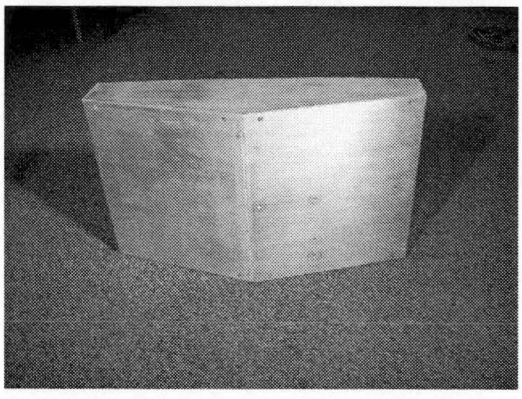

Figure 3.5.4 Wedge15. Cross-section and location of pressure transducers.

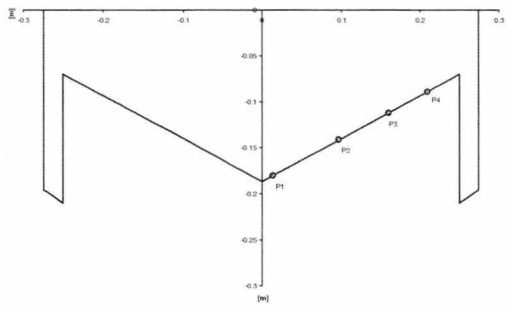

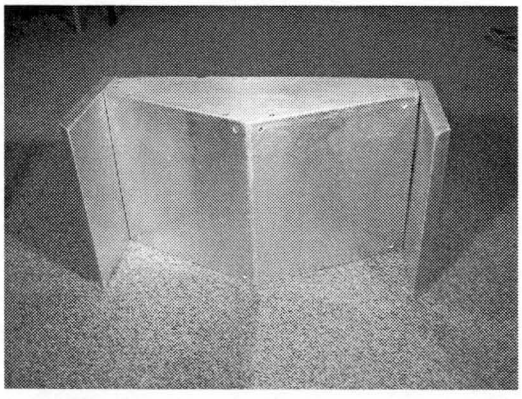

Figure 3.5.5 Wedge25 with sideplates. Cross-section and location of pressure transducers

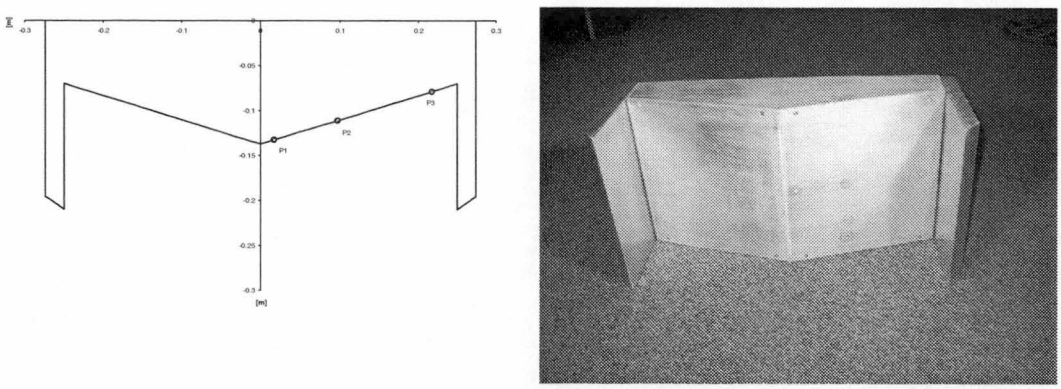

Figure 3.5.6 Wedge15 with sideplates. Cross-section and location of pressure transducers.

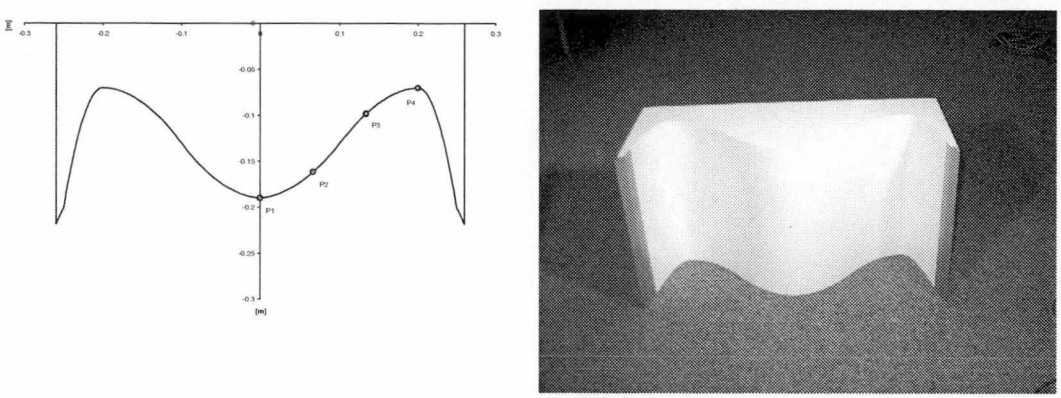

Figure 3.5.7 J1. Cross-section and location of pressure transducers.

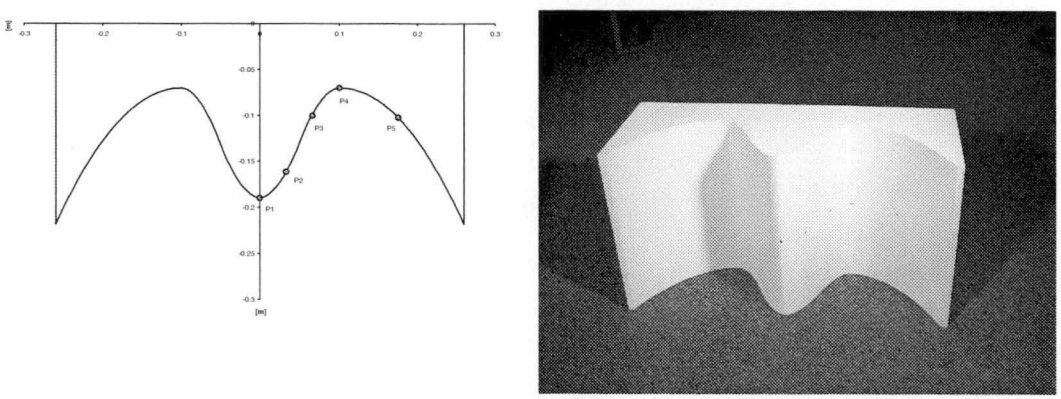

Figure 3.5.8 J2. Cross-section and location of pressure transducers.

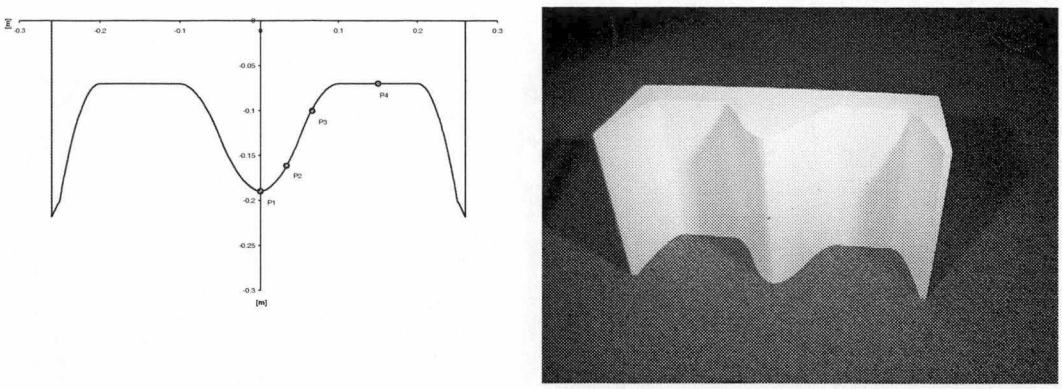

Figure 3.5.9 J3. Cross-section and location of pressure transducers.

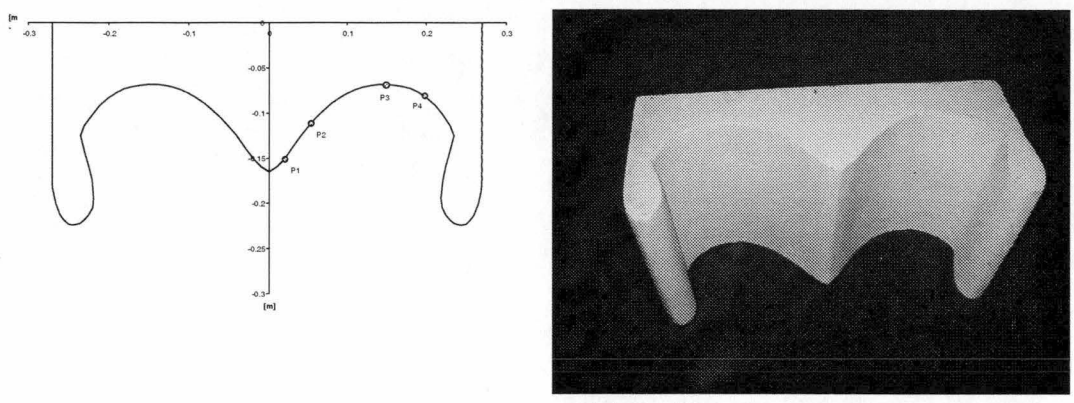

Figure 3.5.10 Incat1. Cross-section and location of pressure transducers.

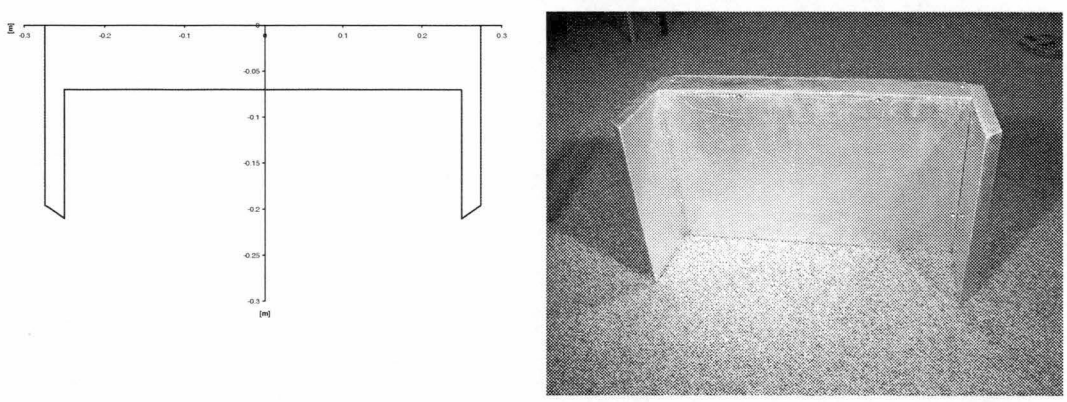

Figure 3.5.11 Flat1. Cross-section. No pressure transducers were mounted on the flat model

3.6. Conduct of Experiments and Data Processing

Pressure and acceleration time records were obtained for each of the nine models at mass numbers of 0.29 and 0.58 and normalised drop heights ranging from 0.70 to 1.35. Each drop test configuration (model geometry, mass number and normalised drop height) was drop tested five times to ensure

repeatability and to obtain an estimate of the scatter inherent in the experimental results. The $\ddot{y}(t)$ and $p(t)$ results were obtained by averaging the results for each of the five tests of each experimental configuration. The time basis for each configuration was determined by matching the peak acceleration, which was well defined. The time history results were then averaged and the origin of the time scale in the plots was selected to coincide with the initial impact of the model with the water surface. The initial model impact was found by integrating the mean $\ddot{y}(t)$ data twice to obtain $y(t)$ and then solving for t from the normalised drop height.

The behaviour of each model for a particular test configuration was additionally quantified in terms of the peak acceleration, peak pressure, velocity ratio and penetration number as defined in Table 3.6.1.

Parameters	Definition
$\ddot{y}_{peak}$	$\mathrm{Max}[\ddot{y}(t)]$
p_{peak}	$\mathrm{Max}[p(t)]$
Velocity Ratio	$\frac{\dot{y}(t)}{V_C}$ at t corresponding to $\ddot{y}_{peak}$
Penetration Number	$\frac{y(t)}{B}$ at t corresponding to $\ddot{y}_{peak}$

Table 3.6.1 Experimental parameter definitions.

The measured parameters defined in Table 3.6.1 were considered significant for a number of reasons.

- The peak pressure at each transducer location provides data on the local pressure loading experienced by the model. In terms of a full-scale vessel this is useful for determining the strength required for local plating.
- The peak acceleration provides an understanding of the peak global loading experienced by the model. For a full-scale vessel knowledge of peak global loading is important, as it is this which causes non-local structural damage such as the buckling of frames.
- The velocity ratio is the ratio of the model velocity at the time of peak acceleration to the model velocity at time of initial water impact. This quantity is a measure of impulse experienced by the model during impact and its square is a measure of the energy imparted to the model during the entry event. For a full-scale vessel the impulse will influence the structural whipping response and the global motions of the vessel.
- The penetration number is a measure of the penetration of the initial free surface that the model had obtained when it experiences peak acceleration. The peak acceleration of the arch like models coincides with the complete filling of the arch void and at full-scale this is equivalent to a substantial wetdeck slam. An understanding of the effect of model geometry on penetration number is of interest because it may influence the frequency at which a full-scale vessel will experience wetdeck slamming for a given seaway. The frequency of wetdeck slamming is a strong function of the vertical clearance between the calm water surface and the wetdeck. The greater this clearance the lower the chance of a

wetdeck slam for a particular seaway. The presence of a centre bow may cause an effective reduction in the tunnel height due to the piled up water around the centre bow and this effect is quantified by the penetration number.

3.7. Preliminary Analysis of Results

To provide confidence in the data obtained in this experimental program an initial analysis of selected results from the experimental program was undertaken. The effect of low pass filtering on the acceleration time history for model J1 was examined, the wedge results were compared with previous experimental wedge results and finally a representative error analysis was undertaken.

3.7.1. Effect of Filtering Time Records

The experimental results presented in this chapter are drawn from transient acceleration and pressure time records obtained for the different model geometries. As stated in section 3.4 no filtering was carried out on the time records as it had no significant influence on the data recorded. An example of the effect of low pass filtering is shown in Figure 3.7.1 for model J1 tested at mass number 0.29 and normalised drop height 0.89. The low pass filter was set at four different levels, these being no filtering, 10kHz, 4kHz and 0.4kHz. Examination of Figure 3.7.1 reveals that there was essentially no effect on the form of the time record for filtering at 10kHz and 4kHz when compared with no filtering. When filtering was undertaken at 0.4kHz there were substantial changes in the time record, particularly following the acceleration spike. Low pass filtering at 0.4kHz represents a relatively low cut off frequency and indeed low pass filtering at this level may obscure some of the features which are of interest from the experiment. Hence the time records were not low pass filtered.

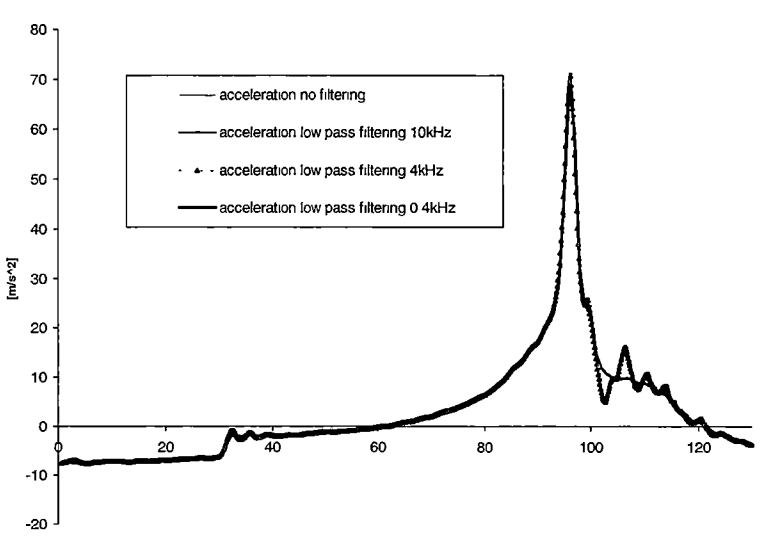

Figure 3.7.1: Acceleration against time record for model J1 (mass number 0.29, normalised drop height 0.89). Three different filtering techniques are shown.

3.7.2. Comparison of Wedge Results with Previously Published Data

One of the stated objectives of the drop tests involving the 15 and 25 degree wedge models was to allow comparison with previous experimental results for the wedge entry problem and thus provide confidence in the experimental results. To this end the experimental results obtained for the wedge models in this experimental series were compared with the experimental results of Bisplinghoff and Doherty (1952). This comparison is shown in Figure 3.7.2. This figure relates deadrise angle to the apparent mass ratio. The apparent mass ratio is the ratio of the added mass associated with the wedge as it enters the water and the von Karman (1929) added mass. The concept of using added mass to investigate the impact of wedges with water is discussed in detail in chapter 4. Examination of Figure 3.7.2 indicates that the apparent mass ratio for the 15 degree wedge lies within the expected range as indicated by the Bisplinghoff and Doherty (1952) results for the 10 and 20 degree wedges. The apparent mass ratio for the 25 degree wedge lies slightly below the expected range as indicated by the 20 and 30 degree wedge results of Bisplinghoff and Doherty (1952). On this basis it was concluded the experimental apparatus allowed the measurement of water entry of events in such a manner that the experimental data obtained was not grossly in error.

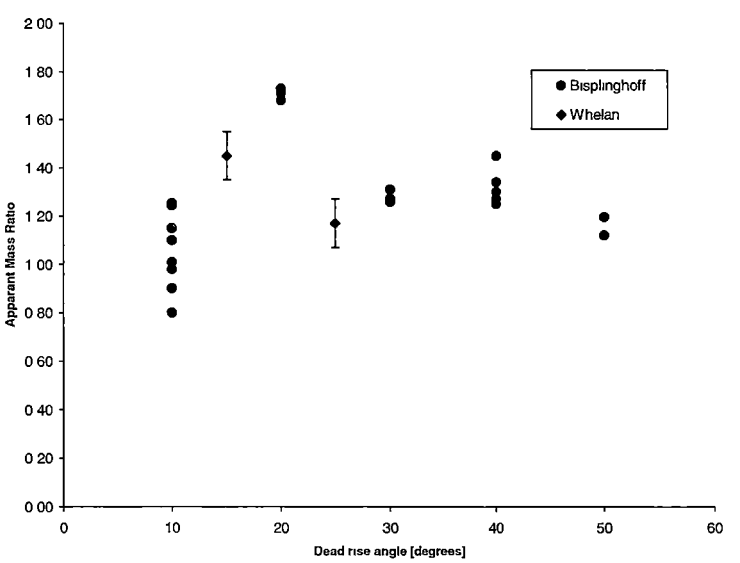

Figure 3.7.2: A comparison of the experimental results of Bisplinghoff and Doherty (1952) and the experimental results for the two wedge models.

3.7.3. Experimental Error Analysis

To provide confidence in the experimental results presented in this chapter an error analysis was carried out. The error analysis was based on the data obtained for model J1 tested at normalised drop height 0.89 and mass number 0.29. The parameters required to specify this particular experimental set up have the values and error bounds listed in Table 3.7.1. The quantities that are calculated based on

the measured parameters are shown in Table 3.7.2 together with error bounds expressed as both absolute values and as percentage errors. Examination of Table 3.7.2 reveals that for all calculated quantities except the normalised wall clearance, the error bound was less than 1.3% which is acceptable given the inherent scatter observed in the experimental data. The error bound associated with the normalised wall clearance is ±15% in percentage terms and ±0.005 in absolute terms. This large percentage error bound is a result of the small value of normalised wall clearance and thus percentage error is not a good basis upon which to consider this error bound. The normalised wall clearance error bound is not large when compared to the range of values that the normalised wall clearance may obtain over the entire experimental series (0.033 to 0.25 ±0.005) and thus does not create a significant error.

Parameter	Value	Error Bound
g	9.81m/s^2	±0.01
H	0.202m	±0.0002
m_m	22.92kg	±0.001
w	0.290m	±0.001
B	0.120m	±0.001
W_t	0.300m	±0.0002
ρ	1000kg/m^3	±1
L	0.522m	±.001
χ	0.200m	±.001
p	80kPa	±0.2
$\ddot{y}$	80m/s^2	±1
t	0.09s	±0.00002
V_C	0.89m/s	±0.001
$\forall$	0.404m^2	±0.0005
$\ddot{y}_{peak}$	80m/s^2	±0.2
y	0.840m	±0.002

Table 3.7.1: Parameter values and error bounds for error analysis. Model J1, normalised drop height 0.89, mass number 0.29.

Calculated Quantity	Value	Error Bound	Percentage Error
H^*	0.8797	0.0009	0.1%
m^*	0.290	0.0015	0.5%
C_F	23.11	0.3	1.3%
C_p	63.0	0.3	0.5%
t^*	0.170	0.0004	0.2%
Normalised Wall Clearance	0.033	0.005	15.2%
Area Ratio	0.404	0.001	0.2%
Highest Point in Arch	0.769	0.004	0.5%
Velocity Ratio	0.89	0.002	0.2%
Penetration Number	0.74	0.006	0.8%

Table 3.7.2: Calculated quantities and error bounds. Model J1, normalised drop height 0.89, mass number 0.29.

3.8. Visualisation Results and Relation to Acceleration and Pressures

Flow visualisation was conducted for each model geometry at a mass number of 0.29 and a normalised drop height in the range 0.85 to 0.89. This combination of mass number and range of normalised drop heights was selected as it corresponds to typical slam conditions at full-scale (Section 3.2). In each case a digital image sequence of the entry process and the time records of acceleration and pressure signals are presented. The digital images are time stamped for cross-referenced with the acceleration and pressure records. Examination of each of the digital image sequences (Figure 3.8.1 to Figure 3.8.9) shows evidence of disturbed water passing up the void between the end face of the model and the tank wall and then venting into the air space above the model. This three-dimensional effect is a result of the necessary wall clearance between the model end and the tank wall and its effects are examined, and found not to be significant (Section 3.20). However, examination of this flow feature reveals that it is generally symmetrical about the centre line of the each model. This is an indication that the models were entering the water perpendicular to the initial water surface and were manufactured accurately. Attention should be focussed on the deformation of the free surface and the formation of spray jets evident on the under surfaces and sides of the models.

For the simple wedge geometries we see that for the first 80ms for the 25° wedge (Figure 3.8.1) and 40ms for the 15° wedge (Figure 3.8.2), a jet is formed along the wedge lower surface and separates tangential to that surface. Once the wedge underside is fully immersed (for times greater than 100ms

or 60ms respectively) we see that the separated flow is at a much steeper angle than the lower surface. This is approximately 60° for the 25° and 65° for the 15°wedge, although the water surface is not exactly straight and is somewhat concave upwards as would be expected if the initial flow very close to the corner is tangential to the wedge lower surface.

The vertical acceleration rises steadily to a maximum and then reduces rapidly at about 70ms (25° wedge) and 35ms (15° wedge). The reduction in acceleration coincides with the time the wedge is fully immersed and the jet flow along the wedge lower surface gives way to steep separated flow at the wedge corner. The surface pressures on the wedge lower surface show very sharp maxima as they become immersed rather than simply being covered by the jet flow. These maxima reduced progressively as the immersion point moves upward along the wedge lower surface. In cases of pressure transducers 2 and 3 on the 25° wedge and transducer 3 on the 15° wedge there is evidence of a moderately raised pressure in the presence of jet flow.

With sideplates fitted to the 25° and 15° wedges (Figure 3.8.3 and Figure 3.8.4) the jet flow from the wedge is obstructed and it appears that this sets up a circulating flow of water and entrained air in the corner between the wedge and the sideplates. The peak acceleration for both wedges with sideplates (at 88ms and 97ms respectively) is seen to coincide with the complete filling of the arch void. Once the void is filled there is a rapid reduction in the vertical acceleration. The pressures on the wedge underside generally obtain similar maxima as experienced when there are no sideplates for those transducers located near the centre line of the model. However, near the sideplates higher pressures are caused by the obstructing effect of the sideplates. Also evident in the pressure records for these two models is a secondary pressure spike. For the simple wedges the pressure records display a single spike associated with the initial wetting of the pressure transducers. When sideplates are attached a second pressure spike which coincides with the complete filling of the arch void is evident. For the pressure transducers located nearest to the top of the arch (P4 for wedge25 with sideplates, P3 for wedge15 with sideplates) the pressure spike caused by the initial wetting and the pressure spike caused by the arch void completely filling cannot be distinguished as they essentially coincide.

The J-series models (Figure 3.8.5 to Figure 3.8.7) show a somewhat similar flow pattern to the wedge with sideplate models. However, the jet flow initially detaches from the centre bow, where the geometry is convex. Later where the centre bow is concave the jet reattaches. If the highest point in the arch is located far from the centre hull (Figure 3.8.5) it is observed that a residual air/water eddy forms at the top of the arch and then moves down the outer hull inner surface as with the wedge model. However, with the highest point of the arch located close to the centre line (Figure 3.8.6) the eddy appears to remain at the top of the arch and perhaps moves slightly towards the centre of the model. With a flat top to the arch (Figure 3.8.7) the eddy initially forms slightly inboard of the outer edge of the flat arch top but then moves outboard until it reaches the side hull.

In a similar manner to the wedge with sideplates models the J-series models experience peak acceleration when the arch void completely fills with fluid. The acceleration spike for the J-series models is generally sharper and of significantly higher magnitudes than the acceleration spike experienced by the wedge with sideplate models. The acceleration record for model J1 displays a near step change at approximately 30ms which is evidently associated with the impact of the bluff centre bow. The pressure records for the J-series models generally display only very minor spikes when they initially become wet, but a significant spike on all pressure transducers coincides with the peak acceleration.

For model J1 (Figure 3.8.5) it is observed that pressure transducer P2 (located closest to the centre line of the model) experiences a pressure spike of 5kPa when it initially becomes wet and then a second pressure spike of 9kPa is observed when the arch void completely fills. Pressure transducer P3, which is, located near the point of inflection on the centre bow, experience a pressure spike which is of a duration of 10ms with a fairly constant magnitude of 9kPa. This transducer then experiences a second pressure spike of short duration (3ms) and magnitude 18kPa that coincides with the complete filling of the arch void. The pressure record for transducer P4 located at the top of the arch shows a steady rise in pressure collimating in a pressure spike of magnitude 43kPa when the arch void completely fills. The pressure transducer P4 reading has risen from an initial reading of 0kPa to 6kPa by time 80ms and yet as can be seen in the time series photos at 80ms the transducer has not come into contact with the water. This increase in pressure is attributed to a rise in air pressure at the top of the arch void.

The pressure against time records for model J2 for all transducer locations display very similar forms. For each transducer location there is only a very moderate rise in pressure to less than 10kPa when the transducers comes initially into contact with water. When the arch void completely fills with fluid all pressure transducers record a pressure spike of short duration and magnitude ranging from 20kPa to 60kPa. The peak pressure on each transducer occurs within 2ms of each other. The pressure reading taken at the top of the arch is higher than are those taken further from this location. For example P4 (located at the top of the arch) records a peak pressure of 60kPa whilst P3 (the next closest pressure transducer to the top of the arch) experiences at peak pressure of 37kPa.

Model J3 experiences pressure transients that are almost identical in form to those experienced by model J2. That is the pressure records show only a very limited pressure reading until the arch void is substantially full of fluid at which time a pressure spike of short duration (5ms) and magnitude ranging from 20kPa to 51kPa is experienced on the three pressure transducers.

The centre bows on models J2 and J3 are identical and the location of pressure transducers P2 and P3 on both these models is the same. It is observed that the peak pressures measured on pressure transducer P2 on both model J2 and J3 are the same (20kPa) whilst the peak pressures measured on pressure transducer P3 vary from 37kPa for model J2 to 28kPa for model J3. This indicates that the detailed geometry at the top of the arch and demi-hull geometry influences how the arch void fills

with fluid and this in turn effects the peak pressure experienced near the top of the arch. However the further a transducer is located from the top of the arch the less the effect this part of the model geometry has on the peak pressure reading. Pressure transducers P2 are located near the bottom of the centre bow and as noted previously these two pressure transducers recorded the same peak pressure readings.

The Incat1 model (Figure 3.8.8) in general performs in a similar manner to model J1. The air/water residual eddy that forms at the top of the arch tends to move down the inner surface of the outer hull following the complete filling of the arch void. Jets can be seen to form on the centre bow and these do not detach. The peak acceleration is high and of short duration. The peak pressures correspond to the time of arch closure and those pressures recorded on the centre bow are significantly lower than those recorded near the top of the arch.

The Flat1 model results (Figure 3.8.9) shows that the water surface remains essentially flat until simultaneous contact occurs all over the model undersurface. There is evidence of a distributed residual air/water mixture along the entirety of the model underside and there is no evident tendency for a concentrated eddy containing the residual air to form. The Flat1 model experiences a sharp acceleration spike, followed by a rapid fall.

Following the peak acceleration for models J2, J3 and Flat1 (these three models experience the highest peak accelerations, Section 3.13) there occurs a period of negative acceleration, or snap back. This effect is also present in the other arch models, but to a significantly less extent. A similar, and perhaps related, snap back effect has been commented on by Thomas et al (2001) and Steinman et al (1999) in the context of full-scale ship trials investigating slamming of high speed catamarans, and is evident in the full-scale trials data presented in Chapter 2.

The cause of the snap back effect is likely to be a combination of the elasticity of the entrapped air and water and also the elasticity of the test apparatus. The frequencies of the snap backs are 73Hz for model Flat1, 124Hz for model J3 and 184 Hz for model J2. The lowest three natural frequencies of the test apparatus when in a suitable test configuration for a mass number of 0.29 are 393, 632 and 753Hz. Clearly the lowest natural frequency of the test apparatus is not as greatly different from the frequency of the response of the model entering the water as would be ideal. However, it is possible to distinguish the contribution to the acceleration record due to model entry from the response of the test apparatus. Thus it is concluded, based upon the difference in frequencies of the snap back and test apparatus natural frequency, that the snap back effect is principally due to the elasticity of the entrapped air and water. The higher frequency response of the test apparatus appears as noise overlaid on the underlying hydrodynamic phenomena in the acceleration time records. It should be noted that in this experimental program it is the acceleration time record up until the model experiences peak acceleration that is of most interest. For this period of the acceleration time record the vibrational response of the test apparatus is not apparent.

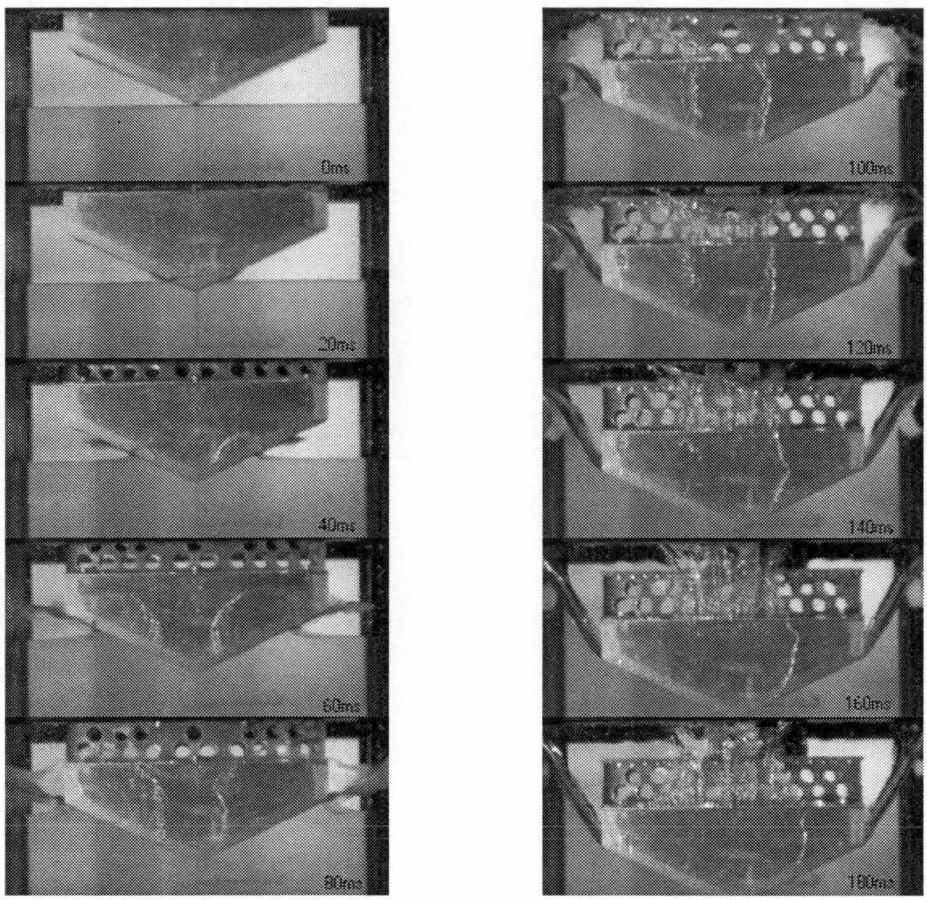

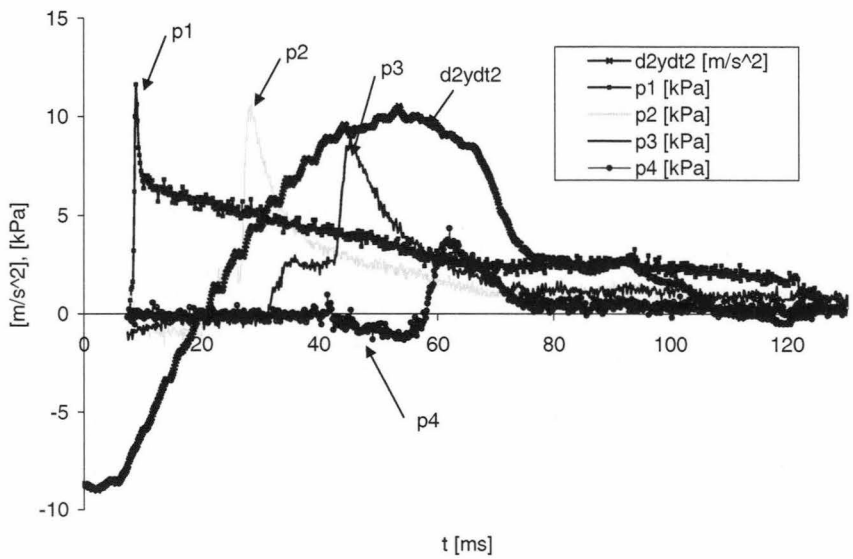

Figure 3.8.1 Wedge25. Normalised drop height=0.89, Mass number=0.29. Visualisation and $\ddot{y}$ (t), p1(t), p2(t), p3(t), p4(t) results.

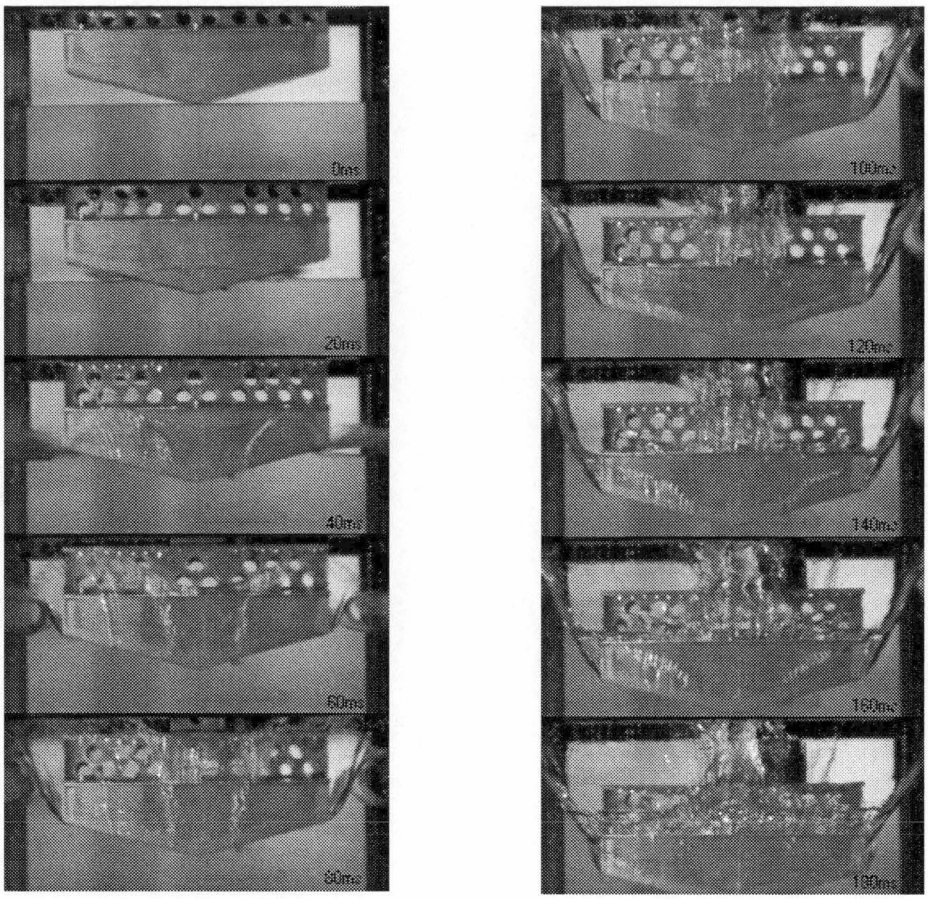

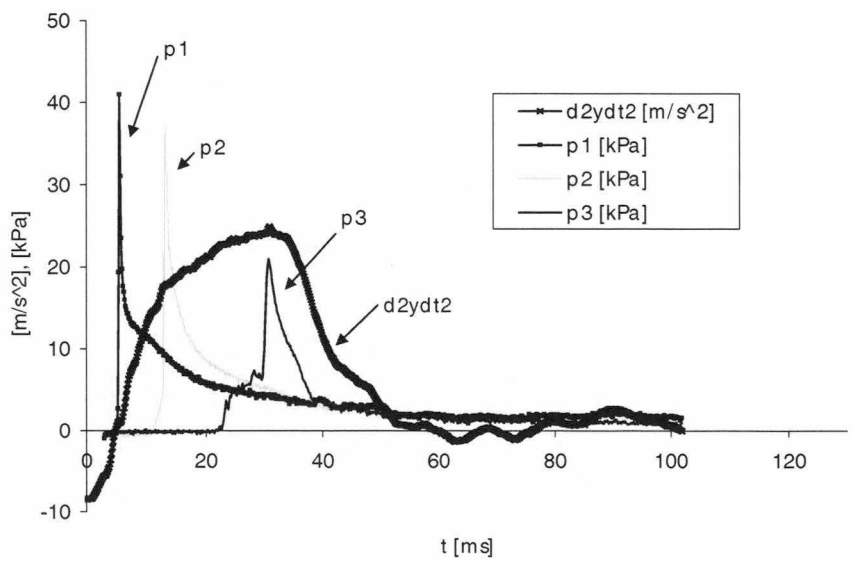

Figure 3.8.2 Wedge15. Normalised Drop Height=0.89, Mass Number=0.29. Time series photographs and $\ddot{y}$ (t), p1(t), p2(t), p3(t) results.

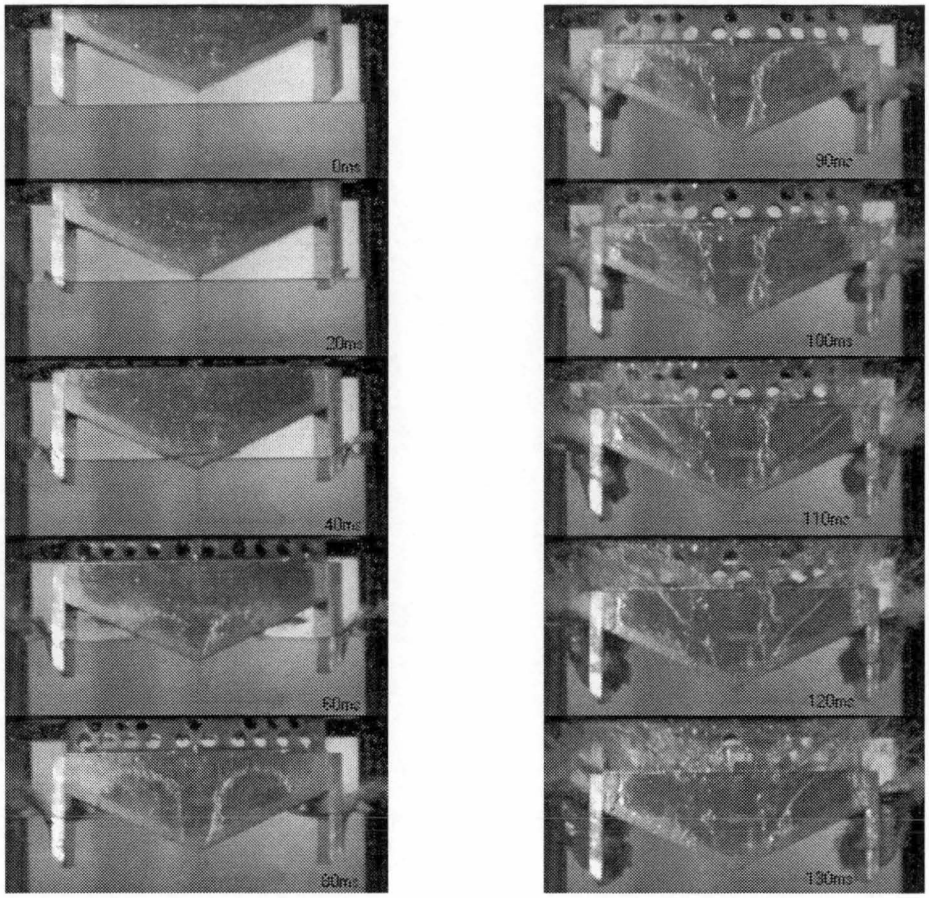

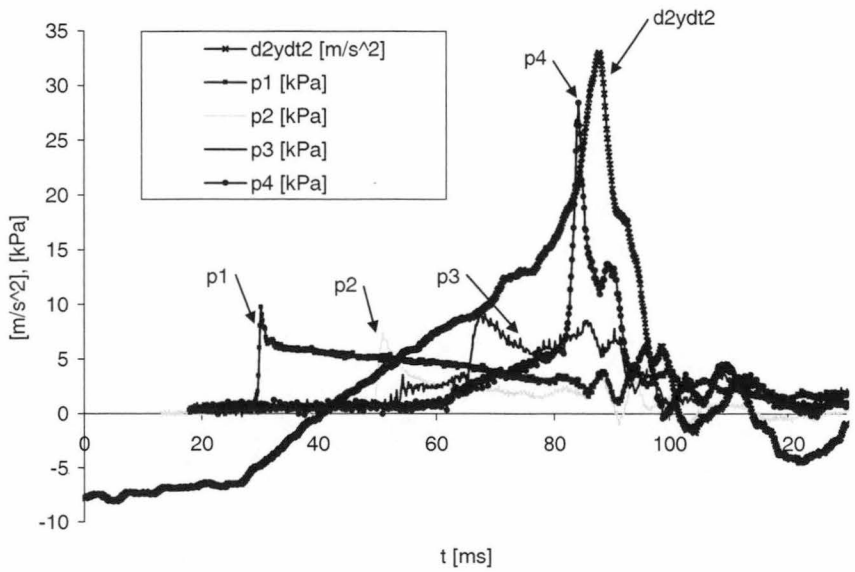

Figure 3.8.3 Wedge25 with sideplates. Normalised Drop Height=0.85, Mass Number=0.29. Time series photographs and $\ddot{y}$ (t), p1(t), p2(t), p3(t), p4(t) results.

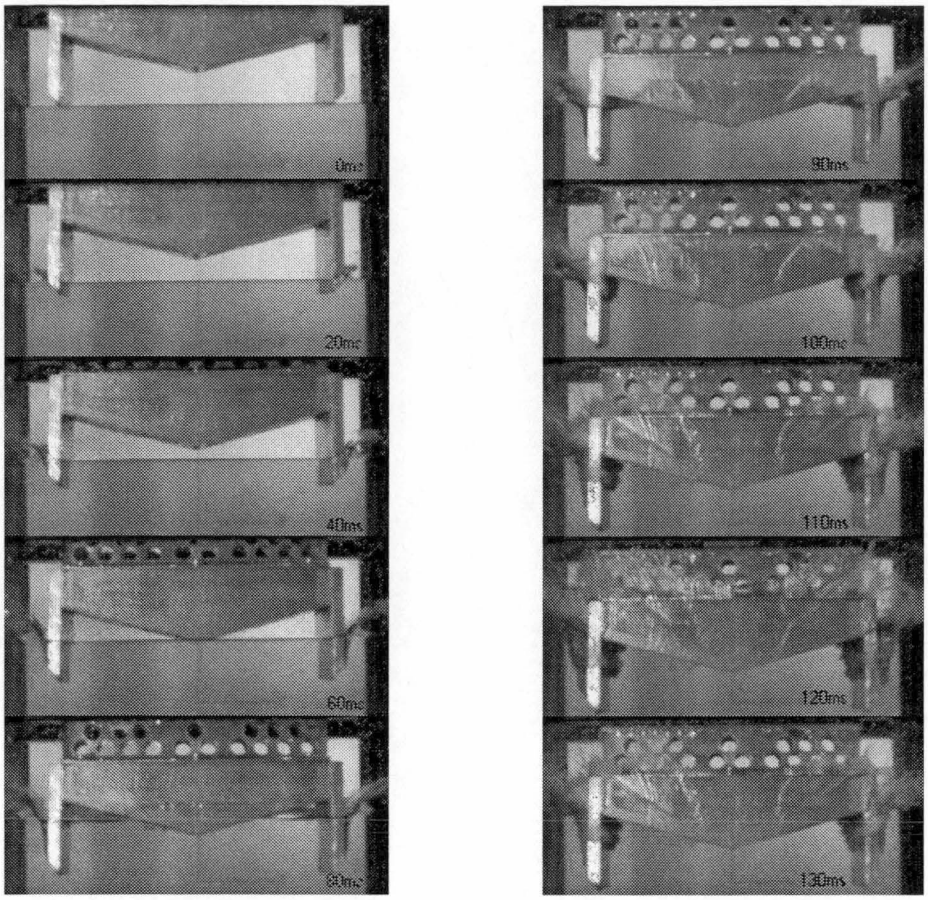

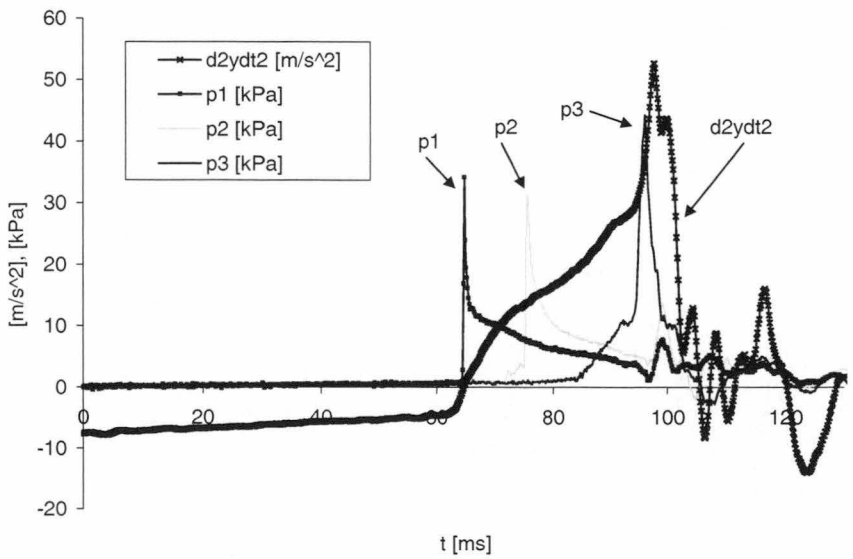

Figure 3.8.4 Wedge15 with sideplates. Normalised Drop Height=0.85, Mass Number=0.29. Time series photographs and $\ddot{y}$ (t), p1(t), p2(t), p3(t) results.

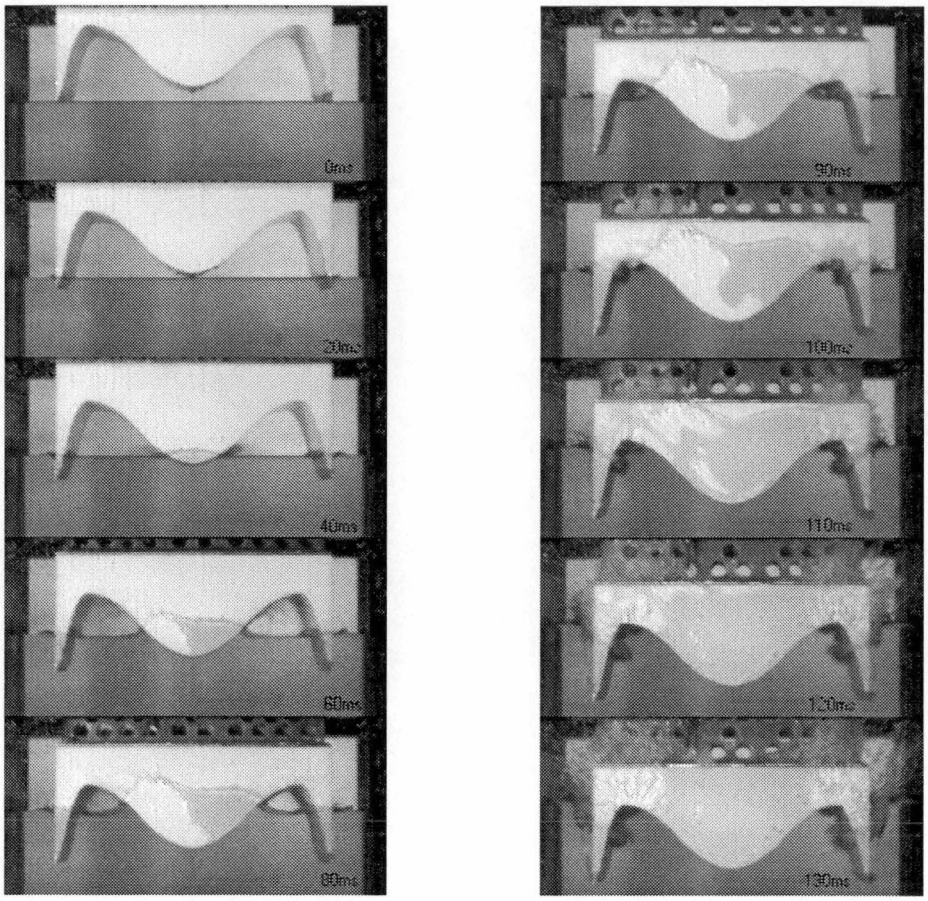

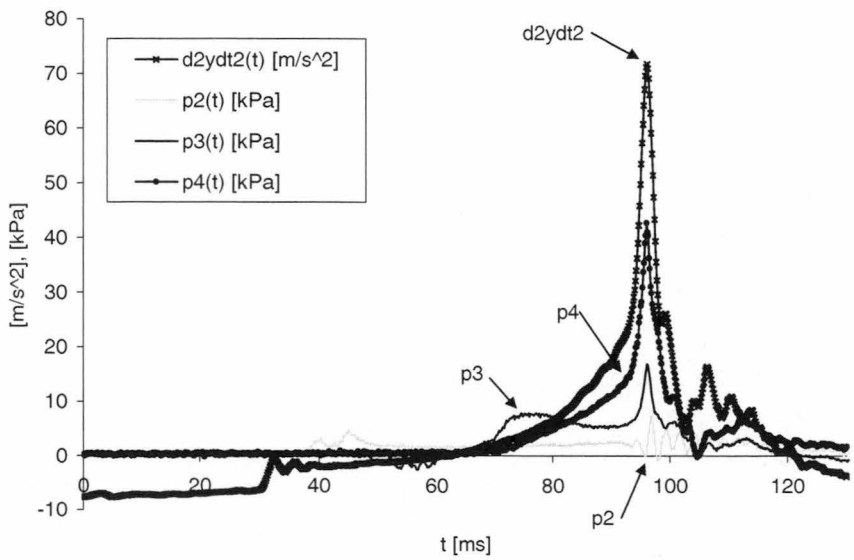

Figure 3.8.5 J1. Normalised Drop Height=0.88, Mass Number=0.29. Time series photographs and $\ddot{y}$ (t), p2(t), p3(t), p4(t) results.

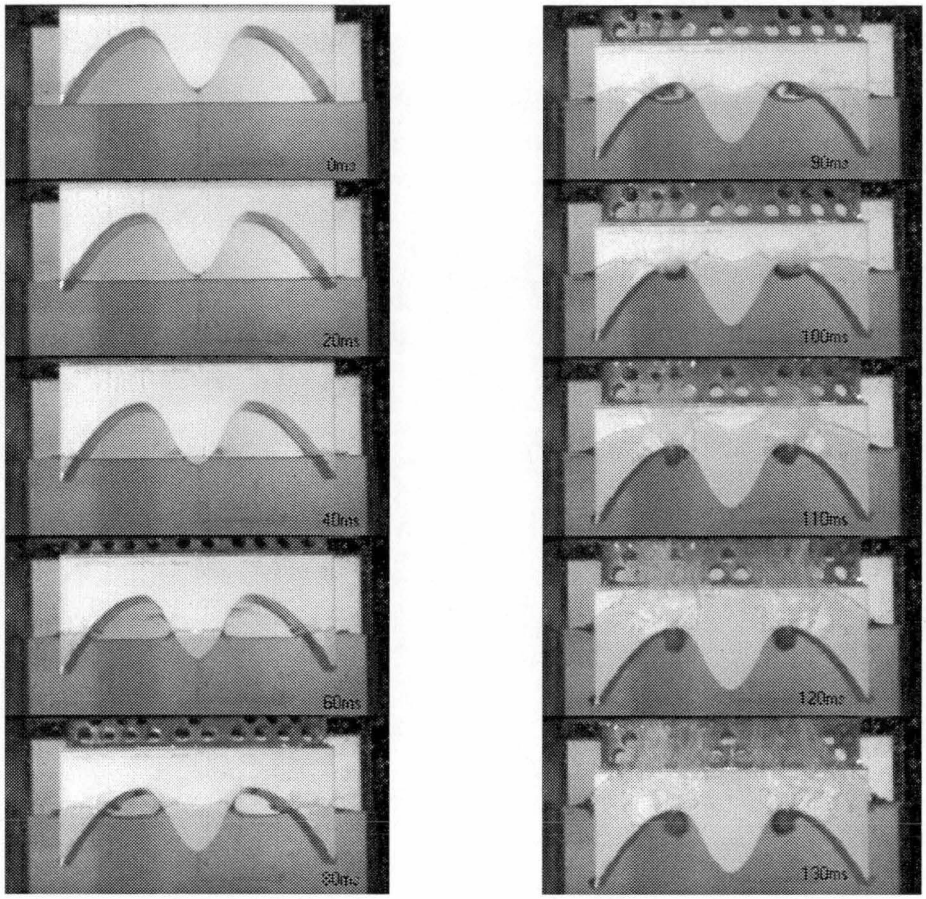

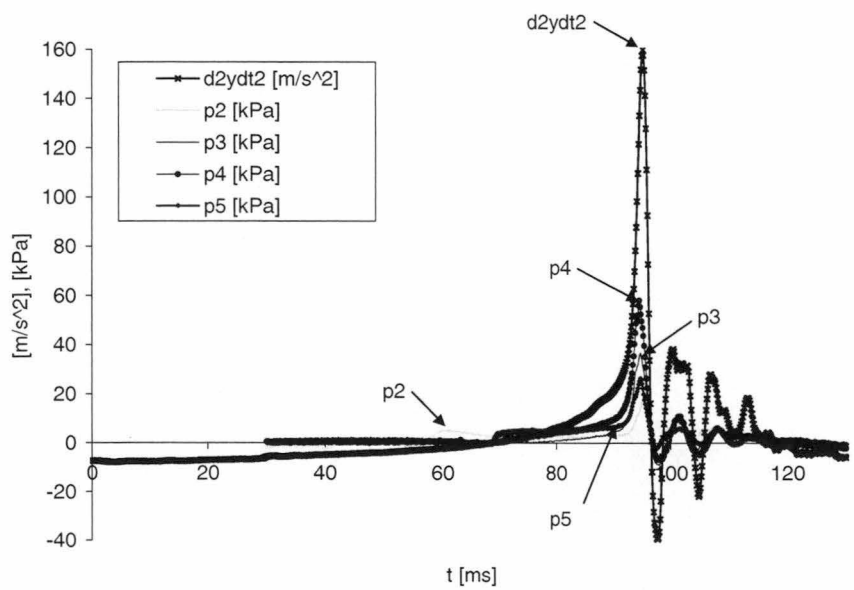

Figure 3.8.6 J2. Normalised Drop Height=0.88, Mass Number=0.29. Time series photographs and $\ddot{y}$ (t), p2(t), p3(t), p4(t), p5(t) results.

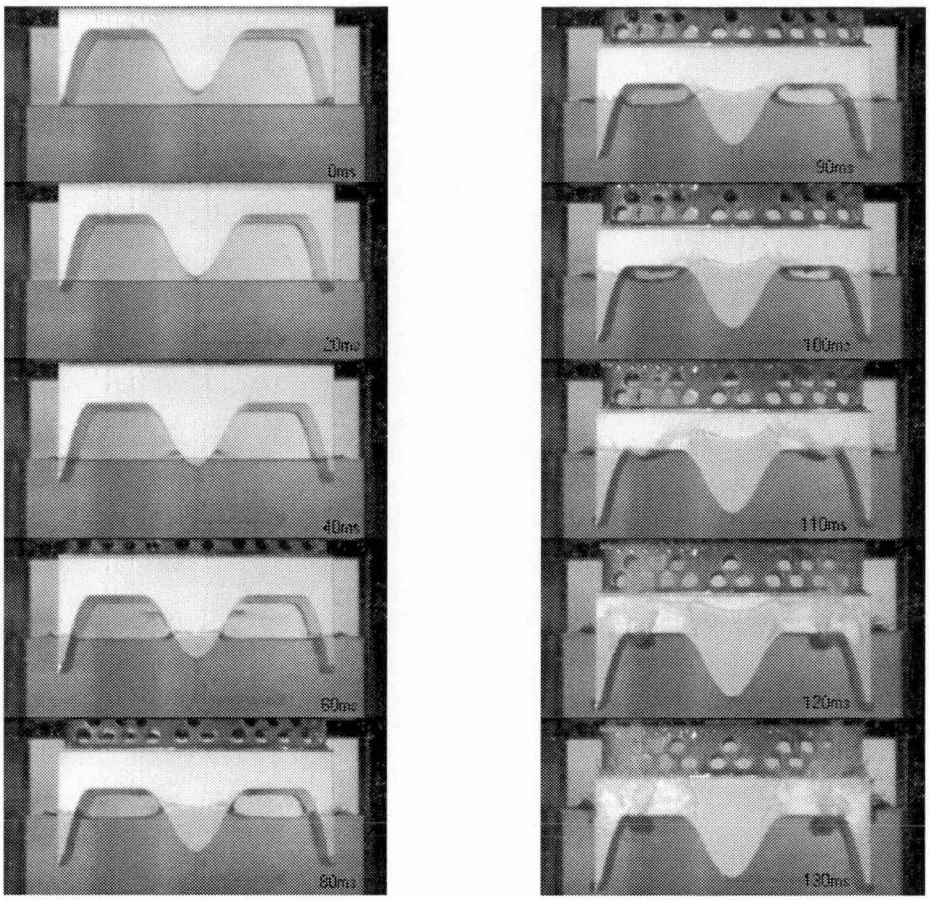

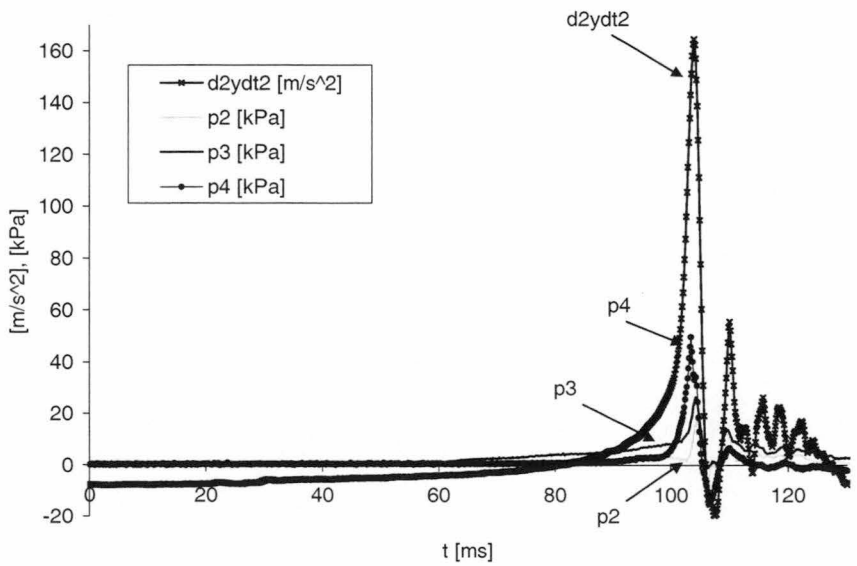

Figure 3.8.7 J3. Normalised Drop Height=0.88, Mass Number=0.29. Time series photographs and $\ddot{y}$ (t), p2(t), p3(t), p4(t) results.

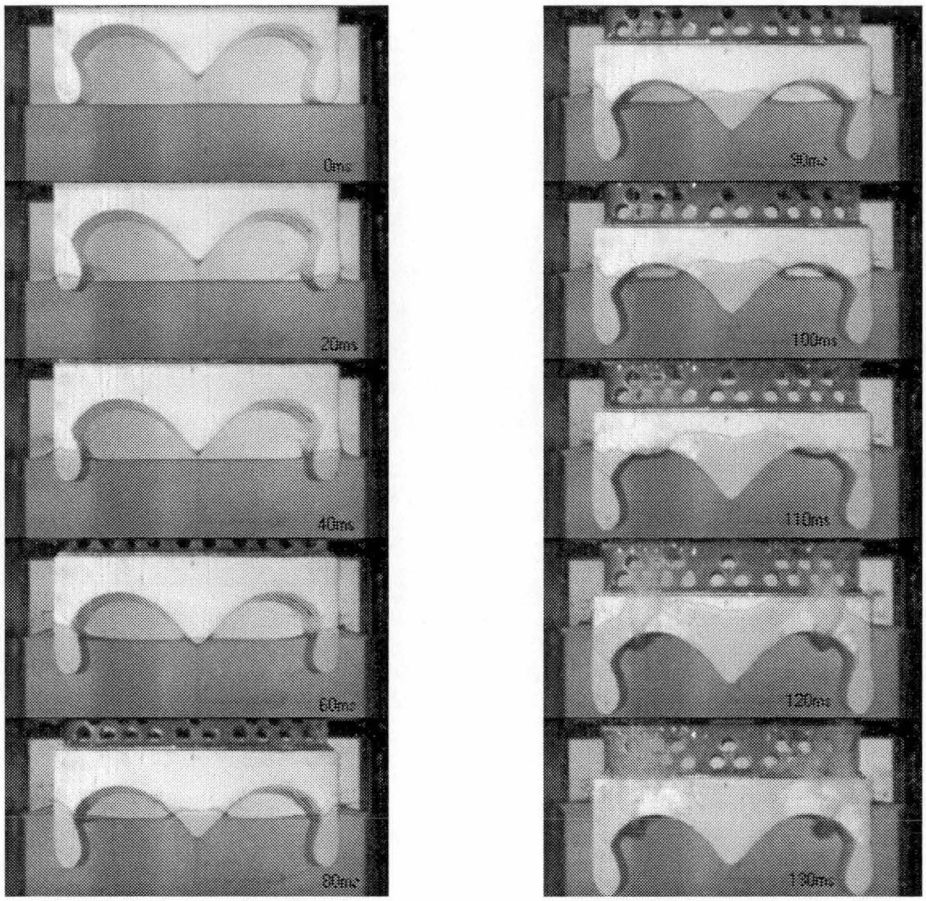

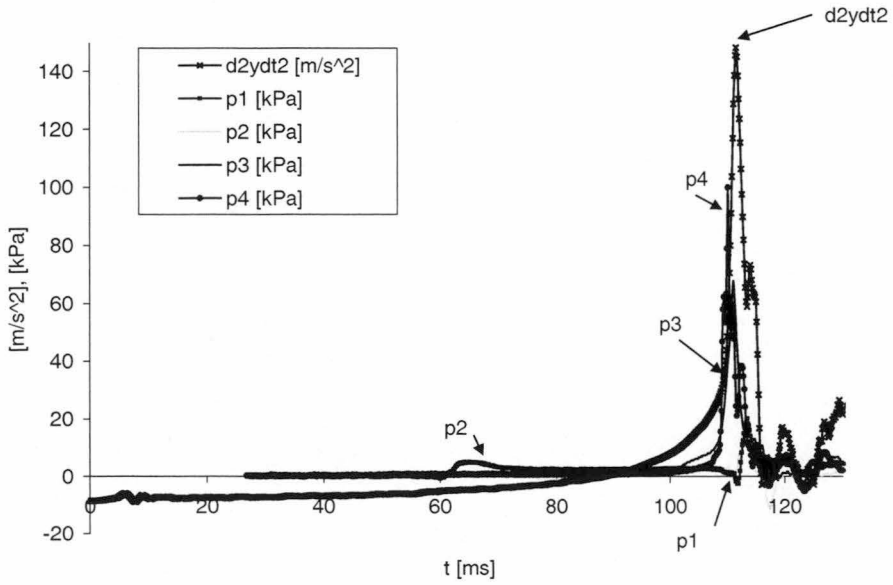

Figure 3.8.8 Incat1. Normalised Drop Height=0.86, Mass Number=0.29. Time series photographs and $\ddot{y}$ (t) results, p1(t), p2(t), p3(t), p4(t).

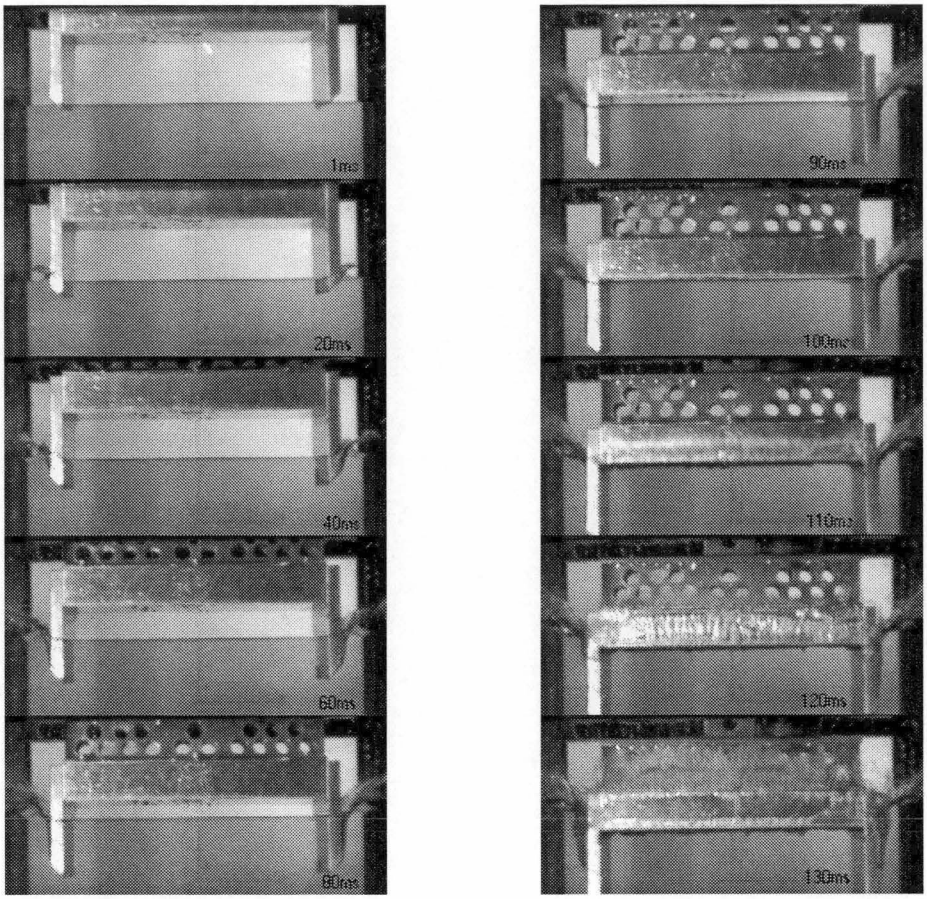

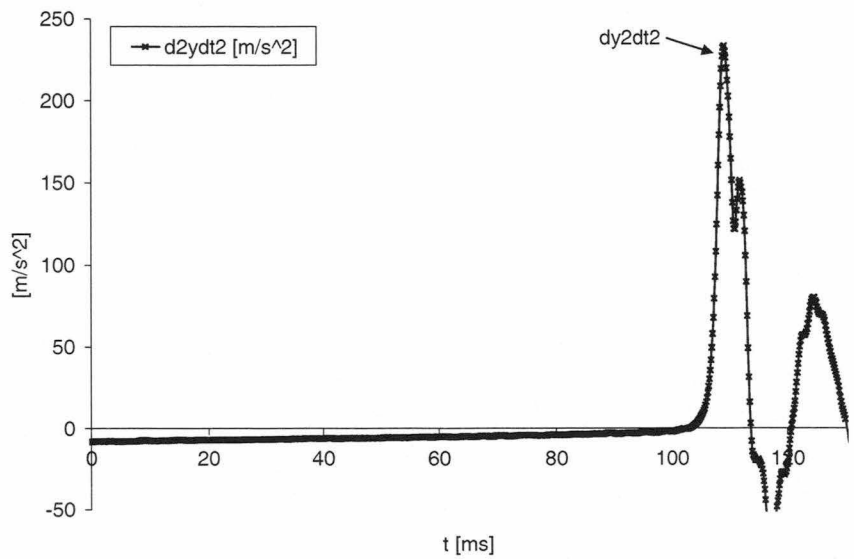

Figure 3.8.9 Flat1. Normalised Drop Height=0.85, Mass Number=0.29. Time series photographs and $\ddot{y}$ (t) results.

3.9. Acceleration Time Records

Acceleration time records for all models over a range of normalised drop heights and for two mass numbers are presented in Figure 3.9.1 to Figure 3.9.9. For each set of results it is evident that increasing the normalised drop height moves the maximum acceleration to earlier times. Clearly this aspect is associated with a higher entry velocity since the time origin is taken at the point of first water contact (not drop release). The acceleration records for each model, in general, displays the same form for the different normalised drop heights and mass numbers tested. This indicates that the flow features identified in the flow visualisation (Section 3.8) occur consistently over the range of drop heights and mass numbers tested.

The acceleration records of model wedge25 and model wedge15 are shown in Figure 3.9.1 and Figure 3.9.2 respectively. Both models experience lower peak accelerations at mass number 0.29 compared with mass number 0.58. The form of the acceleration curves for each of these models at each mass number is of a similar form. That is, there is a steady increase in acceleration until a maximum is obtained and then the acceleration decreases to approximately zero. The accelerations of wedge15 are larger in magnitude but of shorter duration than the accelerations of wedge25.

Figure 3.9.3 and Figure 3.9.4 show the acceleration records of wedge25 with sideplates and wedge15 with sideplates respectively. For both these models the acceleration is initially negative which occurs when only the very fine demi-hulls (or sideplates) are in contact with the water. When the centre bow of each of these models impacts with the water the models experiences significantly larger accelerations until a maximum is reached which coincides with the complete filling of the arch void with fluid. The keel of the centre bow of model wedge15 with sideplates is initially further from the initial water surface than the wedge25 with sideplates centre bow keel. This accounts for the extended period of negative acceleration experienced by model wedge15 with sideplates compared with model wedge25 with sideplates. For both models, at the higher mass number some vibrations are evident once peak acceleration has been reached. These vibrations are significantly less pronounced at the lower mass number.

The accelerations of the J-series models are shown in Figure 3.9.5 to Figure 3.9.7. Examination of Figure 3.9.5 reveals that as model J1 enters the water initially the accelerations are negative, then when the bluff centre bow impacts the water there is a near step rise in acceleration and some vibrations are induced. The acceleration then increases steadily until a maximum is reached. This trend in acceleration is observed for all normalised drop heights tested and both mass numbers. Following the peak acceleration a snap back in the acceleration is apparent for all normalised drop height at mass number 0.58 but only for a normalised drop height of 0.78 for mass number 0.29. Some vibrations are also apparent following peak acceleration however these occur once the acceleration records are no longer of interest.

The acceleration records for both model J2 (Figure 3.9.6) and J3 (Figure 3.9.7) show similar trends. Initially these two models experience low accelerations that then rise steadily to a high peak value. A slight increase in acceleration is observed to coincide with the entry of centre bow all through this is not large because the centre bows on these two models are very fine. A snap back in acceleration is observed in all the acceleration records for each of these models.

The acceleration records for model Incat1 are shown in Figure 3.9.8. Unfortunately this model was damaged before the tests at mass number 0.58 could be undertaken. For the lower mass number results the model performs in a similar manner to the J-series models. There are some small vibrations that commence 5ms after initial impact. These are attributed to the demi-hull entry. The demi-hulls on model Incat1 are significantly bluffer than the demi-hulls on any other model.

The accelerations during impact of model Flat1 are shown in Figure 3.9.9 for two mass numbers and a limited range of normalised drop height. The normalised drop heights tested were limited for this model because the peak accelerations experienced by this model caused the accelerometer to saturate. This occurred when the acceleration exceeded $300m/s^2$. For all acceleration records presented model Flat1 experiences essentially no acceleration other than a gravitational acceleration until a large acceleration spike which occurs when the flat cross structure impacts the water surface. A snap back and some vibrations are evident following the peak acceleration. The duration of the acceleration spike is approximately twice that of the J-series models.

It has been noted that several models show evidence of oscillation after the main impact. This was not evident for the wedge sections without sideplates. It seems likely therefore that the oscillations or vibrations are caused by the motions of the residual air trapped at the top of the arch void. Whilst it would be difficult to attempt an analysis of this effect, it is apparent from the test results that the oscillatory mechanism for a given model and drop height is relatively repeatable and regular.

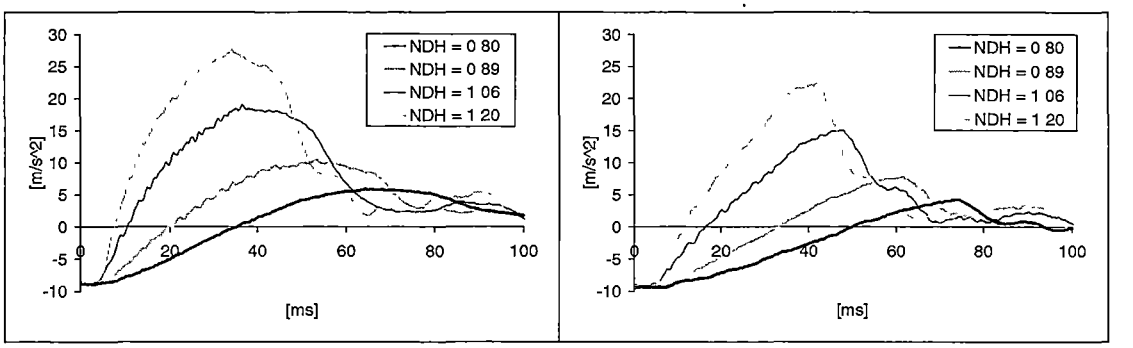

Figure 3.9.1 Wedge25. $\ddot{y}(t)$ for various normalised drop heights. Mass Number=0.29 (left). Mass Number=0.58 (right).

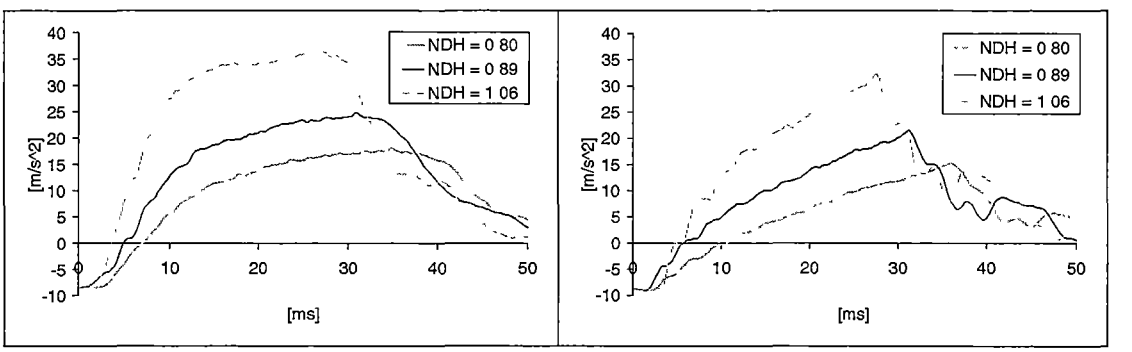

Figure 3.9.2 Wedge15. $\ddot{y}(t)$ for various normalised drop heights. Mass Number=0.29 (left). Mass Number=0.58 (right).

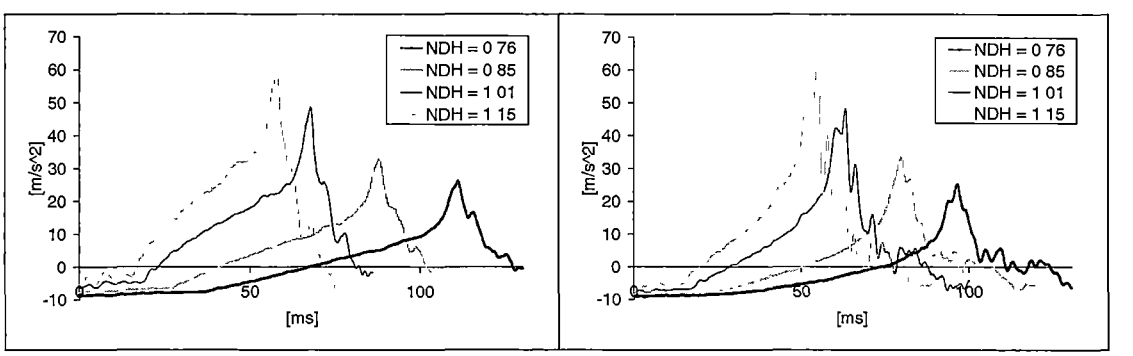

Figure 3.9.3 Wedge25 with sideplates. $\ddot{y}(t)$ for various normalised drop heights. Mass Number=0.29 (left). Mass Number=0.58 (right).

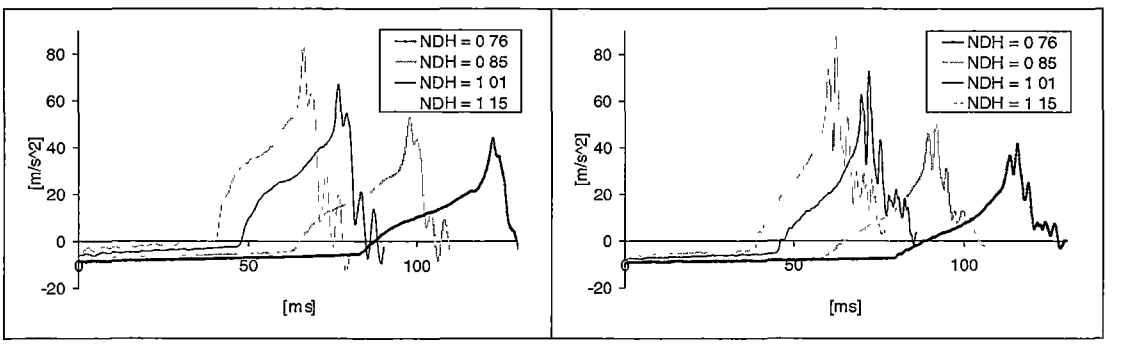

Figure 3.9.4 Wedge15 with sideplates. $\ddot{y}(t)$ for various normalised drop heights. Mass Number=0.29 (left). Mass Number=0.58 (right).

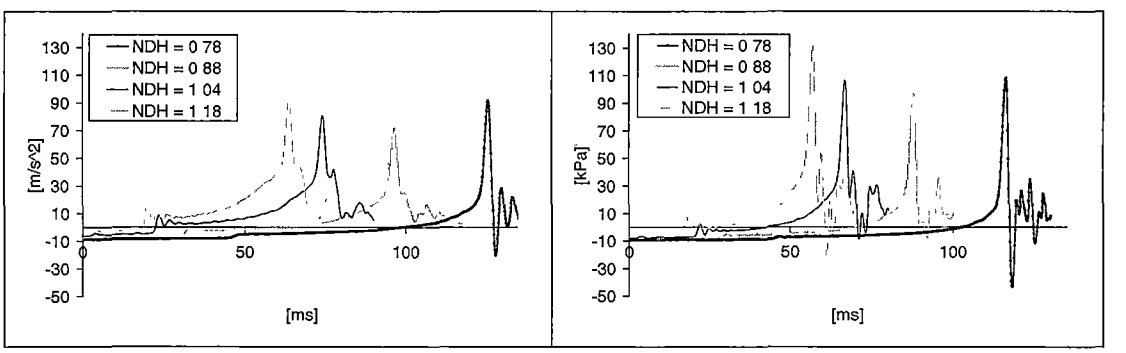

Figure 3.9.5 J1. $\ddot{y}(t)$ for various normalised drop heights. Mass Number=0.29 (left). Mass Number=0.58 (right).

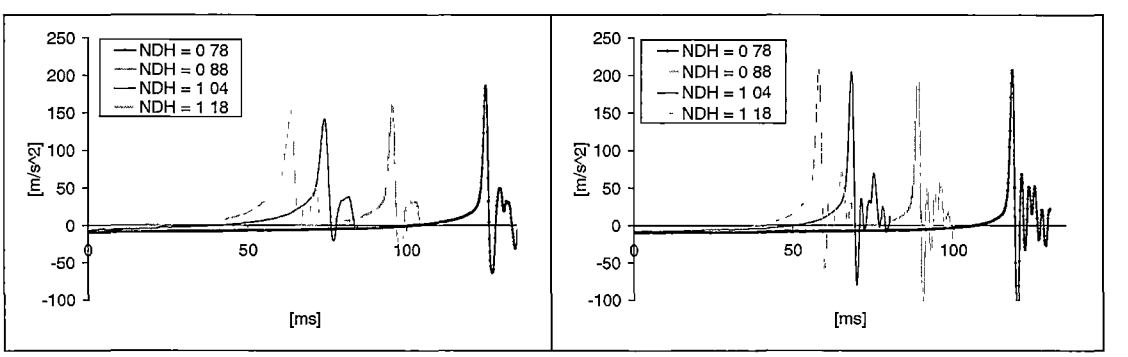

Figure 3.9.6 J2. $\ddot{y}(t)$ for various normalised drop heights. Mass Number=0.29 (left). Mass Number=0.58 (right).

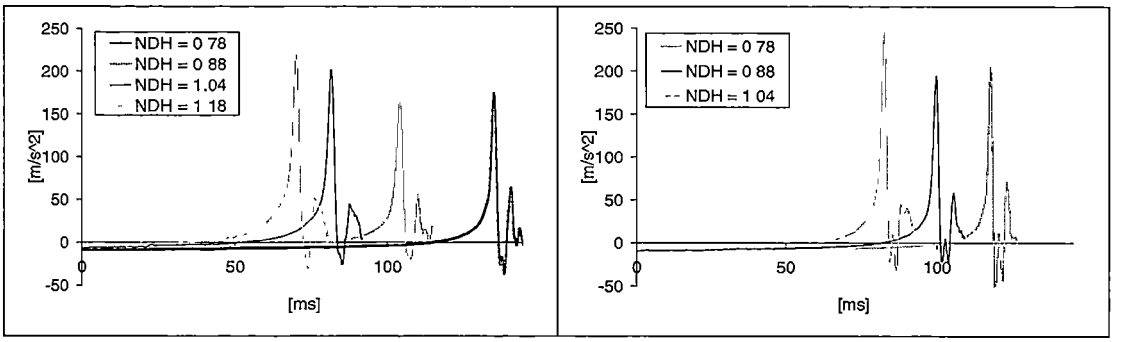

Figure 3.9.7 J3. $\ddot{y}(t)$ for various normalised drop heights. Mass Number=0.29 (left). Mass Number=0.58 (right).

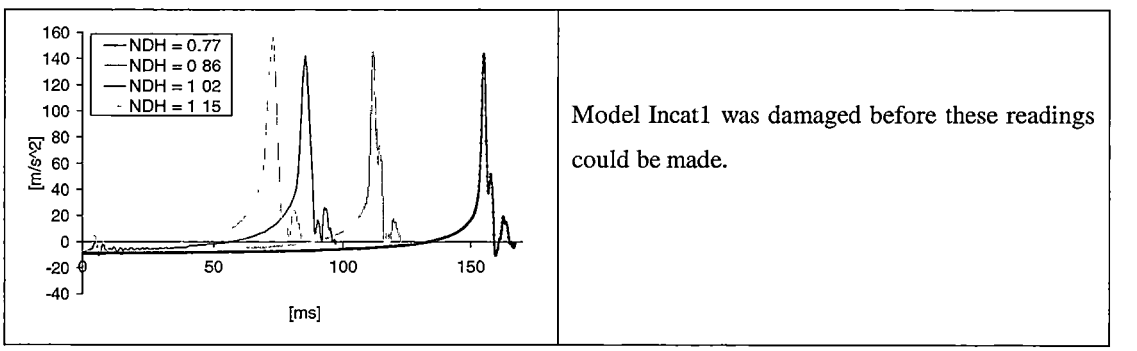

Figure 3.9.8 Incat1. $\ddot{y}(t)$ for various normalised drop heights. Mass Number=0.29 (left). Mass Number=0.58 (right).

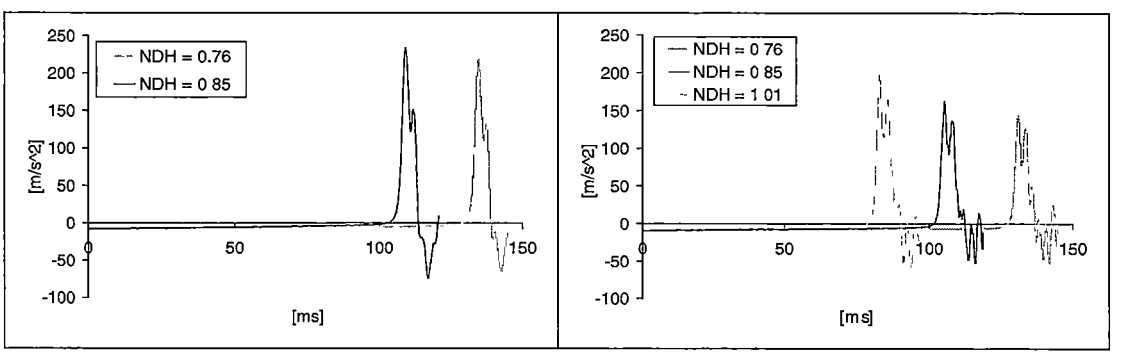

Figure 3.9.9 Flat1. $\ddot{y}(t)$ for various normalised drop heights. Mass Number=0.29 (left). Mass Number=0.58 (right).

3.10. Similarity of Wedge Acceleration Time Records

The water entry of a wedge displays similarity when the inertia forces are dominate over the other forces (i.e. the buoyancy, viscous and surface tension forces) acting on the wedge during entry. When similarity applies, the acceleration time records obtained at different normalised drop heights for wedge entry collapse when acceleration and time are appropriately scaled. Acceleration is scaled by conversion to force coefficient (Table 3.2.1) and time is scaled by conversion to dimensionless time (Table 3.2.1). The acceleration time records for both the 25 degree wedge and 15 degree wedge were scaled in this manner for mass number 0.29 and the results of this analysis are shown in Figure 3.10.1 and Figure 3.10.2.

The scaled acceleration time results for the 15 degree wedge (Figure 3.10.2) are observed to collapse in the expected way. The scaled acceleration time results for the 25 degree wedge (Figure 3.10.1) do not collapse as well as those obtained for 15 degree wedge. This was attributed to the relative magnitude of the buoyancy force compared with the inertia force for the 25 degree wedge compared with the 15 degree wedge. It was observed that as the normalised drop height increases, and thus the inertia force increases relative to the buoyancy force, the force coefficient against dimensionless time curves converge to a single form. That is display similarity. This is clearly shown for the results obtained at normalised drop height 1.06 and 1.20 for the 25 degree wedge as both these curves show similarity as expected. Thus it was concluded that the experimental data collapses in the expected manner. This is an additional verification of the quality of the experimental presented in this chapter.

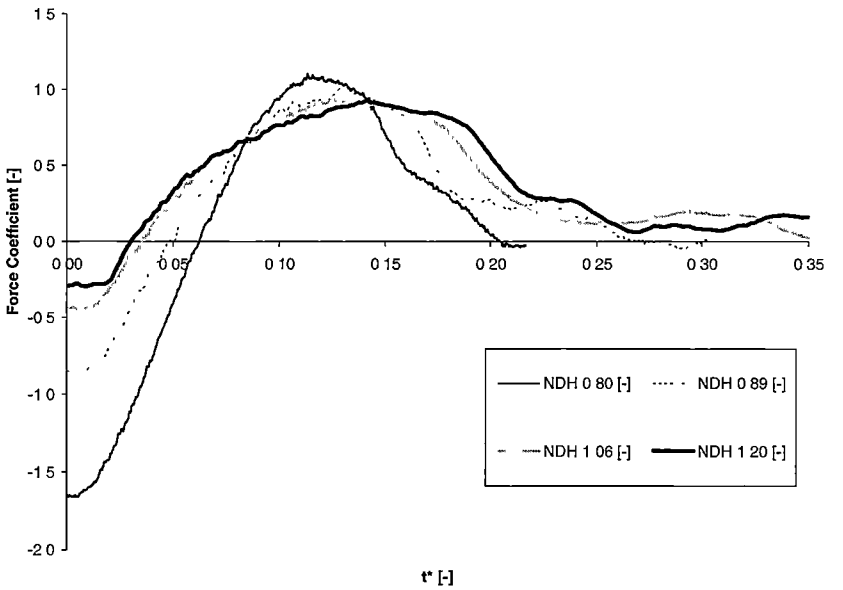

Figure 3.10.1: Scaled acceleration results for 25 degree wedge. (mass number 0.29).

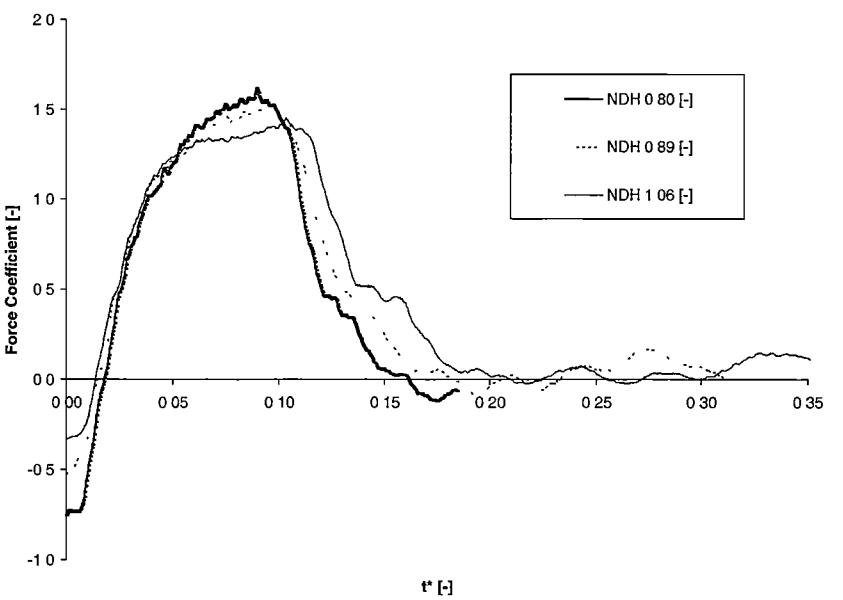

Figure 3.10.2: Scaled acceleration results for 15 degree wedge. (mass number 0.29).

3.11. Velocity Time Records

Velocity time records are presented in Figure 3.11.1 to Figure 3.11.9 for all the models. These records were obtained by integrating the acceleration time records once. The initial velocity at the point of first water contact (zero on the time base) is directly related to the normalised drop height. For all models there is then a further velocity increase until the acceleration reverses sign. The models with arch like geometry experience a much more rapid reduction in velocity once the peak velocity is obtained than the simple wedge geometries. This is particularly the case for model Flat1, and is due to the acceleration spike associated with the arch void completely filling with fluid as mentioned in section 3.8.

The velocity records for the wedge models with and without sideplates are shown in Figure 3.11.1 to Figure 3.11.4. Examination of these figures reveals that as the initial velocity decreases so too does the net reduction in velocity experienced by these models. The two 25° wedge based models and the 15° wedge with sideplate model indeed experience a net velocity increase for each of the lowest normalised drops presented. The net reduction in velocity for all four models is greater for mass number 0.29 than 0.58, except of course for the case where there is a net velocity increase. The velocities after impact remain larger for higher initial impact velocities for all four models. The addition of sideplates to the wedge models has the effect of increasing the magnitude of the velocity reduction and also to reduce the time interval over which it occurs owing of course to the sharper acceleration spike.

For the J-series models (Figure 3.11.5 to Figure 3.11.7) the velocity reduction is very rapid, as the acceleration spike is sharp for these models, compared with the wedge models. The trend for the overall velocity reduction to increase with drop height is similar to that for the wedge models, as also is the trend for only a modest increase in minimum velocity with drop height after the impact event. The models J2 and J3 show a sharper and larger velocity reduction than the model J1. Incat1 model (Figure 3.11.8) shows the same general behaviour as model J2. Model Flat1 (Figure 3.9.9) shows a very sharp reduction of velocity as expected due to the sharp acceleration spike.

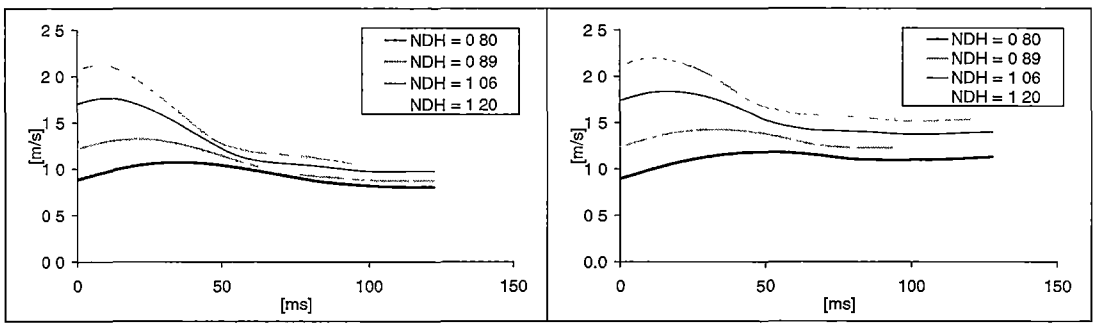

Figure 3.11.1 Wedge25. $\dot{y}(t)$ for various normalised drop heights. Mass Number=0.29 (left). Mass Number=0.58 (right).

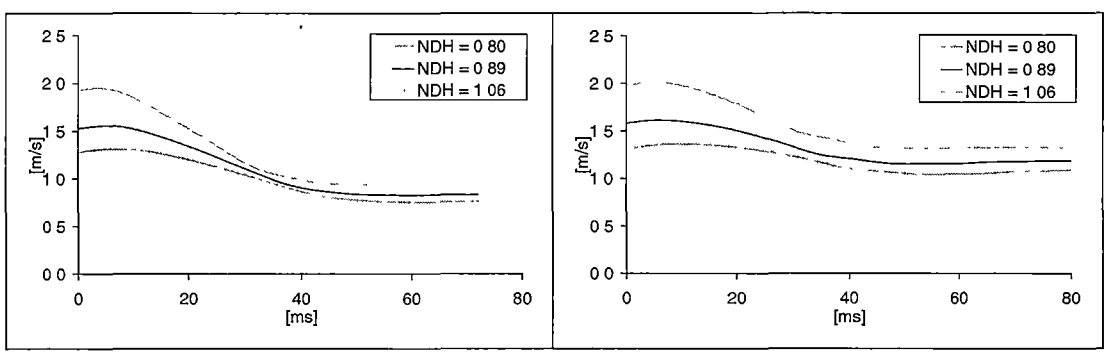

Figure 3.11.2 Wedge15. $\dot{y}(t)$ for various normalised drop heights. Mass Number=0.29 (left). Mass Number=0.58 (right).

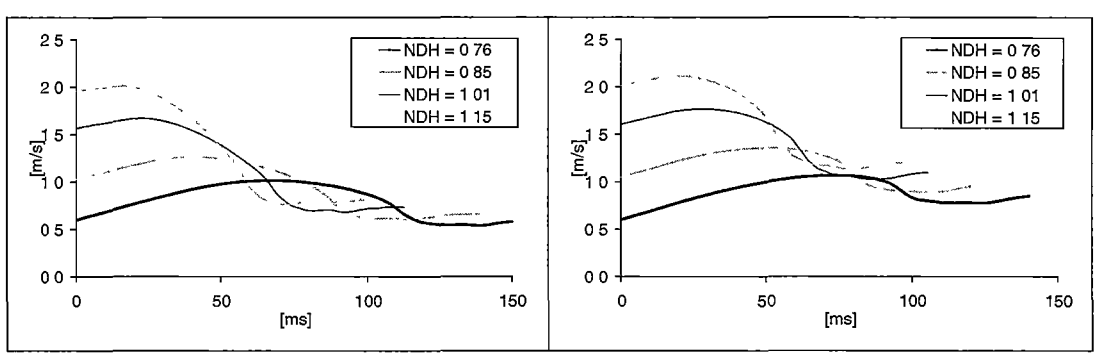

Figure 3.11.3 Wedge25 with sideplates. $\dot{y}(t)$ for various normalised drop heights. Mass Number=0.29 (left). Mass Number=0.58 (right).

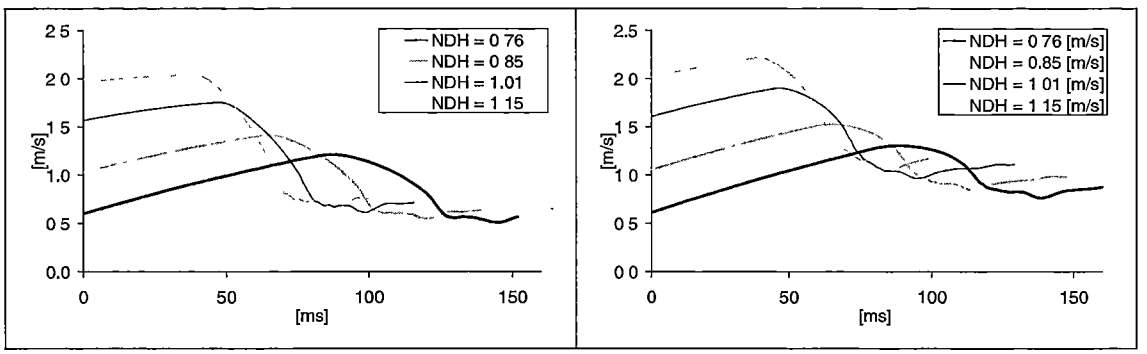

Figure 3.11.4 Wedge15 with sideplates. $\dot{y}(t)$ for various normalised drop heights. Mass Number=0.29 (left). Mass Number=0.58 (right).

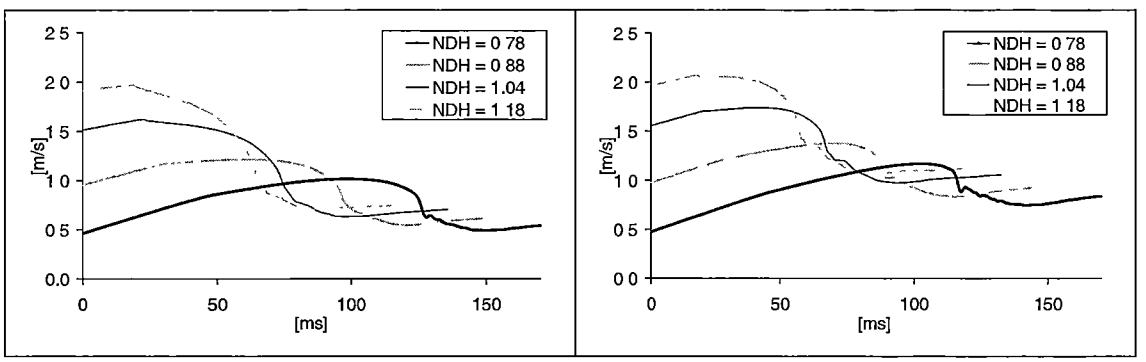

Figure 3.11.5 J1. $\dot{y}(t)$ for various normalised drop heights. Mass Number=0.29 (left). Mass Number=0.58 (right).

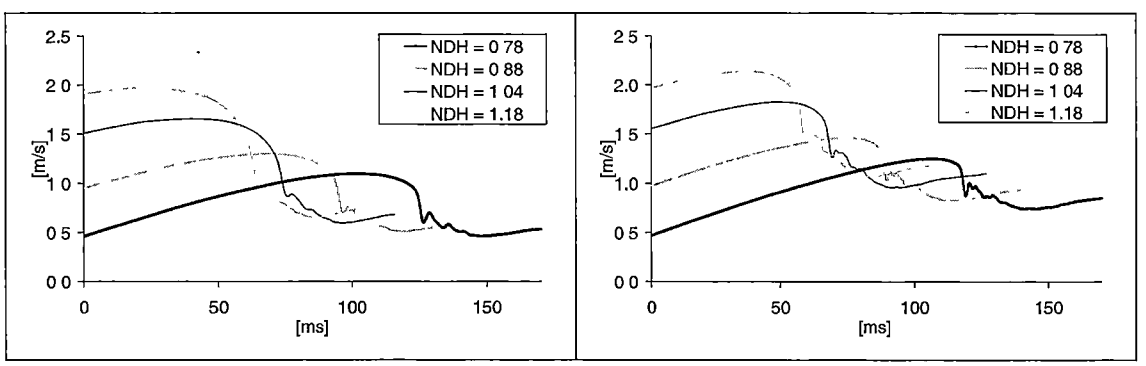

Figure 3.11.6 J2. $y(t)$ for various normalised drop heights. Mass Number=0.29 (left). Mass Number=0.58 (right).

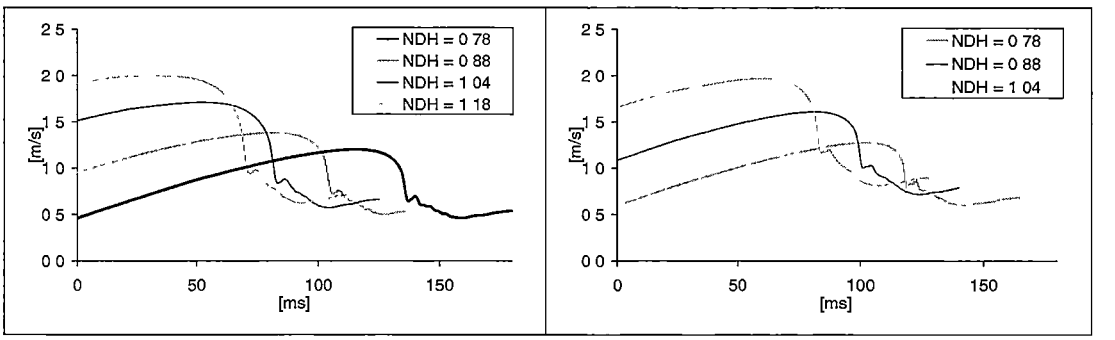

Figure 3.11.7 J3. $\dot{y}(t)$ for various normalised drop heights. Mass Number=0.29 (left). Mass Number=0.58 (right).

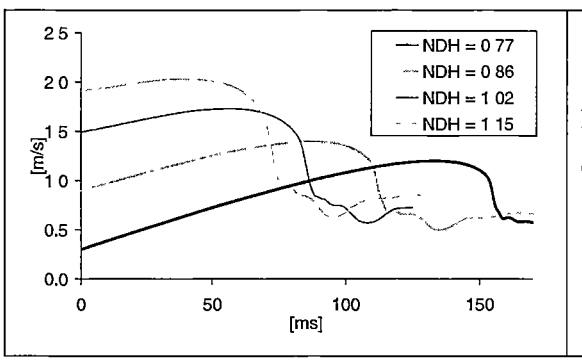

Model Incat1 was damaged before these readings could be made.

Figure 3.11.8 Incat1. $\dot{y}(t)$ for various normalised drop heights. Mass Number=0.29 (left). Mass Number=0.58 (right).

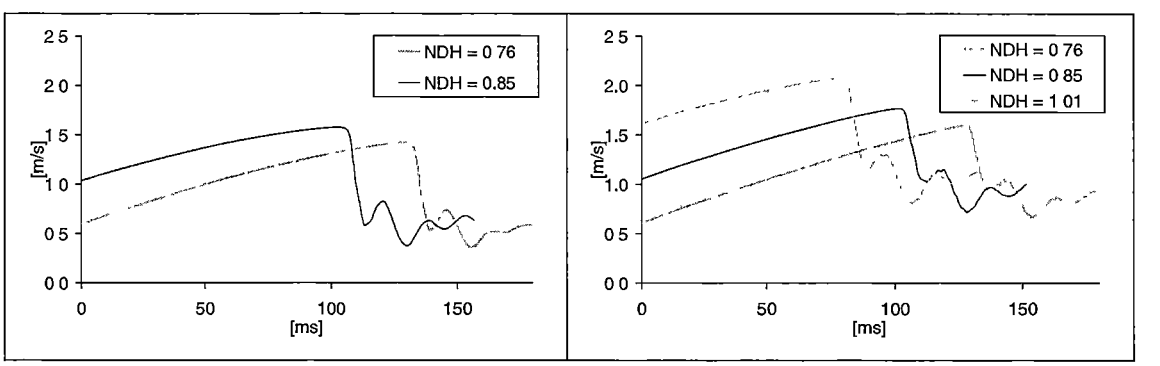

Figure 3.11.9 Flat1. $\dot{y}(t)$ for various normalised drop heights. Mass Number=0.29 (left). Mass Number=0.58 (right).

3.12. Pressure Time Records

Pressure time records for a range of drop heights and two mass numbers are shown in Figure 3.12.1 to Figure 3.12.28 for each of the pressure transducer locations on each model. The pressure time records display a similar form for each model over the range of normalised drop heights and mass numbers tested which was also the case for the acceleration records as noted previously. No results are given for the pressure transducer location P1 on the J-series models because pressure results for these locations were unusual in nature. These pressure readings ranged from no response to a very sharp pressure spike of approximate magnitude 100kPa with a duration of a few milliseconds. The cause of the spurious results is attributed to the pressure transducer face impacting the water surface squarely. This caused the amount of trapped air on the transducer face to vary significantly because any small disturbance of the water surface or slight change in transducer face orientation effects the venting of air greatly. The apparent short duration of the pressure spike evidently exaggerated the effect of the variable amount of trapped air due to the compressibility of the air. This variable amount of trapped air effect did not present a problem at the other transducer locations. For the transducers located other than at the top of the arch the transducer face became wetted because of predominantly tangential water flow across the transducer face. Tangential flow allows the air surrounding the transducer face to vent in a regular and consistent manner and thus no air is trapped. Pressure transducers located at the top of the arch measured the pressure in the trapped air/water eddy. This air/water eddy was a significant feature of the entry process rather than an artefact of the instrumentation.

The transient pressure records measured on the wedge25 and wedge15 models for all pressure transducer locations, two mass numbers and a range of normalised drop heights are shown in Figure 3.12.1 to Figure 3.12.4 (wedge25) and Figure 3.12.5 to Figure 3.12.7 (wedge15). For all these records the form of the pressure transients at all normalised drop heights show a similar profile. Initially there is a slight elevation in the pressure reading as the transducer comes into contact with the jet front, then there is a substantial, sharp pressure spike when the transducer comes into contact with the main body of the water. Following the pressure spike the pressure reading reduces steadily. The rate of reduction of pressure is greater the closer a transducer is located to the apex of either of the wedges. For a particular transducer location, model and mass number the peak pressure will occur at a later time for a lower normalised drop height because of the lower initial impact velocity of the model.

The pressure transients for model wedge25 with sideplates are shown in Figure 3.12.8 to Figure 3.12.11. The initial stages of these pressure transients for pressure transducer P1, P2 and P3 are similar to the wedge25 model, however the presence of the sideplates causes a secondary pressure spike which coincides with the arch closure event. The relative magnitude of the two spikes varies depending on the transducer location, mass number and normalised drop height. For pressure transducer P1 and P2 which are located nearest the apex of the wedge centre bow the initial pressure spike is generally of larger magnitude than the pressure spike due to arch closure. The exceptions to

this statement are for the case of mass number 0.59 and normalised drop height 0.76 and 0.85 for transducer P1 and for mass number 0.59 and normalised drop height 0.76 for transducer P2. For these test conditions the initial pressure spike is of lower magnitude than the spike due to arch closure. For pressure transducer location P3 the initial pressure spike is of larger magnitude than the arch closure pressure spike for mass number 0.29 and for mass number 0.59 the reverse is the case. For transducer P4, located nearest the top of the arch, it is not possible to distinguish between the initial spike and the arch closure pressure spike.

For wedge15 with sideplates similar trends in pressure records are displayed to those observed for wedge25 with sideplates and are shown in Figure 3.12.12 to Figure 3.12.14. Pressure transducer P1 and P2 records are initially similar to that observed for the 15° wedge. Once arch closure has commenced there is a secondary pressure spike associated with this event. The relative magnitude of these two pressure spikes is that the initial spike is greater than the second pressure spike. For pressure transducer P3 there is only one discernible pressure spike which can be observed and this spike coincides with the arch closure event.

Pressure transients are shown in Figure 3.12.15 to Figure 3.12.17 for model J1 for two mass numbers and a range of normalised drop heights. Over the range of normalised drop heights pressure transducer P2 (located near the foot of the centre bow) experiences a small rise in pressure when it initially contacts the water and a second pressure spike is then observed which is evidently associated with the arch closure event. The second pressure spike is of a similar or greater magnitude to the first pressure spike. Pressure transducer P3 (located at the point of inflection) on the centre bow profile experiences a steady increase in transient pressure before a sharp peak occurs that coincides with the arch closure event. The pressure recorded at the top of the arch, location P4, displays for all normalised drop heights an initial steady rise in pressure prior to a substantial pressure spike that is of a larger magnitude than that recorded at transducer location P3.

Figure 3.12.18 to Figure 3.12.21 detail the pressure transients experienced by model J2 for a range of normalised drop height and two mass numbers. The form of all pressure records is quite consistent over this range of test conditions and transducer locations. There is a an initial gradual rise in pressure as each transducer becomes wet and then there is a significant pressure spike associated with the arch closure event. The pressure then reduces rapidly and becomes small (less than 5kPa) or negative for a short period. A generally similar trend is shown for model J3 pressure records (Figure 3.12.22 to Figure 3.12.24) and for model Incat1 (Figure 3.12.25 to Figure 3.12.28) although the gradual rise in pressure prior to the arch closure pressure spike is generally substantially less than for either model J2 or J3.

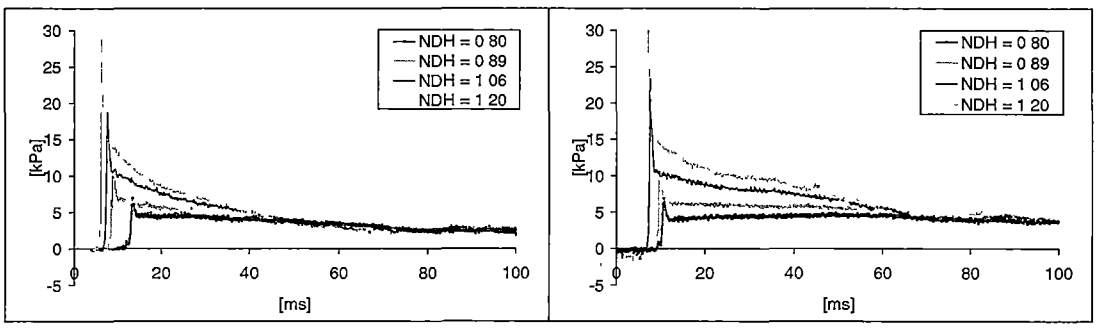

Figure 3.12.1 Wedge25. $p_1(t)$ for various normalised drop heights. Mass Number=0.29 (left), Mass Number=0.58 (right).

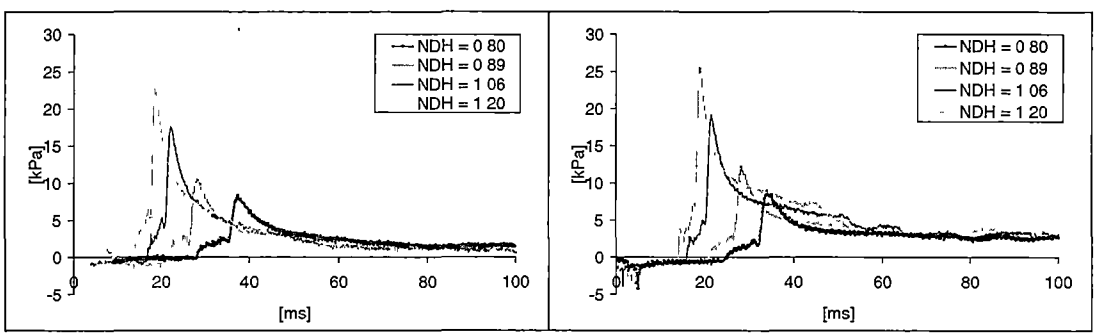

Figure 3.12.2 Wedge25. $p_2(t)$ for various normalised drop heights. Mass Number=0.29 (left), Mass Number=0.58 (right).

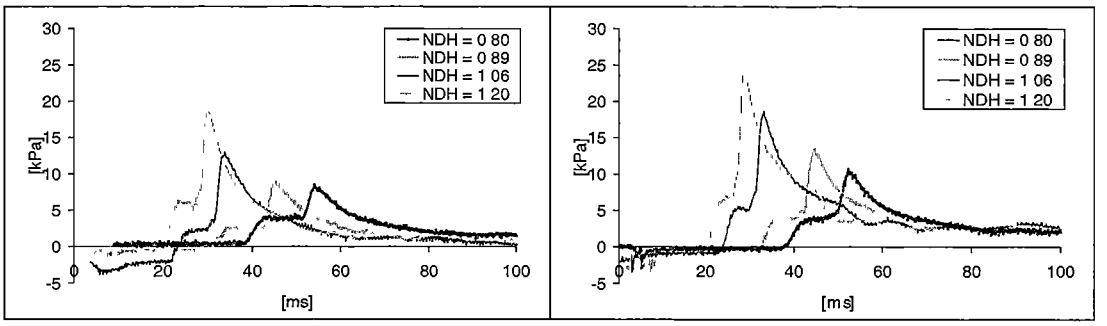

Figure 3.12.3 Wedge25. $p_3(t)$ for various normalised drop heights. Mass Number=0.29 (left), Mass Number=0.58 (right).

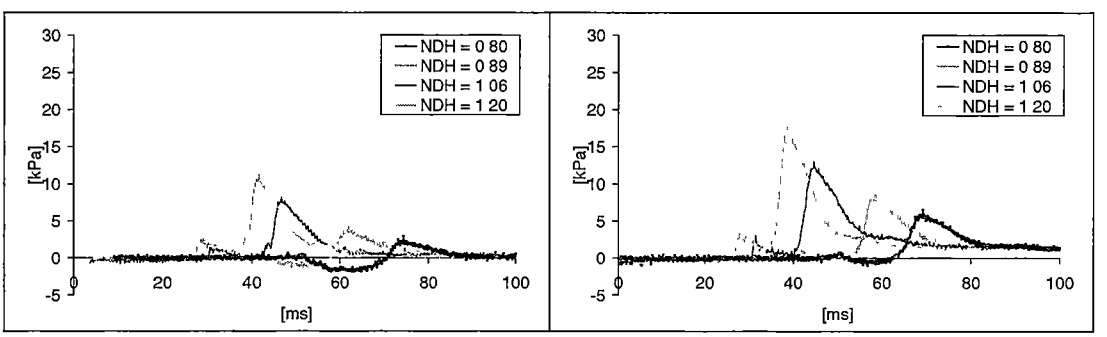

Figure 3.12.4 Wedge25. $p_4(t)$ for various normalised drop heights. Mass Number=0.29 (left), Mass Number=0.58 (right).

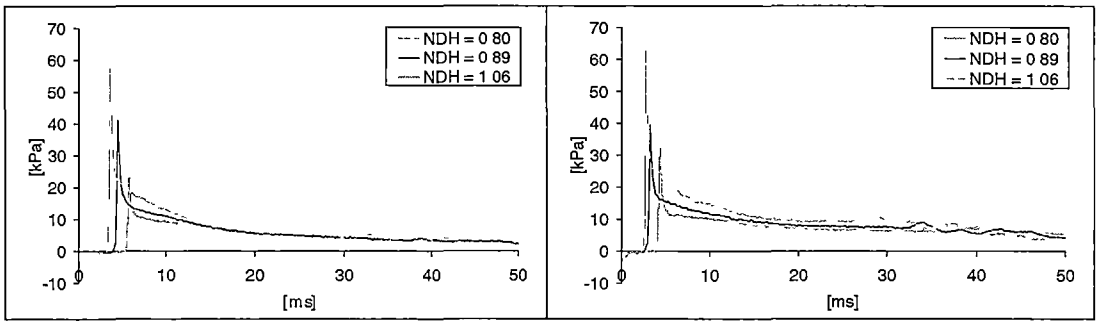

Figure 3.12.5 Wedge15. $p_1(t)$ for various normalised drop heights. Mass Number=0.29 (left), Mass Number=0.58 (right).

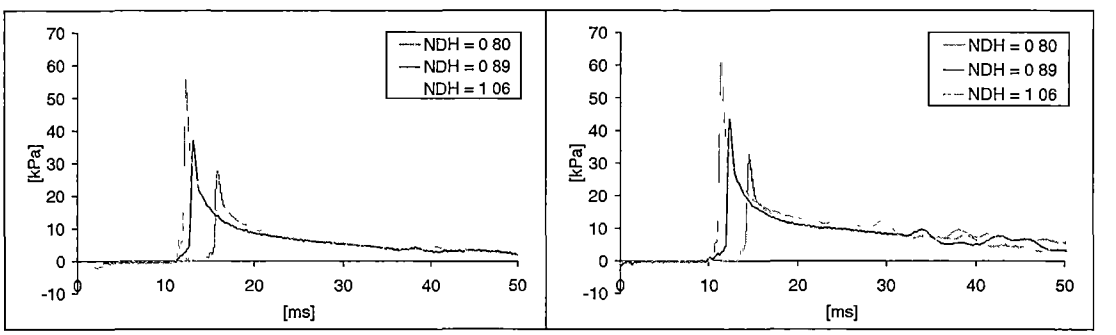

Figure 3.12.6 Wedge15. $p_2(t)$ for various normalised drop heights. Mass Number=0.29 (left), Mass Number=0.58 (right).

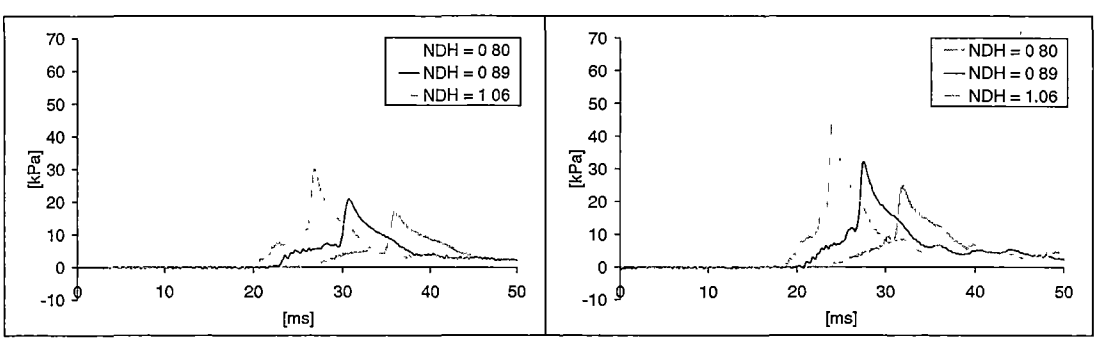

Figure 3.12.7 Wedge15. $p_3(t)$ for various normalised drop heights. Mass Number=0.29 (left), Mass Number=0.58 (right).

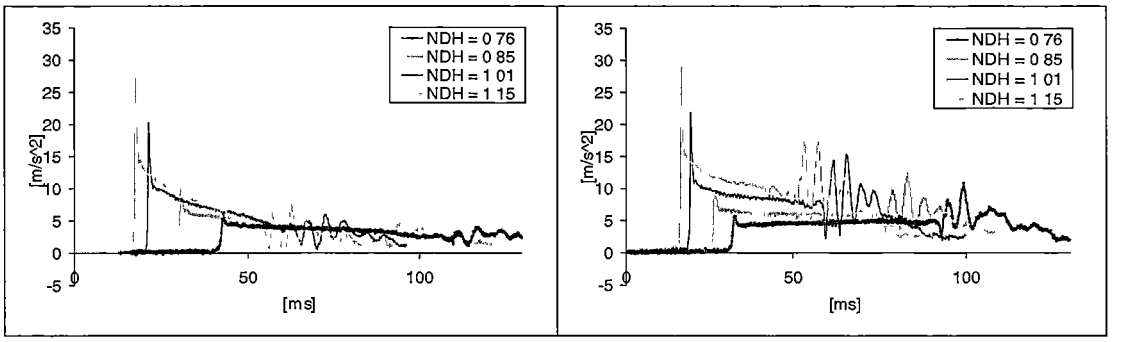

Figure 3.12.8 Wedge25 with sideplates. $p_1(t)$ for various normalised drop heights. Mass Number=0.29 (left), Mass Number=0.58 (right).

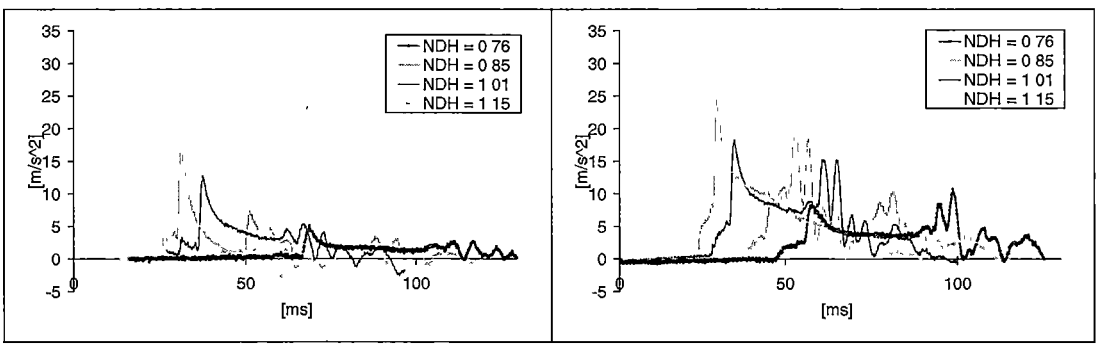

Figure 3.12.9 Wedge25 with sideplates. $p_2(t)$ for various normalised drop heights. Mass Number=0.29 (left), Mass Number=0.58 (right).

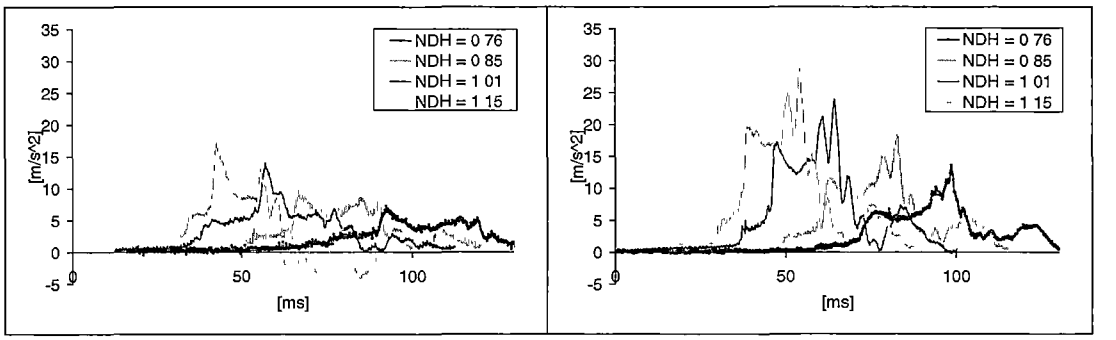

Figure 3.12.10 Wedge25 with sideplates. $p_3(t)$ for various normalised drop heights. Mass Number=0.29 (left), Mass Number=0.58 (right).

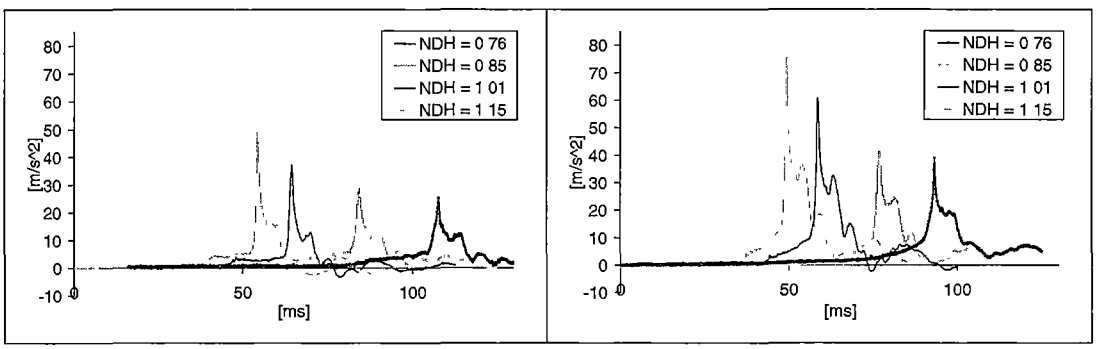

Figure 3.12.11 Wedge25 with sideplates. $p_4(t)$ for various normalised drop heights. Mass Number=0.29 (left), Mass Number=0.58 (right).

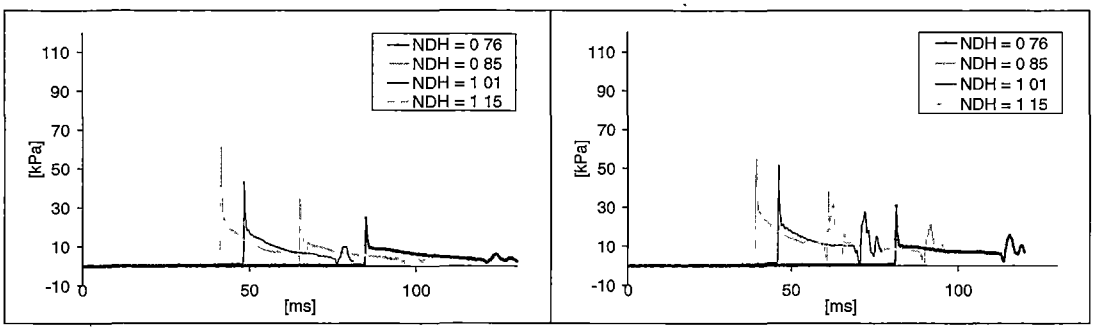

Figure 3.12.12 Wedge15 with sideplates. $p_1(t)$ for various normalised drop heights. Mass Number=0.29 (left), Mass Number=0.58 (right).

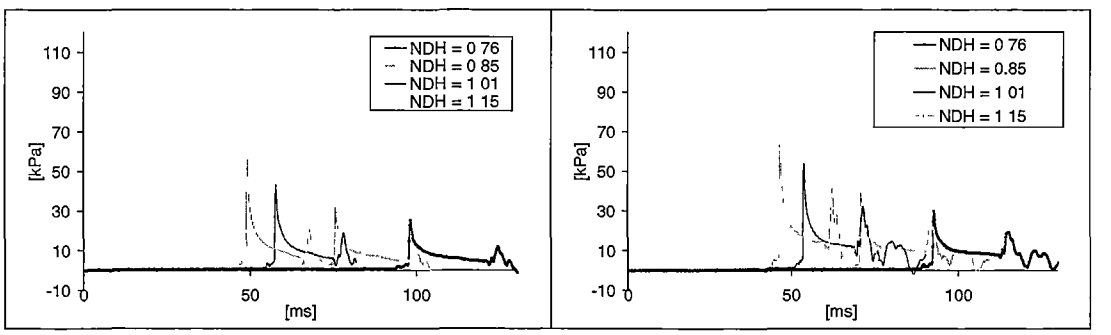

Figure 3.12.13 Wedge15 with sideplates. $p_2(t)$ for various normalised drop heights. Mass Number=0.29 (left), Mass Number=0.58 (right).

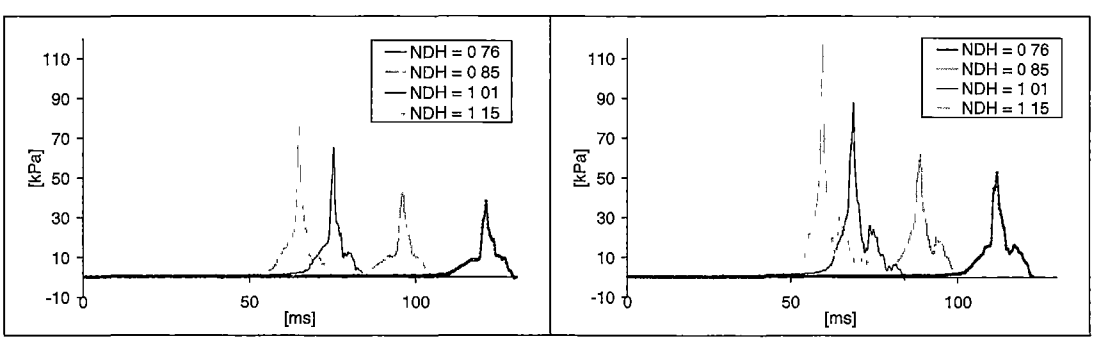

Figure 3.12.14 Wedge15 with sideplates. $p_3(t)$ for various normalised drop heights. Mass Number=0.29 (left), Mass Number=0.58 (right).

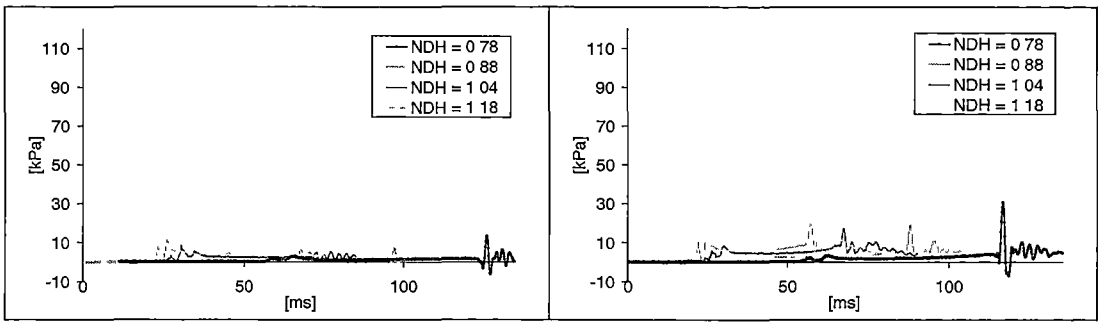

Figure 3.12.15 J1. $p_2(t)$ for various normalised drop heights. Mass Number=0.29 (left), Mass Number=0.58 (right).

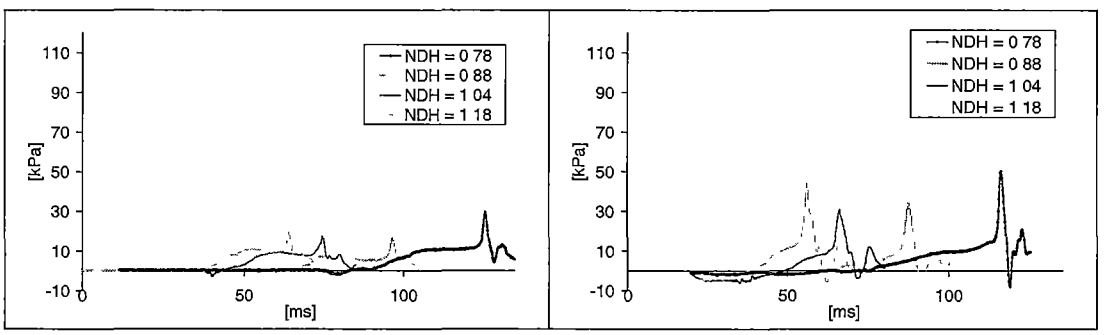

Figure 3.12.16 J1. $p_3(t)$ for various normalised drop heights. Mass Number=0.29 (left), Mass Number=0.58 (right).

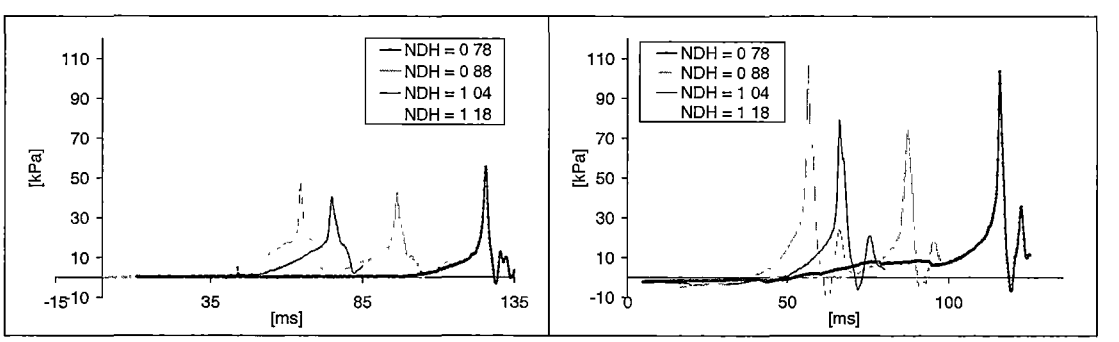

Figure 3.12.17 J1. $p_4(t)$ for various normalised drop heights. Mass Number=0.29 (left), Mass Number=0.58 (right).

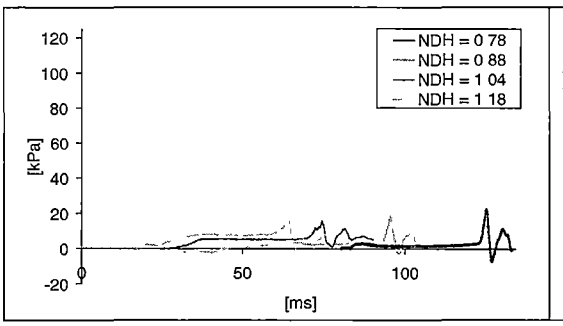

Pressure transducers were broken before these measurements could be made.

Figure 3.12.18 J2. $p_2(t)$ for various normalised drop heights. Mass Number=0.29 (left), Mass Number=0.58 (right).

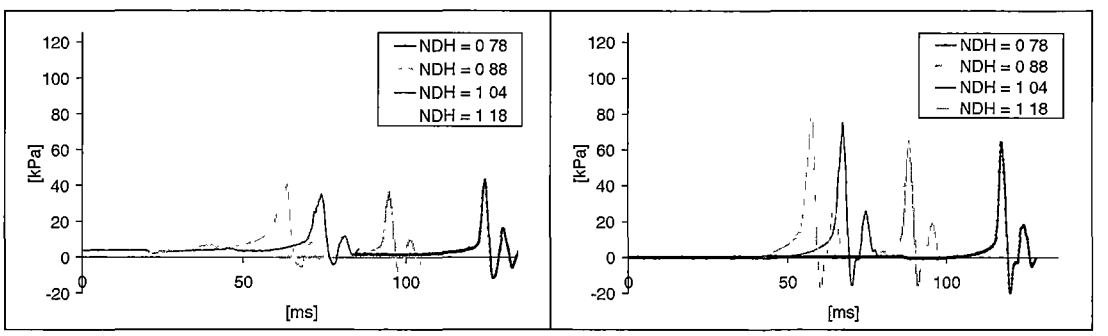

Figure 3.12.19 J2. $p_3(t)$ for various normalised drop heights. Mass Number=0.29 (left), Mass Number=0.58 (right).

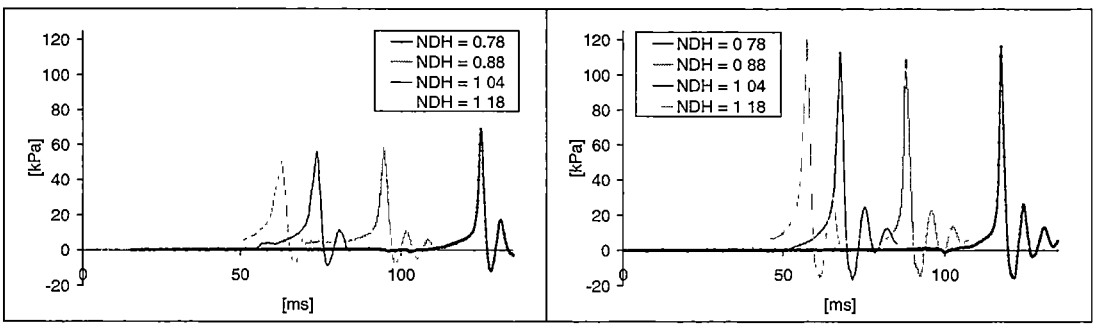

Figure 3.12.20 J2. $p_4(t)$ for various normalised drop heights. Mass Number=0.29 (left), Mass Number=0.58 (right).

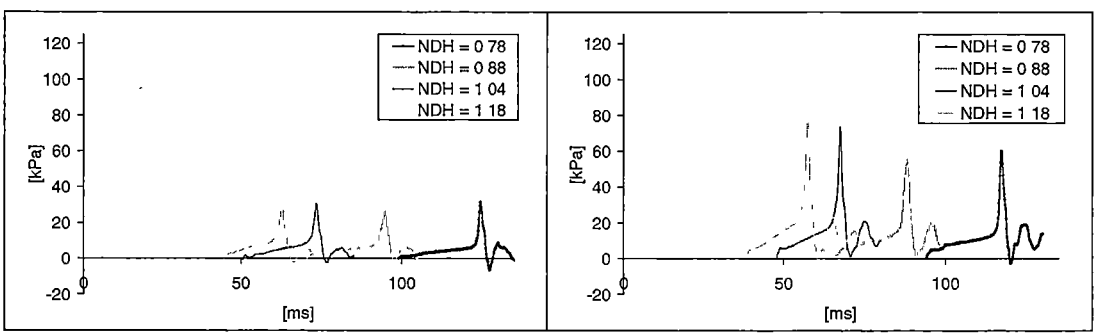

Figure 3.12.21 J2. $p_5(t)$ for various normalised drop heights. Mass Number=0.29 (left), Mass Number=0.58 (right).

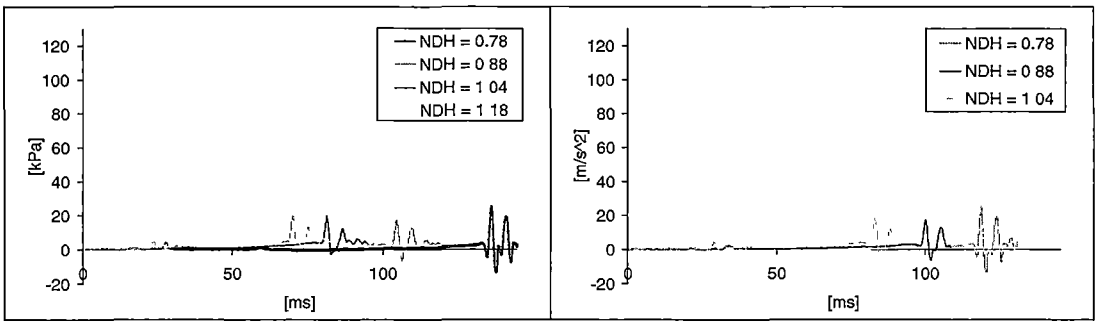

Figure 3.12.22 J3. $p_2(t)$ for various normalised drop heights. Mass Number=0.29 (left), Mass Number=0.58 (right).

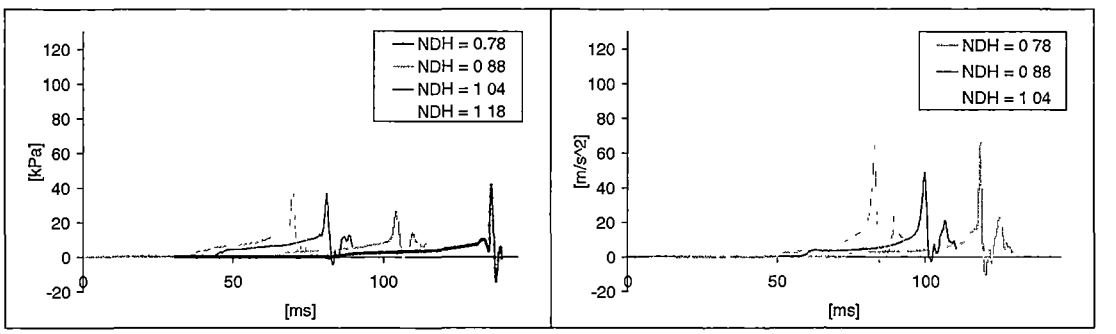

Figure 3.12.23 J3. $p_3(t)$ for various normalised drop heights. Mass Number=0.29 (left), Mass Number=0.58 (right).

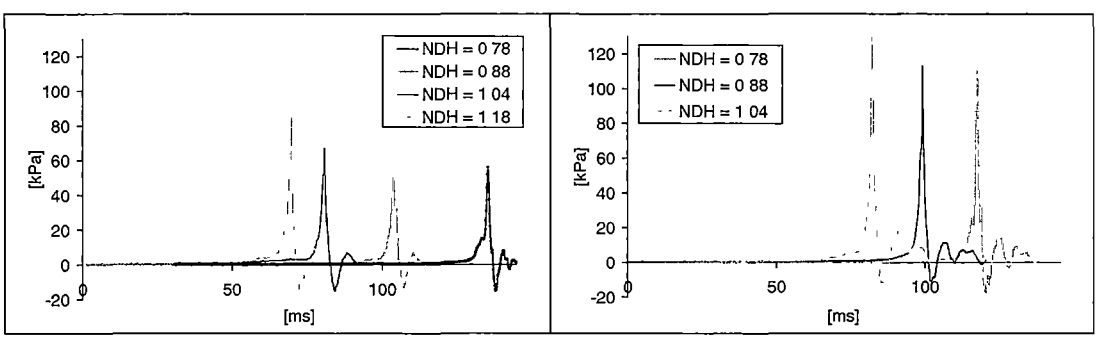

Figure 3.12.24 J3. $p_4(t)$ for various normalised drop heights. Mass Number=0.29 (left), Mass Number=0.58 (right).

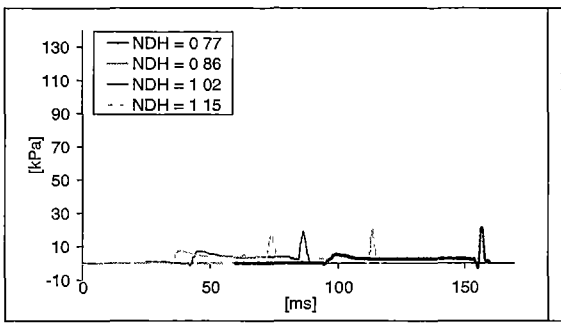

Model Incat1 was damaged before these readings could be made.

Figure 3.12.25 Incat1. $p_1(t)$ for various normalised drop heights. Mass Number=0.29 (left), Mass Number=0.58 (right).

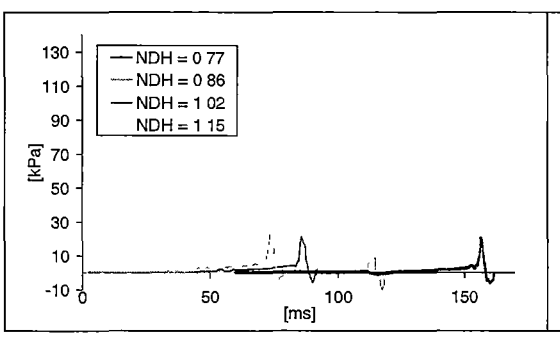

Model Incat1 was damaged before these readings could be made

Figure 3.12.26 Incat1. $p_2(t)$ for various normalised drop heights. Mass Number=0.29 (left), Mass Number=0.58 (right).

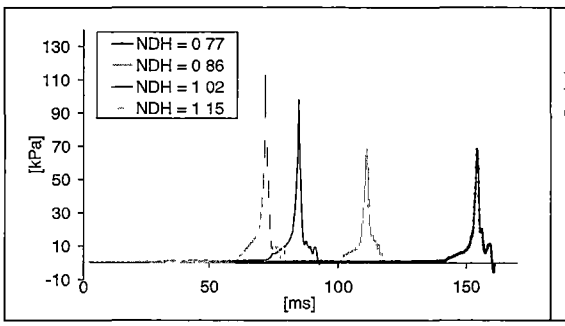

Model Incat1 was damaged before these readings could be made

Figure 3.12.27 Incat1. $p_3(t)$ for various normalised drop heights. Mass Number = 0.29 (left), Mass Number = 0.58 (right).

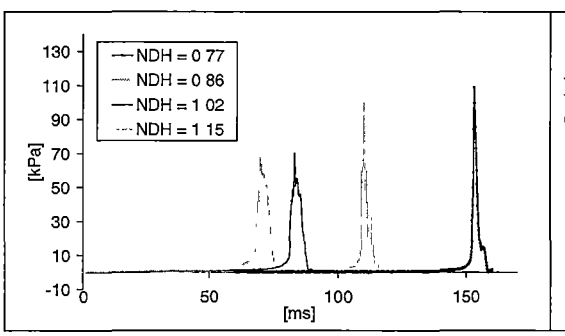

Model Incat1 was damaged before these readings could be made

Figure 3.12.28 Incat1. $p_4(t)$ for various normalised drop heights. Mass Number = 0.29 (left), Mass Number = 0.58 (right).

3.13. Peak Accelerations

Peak acceleration results for all models over a range of normalised drop heights and two mass numbers are shown in Figure 3.13.1 and Figure 3.13.2.

All the wedge-based geometries at both mass numbers display a monotonic increase of peak acceleration with normalised drop height. The 25° wedge experiences lower peak accelerations than the 15° wedge model. When sideplates are attached to either of these models the peak accelerations are increased by a factor of approximately 2 for all normalised drop heights.

The J-series models all experience higher peak accelerations than the wedge models. However, unlike the wedge-based models, the peak accelerations tend first to decrease with normalised drop before increasing. The normalised drop height corresponding to the minimum peak acceleration for the J-series models varies depending on model geometry. The minimum peak acceleration for model J1 occurs at a normalised drop height of approximately 0.90 for both mass numbers, for model J2 at 1.05 for the lower mass number and at 0.95 for the higher mass number and for model J3 at 0.81 for both mass numbers. This phenomenon is quite unexpected and is discussed in more detail in Section 3.14. Once the peak acceleration of the J-series models begins to increase, the rate of increase is similar to that experienced by the wedge-based models. The Incat1 model performs similarly to the J-series models.

Model Flat1 experiences the highest peak accelerations of all models for a mass number of 0.29. However its peak accelerations are less than that experienced by both models J2 and J3 for a mass number of 0.58. The Flat1 model displays a monotonic increase in peak acceleration with normalised drop height.

The effect on peak acceleration for all models of mass number is as follows. Models wedge15, wedge25 and Flat1 all experience higher accelerations at mass number 0.29 whereas the J-series and the wedge with sideplate models all experience lower peak acceleration at the lower mass number compared with the peak accelerations observed at the higher mass number. This effect is attributed to the observation that the peak acceleration is associated with the arch closure event. It is thus the model velocity during this event that is of particular importance in determining peak acceleration. The J-series and wedge with sideplates models experience significant deceleration during the entry of their substantial centre bows which slow the lighter (low mass number) models more than the heavier high mass number tests. This is because the hydrodynamic force associated with the centre bow and demi-hulls is proportionately larger compared with the gravitational force for the low mass number configuration. This slows the low mass number configurations more causing the arch closure event to be less extreme compared with the arch closure event experienced with the higher mass number. This effect does not of course influence the simple vee wedges, as they do not experience arch closure.

The Flat1 model does not have a centre bow and its demi-hulls are very fine thus very small hydrodynamic forces act on this model prior to the onset of arch closure.

The experimental scatter in peak acceleration amongst the 5 tests conducted for each test configuration (as indicated by the 95% confidence error bars) is significantly greater for the models that have an arch like geometry than for the simple wedge models. It is also observed that the peak accelerations experienced at a particular normalised drop height vary significantly depending on model geometry. For example at a normalised drop height of 0.89 and mass number of 0.29 the 25° wedge model experiences a peak acceleration of 11±0.3 m/s^2 and the Model Flat1 experiences a peak acceleration of 238±17 m/s^2. This indicates very clearly that peak acceleration is a strong function of geometric form.

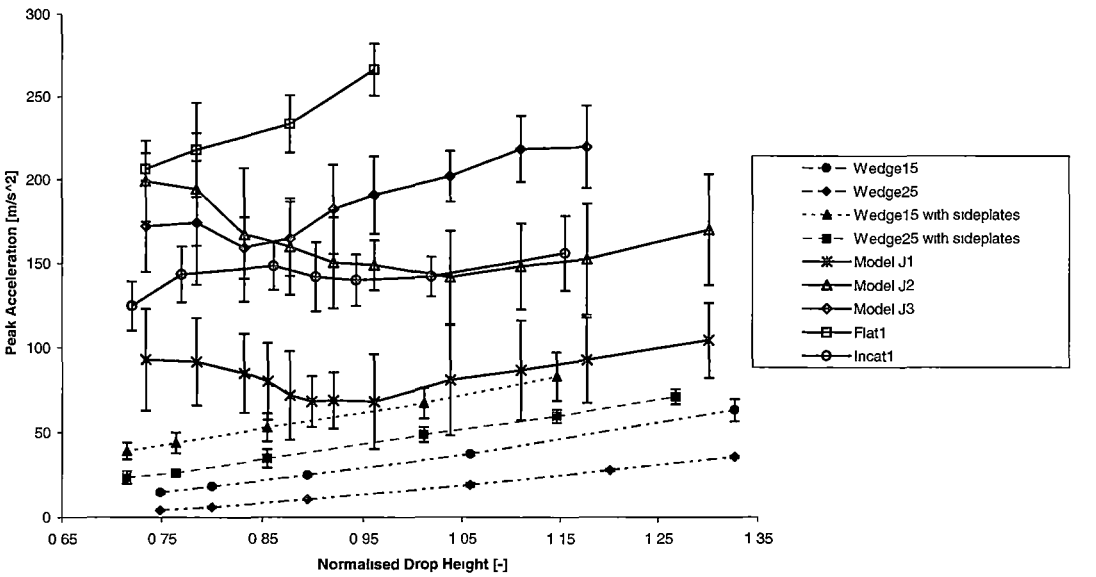

Figure 3.13.1 Peak acceleration values for all models. Mass Number=0.29.

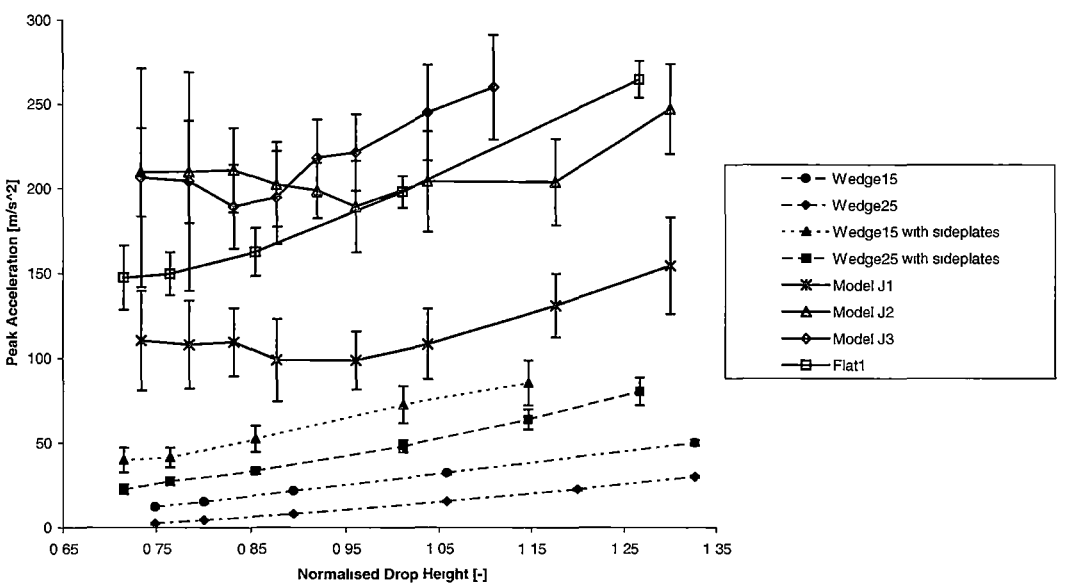

Figure 3.13.2 Peak acceleration values for all models (except Incat1). Mass Number=0.58

3.14. The Non-Monotonic Nature of the J1 Peak Acceleration Curve

Examination of the variation of the peak acceleration with drop height (Figure 3.13.1 and Figure 3.13.2) reveals that the peak acceleration values for non-wedge based models show an initial reduction in peak acceleration with normalised drop height before the peak acceleration begins to increase with normalised drop height. This occurs, for example, at a normalised drop height of approximately 0.88 for model J1. Figure 3.14.1 shows model J1 penetrating the water for three different normalised drop heights. Times shown on the photos are zeroed such that 0ms occurs when the peak acceleration value occurs. The temporal alignment of these times with the peak acceleration is to within 1ms. Explanations for this unusual feature include: (1) Separation of the free surface from the centre bow. This increases the amount of the air in the void. However the visualisation evidence seems not to support this proposition. (2) The piling up of the water around the centre and side hulls causes the free surface to be more deformed when the arch closure event occurs. This means that there is more air trapped when the arch closes. There is also not definitive support for this conclusion in Figure 3.14.1. (3) The preferred explanation is that the location of the final arch closure event moves around the top of the arch at different drop heights. There is some weak evidence for this in the visualisation. Evidence for this proposition was also presented in Section 3.15 with respect to the peak pressure measured near the top of the arch for model Incat1. The effect of the location of the highest point in the arch on the peak acceleration is observed to be strong (Section 3.19) and thus a small change in the location of the final arch closure event may plausibly cause a significant change in the peak acceleration.

The three propositions suggested above are speculative in nature and additional work is required to fully understand this feature of the experimental results.

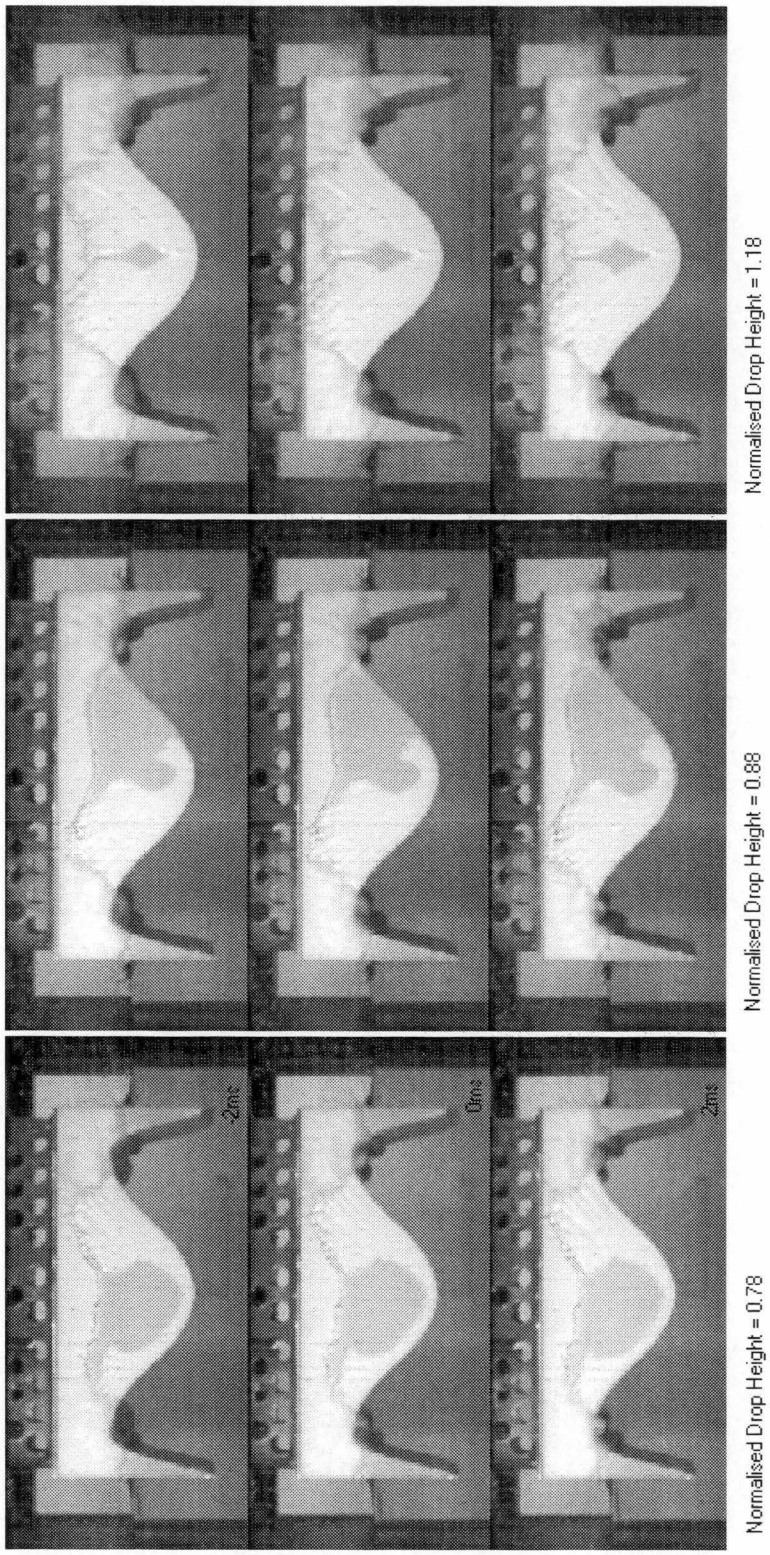

Figure 3.14.1 Understanding the non-monotonic nature of the peak acceleration against normalised drop height curve of model J1. Mass Number=0.29

3.15. Peak Pressures

Peak pressure results for all models over a range of normalised drop heights, at mass numbers of 0.29 and 0.58 are shown in Figure 3.15.1 to Figure 3.15.15.

The peak pressures for the wedge25 and wedge15 models are shown in Figure 3.15.1 to Figure 3.15.4. With a few minor exceptions these display the same trends as the peak accelerations. That is the peak pressure measured at each gauge location generally increases with normalised drop height. The scatter in results is observed not to increase with normalised drop height significantly except for the case of pressure transducer P1 on both these models. The trend in relative magnitude of the different peak pressure transducer readings with normalised drop height displayed for model wedge25 displays a note worthy feature. At mass number 0.29 and for peak pressures above normalised drop height 0.88 there is a well established trend in the relative magnitudes of the peak pressure for the four transducer readings. That is for a particular normalised drop height the further a pressure transducer is located from the apex of the wedge the lower the peak pressure is. For normalised drop heights below 0.88 the relative magnitude of the peak pressure for each transducer at some particular normalised drop shows a different order. Peak pressure P3 is the greatest, pressure P2 the second greatest and pressure P1 the third greatest. Peak pressure P4 remains the smallest in relative magnitude. This is attributed to wedge25 continuing to accelerate once it has initially contacted the fluid for a short while before decelerating. This causes the velocity of the wedge to be higher when pressure transducer P2 and P3 initially impact the water compared with the model velocity when pressure transducer P1 contacts the water (Figure 3.11.1). This trend is also evident for mass number 0.58 for the model wedge25. A similar but less pronounced trend is evident for the wedge15 model. Also, for both model wedge25 and wedge15 peak pressure increased with mass number.

When sideplates are attached to the 25° and 15° wedges as shown in Figure 3.15.5 and Figure 3.15.8 it is observed that the nature of the peak pressures change markedly. The peak pressure measured at the transducers located close to the top corner (P4 for 25° wedge and P3 for 15°wedge) changes from being the lowest peak pressure (simple wedge geometry) to the highest peak pressure (sideplates attached). This change in magnitude of peak pressure is attributed to the arch closure event that occurs when the arch void completely fills with fluid as identified in the visualisation results (Section 3.8). The variation of the peak pressure measured on P3 with normalised drop height for model wedge25 with sideplates at mass number 0.29 displays a somewhat irregular trend. For normalised drop heights less than 1.05 this transducer records the second highest relative peak pressures. However for normalised drop heights greater than 1.05 the relative magnitude of the pressure reading changes and it displays the smallest relative peak pressure values. This change in relative magnitude of this peak pressure is attributed to the local pressure transients associated with the complete filling of the arch void. That is, when the arch void fills a region of high pressure is produced at the top of the arch (as indicated by the high P4 values). The pressure then decreases as the distance from the top of the arch increases (as revealed by P1 and P2 peak pressures). Clearly at the lower normalised drop

heights the effects of the arch closure pressure spike are either less localised or located closer to the transducer P3 than at the higher normalised drop heights. Transducer P3 is located in such a position that the local variations in the arch closure pressure effects are measured. At mass number 0.58 the relative magnitudes of transducer P3 with respect to the other transducers there is a similar, although less pronounced trend as for mass number 0.29. Transducer P3 records for normalised drop heights less than 1.15 have the second highest relative magnitudes however for normalised drop heights greater than 1.15 transducer P3 has the third highest relative magnitude in peak pressure. None of the pressure transducers on wedge15 with sideplates display the effect observed on wedge25 with sideplates transducer P3. This is attributed to either the effect not being present or the transducers were not suitably located to resolve this effect. For both wedge with sideplate geometries the peak pressures for the other transducer locations are essentially unchanged compared with the simple wedge geometries. This is because it is the initial contact with the water, rather than the arch closure event, which determines the peak pressure for these transducer locations (Section 3.12).

The peak pressures recorded on model J1 are shown in Figure 3.15.9 and Figure 3.15.10. Peak pressure is observed to increase with mass number. It is also observed that the peak pressures display a similar trend with normalised drop height as the peak acceleration graph. That is the peak pressures are initially high and then decrease to a minimum at a normalised drop height of 0.95, before increasing with normalised drop height. The relative magnitudes of the peak pressure is constant with normalised drop height, mass number and distance from the top of the arch. Transducer P4 (located at the top of the arch) experiences the highest peak pressures followed by transducer P3 (located midway down the centre bow) and then P2 (located furthest from the top of the arch).

Model J2 (Figure 3.15.11 and Figure 3.15.12) displays similar trends in peak pressure as model J1. The relative magnitude of the pressure readings decreases with increasing distance from the highest point in the arch. Also an initial decrease in peak pressure followed by an increase in peak pressure with normalised drop height is evident for all transducer locations at mass number 0.29. At mass number 0.58 this trend is less clear. Transducer location P4 displays a clear minimum in peak pressure values, as does transducer P5. However the minimum obtained for location P5 occurs at a normalised drop height of 0.85 where as the minimum for P4 occurs at normalised drop height 0.92. Transducer P3 displays a monotonic increase in peak pressure with normalised drop height. The peak pressures increase significantly at mass number 0.58 compared with the lower mass number.

The model J3 peak pressures are shown in Figure 3.15.13 and Figure 3.15.14. It is observed that the scatter in peak pressure values for location P4 (located on the flat cross structure at the top of the arch) is significantly greater than that observed for the other two transducer locations on this model. The scatter is also generally greater compared with the scatter observed on the other two J-series models for any transducer location. This is attributed to the effect of the flat cross structure on the flow regime during arch closure. The trend of peak pressure, for mass number 0.29, is to initially decrease with normalised drop height until a normalised drop height of 0.85 before increasing with normalised

drop height. The trend is slightly more complex for transducer P4 and mass number 0.58. The substantial scatter in transducer P4 results causes the minimum in the peak acceleration against normalised drop height graph to be less well defined but it occurs somewhere in the range 0.84 to 0.90.

The centre bow on model J2 is identical to that on model J3 and pressure transducers P2 and P3 are located in identical positions on each model. The peak pressure readings for these transducer locations display the same trends in relative magnitude, but the absolute peak pressure reading is not the same for the same pressure transducer location on different models under the same test configuration. This is attributed to the observation made in section 3.12 that the peak pressure recorded on these two models is due to the arch closure event. The detailed arch top geometry of these two models is significantly different and thus the behaviour of the fluid during arch closure thus is different also.

The peak pressures experienced by the Incat1 model are shown in Figure 3.15.15. As for the J-series models the peak pressure measurements made nearest the top of the arch are the largest. For this model a pressure transducer was not placed at the very top of the arch but was placed slightly inboard (P3) and slightly outboard (P4) (Figure 3.5.10). The peak pressures recorded at location P3 are initially larger than those recorded at location P4, but as the normalised drop height increases this trend is reversed. The cross over occurs at a similar normalised drop height (approximately 0.95) to a slight dip in the peak acceleration record for this model. As observed previously, the peak pressure is associated with the arch closure event and the change in location of maximum peak pressure may indicate that the location of the arch closure event is not always the highest point in the arch but varies with normalised drop height. This feature is discussed further is Section 3.14 and the importance of the location of the highest point in the arch is identified in Section 3.19. The pressure transducers located near the foot of the centre bow experience significantly lower pressures than those recorded at the top of the arch.

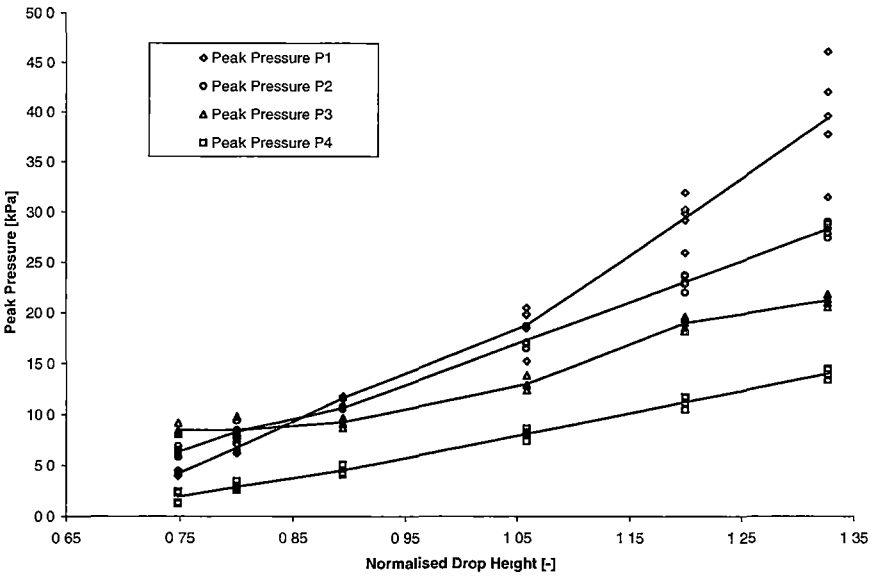

Figure 3.15.1 Wedge25. Mass Number=0.29. Peak pressure values for p1, p2, p3 and p4 locations.

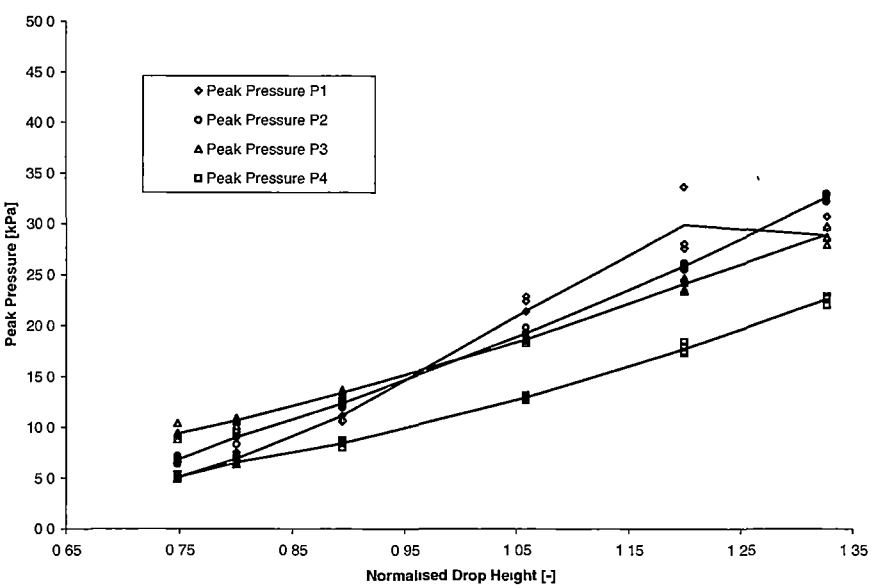

Figure 3.15.2 Wedge25. Mass Number=0.58. Peak pressure values for p1, p2, p3 and p4 locations.

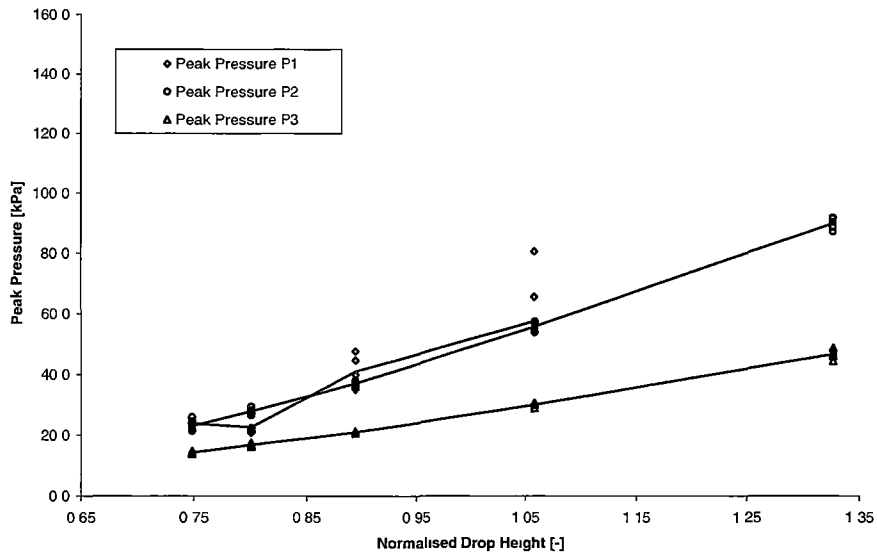

Figure 3.15.3 Wedge15. Mass number=0.29. Peak Pressure values for p1, p2 and p3 locations.

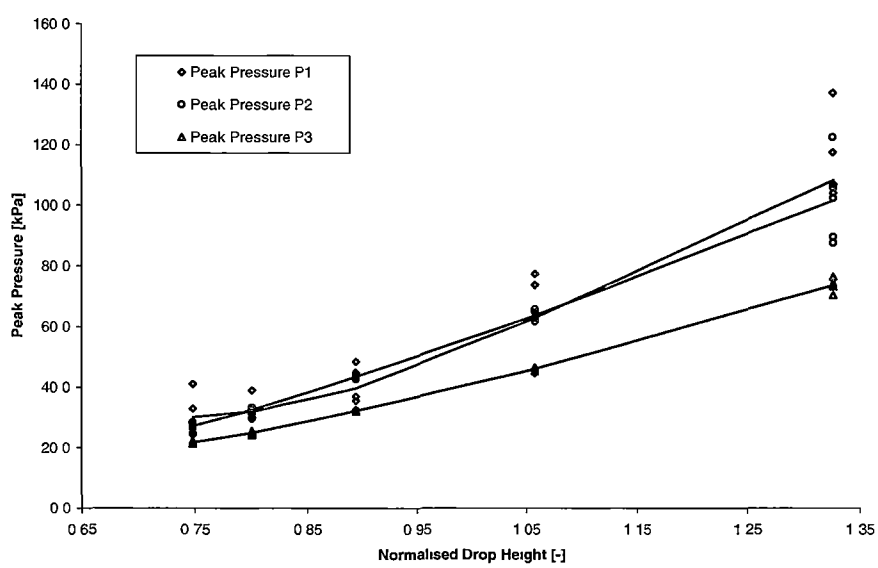

Figure 3.15.4 Wedge15. Mass Number=0.58. Peak pressure values for p1, p2, and p3 locations.

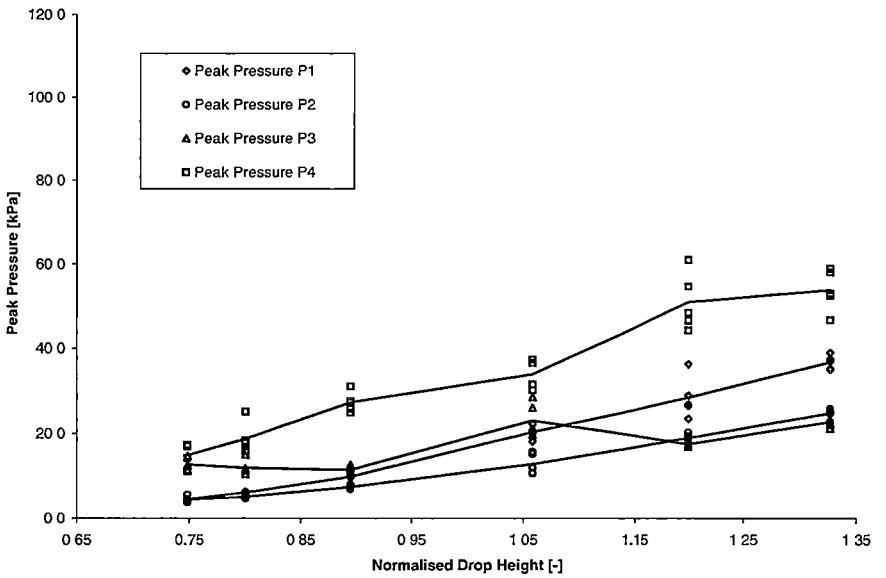

Figure 3.15.5 Wedge25 with sideplates. Mass Number=0.29. Peak pressure values for p1, p2, p3, and p4 locations.

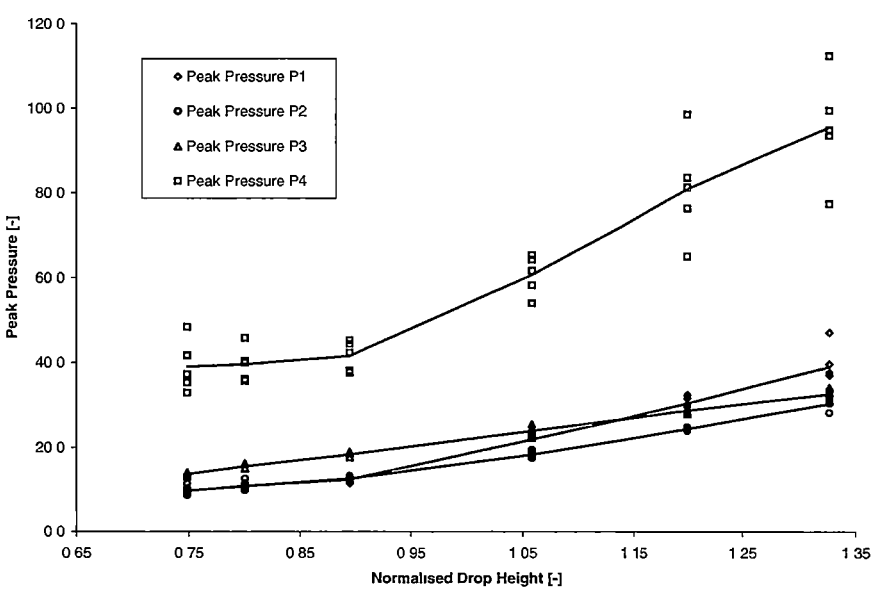

Figure 3.15.6 Wedge25 with sideplates. Mass Number=0.58. Peak pressure values for p1, p2, p3 and p4 locations.

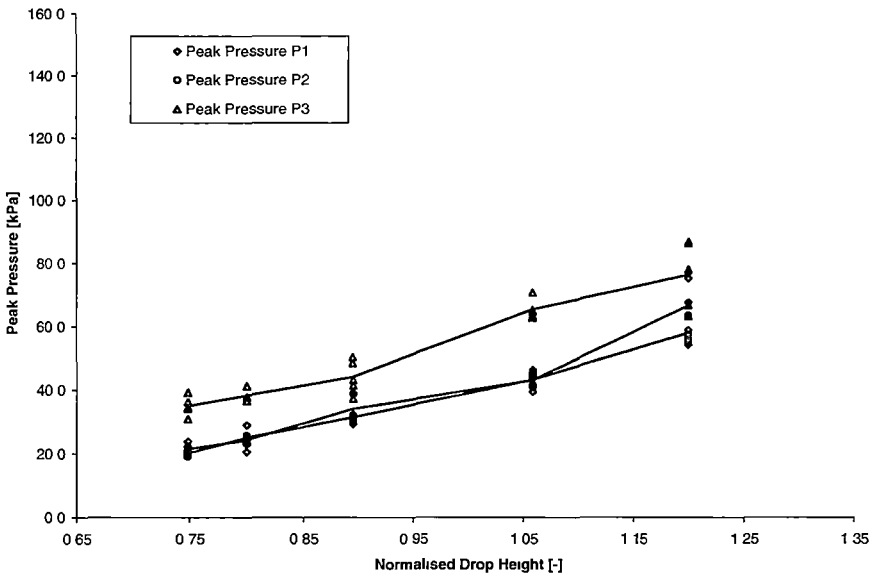

Figure 3.15.7 Wedge15 with sideplates. Mass Number=0.29. Peak pressure values for p1, p2, and p3 locations.

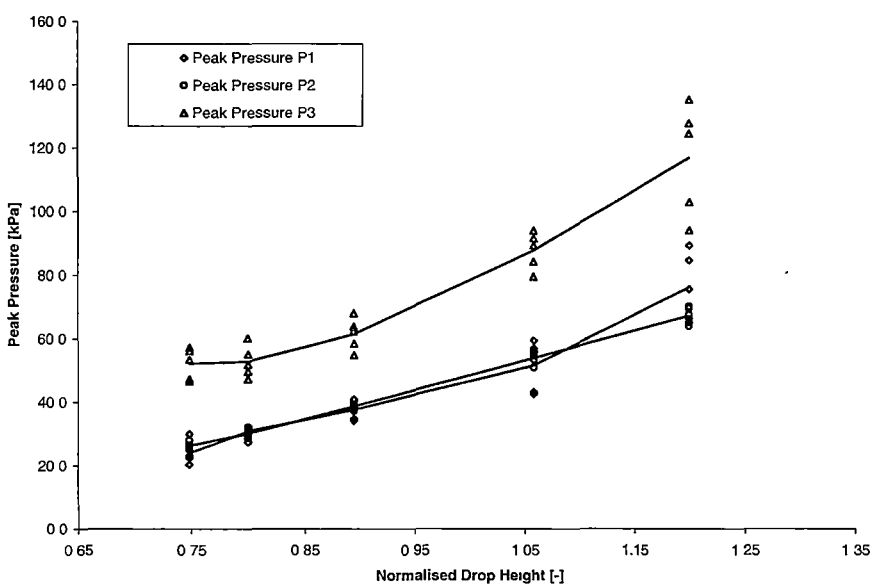

Figure 3.15.8 Wedge15 with sideplates. Mass Number=0.58. Peak pressure values for p1, p2 and p3 locations.

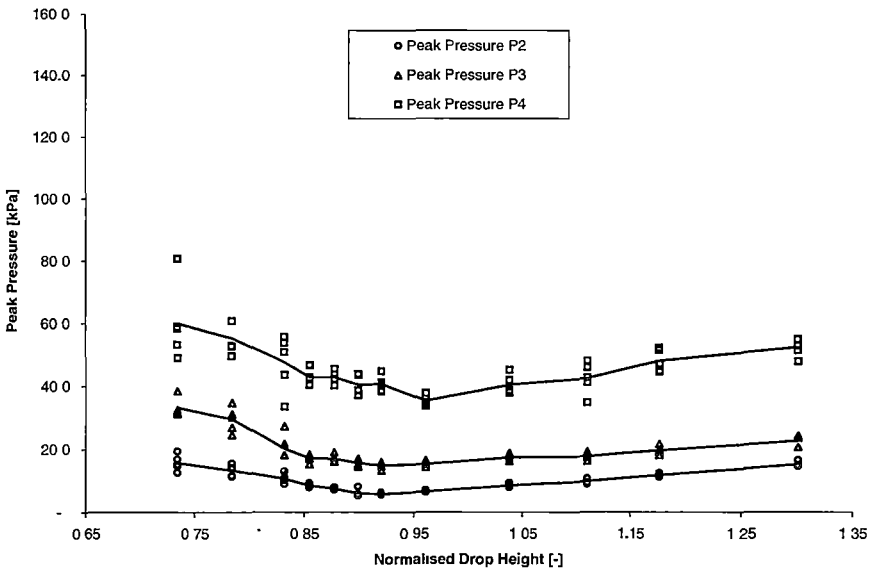

Figure 3.15.9 J1. Mass Number=0.29. Peak Pressure values for p2, p3, and p4 locations.

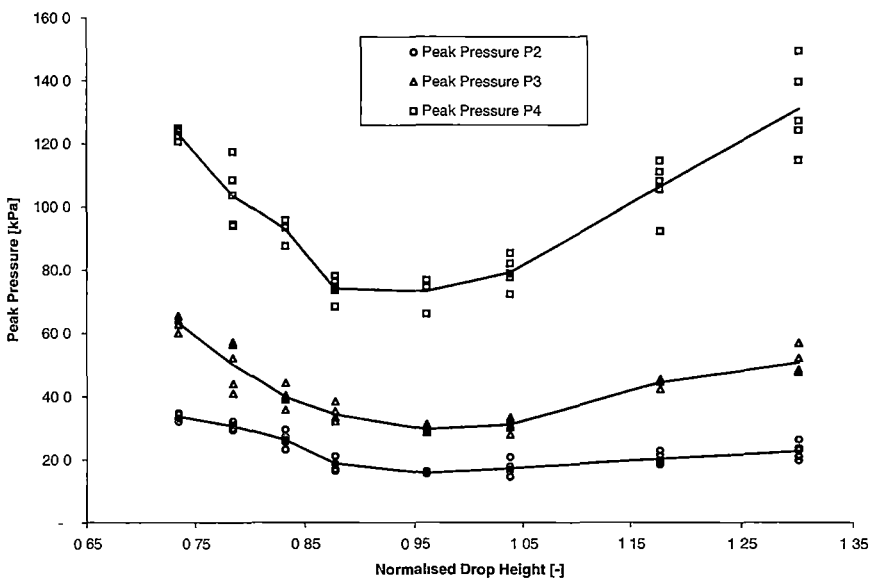

Figure 3.15.10 J1. Mass Number=0.58. Peak pressure values for p2, p3 and p4 locations.

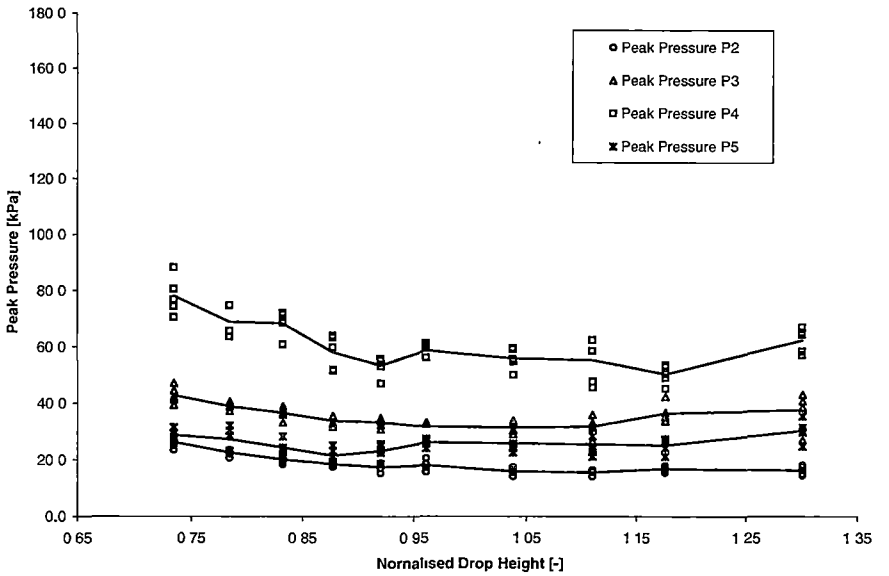

Figure 3.15.11 J2. Mass Number=0.29. Peak pressure values for p2, p3, p4 and p5 locations.

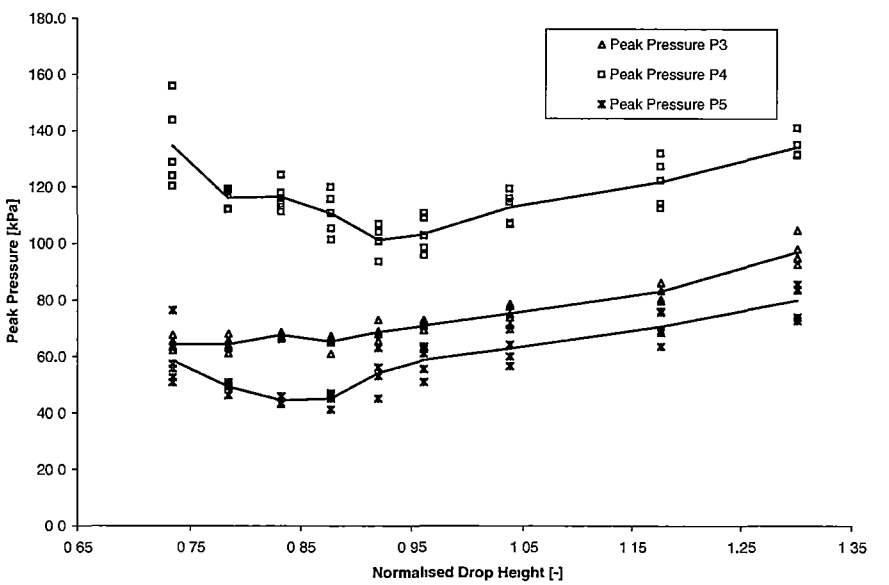

Figure 3.15.12 J2. Mass Number=0.58. Peak pressure values for p3, p4 and p5 locations.

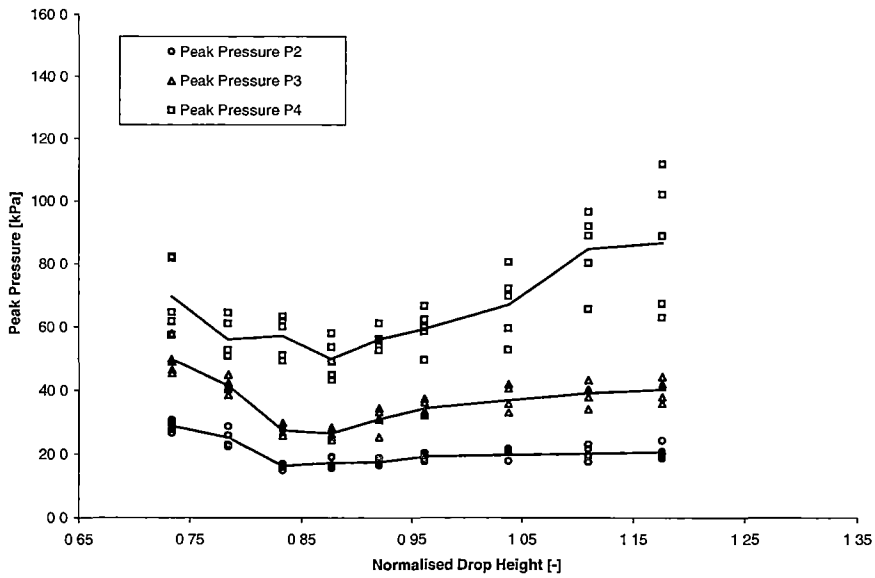

Figure 3.15.13 J3. Mass number=0.29. Peak pressure values for p2, p3 and p4 locations.

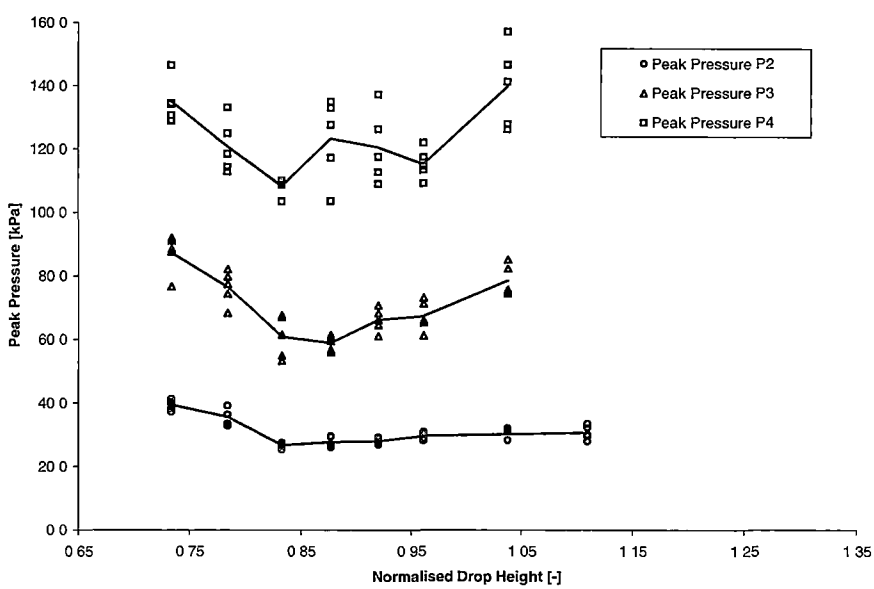

Figure 3.15.14 J3. Mass Number=0.58. Peak pressure values for p2, p3, and p4 locations.

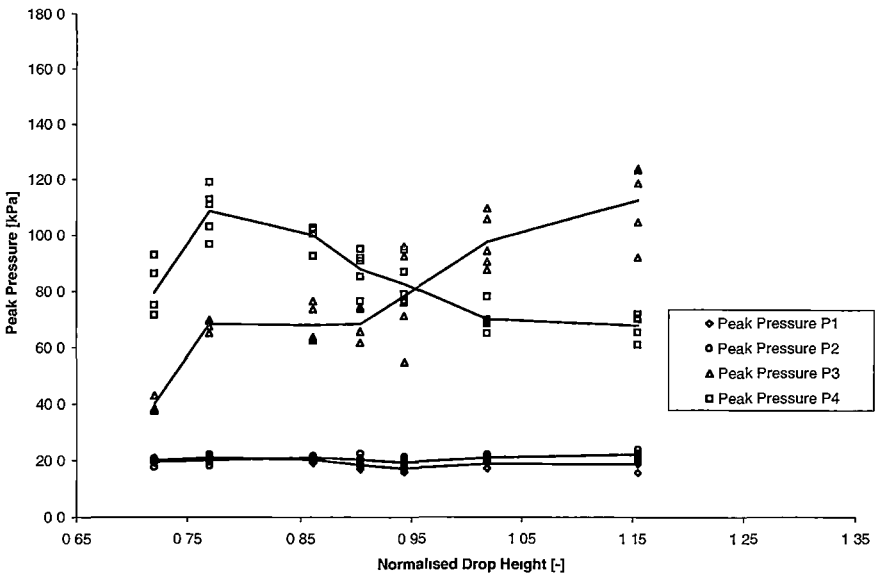

Figure 3.15.15 Incat1. Mass Number=0.29. Peak pressures values for p1, p2, p3 and p4 locations.

3.16. Comparison of Peak Acceleration and Maximum Peak Pressure

The peak acceleration and maximum peak pressure measured for each model at a normalised drop height of 0.87±0.02 and a mass number of 0.29 is plotted in Figure 3.16.1. The maximum peak pressure measured is not necessarily the highest pressure experienced by the model due to the sparseness of the pressure transducer array and the localised nature of pressure effects. However these results do give an indication of a likely trend between peak acceleration and maximum peak pressure. While there is some general correlation the peak acceleration and maximum peak pressure experienced by a model are not even approximately in a fixed ratio. For example if model J1 and J2 are compared, model J2 experiences a significantly higher peak acceleration than model J1, but only a slightly higher maximum peak pressure. This observation is of interest because it indicates that a geometry maybe contrived which experiences both relatively low peak accelerations and relatively low peak pressures.

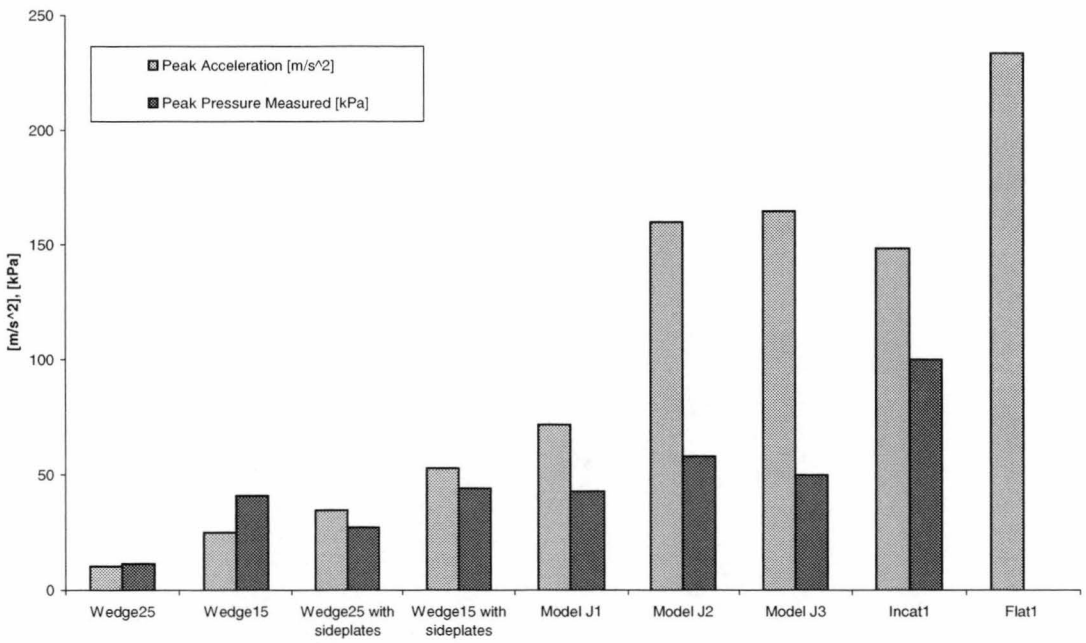

Figure 3.16.1 Peak acceleration and measured peak pressure. (Mass Number=0.29, Normalised Drop Height=0.87+/-0.02)

3.17. Velocity Ratios

The velocity ratio for all models as a function of normalised drop height is plotted in Figure 3.17.1 and Figure 3.17.2 for mass numbers of 0.29 and 0.58 respectively. The velocity ratio, defined in Table 3.6.1, is the ratio of the model velocity at the time corresponding to peak acceleration to the initial impact velocity. The velocity ratio is a measure of the impulse experienced by the model during the period from initial impact to the time of peak acceleration. The trend in velocity ratio is to decrease with increasing normalised drop height for all geometries. This is in part a consequence of the lower initial velocities of the model at lower normalised drop heights. Examination of the two velocity ratio graphs reveals that the velocity ratio increases with mass number, and that models which share similar geometric characteristics display similar trends in velocity ratio. The wedge15 with sideplates and wedge25 with sideplates models have almost identical velocity ratios for a given mass number and normalised drop height. The 15° wedge and 25° wedge results have the same shape however the 25° wedge velocity ratios are greater. The results for models J1, J2, and J3 all display a similar form. The results for J1 and J2 are almost identical for both mass numbers. The velocity ratios for J3 are greater at a mass number of 0.29 over all normalised drop heights compared with models J1 and J2, but at mass number 0.58 model J3 displays similar velocity ratios as models J1 and J2.

Considering a full-scale vessel the impulse experienced during a wetdeck slam event will effect global vessel motions and also the structural whipping response. Both of these effects are complex and beyond the scope of this discussion. However, a centre bow design which experiences a lower impulse will in general induce lower structural whipping and the effect on global motions will also be less. Thus centre bow geometries that experience a lower impulse, equivalent to a lower velocity ratio, are preferable.

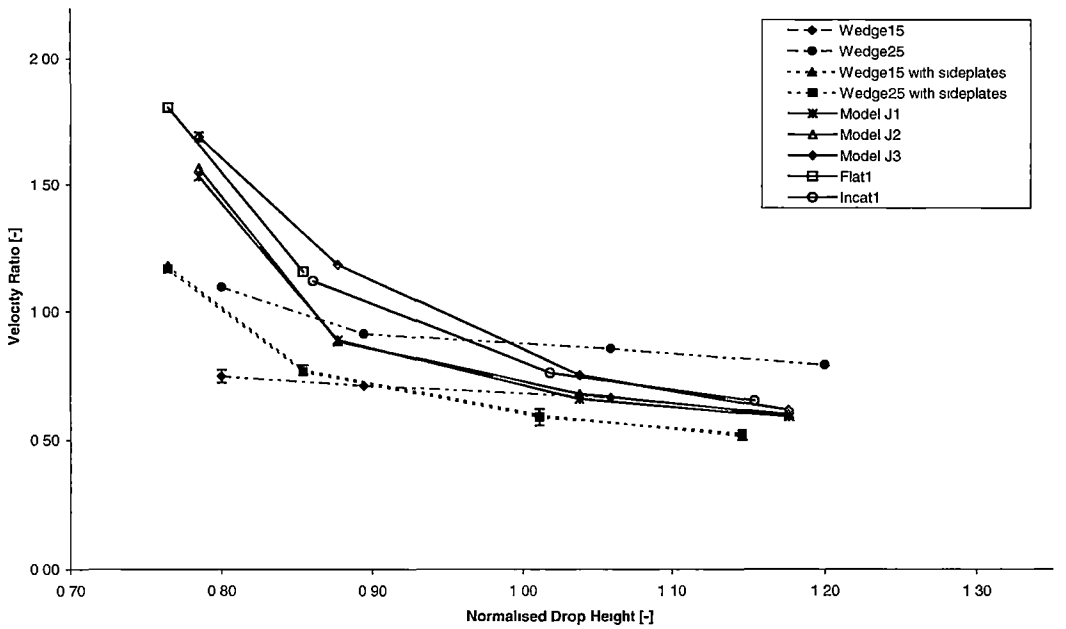

Figure 3.17.1 Velocity ratio for all models. Mass Number=0.29

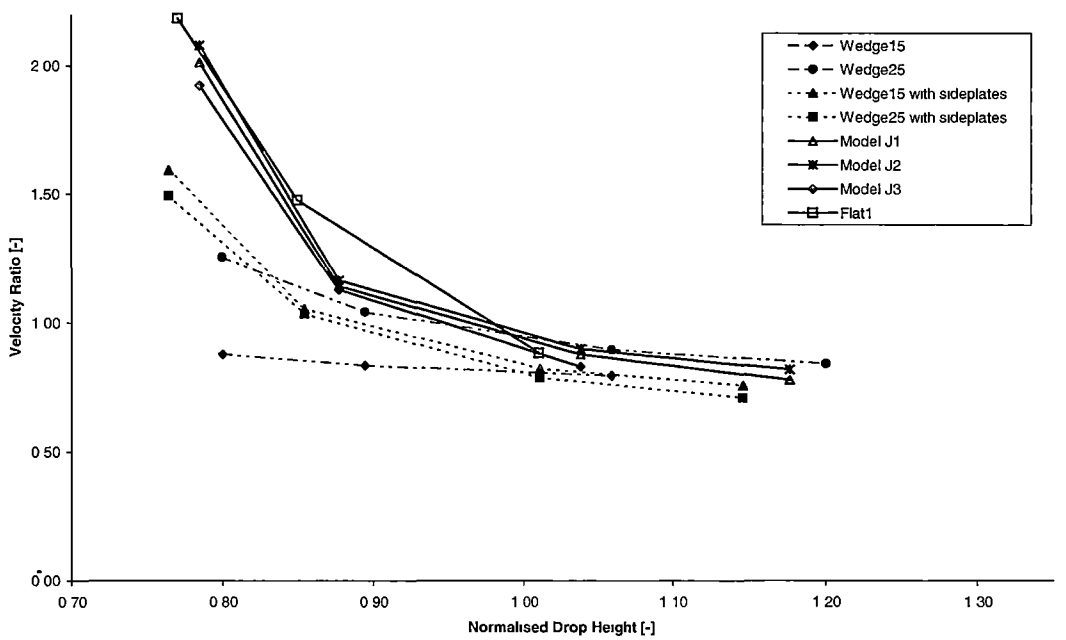

Figure 3.17.2 Velocity Ratio for all models (except Incat1). Mass Number=0.58

3.18. Penetration Number with Normalised Drop Height and Area Ratio

During the entry process of a model into water the water surface is deformed and fluid is piled up in the immediate vicinity of the model. It was observed in Section 3.8 (visualisation results) that the peak acceleration experienced by a model with arch geometry coincided with the complete filling of the arch void. The extent to which a particular model geometry deforms the water surface during entry will influence when the arch void completely fills with fluid and thus the penetration of the undisturbed free surface that a model will obtain before experiencing peak acceleration. This effect is quantified by the penetration number, the ratio of model displacement at time of peak acceleration divided by the vertical distance between the top of the arch and the demi-hull keel (B). The relationships between the penetration number, normalised drop height and area ratio are examined in this section.

Figure 3.18.1 and Figure 3.18.2 show the relationship between the penetration number and normalised drop height at mass numbers of 0.29 and 0.58 respectively for each of the models except the two simple wedges for which the penetration number is undefined due to the absence of an arch or equivalent. All results at a mass number of 0.29 display a simple linear trend that increases with normalised drop height, and for a mass number of 0.58 they also generally display an increasing trend with normalised drop height. The penetration number for each model at a given normalised drop height is generally in the same sequence as that for a mass number of 0.29. The exceptions are model J3 for a normalised drop height less than 0.85, and model wedge25 with sideplates, which has a penetration number slightly larger than model J1 for the same normalised drop height. For both mass numbers model Flat1 has a penetration number greater than 1.0, as does model J3 for normalised drop heights greater than 1.0 and mass number 0.58. This indicates that these models do not experience peak acceleration until the tops of their arches are beneath the initial water surface under the test conditions specified. All the other models have penetration numbers less than 1.0, indicating that the arch void is filled completely before the top of the arch has reached the initial water surface. However, all values are close to 1.0, indicating that the peak acceleration is related to the arch closure, as was also observed in Section 3.9 with respect to the acceleration time records. The early filling of the arch void is attributed to the piling up of water around the demi-hulls and centre bow. This effect is apparently less significant for models Flat1 and J3, both of which have either a fine centre bow (J3) or no centre bow (Flat1) and the arches of these models are flat-topped.

The relationships between penetration number and area ratio for mass numbers of 0.29 and 0.58 are plotted in Figure 3.18.3 and Figure 3.18.4 respectively. The area ratio is defined in Table 3.5.1, it is a geometric property of each model which quantifies the relative volume of arch void with respect to the sum of the volumes of the demi-hulls and centre bow. Models with low area ratio (for example model

Flat1, area ratio of 0.083) have fine demi-hulls and a small, or in this case no, centre bow and thus a large arch void. Models with a high area ratio have large centre bow and demi-hulls (for example model J1, area ratio of 0.404). Examination of Figure 3.18.3 and Figure 3.18.4 indicates that as the area ratio of the cross section increases the average penetration number (over a range of normalised drop heights) of the model decreases. The trend observed in both figures is clearly a linear decrease in penetration number with increasing area ratio. This is attributed to the piling up of water around the demi-hulls and centre bow, which of course must satisfy continuity, and hence this causes the arch void to fill more rapidly than would be the case if the pile up of water were not to occur.

The trend of penetration number to decrease with increasing area ratio indicates that at full-scale a catamaran with a voluminous centre bow will effectively experience a reduction in tunnel height compared with a catamaran with no centre bow and the same tunnel height. This is due to the increased area ratio of a given cross section resulting from the presence of the centre bow. Given the strong relationship between tunnel height and wetdeck slamming frequency, the presence of a centre bow may indeed increase wetdeck slamming frequency for a given seaway.

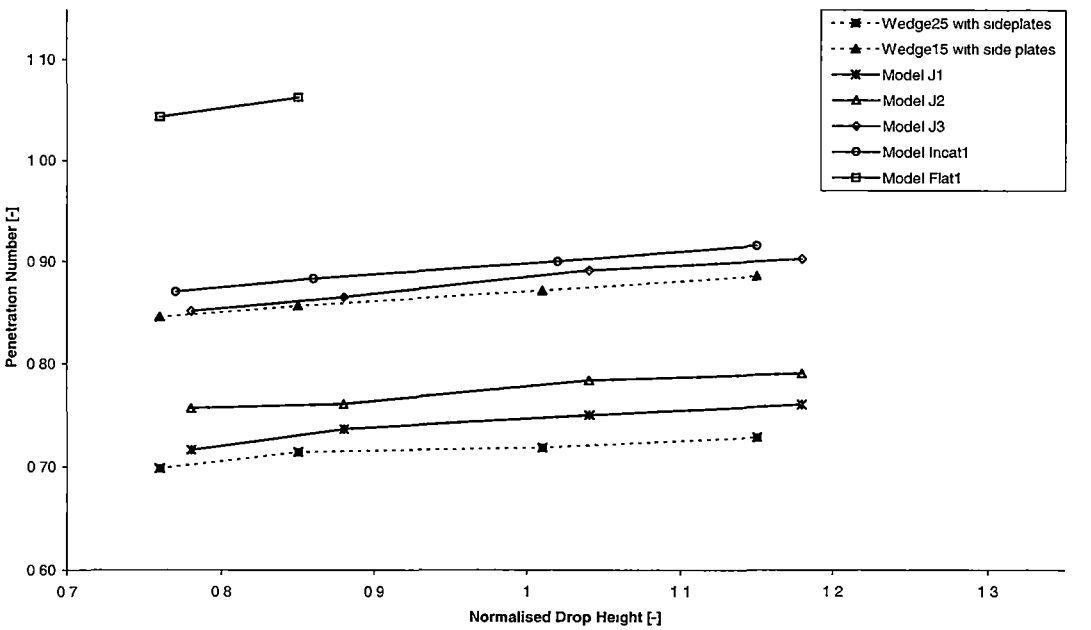

Figure 3.18.1 Penetration number against normalised drop height for all models. Mass Number=0.29

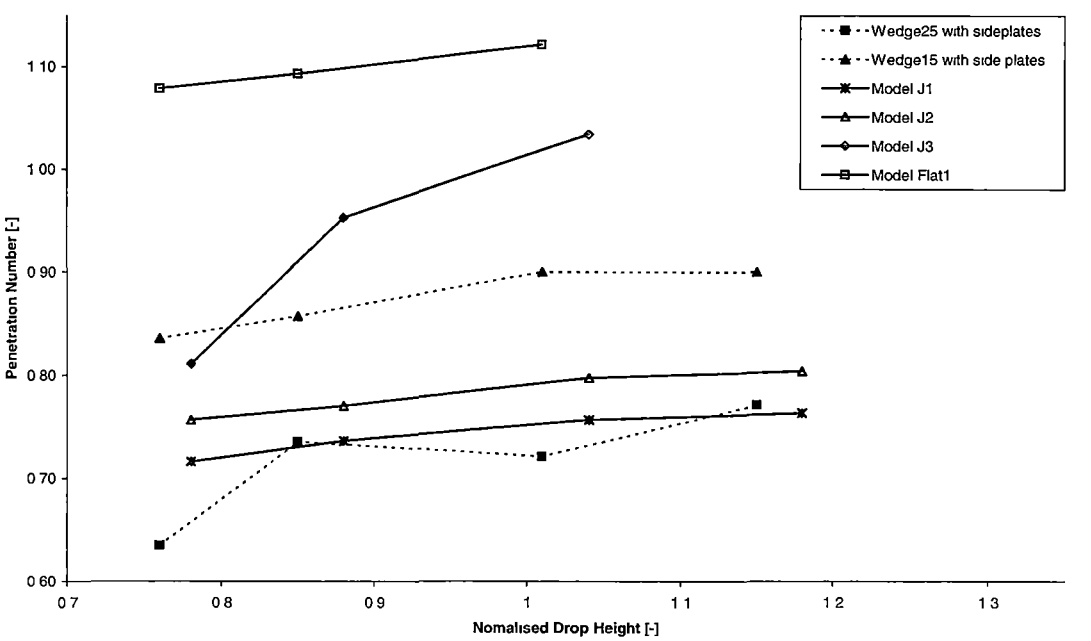

Figure 3.18.2 Penetration number against normalised drop height for all models (except Incat1). Mass Number=0.58

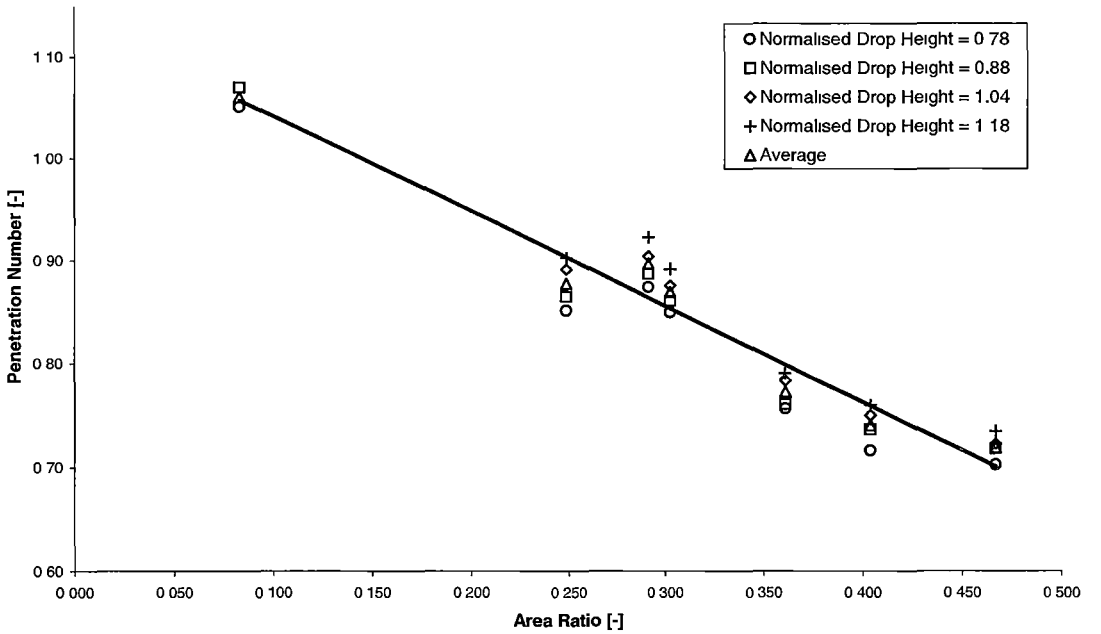

Figure 3.18.3 Penetration number against area ratio for Mass Number=0.29

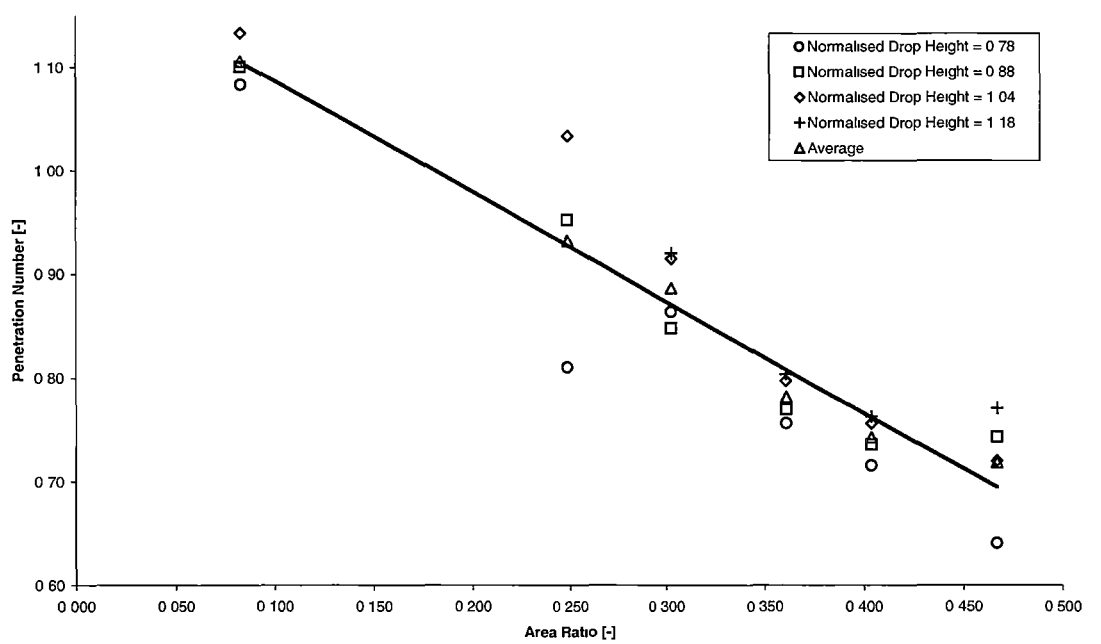

Figure 3.18.4 Penetration number against area ratio for Mass Number=0.58.

3.19. Importance of the Highest Point in Arch

The normalised peak acceleration experienced as a function of the distance that the highest point in the arch is from the centre line (χ) divided by half the model beam (0.5*L) is plotted in Figure 3.19.1 for various normalised drop heights and a mass number of 0.29 and 0.58. The normalisation process for each model is conducted by dividing the peak acceleration experienced by each model at a particular normalised drop height by the peak acceleration experienced by model J2 at the same normalised drop height. Results for models J3 and Flat1 cannot be plotted on this graph, as it is not possible to define the location of the highest point in the arch for these two models, as their arches are flat topped. Examination of Figure 3.19.1 reveals that as the highest point in the arch is displaced further from the centre line of the model the lower the normalised acceleration. If the results for model wedge25 with sideplates and model wegde15 with sideplates are examined, it is evident that despite having the same hight point in the arch location, model wedge15 with sideplates experiences on average a significantly higher normalised peak acceleration. This indicates geometric features other than the location of the highest point in the arch also effect the normalised peak acceleration.

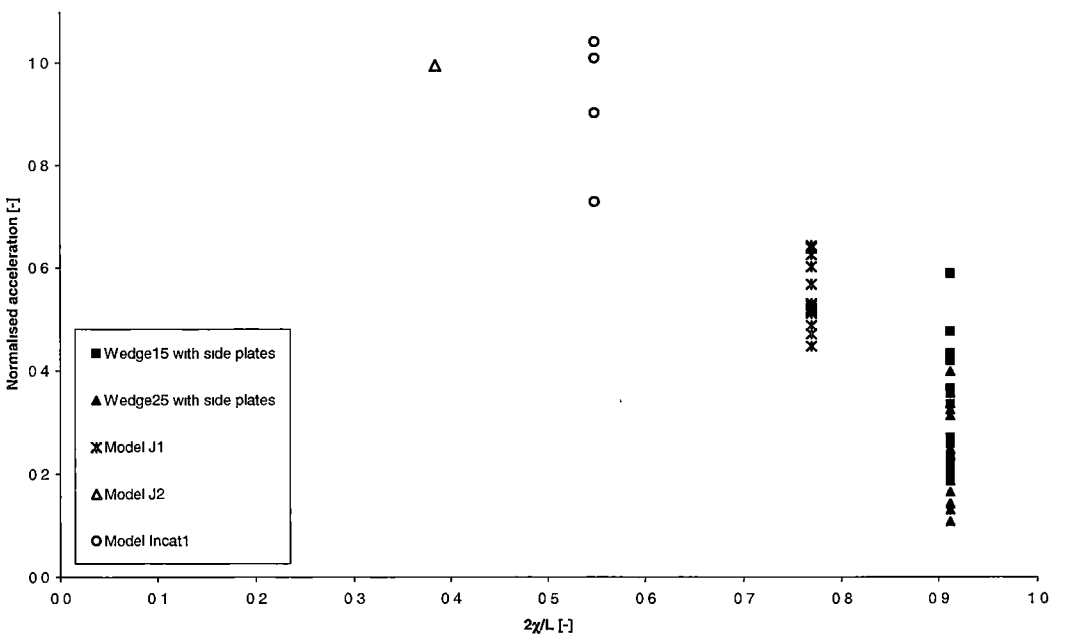

Figure 3.19.1 Effect of location of the highest point in arch on normalised peak acceleration.

3.20. Effect of Model End and Tank Wall Clearance

The three dimensional effects introduced into the two dimensional drop test experiments due to the clearance between the tank wall and the model end was investigated to ensure that this experimental parameter was not unduly influencing the experimental results. The model end tank wall clearance is quantified in terms of the normalised wall clearance (Table 3.5.1) and this was varied from 0.033 to 0.270 for model wedge15 with sideplates over a range of normalised drop heights. As shown in Figure 3.20.1 to Figure 3.20.3 only a very weak relationship exists between the normalised wall clearance and the peak acceleration for the range of normalised drop heights and mass numbers tested. However the scatter of the experimental peak accelerations data is generally significantly smaller at lower normalised wall clearances. And it seems that somewhat variable results would be obtained if large normalised wall clearances were used. As mentioned in Section 3.5 a normalised wall clearance of 0.033 was used in the experiments to minimise experimental scatter.

The limited variation of the normalised wall clearance with peak acceleration indicates that the viscous effects between the moving model end and the fixed tank wall side are not significant. Also the process by which air vents from the top of the arch void does not seem to be strongly influenced by the normalised wall clearance over the test range. It would seem likely that observations of the effect of normalised wall clearance on peak acceleration for the model wedge15 with sideplates holds for pressure values and also arbitrary geometry.

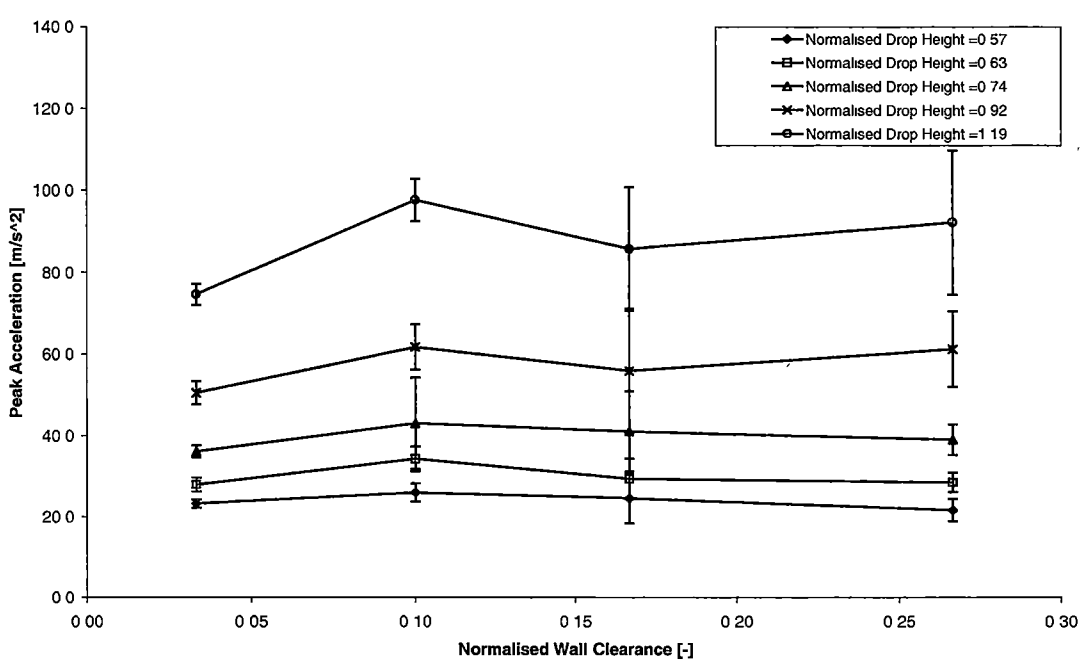

Figure 3.20.1 Model Wedge15 with sideplates. Mass Number=0.28

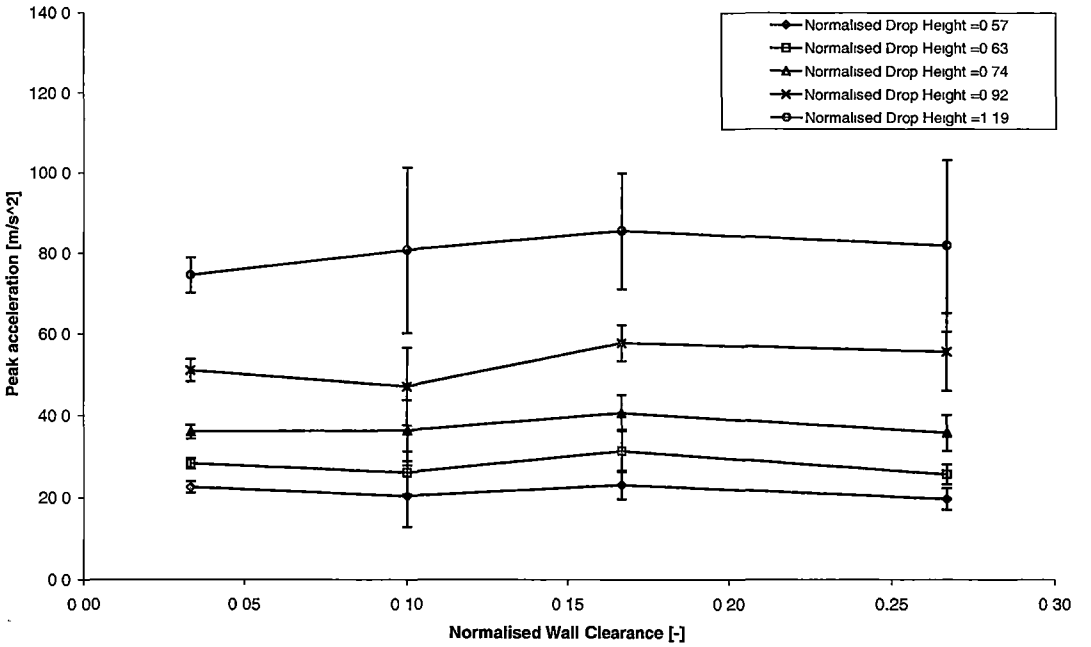

Figure 3.20.2 Model Wedge15 with sideplates. Mass Number=0.44

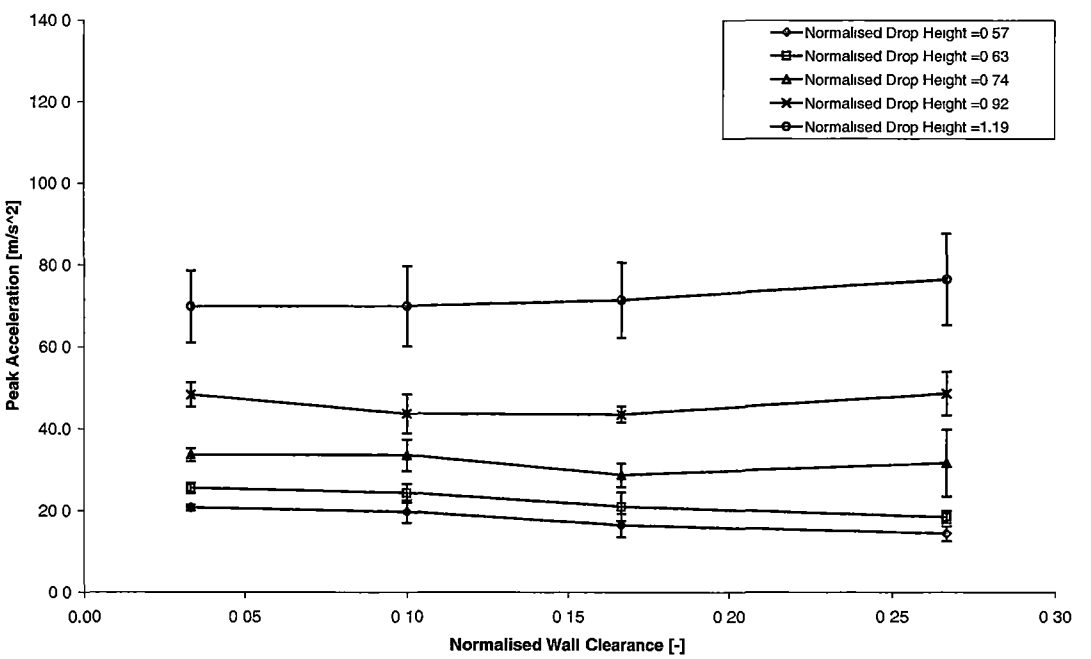

Figure 3.20.3 Model Wedge15 with sideplates. Mass Number=0.58

3.21. Scaling Peak Force to Full-Scale

The experimental program described in this chapter used scale models to investigate the effect hull cross section geometry had on slamming behaviour. Full-scale slam events experienced by INCAT vessel 050 (Chapter 2) were used to provide a basis for scaling the model tests. The scale model peak force results are scaled to full-scale using the scaling terms developed in Section 3.2 and are then compared with the slam load cases developed by Thomas et al (2001,2002a, 2003) for a particular slam event experienced by INCAT vessel 050. The particular slam event studied by Thomas et al (2001,2002a, 2003) was selected from the full-scale slam data set presented in Chapter 2.

To scale the experimental peak force to full-scale we require similarity of the force coefficient at model scale and full-scale.

$$C_{F\,\mathrm{fs}} = C_{F\,\mathrm{m}} \tag{3-19}$$

The results of this calculation are shown in Table 3.21.1 for mass number 0.29 and normalised drop height 0.87 which is appropriate for a typical slam event experienced on INCAT vessel 050.

Also shown in Table 3.21.1 are three slam load cases developed by Thomas et al (2001, 2002a, 2003). The three slam load cases developed by Thomas et al (2001, 2002a, 2003) were based on the most extreme slam event which was measured during the same trials of vessel 050 as detailed in chapter 2. This slam event was the most extreme recorded during the trials and caused some damage to the vessel and also displayed some asymmetry in structural loading. Thomas et al (2001) calculated a quasi-static load case for INCAT hull 050 by empirically matching the stress levels recorded during an extreme slam event with those produced when a static load was applied to a finite element model of the vessel. The loading applied to the finite element model was a cargo and fuel load, an underlying wave load and a symmetrical slam load of 15,700kN distributed over the centre bow and arch region between frames 52 and 69 (62.4m and 82.8m from the transom). Thomas et al (2002a) calculated a quasi-static load case for the extreme slam experienced by INCAT hull 050. The procedure used by et al (2002a) was similar to that used by Thomas et al (2001), however Thomas et al (2002a) modified the slam load component of the structural loading so that it was asymmetric. The load was distributed on the starboard side of the centre bow and archway. The magnitude of the quasi-static asymmetric slam load case was published as above 10,000kN. Thomas et al (2003) further refined the finite element method of calculating the extreme slam event load case by conducting a dynamic finite element analysis. The forces acting on the vessel structure in this calculation were buoyancy forces, a vertical inertial force equivalent to that determined from

the full-scale data and a time varying asymmetric slam load centred on the starboard side of the centre bow and arch way to account for the impact force. The slam load was distributed from frame 57 to frame 68 (68.4m to 81.6m from the transom). The slam load was calculated to be 10,055kN. Each of the three slam load cases developed was comparable with the load case calculated using the DNV design rules for global bending of the hull.

Scale Model Name or Slam Load Case	Force/m [kN/m]	Total Load [kN]
Wedge25	1,900	
Wedge15	4,200	
Wedge25 with sideplates	6,600	
Wedge15 with sideplates	9,600	
J1	12,100	
J2	27,000	
J3	27,700	
Incat1	24,600	
Flat1	38,700	
Quasi-static symmetric load case	1,350	15,700
Quasi-static Asymmetric load case	2,800+	10,000+
Dynamic Asymmetric load case	2,500	10,055

Table 3.21.1 Scaled peak loads and slam load cases for INCAT vessel 050

The loads developed from the scale model tests are given as loads per metre, whereas the loads calculated by Thomas et al (2001, 2002a, 2003) are total loads which are determined by integrating the distributed slam load applied to a number of frames in the bow of the vessel. To allow a better comparison of loads developed by Thomas et al with experimental loads, the loads developed by Thomas et al are converted to a loads per metre. This is done by calculating, from the distributed slam loads used by Thomas et al, the slam load that is applied to each individual frame. The slam load as calculated for each individual frame, which is the greatest in magnitude, is then used to calculate a slam load per unit metre for comparison with the scale model tests. The loads calculated for the two asymmetric loads are multiplied by two so as to be comparable with the symmetric drop test experiments. This was considered the most appropriate basis for comparison with the loads developed by Thomas et al as the scale model drop tests represent a situation in which the wetdeck of the model is extremely well aligned with the water surface during impact. When the loads of Thomas et al and the model drop tests are compared it is observed that the model test loads are approximately 10 times greater than the loads calculated by Thomas et al. However, in each paper by Thomas et al the basis for the form of the distributed slam load that was used is not discussed. Nor was the uniqueness of the form of the distributions proven. Also a sensitivity analysis of the effect of changing the form of the distributed slam load is not presented. Indeed it is the case that form of the slam load varies markedly

between the three slam load cases presented (quasi-static symmetric load case, quasi-static asymmetric load case and dynamic asymmetric load case). Hence although it is the case that the peak stresses experienced by the vessel during slamming agree well with those calculated by Thomas et al, it is not possible to conclude from the work of Thomas et al whether a different slam load distribution, in which the greatest load experienced by a particular frame where of a different magnitude would allow better correlation with full-scale slam stresses.

Scaling of the force values obtained in the model tests to full-scale yield results that are considerably greater than those calculated by Thomas et al (2001, 2002a, 2003). This is because the model slam events represent an extreme case slam in which the water surface is perfectly aligned with the model cross structure. At full-scale this does not occur because the sea surface is rough on a length scale similar to that of the vessel. The vessel also experiences ship motions that cause its alignment with the water surface not to be parallel. Thus the full-scale slam events such as full arch closure with constrained or no venting of the void beneath the arch occur in practice rarely. However, extreme slam events do occur at full-scale and thus the model results are of value for comparative purposes and should provide an upper bound of slam force predictions.

3.22. Summary

The effect of hull cross section on the slamming behaviour of catamarans with a centre bow was experimentally investigated with two-dimensional scale model drop tests. Nine scale models where tested, seven catamaran with centre bow models and two vee-wedge geometries. Model scaling was based on a typical slam event experienced by INCAT vessel 050, a 96m wave piercing catamaran fitted with a centre bow during commercial operations in the Cook Strait New Zealand. Transient pressure and acceleration measurements were made. Flow visualisation was also conducted.

It was found that the accelerations and pressures experienced by the drop test models were significantly effected by model geometry. The simple vee-wedge models experienced substantially lower peak accelerations than the catamaran with centre bow geometries. For all catamaran geometries the peak acceleration coincided with the complete filling of the arch void with fluid. The surface pressure time records measured on the catamaran models generally displayed two pressure spikes during entry. The first pressure occurred when the pressure transducers initially came into contact with the water and the second pressure spike occurred when the arch void completely filled with fluid. The peak pressures recorded near the top of the arch were greater than those recorded on the lower portion of the centre bow. The magnitude of the second pressure spike (associated with the complete filling of the arch void) was significantly greater than the magnitude of the first pressure spike (associated with initial water contact) for all models except the two wedge models with sideplates. The pressure transients recorded on the two simple wedge models display a single pressure spike associated with the initial contact of the transducer with water.

The peak accelerations of the of the vee wedge models with and without sideplates and the catamaran model with flat cross structure were found to increase monotonically with normalised drop height. The peak accelerations of the J-series models and the INCAT model were found to initially decrease with normalised drop height before increasing with normalised drop height. The peak pressures displayed the same trends as for the peak acceleration for all models. The non-monotonic nature of the J-series and INCAT model peak acceleration with normalised drop height was investigated with flow visualisation. These non-monotonic trends were attributed to variation with normalised drop height in the detail of the flow during the final stages of the complete filling of the arch void with fluid. The relationship between the peak acceleration and the maximum peak pressure measured on a model surface was examined and it was found that there was only a very general trend of maximum peak pressure to increase with peak acceleration.

The effects of three gross geometric features of the catamaran with centre bow models were investigated. Firstly the effect the location of the highest point in the arch on peak acceleration was examined. It was found that the models with the highest point in the arch displaced far from the centre line of the model experienced significantly lower peak accelerations than those models with

this point located near the centre line of the model. Secondly the effect of the relative volume of the centre bow was examined. It was found that models with voluminous centre bows experienced peak acceleration at a lower relative penetration of the initial water surface than models with small or no centre bows. This effect was attributed to the piling up of the water around the centre bow and the demi-hulls during the entry process. Thirdly the effect of the necessary clearance between the tank wall and the model end was also investigated and found not to be significant.

The experimental acceleration results were scaled to full-scale and compared with load cases developed by Thomas et al (2001, 2002a, 2003) for INCAT vessel 050. It was found loads determined by Thomas et al (2001, 2002a, 2003) were much lower than those scaled from two dimensional model experiment. This was attributed to the extreme nature of the drop test entry event and also the inherent dissimilarity of a drop test compared with a full-scale ship slam event. The two-dimensional constraint and precise alignment of the test model relative to the smooth test water surface seems to be the main cause of the very high loads occurring in the model tests. This is of particular relevance to methods used to predict slam loads based on two-dimensional computations. Such computations are likely to severely over estimate slam loads as has been found to be the case (DNV, confidential consulting report for INCAT Tasmania, December 2003). Thus results are of most value for comparative purposes when considering the effect of different hull cross section geometry on slamming behaviour.

4. Slamming by Added Mass Theory

4.1. Overview

A method for calculating the acceleration of a symmetrical two-dimensional catamaran cross section with centre bow hull section entering an infinite expanse of initially calm water has been developed. The model is based on conservation of linear momentum and utilises the added mass assumption of von Karman (1929) with a correction term for the pile up of water around the hull section during impact. A secondary theory is developed for the special case of the arch closure event experienced when a catamaran with centre bow hull section penetrates the water surface sufficiently deeply that the arch void completely fills with fluid. This theory was published by Whelan, Holloway, Davis and Roberts (2003).

Theoretical added mass and experimental results are compared for each of the nine model geometries detailed in chapter 3. For each model acceleration against time and free surface elevation records are presented, as also are peak acceleration and velocity ratio results as a function of normalised drop height. Theoretical penetration numbers are also calculated for each model and compared with experiment. It is found that the added mass theory captured the trends displayed in the experimental results.

A simplified added mass method is also used to demonstrate the importance of the highest point in the arch for catamaran with centre bow sections. An optimised low acceleration ogee geometry is also developed for a mono-hull cross section.

4.2. Modified Added Mass Theory

The two-dimensional entry of a catamaran with centre bow cross section was examined experimentally in Chapter 3. In the experiments it was observed that when a hull section with this catamaran geometry entered the water, the surrounding air had a negligible effect on the entry process during the initial stages of the entry. However, as the arch void filled with fluid an air bubble became trapped in the void at the top of the arch. The peak acceleration experienced by the catamaran models coincided with the complete filling of the arch void. This process is discussed in detail and illustrated with experimental visualisation results in Chapter 3. It seems apparent that the trapped compressible air bubble plays a significant role in determining the peak acceleration.

Due to the variation of the significance of the compressible air the during the impact of a catamaran geometry with water, a two-part theory is therefore used to model the entry process (Figure 4.2.1 and Figure 4.2.2). The initial entry of the catamaran geometry (pre-arch closure theory) is modelled by

considering the transfer of momentum between the model and the fluid due to added mass alone. The effects of compressible air are neglected. Once the arch void has filled sufficiently that an air bubble becomes trapped at the top of the arch a second theory is used (arch closure theory). In this second theory the transfer of momentum between the hull section and the fluid is due to added mass, a deficit added mass and a trapped compressible air bubble. The transition between the pre-arch closure theory and the arch closure theory is termed the onset of arch closure and a rational criterion is developed to determine when this occurs.

The modified added mass theory was developed for a catamaran with centre bow geometry, but this theory can also be used for monohull geometries if only the pre-arch closure theory is used and the terms associated with the demi-hulls are neglected. The theory can be used to model the entry of a catamaran with a flat cross structure as well.

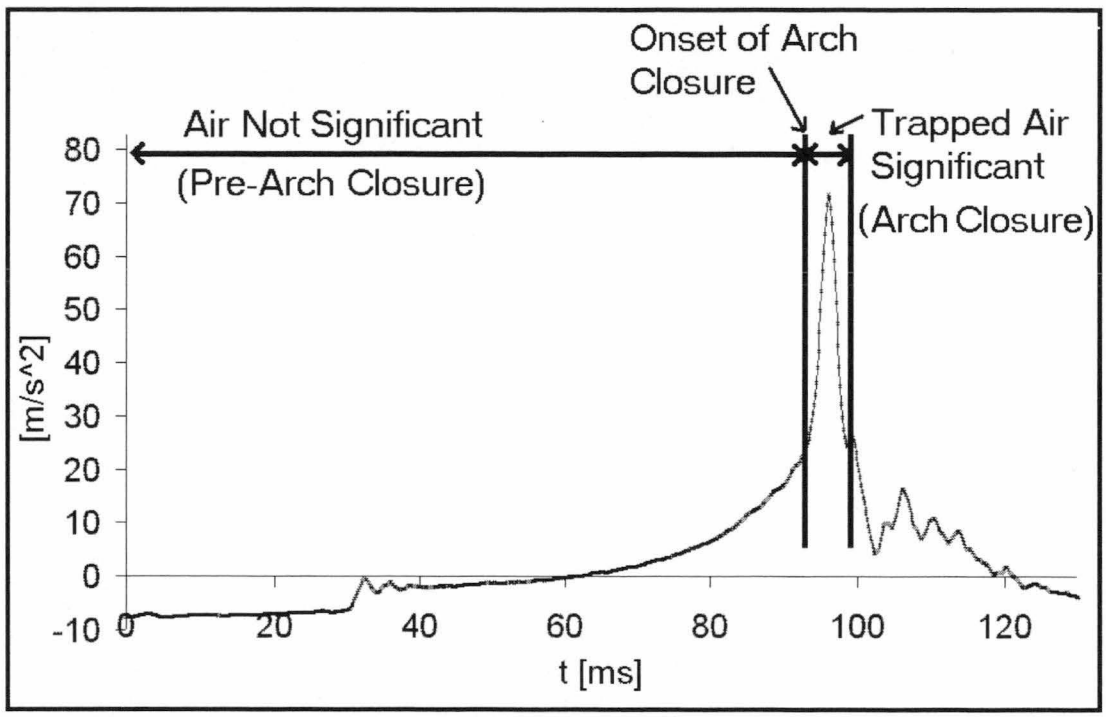

Figure 4.2.1 Acceleration time record for model J1 showing the time period when the trapped air is significant. (Mass Number=0.29, Normalised Drop Height=0.88).

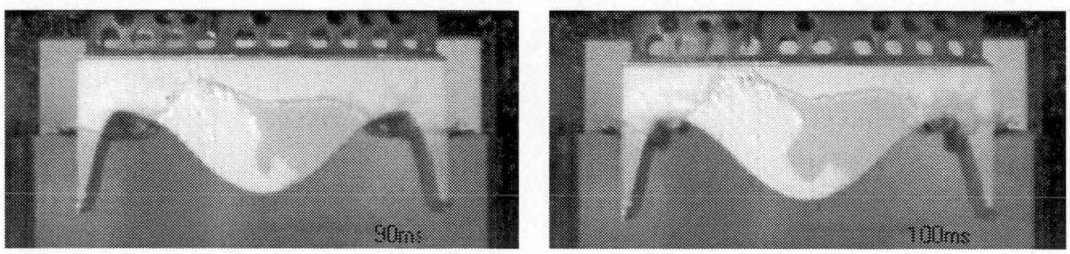

Figure 4.2.2 Visualisation results for model J1 at t = 90ms and t = 100ms. Trapped air can be observed at the top of the arch. Visualisation results correspond to acceleration time record shown in Figure 4.2.1. (Mass Number=0.29, Normalised Drop Height=0.88).

4.3. Pre-Arch Closure Theory

The acceleration as a function of time for a two-dimensional catamaran with centre bow hull section during the pre-arch closure stage of impact is modelled.

4.3.1. Pre-Arch Closure Equations of Motion

The vertical linear momentum (L_m) of the system is assumed to be conserved and the exchange of momentum between the hull and the fluid is modelled using the added mass concept. Here the "system" consists of the solid model mass and a variable quantity of surrounding fluid (the added mass) which if moving at the same speed as the model has equivalent momentum to the actual fluid. Thus

$$\frac{dL_m}{dt} = \Sigma F_m , \tag{4-1}$$

which expands to

$$\dot{m}_a \dot{y} + m_a \ddot{y} + m_m \ddot{y} = F_B + F_G + F_F , \tag{4-2}$$

where m_m is the hull section mass per unit length, m_a the added mass of the hull section per unit length, F_B, F_G and F_F the buoyancy, gravitational and frictional force per unit length acting on the hull section and y is the hull section displacement. The frictional force is that force which results from the rolling friction in the bearings. The gravitational and buoyancy forces acting on the added mass will of course cancel and the viscous frictional forces are assumed negligible. Equation 4-2 was integrated numerically. If y, $\dot{y}$, $\ddot{y}$ and the free surface elevation are known at t_{k-1}, the values of y_k and $\dot{y}_k$ can be calculated with a Taylor series expansion about the $k-1$ time step

$$\begin{aligned} y_k &= y_{k-1} + \dot{y}_{k-1}\Delta t + \tfrac{1}{2}\ddot{y}_{k-1}\Delta t^2 \\ \dot{y}_k &= \dot{y}_{k-1} + \ddot{y}_{k-1}\Delta t \end{aligned} \tag{4-3}$$

The free surface elevation at t_k can thus be computed as in section 4.5 and this allows the calculation of the buoyancy force ($F_{Bk} = -g\rho A_{vk}$) from the submerged hull section volume per unit length. The gravitational force ($F_G = m_m g$) and the frictional force (F_F = Constant) are constant and thus all the terms on the right hand side of equation 4-2 are known. The frictional force always acts so as to oppose the model velocity.

The added mass per unit length (m_a) of the hulls at t_k is the sum of the added mass associated with the centre bow and the added mass associated with each of the demi-hulls. In each case the added mass was assumed to be the mass of a half circle of water with a diameter equal to the wetted width of either the centre bow or the demi-hulls as appropriate. The added mass assumption is based on the solution for a flat plate impacting water developed by von Karman (1929), with a correction for the wetted width due to the pile up of water as proposed by Bisplinghoff and Doherty (1952). The von Karman assumption was based on the potential solution for a single flat plate in an infinite flow field.

In this case there are effectively three separate flat plates impacting with the flow field, which are assumed not to interact. The geometric width of these three flat plates, one associated with the centre bow of width $2C_1$ (Figure 4.3.1) and one associated with each of the demi-hulls both of width $C_3 - C_2$ (Figure 4.3.1), are calculated by finding the intersection points between an estimate of the free surface (section 4.5) and the hull cross section outline. C_1 is the distance from the centre line of the hull section to the intersection point between the centre bow and the free surface. C_2 is the distance from the hull section centre line to the intersection between the free surface and the inside of the demi-hull. C_3 is the distance from the centre line of the hull section to the intersection point between the outside of the demi-hull and the free surface. As the hull section enters the water and the water surface deforms, as discussed in section 4.5, the values of $2C_1$ and $(C_3 - C_2)$ will increase as more of the centre bow and the demi-hulls become submerged beneath the water surface. The total added mass per unit length at time t_k is

$$m_{ak} = \rho \frac{\pi}{2}\left(C_{1k}^2 + 2\left(\frac{C_{3k} - C_{2k}}{2} \right)^2 \right). \tag{4-4}$$

The time rate of change of the added mass per unit length was calculated using a first order asymmetric finite difference expression

$$\dot{m}_{ak} = \frac{m_{ak} - m_{ak-1}}{\Delta t}. \tag{4-5}$$

Rearranging equation 4-2 and substituting yields an expression for $\ddot{y}_k$

$$\ddot{y}_k = \frac{F_{Bk} + F_F + F_G - \dot{m}_{ak}\dot{y}_k}{m_m + m_{ak}}. \tag{4-6}$$

All terms are now computed at time step k and thus the acceleration as a function of time of the hull section can be solved for the pre-arch closure stage of the entry process using an explicit time stepping numeric scheme as discussed above.

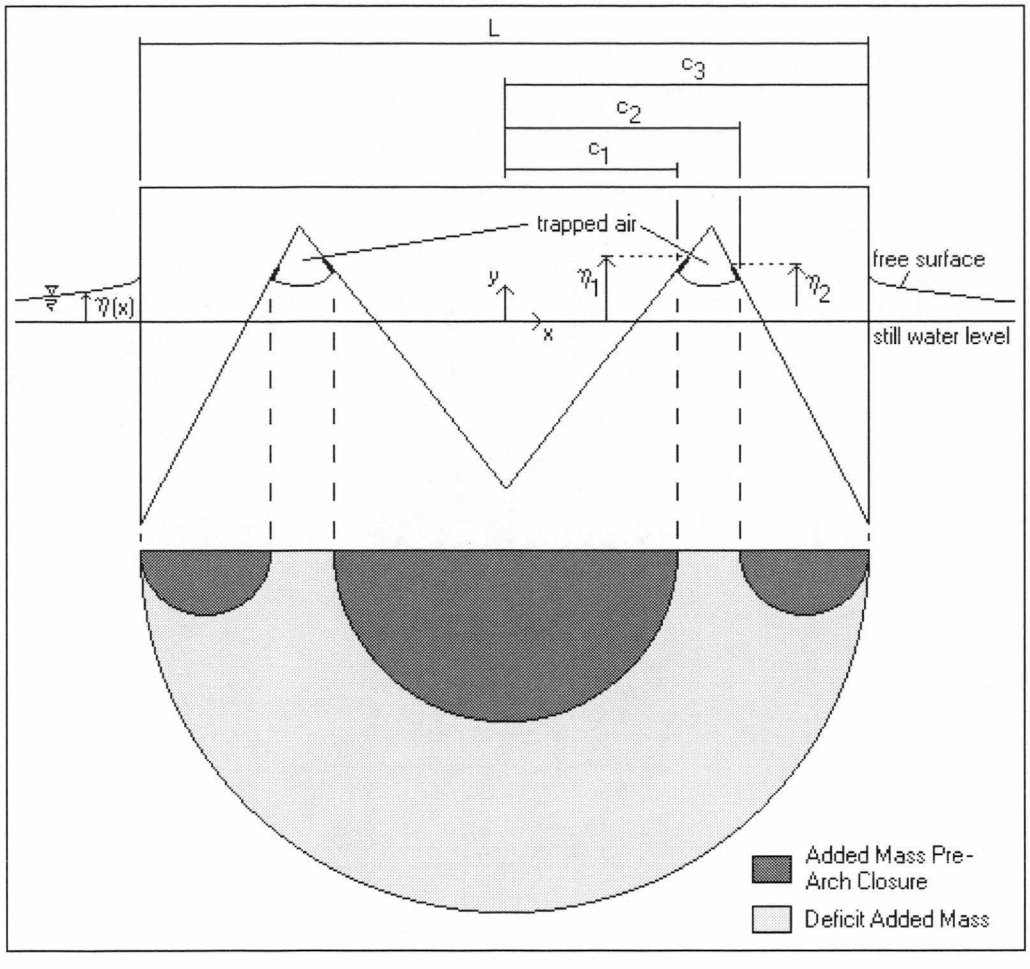

Figure 4.3.1 Added mass, deficit added mass, wetted widths and free surface location definitions

4.4. Arch Closure Process Theory

Once the hull section has penetrated the water sufficiently a wetdeck slam or arch closure event will occur. During this event the added mass associated with the model was assumed to change from the sum of three added mass terms associated with the two demi-hulls and the centre bow to a single larger added mass term with a diameter L. This step change in added mass produced an infinite $\dot{m}_a$ in equation 4-2, which was relieved by considering the trapped air at the top of the arch as a spring (or column of compressible air) with a freely moving mass at each end (Figure 4.4.1). At one end of the air column spring is a mass made up of the model mass and the added mass. At the other end of the air column spring is the deficit added mass. The deficit added mass is the added mass associated with a flat plate of width L minus the added mass associated with the centre bow and the demi-hulls (Figure 4.3.1).

As mentioned previously, the transition between the pre-arch closure theory and the arch closure theory is termed the onset of arch closure. The condition for the onset of arch closure to occur is described in Section 4.5.4.

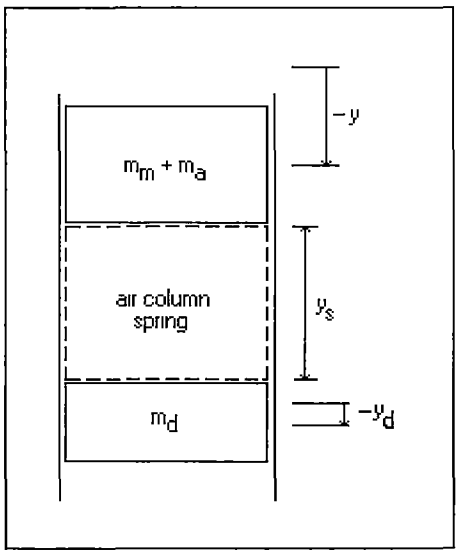

Figure 4.4.1 Air column spring for arch closure theory.

4.4.1. Arch Closure Equations of Motion

The acceleration of the hull section during arch closure was calculated from the conservation of the linear momentum of the pre-arch closure system (model and pre-arch closure added mass) (L_m) and the deficit added mass (L_d),

$$\frac{dL_m}{dt} = \Sigma F_m$$
$$\frac{dL_d}{dt} = \Sigma F_d \qquad (4\text{-}7)$$

The equation in L_m is expanded as in Section 4.3.1 with a force component added due to force exerted by the air column spring (F_S) on the hull section,

$$\dot{m}_a \dot{y} + m_a \ddot{y} + m_m \ddot{y} = F_B + F_G + F_F + F_S \qquad (4\text{-}8)$$

The equation in L_d is also similarly expanded to become

$$\dot{m}_d \dot{y}_d + m_d \ddot{y}_d = -F_S . \qquad (4\text{-}9)$$

The only force acting on the deficit added mass is the air column spring force (F_S) since its gravitational and buoyancy forces cancel. Viscous effects were assumed to be negligible and their inclusion would be inconsistent with the application of the expanding flat plate analogy for the added mass.

Equation 4-8 was numerically solved in precisely the same manner as equation 4-2 (pre-arch closure equation of motion) with two exceptions. Firstly the wetted widths of the demi-hulls and the centre bow, and hence the added mass, were calculated differently as described in the following paragraph.

Secondly, the air column spring force due to the trapped air needed to be calculated in equation 4-8, which was not required to be calculated in the solution of equation 4-2. The same time step (Δt) was used for both the pre-arch closure stage and arch closure stage of the entry process without any numeric difficulties.

The wetted widths of the centre bow and the demi-hulls, and hence m_a, were calculated in the pre-arch closure theory by considering the location of the intersection of the fluid surface and the hull section cross section (Figure 4.3.1). During the arch closure stage of the entry process the increased air pressure in the trapped air bubble causes the method used in the pre-arch closure theory to calculate the wetted widths to become inappropriate. This is because it neglects dynamics effects, takes no account of conservation of air mass nor does it take account of the substantial increase in pressure in the trapped air bubble which will influences the evolution of the free surface significantly. The wetted widths of the centre bow (C_1) and the demi-hulls ($(C_3 - C_2)$ and thus C_2 and C_3 individually) are instead assumed to be functions of the compression of the trapped air bubble and this is modelled by considering the compression of the notional air column spring. The values of C_2 and C_3 are calculated individually.

Consider first the calculation of C_1 and C_2. C_1 and C_2 are both assumed to be quadratic functions of the compressible air spring. That is, as the air spring compresses C_1 will increase (more of the centre bow becomes wet) and C_2 will decrease (more of the demi-hull becomes wet) and this increase in C_1 and decrease in C_2 are assumed to be quadratic functions of the compression of the air column spring. The quadratic functions for C_1 and C_2 each contain three unknowns which need to be found and thus three suitable constraints for each quadratic function are required to solve for the unknowns. For the quadratic function for C_1 and the quadratic function for C_2 the choice of two of the constraints is based on the experimental results. Examination of the experimental visualisation results (chapter 3) indicates that the arch void fills with fluid in a uniform, regular manner. That is, the arch void of the seven catamaran hull sections fill in a smooth continuous manner even when the air becomes trapped at the top of the arch void. A consequence of this is that the wetted width of the centre bow (C_1) and the two demi-hulls ($C_3 - C_2$), and hence C_2 must also vary in a continuous, smooth manner in the theoretical manner. This needs to be reflected in the theory and this is accomplished at the moment of onset of the arch closure process by ensuring that the $C_1(t)$ and $C_2(t)$ are continuous and that $dC_1(t)/dt$ and $dC_2(t)/dt$ are also continuous. The third constraint required to fully specify the two quadratic functions for C_1 and C_2 is found by determining a maximum value of C_1 and a minimum value of C_2 which maybe obtained in the limit as the length of the compressible air column spring approaches zero. The process used to determine the maximum value of C_1 and the minimum value of C_2 obtained was done by assuming that the ratio $(C_3 - C_2)/C_1$ at

the onset of the arch closure process was the same as the limit $\lim_{y_s \to 0} \frac{C_3(y_s) - C_2(y_s)}{C_1(y_s)}$ obtained as the length of the air spring column tends to zero. The two quadratic functions for C_1 and C_2 were written as functions of y^*_{sk}, the non-dimensional ratio of the initial air column height at the onset of arch closure (denoted by a subscript of O) less the air column spring height at the k time step divided by the initial air column height at the onset of the arch closure process. y^*_s is of course a function of time and thus $C_1(y^*_s)$ is equivalent to $C_1(t)$ and similarly $C_2(y^*_s)$ is equivalent to $C_2(t)$. Also the progressive wetting of the centre bow and the demi-hulls is influenced by the trapped air bubble at the top of the arch void and it is for this reason that C_1 and C_2 are written as functions of the air column height.

Considering now the development of the quadratic equations for C_1 and C_2. The equations are written as functions of y^*_{sk} where,

$$y^*_{sk} = \frac{y_{so} - y_{sk}}{y_{so}}.$$

The quadratic function for C_1 has the form

$$C_1 = A_1 y_s^{*2} + A_2 y^*_s + A_3,$$

with boundary conditions

$y^*_s = 0, C_1 = C_{1o}$, and hence $A_3 = C_{1o}$

$y^*_s = 0, \frac{dC_1}{dt} = \dot{C}_{1o}$, thus $\frac{dC_1}{dy^*} = \dot{C}_{1o} / \dot{y}^*_s$ and hence $A_2 = \frac{\dot{C}_{1o}}{\dot{y}^*_{so}}$

$y^*_s = 1, C_{1o} + \Delta C_1$, where $\Delta C_1 = C_1(y^*_s = 1) - C_1(y^*_s = 0)$.

Rearranging and applying boundary condition

$$\Delta C_1 = \frac{(C_{2o} - C_{1o})C_{1o}}{C_{1o} + C_{3o} - C_{2o}} \text{ thus } A_1 = \frac{C_{1o}(C_{2o} - C_{1o})}{C_{1o} + C_{3o} - C_{2o}} - \frac{\dot{C}_{1o}}{\dot{y}^*_{so}}$$

Similarly the quadratic function for $C2$ has the form

$$C_2 = B_1 y_s^{*2} + B_2 y^*_s + B_3$$

with boundary conditions

$y^*_s = 0, C_2 = C_{2o}$, and hence $B_3 = C_{2o}$

$y^*_s = 0, \frac{dC_2}{dt} = \dot{C}_{2o}$, thus $\frac{dC_2}{dy^*} = \dot{C}_{2o} / \dot{y}^*_s$ and hence $B_2 = \frac{\dot{C}_{2o}}{\dot{y}^*_{so}}$

$y^*_s = 1, C_{2o} + \Delta C_2$, where $\Delta C_2 = C_2(y^*_s = 1) - C_2(y^*_s = 0)$.

Rearranging and applying boundary condition

$$\Delta C_2 = \frac{(C_{2o} - C_{1o})C_{2o}}{C_{1o} + C_{3o} - C_{2o}} \text{ thus } B_1 = \frac{\dot{C}_{2o}}{\dot{y}^*_{so}} - \frac{C_{2o}(C_{2o} - C_{1o})}{C_{1o} + C_{3o} - C_{2o}}$$

Thus, substituting

$$C_{1k} = \left(\frac{C_{1o}(C_{2o} - C_{1o})}{C_{1o} + C_{3o} - C_{2o}} - \frac{\dot{C}_{1o}}{\dot{y}^*_{so}} \right) y^{*\,2}_{sk} + \frac{\dot{C}_{1o}}{\dot{y}^*_{so}} y^*_{sk} + C_{1o}$$

$$C_{2k} = \left(\frac{\dot{C}_{2o}}{\dot{y}^*_{so}} - \frac{C_{2o}(C_{2o} - C_{1o})}{C_{1o} + C_{3o} - C_{2o}} \right) y^{*\,2}_{sk} + \frac{\dot{C}_{2o}}{\dot{y}^*_{so}} y^*_{sk} + C_{2o} \qquad (4\text{-}10)$$

Thus the quadratic functions for C_1 and C_2 have been determined. For the hull sections tested C_3 was simply set equal to $L/2$ because the hull sections were wall sided.

The force acting on the hull section due to the compressible air spring was calculated with the following algorithm. First, the criterion discussed below in section 4.5.4 was used to identify the initial moment of the arch closure process. This criterion is based on an estimate of the upwash of the jet fronts. The initial conditions for the air spring (initial height, cross sectional area and mass of trapped air) were calculated based on the elevation of the free surface and the location of the model at the onset of arch closure process. The volume per unit length of trapped air ($\forall_{air}$) was equal to the volume enclosed between the water surface ($\eta(x)$) and the hull section outline ($h(x) + y_o$) at the onset of arch closure process. $h(x)$ is a function which describes the geometry of the hull section, defined so that the hull section is positioned in the first and second quadrants of a Cartesian plane, with the lowest part of the hull section defining $h = 0$. The position of the hull section at the onset of arch closure is y_o, thus

$$\forall_{air} = 2 \int_{x=C_1}^{x=C_2} h(x) + y_o - \eta(x) dx. \qquad (4\text{-}11)$$

The mass of the trapped air per unit length (m_{air}), in the air column spring was calculated with the ideal gas equation. Standard atmospheric conditions were assumed for this calculation. That is atmospheric temperature ($T_a = 20°C$), atmospheric pressure ($P_a = 101.325kPa$) and gas constant ($R = 0.287kJ/kgK$).

$$m_{air} = \frac{P_a \forall_{air}}{R T_a} \qquad (4\text{-}12)$$

The initial height of the air column spring (y_{so}) was set equal to the maximum vertical distance between the fluid surface and the hull section surface.

$$y_{so} = \max[h(x) + y_o - \eta(x)] \quad C_1 \le x \le C_2 \qquad (4\text{-}13)$$

The notional cross sectional area of the air column spring (A_s) which was assumed to remain constant throughout the computations, was determined by dividing the volume of trapped air by the initial height of the air column. The cross sectional area is of unit length.

$$A_s = \frac{\forall_{air}}{y_{so}}. \tag{4-14}$$

The force (F_S) that the air column spring exerts on the hull section and the deficit added mass is calculated from the gauge pressure in the air column spring times the cross sectional area of this spring. This pressure was calculated by assuming the compression of the air to be isentropic that is $P\forall^{\gamma} = \text{Constant}$, where γ is the isentropic index for air and γ is normally to be 1.4. It was assumed that the air column behaved like a spring with a freely moving piston at each end (Figure 4.4.1). It was also assumed that once the arch closure process had occurred the mass of air trapped remained constant.

$$F_S = \left(\frac{m_{air} R T_a \left(\frac{y_{so}}{y_{sk}} \right)^{\gamma-1}}{A_s(y_{sk})} - P_a \right) A_s \tag{4-15}$$

The new height of the air column at each time step was found by adding the change in y (the location of the hull section) and deducting the change in y_d (the position of the deficit added mass) to y_{sk-1}.

$$y_{sk} = y_{sk-1} + \left(\dot{y}_{k-1}\Delta t + \tfrac{1}{2}\ddot{y}_{k-1}\Delta t^2 \right) - \left(\dot{y}_{dk-1}\Delta t + \tfrac{1}{2}\ddot{y}_{dk-1}\Delta t^2 \right). \tag{4-16}$$

The deficit added mass does not of course have an actual position, as it is an abstract quantity determined by integrating over the flow field. However, because the arch closure process is modelled by considering the transfer of momentum between two notional masses connected by the air column spring as shown in Figure 4.4.1, it is thus appropriate to calculate the position of the added mass. This is done so as to be consistent with the model for the arch closure process. The deficit added mass position is then used in the calculation of the compression of the air column spring.

Rearranging equation 4-8 yields an expression for the hull vertical acceleration $\ddot{y}_k$

$$\ddot{y}_k = \frac{F_{Sk} + F_{Bk} + F_F + F_G - \dot{m}_{ak} y_k}{m_m + m_{ak}}. \tag{4-17}$$

Similarly, the acceleration of the deficit added mass during the arch closure process is obtained from equation 4-9 as

$$\ddot{y}_d = \frac{-F_S - \dot{m}_d \dot{y}_d}{m_d}. \tag{4-18}$$

The motion of the deficit added mass is required, as it is needed to calculate the air spring force acting on the hull section. The location and velocity of the deficit added mass at the k time step, y_{dk} and $\dot{y}_{dk}$, were calculated by using a Taylor series expansion about the (k-1) time step,

$$\begin{aligned} y_{dk} &= y_{dk-1} + \dot{y}_{dk-1}\Delta t + \tfrac{1}{2}\ddot{y}_{dk-1}\Delta t^2 \\ \dot{y}_{dk} &= \dot{y}_{dk-1} + \ddot{y}_{dk-1}\Delta t \end{aligned} \qquad (4\text{-}19)$$

The values of y_d and $\dot{y}_d$ at the onset of the arch closure process were both zero as it has been assumed that no force acts on the deficit added mass until the onset of arch closure.

The deficit added mass, m_{dk}, is calculated by subtracting the added mass associated with the hull section at time step k (m_{ak}) from the added mass that would be associated with the hull section where the arch void to completely fill with fluid ($L^2\pi\rho/8$), as shown in Figure 4.3.1.

$$m_{dk} = \frac{L^2\pi\rho}{8} - m_{ak} \qquad (4\text{-}20)$$

The time rate change of the deficit added mass is therefore,

$$\dot{m}_{dk} = -\dot{m}_{ak} \qquad (4\text{-}21)$$

where $\dot{m}_{ak}$ is given in equation 4.5.

All terms are now computed at time step k and thus the acceleration of the hull section as a function of time has been solved for the arch closure stage of the complete entry process.

4.5. Calculation of the Free Surface

When a hull section enters an initially calm body of water, fluid is displaced and piles up around the hull section. This deformation of the water surface causes the portion of the hull section submerged beneath the water surface to be greater than would be the case if the deformation of the free surface were to be neglected. The pile up of water around the hull section increases the amount of the added mass associated with the hull section, which is equivalent as saying the wetted width of the hull section is increased. Also the deformation of the free surface influences the rate at which the arch void fills with fluid for the catamaran hull sections. This in turn influences the penetration number required for a particular hull section for arch closure to occur.

The elevation of the free surface above the initial water level at some time after water impact was calculated by integrating in time the velocity distribution along the initial water surface level. This velocity distribution was induced by the hull section as it progressively became submerged in the

fluid. The flow regime around the hull section, and hence velocity distribution on the initial water level, was modelled by solving the potential function for flow about a symmetric double body at each time step. Symmetric double body flow allowed the no through flow boundary condition to be satisfied an the hull section surface and for the free surface boundary condition to be approximately satisfied by requiring $\phi = 0$ on the initial water surface level.

4.5.1. Potential Solution Method

At the k time step the hull section will be submerged beneath the initial water surface level by some amount y and have a velocity $\dot{y}$. The geometry of the submerged portion of the hull section is used to generate a two-dimensional symmetric double body (ie two perpendicular axes of symmetry).

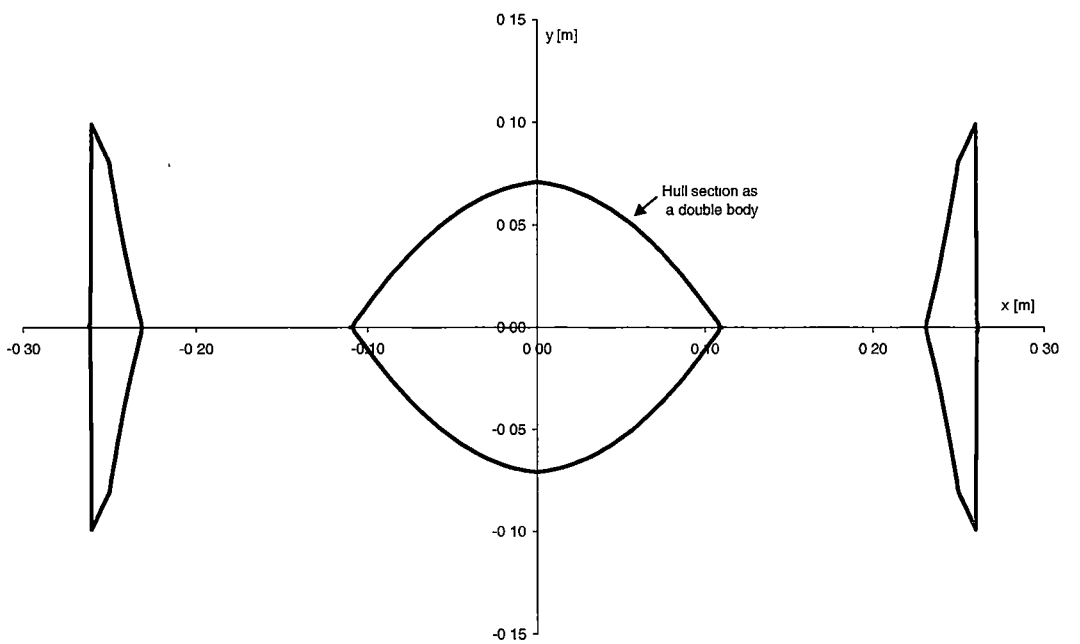

Figure 4.5.1 Two-dimensional symmetric double body (hull section J1).

The potential function for the flow around this double body was solved numerically using a boundary element method. The double body was held fixed in space and the fluid was made to flow around it at a far field velocity of $V_h = -\dot{y}$. The potential at (x, y) is the sum of a potential function for uniform flow with velocity V_h and a series of n basis functions

$$\phi(x, y) = V_h y + \sum_{J=1}^{J=n} \frac{\sigma_J}{2\pi} \phi_{ij} . \tag{4-22}$$

A desingularised simple source with three image sources to model the symmetry about the x and y axes was selected as the basis function, ϕ_{ij} (equation 4-24, Figure 4.5.2).

$$\phi_{ij} = \left(\ln|r_{ij1}| + \ln|r_{ij2}| - \ln|r_{ij3}| - \ln|r_{ij4}| \right) \tag{4-23}$$

where

$$
\begin{aligned}
r_{ij1} &= \left((x_i - x_j)^2 + (y_i - y_j)^2\right)^{1/2} \\
r_{ij2} &= \left((x_i + x_j)^2 + (y_i - y_j)^2\right)^{1/2} \\
r_{ij3} &= \left((x_i + x_j)^2 + (y_i + y_j)^2\right)^{1/2} \\
r_{ij4} &= \left((x_i - x_j)^2 + (y_i + y_j)^2\right)^{1/2}
\end{aligned}
\tag{4-24}
$$

The signs of terms in 4-23 ensures $\phi = 0$ on the horizontal axis $y = 0$ and $\partial\phi/\partial x = 0$ on the vertical axis $x = 0$ giving appropriate flow symmetry.

The desingularised source associated with each panel was positioned normal to the panel at a fixed proportion of the panel length (ΔS) from the centre of the panel (control point) and outside the fluid domain, thus

$$
\bar{x}_{s\,j=i} = \bar{x}_{c\,j=i} - \varpi \Delta S \hat{n}_i \tag{4-25}
$$

where $\bar{x} = x\hat{i} + y\hat{j}$. A desingularisation constant of $\varpi = 1.2$ was selected based on the work of Beck (1994). Beck (1994) noted that the accuracy and convergence of the solutions to the potential function were relative insensitive to the choice of desingularisation distance.

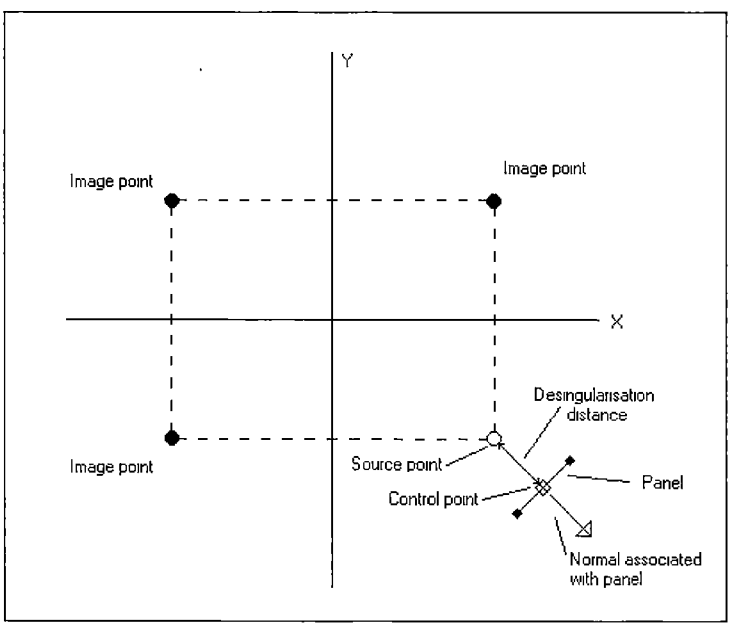

Figure 4.5.2 Diagram of a desingularised simple source boundary element.

At the i th control point on the hull section surface the no through flow boundary condition was satisfied

$$
\frac{\partial\phi(x,y)}{\partial\hat{n}_i} = \vec{V}_h \cdot \hat{n}_i + \sum_{j=1}^{j=n} \frac{\sigma_j}{2\pi} \frac{\partial\phi_{ij}}{\partial\hat{n}_i} = 0 . \tag{4-26}
$$

This boundary condition gave rise to a system of linear equations for the source strengths of the basis functions

$$\left[\frac{1}{2\pi}\frac{\partial\phi_{ij}}{\partial\hat{n}_i}\right]\{\sigma_j\}=\{-\vec{V}_h\cdot\hat{n}_i\}. \tag{4-27}$$

Solution for the unknown $\{\sigma_j\}$ in equation 4-27 allows ϕ to be obtained.

4.5.2. Grid Generation

The distribution of the boundary elements over the hull section surface was undertaken in the following manner. The right hand half of the hull section geometry is described by a function $h(x)$. To aid in the grid generation process $h(x)$ is divided into a number of smaller geometric functions. For example in the case of a catamaran with centre bow geometry $h(x)$ is divided into three smaller functions. $h(x)_1$ described the model geometry from the keel of the centre bow to the top of the arch. $h(x)_2$ was the model geometry from the top of the arch to the keel of the demi-hull and $h(x)_3$ was the model geometry from the keel of the demi-hull to the top of the outside of the demi-hull. At the k time step the hull section will be submerged beneath the initial water surface by some amount y. Consequently only a portion of $h(x)_1$, $h(x)_2$ and $h(x)_3$ will be wet and thus require gridding. If $h(x)_1$ is considered as an example ($h(x)_2$ and $h(x)_3$ are treated in precisely the same manner). A series of contiguous linear panels of variable length is distributed along the submerged portion of $h(x)_1$. This is done by calculating the length of $h(x)_1$ submerged beneath the initial water surface (S_1). The submerged portion of $h(x)_1$ is then dividend into n_1 panels of variable length, with the i th panel having length

$$\Delta S_{1_i} = w_{1_i} S_1 \tag{4-28}$$

where

$$w_{1_i} = \frac{\Psi^2}{n}\left(\sqrt{1-\left(\frac{2i}{n}-1\right)^2}+\sqrt{1-\left(\frac{2(i-1)}{n}-1\right)^2}\right). \tag{4-29}$$

and

$$\Psi = \sqrt{2/\pi} \tag{4-30}$$

This grid generation algorithm creates panels on $h(x)_1$, which are shorter at the keel of the centre hull and at the intersection of the centre bow with the free surface, and longer in the middle of the wetted part of $h(x)_1$ (Figure 4.5.3). This algorithm may also be applied to $h(x)_2$ and $h(x)_3$ to allow gridding of the demi-hull. It was desirable to distribute the panels in this manner as it allows a good numeric solution of the potential function to be found, particularly where the keel is pointed, or the

hull side is not vertical where it intersects the free surface as these situations give rise to a steep gradient of ϕ, requiring a denser distribution of ϕ_{ij}

Two additional panels were located at the keel of the centre bow and the keel of the demi-hull. The normal associated with each of these panels was $\hat{n} = 0\hat{i} - 1\hat{j}$ and the desingularised distance was set equal to the desingularised distance of the nearest adjacent panel. These two additional panels ensured that the no through flow boundary condition was correctly satisfied at these points.

The source and control points are located in the 4th quadrant of the x-y plane. The three image points associated with each source are of course located in the 1st, 2nd and 3rd quadrants. The desingularisation offset procedure described above occasionally incorrectly places a source in either the 1st or 3rd quadrant. These sources need to be moved so that they are correctly placed in the 4th quadrant. If a source is incorrectly located in the 1st quadrant then it is relocated along the same normal halfway towards the x axis from its corresponding control point (ie by reducing ϖ). A source incorrectly located in the 3rd quadrant is relocated similarly half way towards the y axis.

An example of a grid generated using the above procedure is shown in Figure 4.5.3.

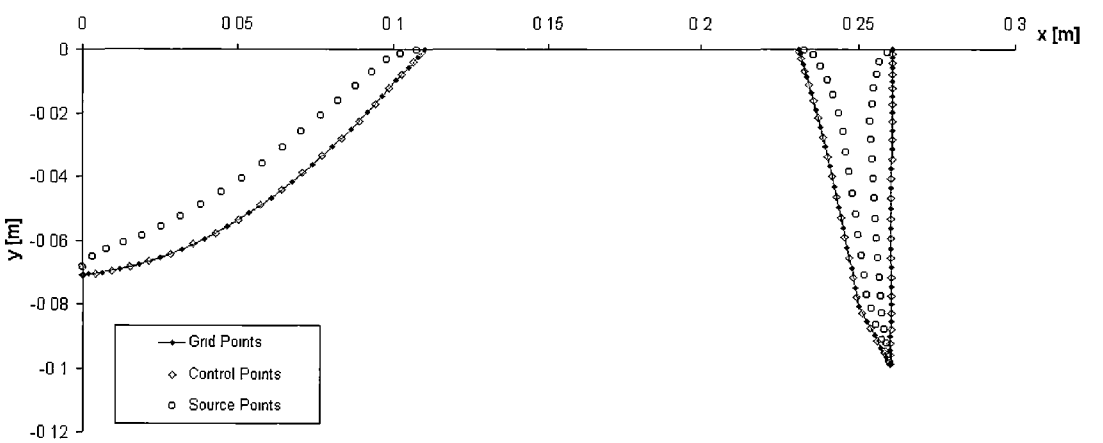

Figure 4.5.3 An example grid. Grid is for hull section J1 with y = -0.10m

4.5.3. Free Surface Elevation

The elevation of the free surface above the initial water surface level at time step k was calculated by numerically integrating in time the vertical velocity distribution along the initial water surface level. The velocity distribution at time step k was found from the solution of the potential function for flow about the hull section at each time step, thus

$$\eta(x,t) = \int_0^t \frac{\partial \phi(x,0)}{\partial y} dt, \quad C_1 \le x \le C_2, x \ge C_3 \tag{4-31}$$

Separation and dynamic effects were neglected, as too were effects due to variation in surface air pressure.

4.5.4. The Condition for the Onset of the Arch Closure Process

The entry of a catamaran with centre bow is modelled as a two-part theoretical entry process; pre-arch closure theory and then arch closure process theory. Three criteria are presented below for the transition from the pre-arch closure theory to the arch closure theory. It is assumed that the onset of arch closure is when the water surface deforms in such a manner to effectively terminate the venting of air from the arch cavity. When the air becomes trapped at the top of the arch it will begin to increase in pressure due to the relative motions of the free surface and hull section. This will cause an increase in the pressure applied to the free surface by the air pressure in this region of the flow. For the purposes of modelling the arch closure process it was assumed that the change in the boundary condition caused by the increase in pressure caused the deficit added mass to begin accelerating and this was independent of the acceleration of the added mass. It was assumed that the jets originating from the centre bow and the inside of the demi-hulls was the flow feature that dominated when the arch cavity ceased venting air and thus caused increase in air pressure. The elevation or upwash of the jet fronts above the initial water surface level was estimated by applying equation 4-31 at the intersection of the hull cross section with the free surface. This is an appropriate basis for estimating the vertical rise of the jets above the undisturbed water surface because the jets are formed at the intersection points between the free surface and the hull section cross section. The velocity of the jets is related to the fluid velocity at these points. The upwash of the jet adjacent to the centre bow is η_1 and the upwash of the jet adjacent to the inside of the demi-hulls is η_2.

$$\eta_1 = \int_0^t \frac{\partial \phi(C_1,0)}{\partial y} dt$$
$$\eta_2 = \int_0^t \frac{\partial \phi(C_2,0)}{\partial y} dt \qquad (4\text{-}32)$$

This procedure for estimating the velocity of the fluid at the jet roots does not introduce an infinite vertical velocity because the potential function is solved for the flow about that part of the hull section which is submerged beneath the undisturbed water surface. When the increase in the wetted width of the hull section due to the upwash of the free surface is considered (as it is for the calculation of C_1 and C_2) the intersection point between the hull surface and the free surface and thus the location of the jet roots is displaced from the stagnation points of the potential function.

The inherent limitations of the method used to estimate the shape of the free surface and the evolution of the jet fronts were such that the time calculated for the jet impacts with the top of the arch was approximate. Also, there was uncertainty whether both jet fronts, or just one of the jet fronts, was required to reach the top of the arch to initiate arch closure process. To bound the uncertainty due to model and physical understanding limitations, three arch closure conditions were developed,

$$
\begin{aligned}
B + y &\le \max(\eta_1, \eta_2) \\
B + y &\le (\eta_1 + \eta_2)/2 \\
B + y &\le \min(\eta_1, \eta_2)
\end{aligned}
\tag{4-33}
$$

The solution procedure was run once for each arch closure condition and an error bound was thus calculated.

4.6. Results

Experimental and theoretical results are compared for each of the nine hull sections presented in chapter 3. For each hull section a record of acceleration and free surface elevation as a function of time is presented for a particular normalised drop height in the range 0.85 to 0.89. This range corresponds to the normalised drop heights required for scaling a typical slam event on Incat vessel 050 (chapter 2). For each hull section an experimental visualisation result is presented and this is compared with the theoretical free surface elevation calculated from the series of potential function solutions. Free surface elevations are only presented for the pre-arch closure stage of the entry process. This is because the free surface is not calculated once arch closure has commenced. Also presented for each hull section is a comparison of experimental and theoretical acceleration against time records. As noted in section 4.5.4 there are three on set of arch closure conditions, the results presented here are for the cases that produced the medium peak acceleration value. Also peak acceleration results and velocity ratio results are presented for mass numbers 0.29 and 0.58 and for a range of normalised drop heights. Also the relationship between penetration number and the hull section area ratio predicted by the modified added mass theory is compared with that obtained from experiment.

4.6.1. Wedge Results

Theoretical and experimental acceleration and free surface elevation results for the two simple wedge models are shown in Figure 4.6.1 (wedge25) and Figure 4.6.2 (wedge15). A further comparison of the theoretical and experimental acceleration results with six other similar added mass theories is presented in Figure 4.6.3 and Figure 4.6.4.

Examining the results for the wedge25 hull section initially. The initial rate of increase of the theoretical acceleration record is almost identical to that of the experimental record. The theoretical record obtains a peak acceleration of $8.8m/s^2$ at time 48ms which is 4.5ms earlier than the experimental peak acceleration of $10.5m/s^2$. This temporal misalignment is also evident during the period of initial increasing acceleration during which the theoretical acceleration generally obtains a particular acceleration value approximately 4ms prior to the experimental acceleration value. Once the peak acceleration is obtained the rate of decrease in acceleration is similar for both the experimental and theoretical results until 68ms when the experimental acceleration commences decreasing significantly more rapidly than the theoretical acceleration. This is attributed to separation effects that are not modelled by the theory. During the entry of the 25° wedge the water is observed to pile up in the vicinity of the model and for jets to evolve along the wedge underside. The theoretical free surface elevation result is observed to show good agreement with the experimental free surface shape. This is with the exception of the jet flow. The theoretical model only calculates the vertical height of the jet above the undisturbed water surface. Results of this calculation are not shown here. It is evident that the rapid decrease in experimental acceleration that commences at 68ms coincides

with the onset of the main water body separation (as distinct from the separation of the jets) from the wedge corner. That is, only jet separation is evident in the experimental time series photo taken at 60ms. However photo taken at 80ms separation of the main water body from the wedge corner is evident. The estimated onset of separation at 68ms of course occurs between photos taken at 60ms and 80ms. This rapid decrease in acceleration is not modelled by theory, as the theory does not take account of the effect of separation.

In Figure 4.6.2 the theoretical and experimental entry of a 15° wedge is shown. The 15° wedge result displayed similar trend as were observed for the 25° wedge entry. The calculated and experimental acceleration graphs both show similar rates of increase of acceleration during the first 15ms of the entry process. The theoretical peak acceleration of 22.9m/s^2, which is 10ms prior to the experimental peak acceleration of 24.8. Following the theoretical peak acceleration the theoretical acceleration decreases at a rate that is significantly less than the rate of decrease in experimental acceleration following the peak acceleration. This is attributed to the separation of the jest and the main water body from the wedge corner. The separation effects are of course not modelled by the modified added mass theory as noted previously. The theoretical free surface elevation is observed to be quite similar to that measured during the experiments expect for the photo taken at 60ms. At 60ms significant separation has occurred and this has not been modelled by the theoretical calculations. The acceleration of the 15° wedge at 60ms is approximately 0m/s^2.

A comparison of the acceleration results for the added mass theory developed in this chapter for the water entry of the two wedge models with acceleration predictions of five other added mass theories is presented in Figure 4.6.3 and Figure 4.6.4. The predictions for the 25 degree wedge are shown in Figure 4.6.3. Examination of this figure reveals that the added mass theory developed in this chapter agrees at least as well with the experimental acceleration result as the other five theories. This theoretical comparison also gives additional confidence in the quality of the experimental results. At 0.07s all the added mass theories predict significantly higher accelerations than those measured in experiments. This is attributed to the separation of flow from the knuckles of the wedge as discussed above. The predictions for the 15 degree wedge are shown in Figure 4.6.4. The theory presented in this chapter agrees at least as well with the experiment as the other five theories and indeed the modified added mass theory is relatively accurate in predicting the peak acceleration compared with the other five theories. For both the 25 and 15 degree wedges it is observed that all the theoretical predictions obtain maximum acceleration consistently prior to the experimental maximum acceleration. The above comparisons are an additional verification of the modified added mass theory.

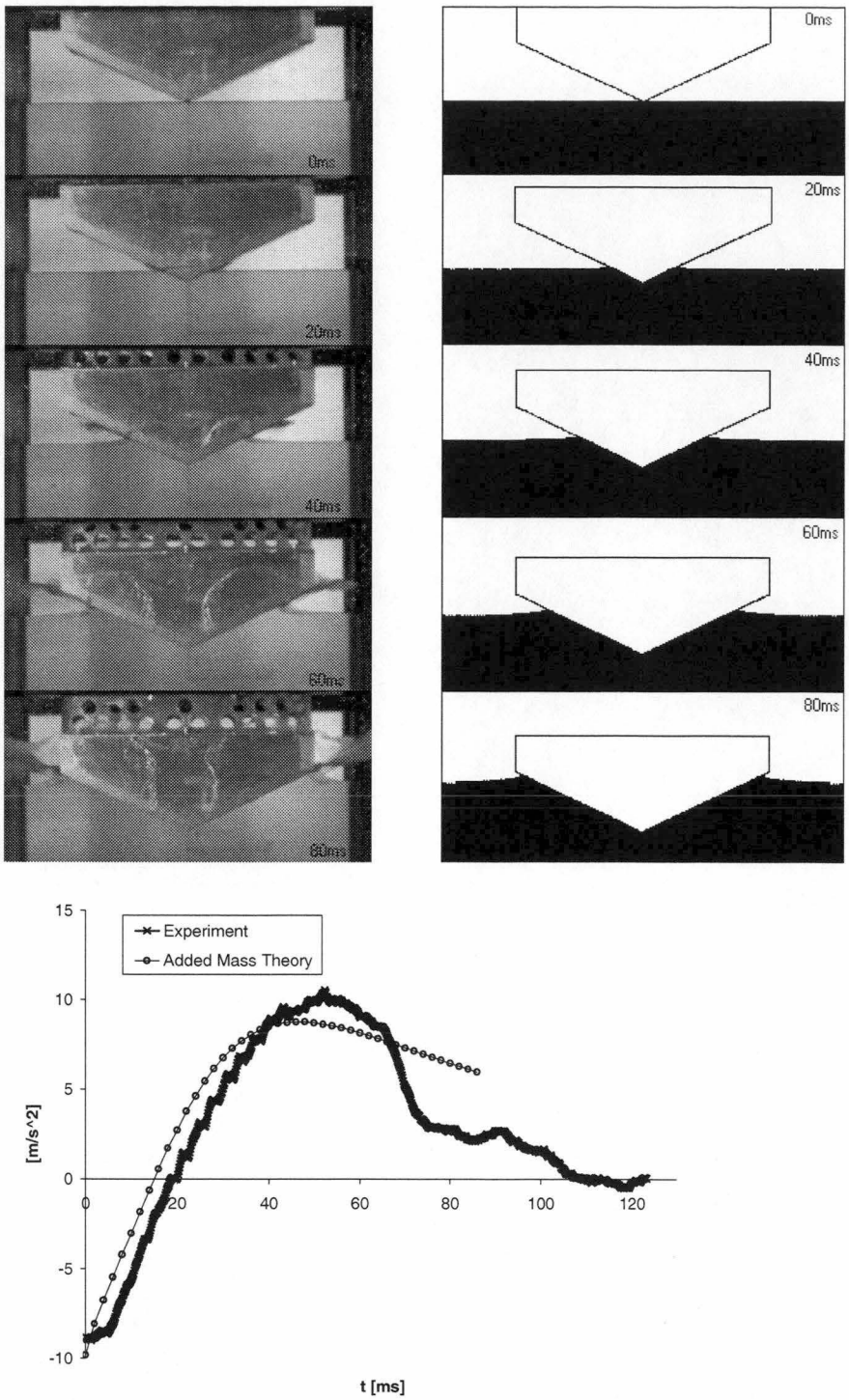

Figure 4.6.1 Wedge25. Normalised drop height=0.89, mass number=0.29. Comparison of free surface and acceleration results for experiment and added mass theory.

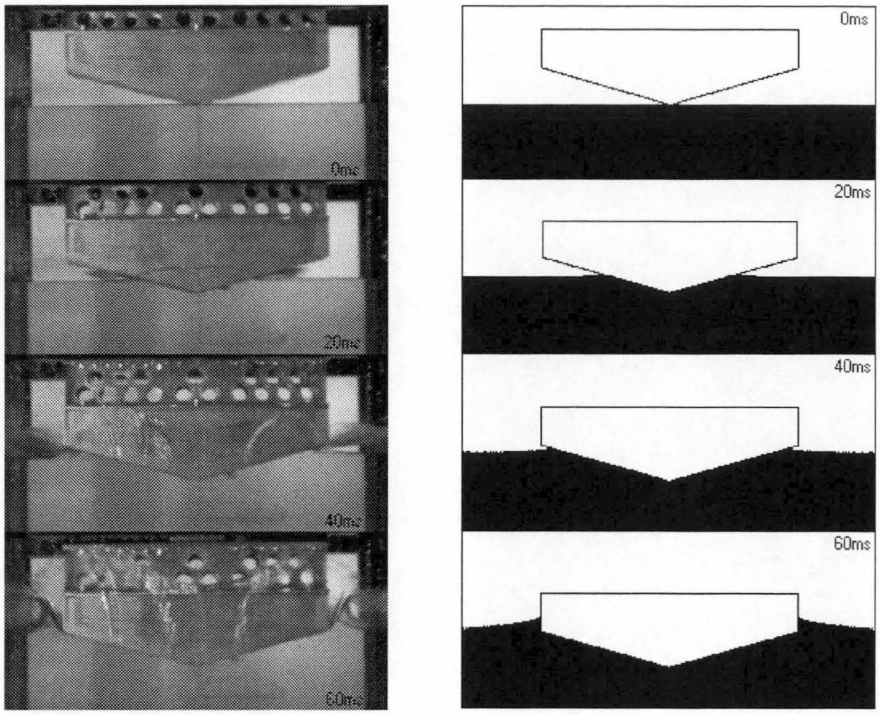

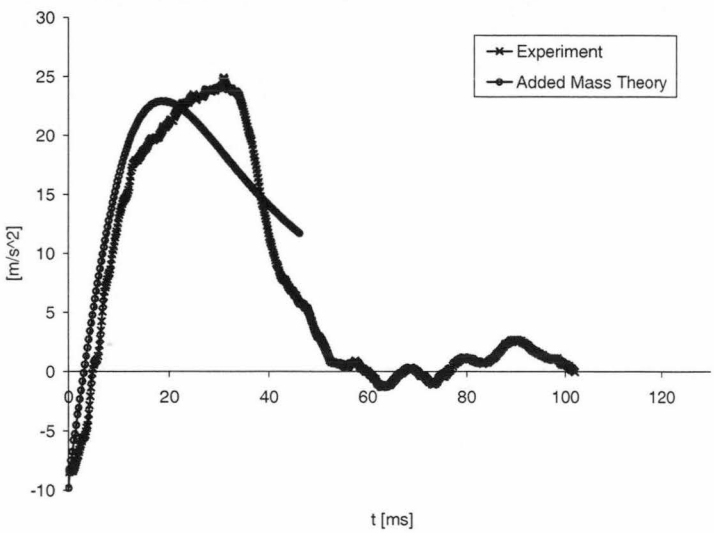

Figure 4.6.2 Wedge15. Normalised drop height=0.89, mass number=0.29. Comparison of free surface and acceleration results for experiment and added mass theory.

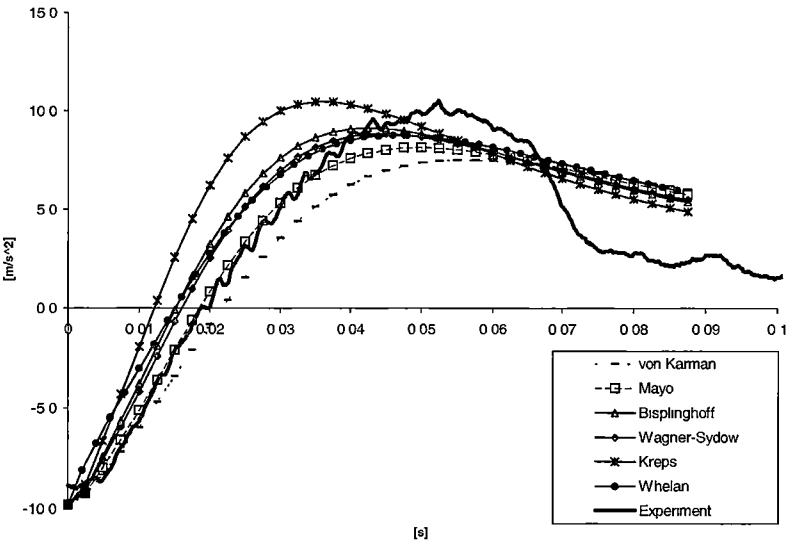

Figure 4.6.3: Comparison of five added mass based wedge impact theories with experimental results and modified added mass theory for the wedge25 model. (Normalised drop height=0.89, mass number=0.29.)

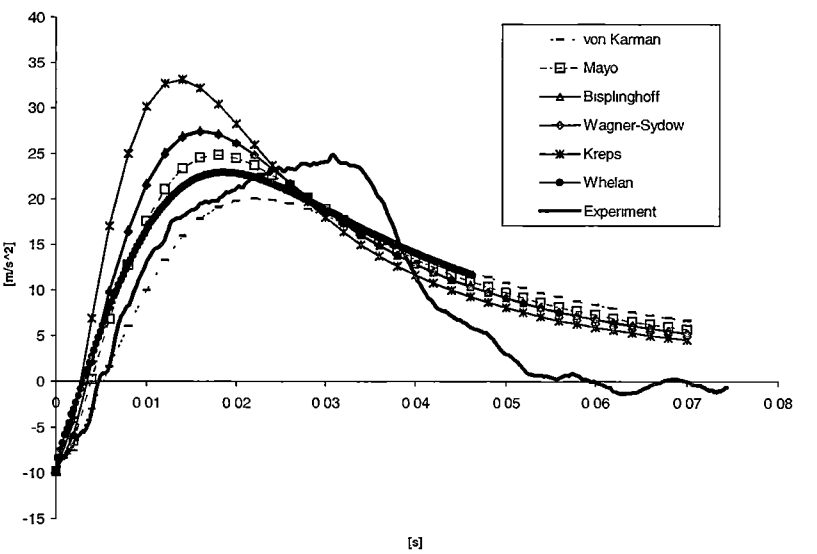

Figure 4.6.4: Comparison of five added mass based wedge impact theories with experimental results and modified added mass theory for the wedge15 model. (Normalised drop height=0.89, mass number=0.29.)

4.6.2. Wedge with Sideplates Results

The theoretical results for both hull sections wedge25 with sideplates (Figure 4.6.5) and wedge15 with sideplates (Figure 4.6.6) display poor correlation with the experimental results.

The theoretical acceleration of hull section wedge25 with sideplates shows reasonable agreement with experiment up until the onset of the arch closure process. From 0ms to 22ms, as the demi-hulls initially impact the water surface, a negative acceleration of approximately $-9.0m/s^2$ is experienced by both the experimental and theoretical hull sections. At 22ms the centre bow of the theoretical section enters the water and the acceleration increases gradually until 72ms when a value of $17m/s^2$ is obtained. This compares well with the corresponding part of the experimental acceleration profile. That is at 24ms the centre bow of the experimental section impacts the water and this causes the acceleration of the hull section to increase at a rate which is slightly lower than the theoretical acceleration up until time 76ms. After 76ms the theoretical and experimental acceleration graphs diverge significantly in form. The experimental graph displays an acceleration spike of magnitude $34m/s^2$, however the theory does not predict this spike at all. Following the spike the two acceleration records display a similar rate of decrease in acceleration. This part of the acceleration record is not especially of interest as it is after acceleration spike and the entry process is effectively over. The prediction of the free surface is also in error. The predicted pile up of water is over predicted around the inside of the demi-hulls and under predicted around the centre bow. These errors are clearly evident in the photo taken at time 60ms.

The predicted acceleration against time record for the hull section wedge15 with sideplates differs significantly from that measured experimentally. From time 0ms to 57ms both the predicted and experimental accelerations display negative accelerations in the range $-9.8\ m/s^2$ to $-6.0m/s^2$. The experimental accelerations are $-9.8\ m/s^2$ at 0ms and increase steadily to $-6.0m/s^2$ at 57ms. The predicted result however is $-9.8\ m/s^2$ at 0ms and remains relatively constant until 57ms. Both the experimental and theoretical acceleration records display an increase in acceleration that coincides with the impact of the centre bow with the water. This process starts at 57ms for the theoretical acceleration record and at 62ms for the experimental record. The rate of increase in acceleration displayed by the theory is greater than that observed in the experiments. The theoretical onset of arch the arch closure process commences at 70ms. The acceleration spike which is significantly less sharp than the acceleration spike measured in the experiments, however they are both of a similar magnitude.

The cause of the substantial errors for both these models is attributed to two causes. The error in the free surface prediction causes the mass of trapped air at the onset of arch closure to be incorrect. The mass of trapped air in the column is calculated by integrating the area enclosed between the top of the arch and the free surface. This causes the behaviour of the compressible air spring to be in error as it

contains an inappropriate amount of air and has the wrong dimensions. Secondly, the sharp corner at the top of the top of the arch where the centre bow meets the top of the demi-hulls causes the extrapolation procedure used to calculate the added mass during arch closure to be significantly in error. The variation of the added mass during the arch closure process is extrapolated from the wetted widths of the centre bow and the demi-hulls at the instant of the onset of the arch closure process. Clearly the erroneous calculation of the upwash about the centre bow and the demi-hulls causes the calculation of the variation of the added mass during the arch closure process to be grossly in error for these two hull sections. This problem is less evident for the other arch models that have smoothly curved arch tops.

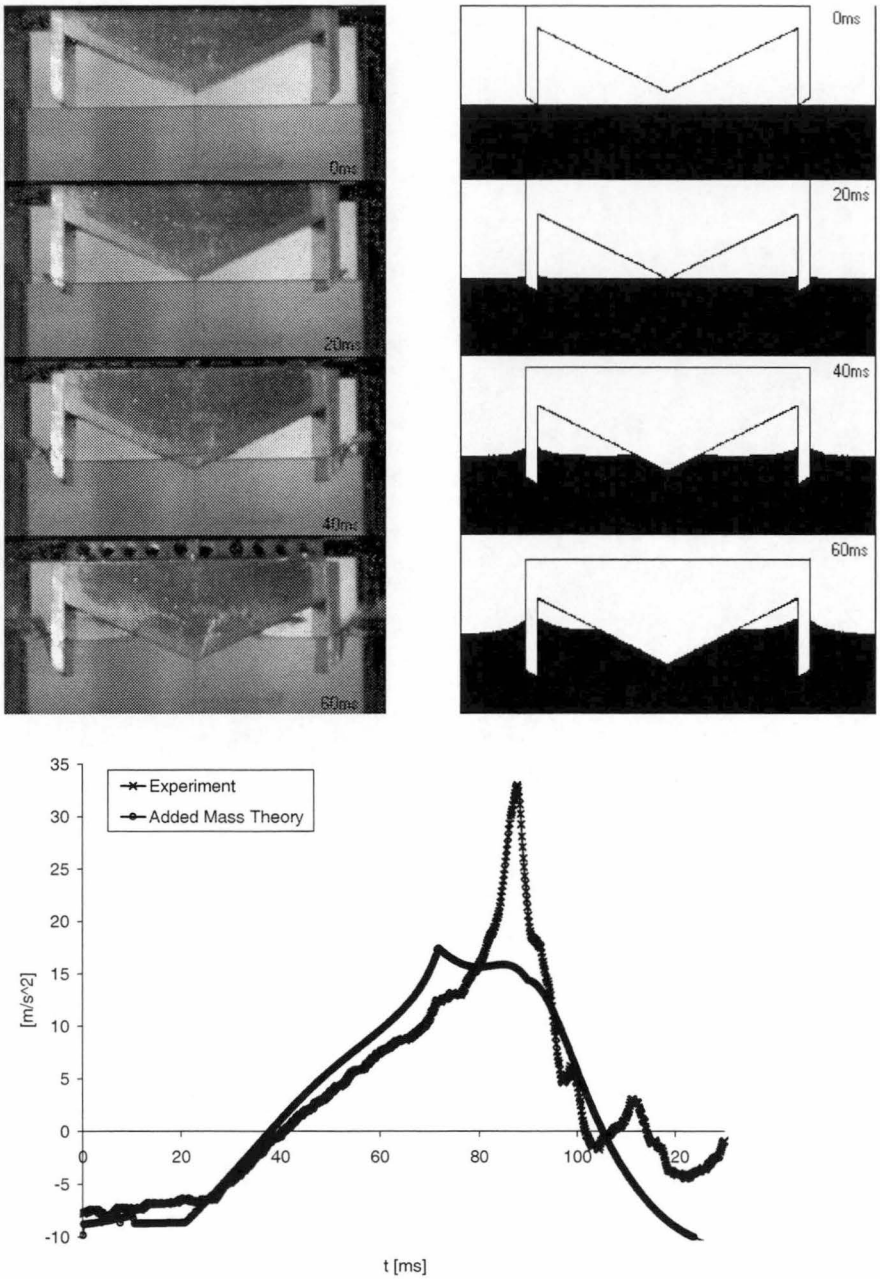

Figure 4.6.5 Wedge25 with sideplates. Normalised drop height=0.85, mass number=0.29. Comparison of free surface and acceleration results for experiment and added mass theory.

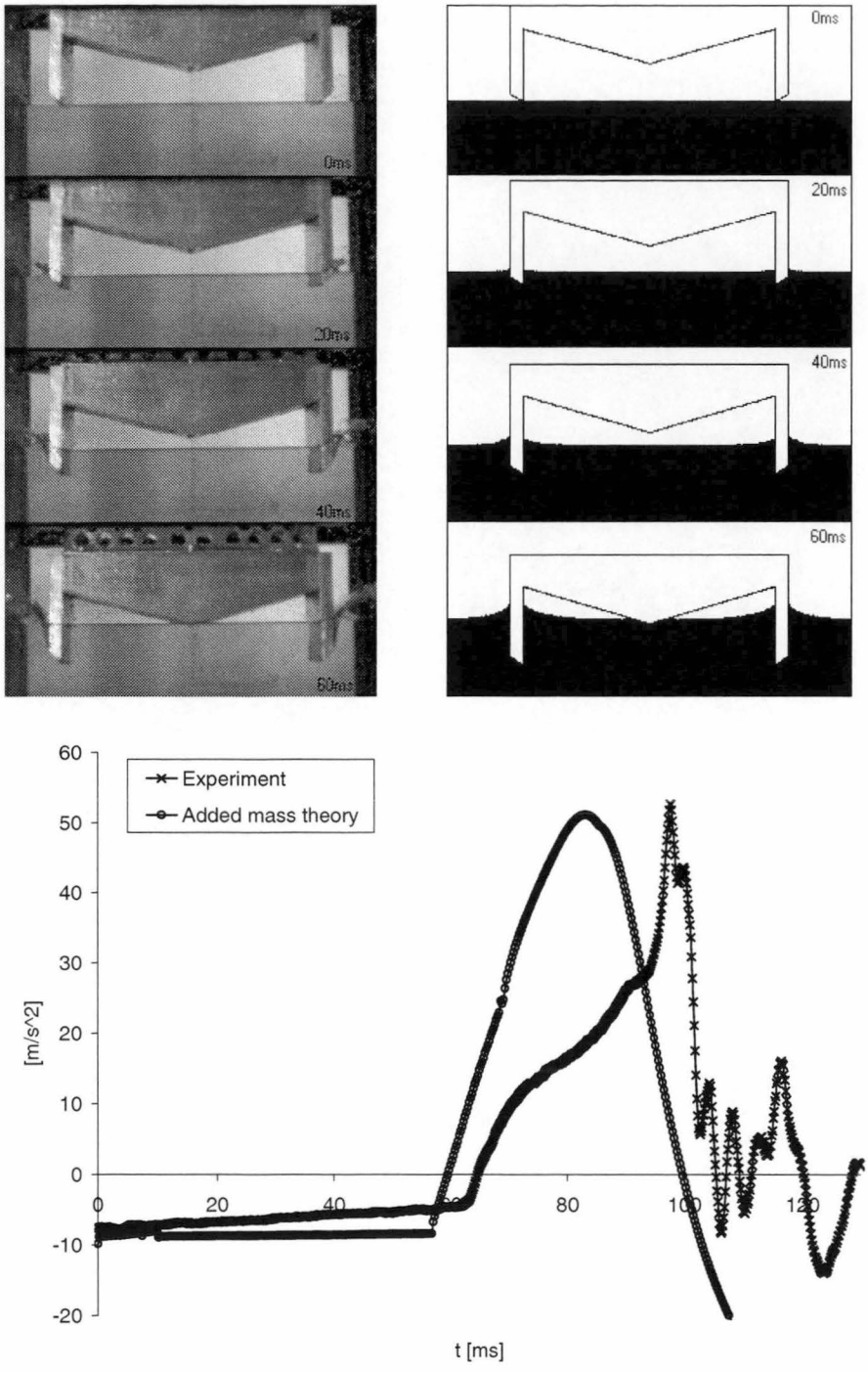

Figure 4.6.6 Wedge15 with sideplates. Normalised drop height=0.85, mass number=0.29. Comparison of free surface and acceleration results for experiment and added mass theory.

4.6.3. J-Series Hull Section Results

A comparison between experimental and theoretical acceleration and free surface elevation records for the three J-series hull sections as shown in Figure 4.6.7 to Figure 4.6.9. Generally theoretical results display similar features as observed in the experimental measurements. That is, the accelerations for all these hull sections are generally moderate until a significant acceleration spike occurs that coincides with the arch closure process. The magnitude of the theoretical peak acceleration is similar to the experimental peak for model J1 and J3 although it is under predicted for model J2. For each of the three hull sections the time over which the theoretical acceleration spike occurs is approximately twice as long for the experimental acceleration spike.

The theoretical and experimental acceleration and free surface elevation records for hull section J1 are shown in Figure 4.6.7. In this figure the calculated accelerations for all three arch closure conditions are plotted so that the effect of the different arch closure conditions can be examined. It can be observed that the arch closure condition based on the maximum estimated jet height is trigger first and this arch closure condition calculates the lowest theoretical peak acceleration. The arch closure condition based on the average of the two estimated jet heights triggers second and this calculates the second greatest peak acceleration. Finally the third arch closure condition which requires that both estimated jets have impacted the top of the arch triggers last and calculates the highest peak acceleration. As can be observed each of the three arch closure conditions calculates a similar peak acceleration as that measured experimentally. The time of the three theoretical peak accelerations are all relatively quite close to the time of theoretical peak acceleration.

Considering now a detailed comparison of the calculated acceleration record based on the second arch closure condition and the experimental record for model J1. Initially the acceleration experienced by the hull section, both theoretical and experimental, are approximately $-9.0m/s^2$. This is because the gravitational forces are substantially larger than the hydrodynamic and buoyancy forces associated with the initial entry of the very fine demi-hulls. At 27ms the theoretical acceleration displays a near step change in value to $-4.0m/s^2$. A similar step change in experimental acceleration is observed at 32ms. This step change in acceleration is attributed to the entry of the bluff centre bow. Following the initial impact of the centre bow both the experimental and theoretical acceleration are almost identical until 70ms when the Experimental acceleration progressively becomes greater than the theoretical acceleration. At 90ms the onset of arch closure process condition is satisfied and the theoretical acceleration begins to rapidly increase until a maximum of $63.3m/s^2$ is obtained at 100.5ms. The rate of increase of the theoretical acceleration is observed to be similar to that of the experimental acceleration. The peak experimental acceleration is $71.8m/s^2$ and it is obtained 4.4ms prior to the theoretical peak acceleration. Following the peak acceleration both the experimental and the theoretical decreases rapidly. The theoretical deformation of the free surface is observed to be

similar to that measured in experiments. That is, water is piled up around the centre bow and the inside of the demi-hulls.

The results for hull section J2 (Figure 4.6.8) display many of the same features as for hull section J1. The free surface elevation is predicted quite well and some of the finer details are resolved. The pile up of water around the centre bow is more substantial in the experimental results than the pile up of water around the inside of the demi-hulls and a similar trend is displayed in the theoretical results. Both the theoretical and experimental acceleration records display initially low accelerations of a similar magnitude until 75ms after the initial impacts when the experimental acceleration becomes progressively greater than the theoretical acceleration. At 89ms the theoretical onset of arch closure condition is satisfied and the theoretical acceleration begins to increase rapidly until at 91ms it becomes greater than the experimental acceleration. At time 94.9ms the experimental acceleration obtains a peak value of 159.89m/s^2 and 2.9ms later at time 97.8ms the theoretical acceleration obtains a substantially lower peak acceleration of 102.7ms. Following the peak theoretical and peak accelerations the experimental acceleration decreases significantly more rapidly than the theoretical acceleration. The experimental acceleration spike is observed to be sharper than the theoretical acceleration spike.

In Figure 4.6.9 the theoretical and experimental acceleration and free surface elevation results are shown for normalised drop height 0.88 and mass number 0.29 for hull section J3. During the initial entry of the fine demi-hulls and centre bow the hull section experiences low accelerations which is accurately predicted by the modified added mass theory. A 80ms the experimental acceleration becomes greater than the theoretical acceleration. At 87ms the onset of arch closure process condition is satisfied and the hull section acceleration increases rapidly until a maximum is obtained at time 96.8ms. The experimental acceleration spike of magnitude 164.7m/s^2 is seen to be significantly sharper than the theoretical acceleration spike of magnitude 164.6m/s^2. The free surface elevation is predicted adequately. A pile up of water about the centre and the demi-hulls this is observed to be most substantial within the arch structure.

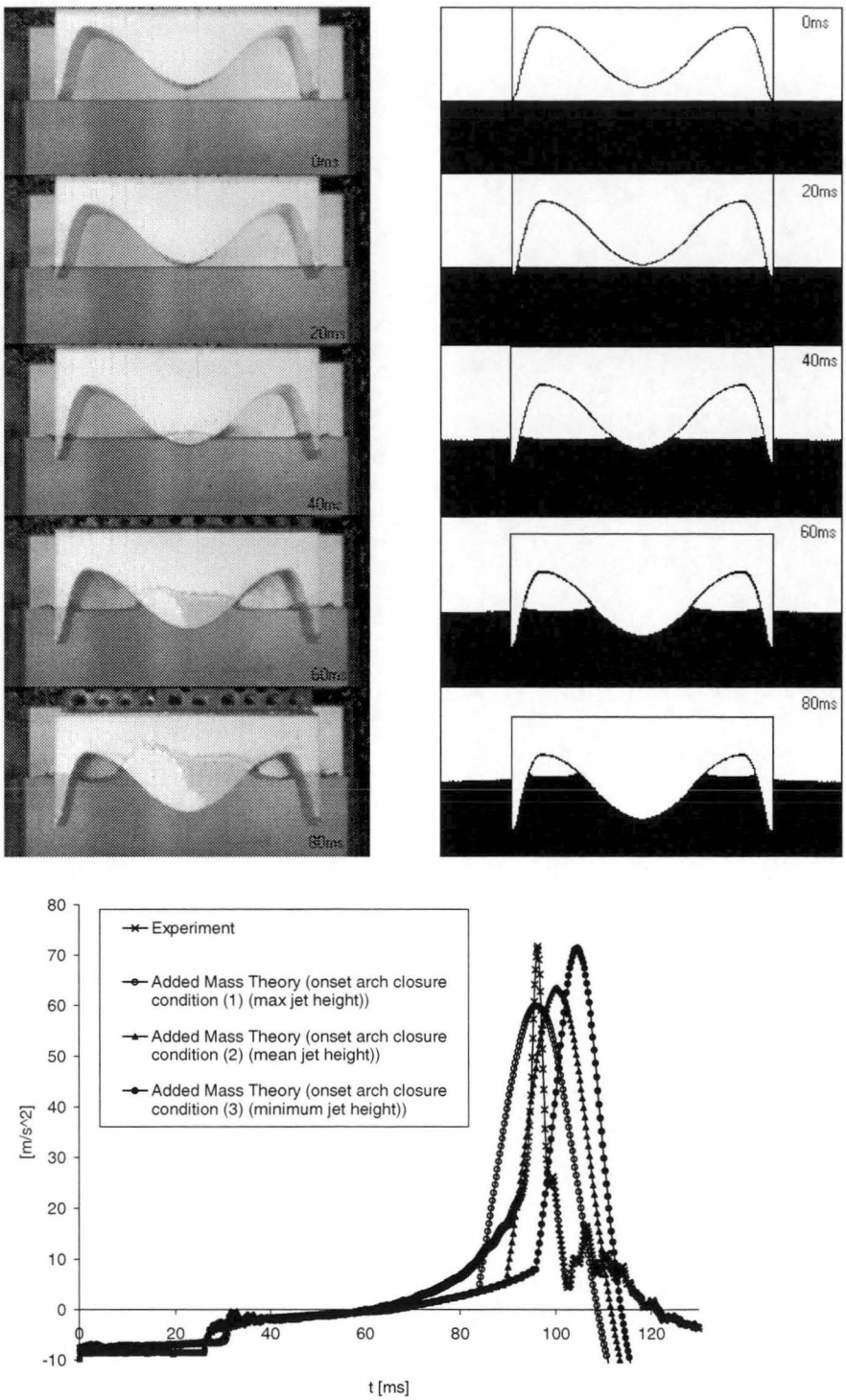

Figure 4.6.7 J1. Normalised drop height=0.88, mass number=0.29. Comparison of free surface and acceleration results for experiment and added mass theory. Calculations for all three arch closure conditions are also shown for comparison.

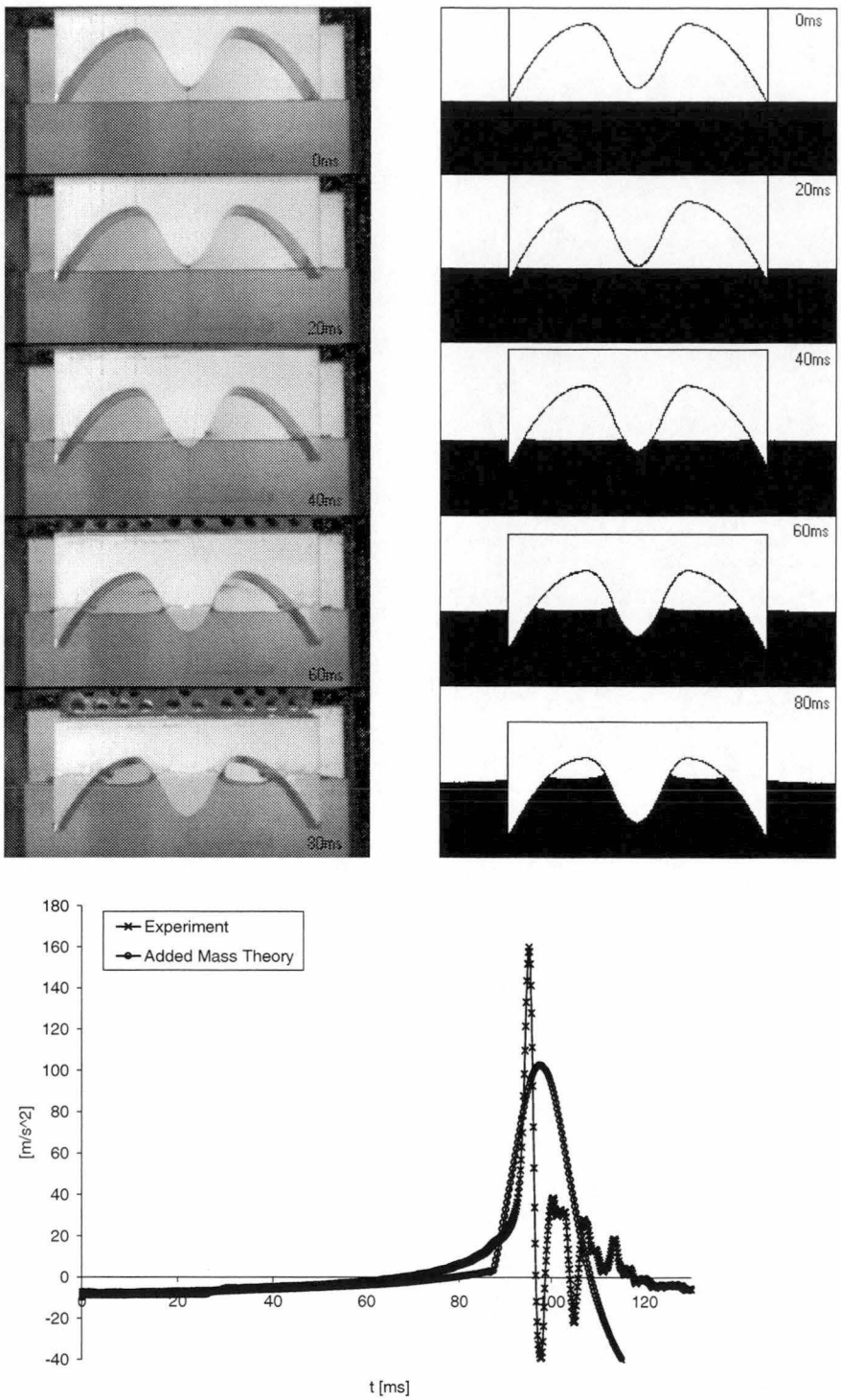

Figure 4.6.8 J2. Normalised drop height=0.88, mass number=0.29. Comparison of free surface and acceleration results for experiment and added mass theory.

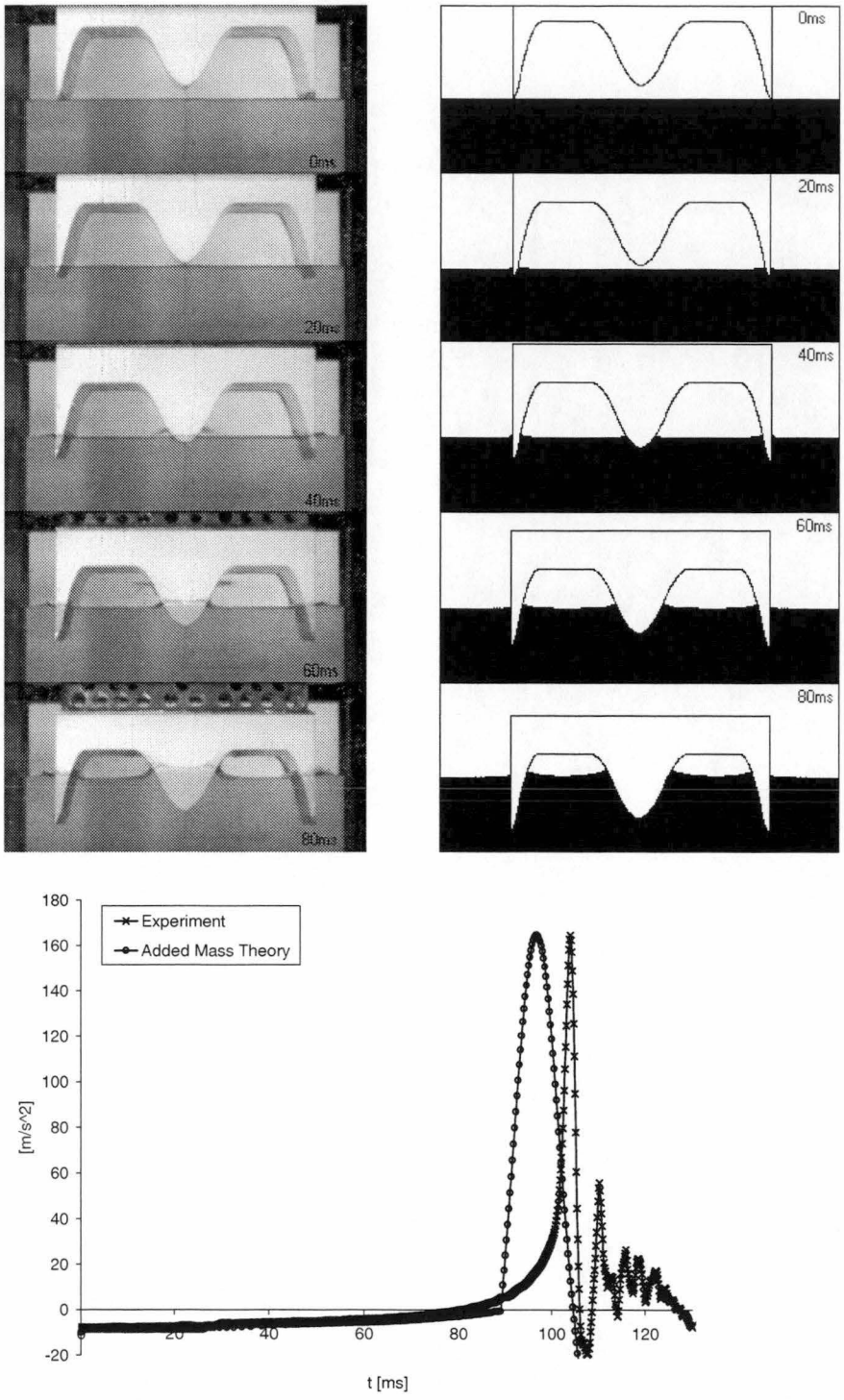

Figure 4.6.9 J3. Normalised drop height=0.88, mass number=0.29. Comparison of free surface and acceleration results for experiment and added mass theory.

4.6.4. Incat1 Results

The performance of hull section Incat1 is presented in Figure 4.6.10. The modified added mass theory was developed for hull sections that could have their geometry described by functions. Examination of the geometry of Incat1 reveals that the demi-hulls of the hull section can not be described by a function due to their bulbous form. The demi-hulls have been re-shaped so that their geometry could be specified with a function. As noted in chapter 3 the demi-hulls have only a minor effect on the entry process when they are fine. The hull section beam (L) and height (B) and the area ratio (ratio of the model cross sectional area to $L \times B$) of the modified section remain the identical to the unmodified Incat1 hull section.

The theoretical acceleration and experimental acceleration results are practically identical until time 98ms. At this time the onset of the arch closure process begins and the theoretical acceleration increases rapidly to a maximum of 139.2m/s^2. Following the 98ms time the experimental acceleration increases initially more slowly than the theoretical acceleration however at approximately 110ms the experimental acceleration begins to increase very rapidly indeed until a maximum is obtained at 111.6ms of 148.4m/s^2. Evidently for this hull section the onset of arch closure condition occurs too early and this causes the theoretical acceleration peak to occur prior to the experimental peak.

The predicted free surface elevation displays reasonable agreement with theory. A significant pile up of water on the outside of the demi-hull is apparent in both the experimental and theoretical results. The free surface elevation near the inside of the demi-hull is over predicted by the theory. The modification to the hull section form my impart account for this minor error.

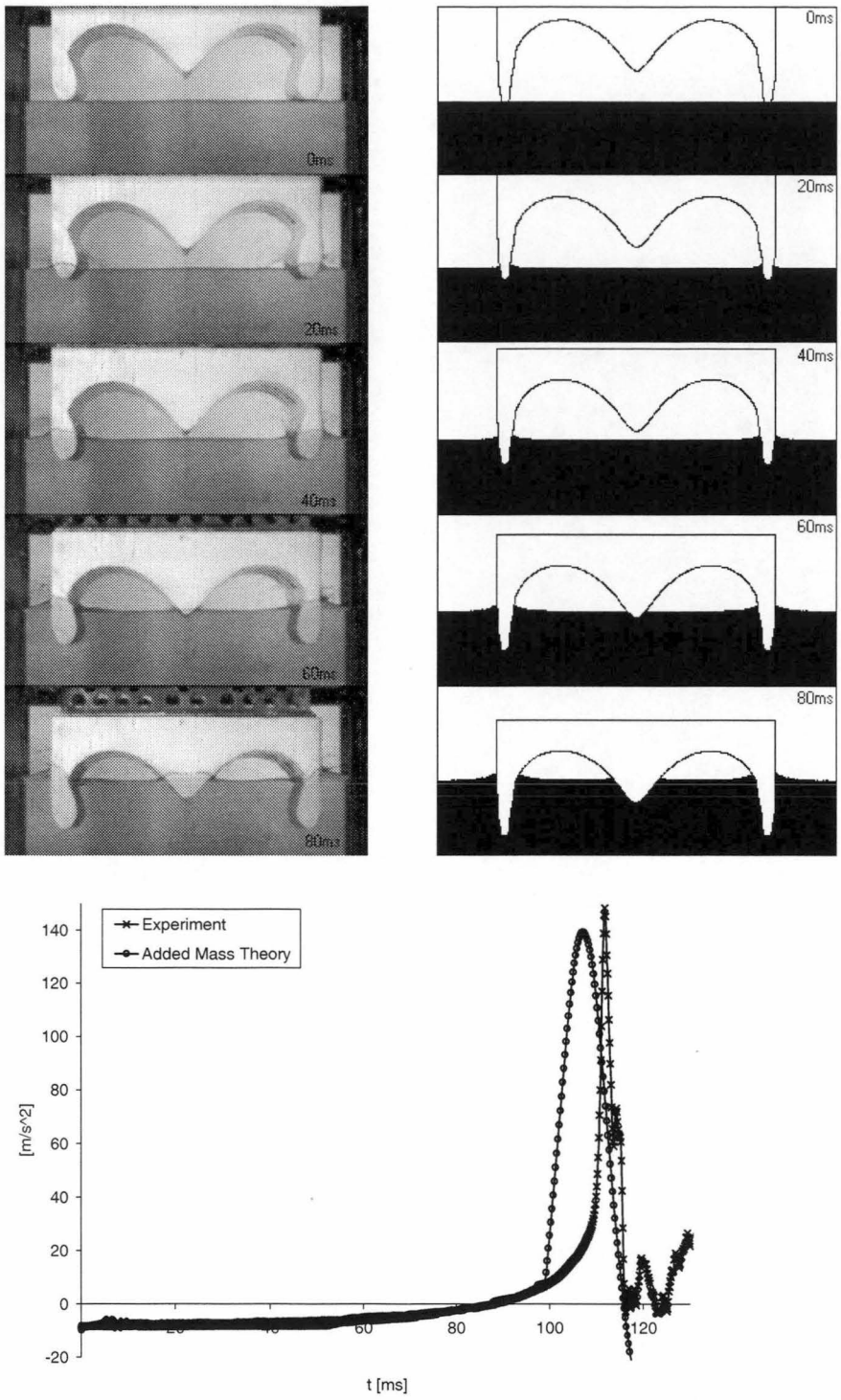

Figure 4.6.10 Incat1. Normalised drop height=0.86, mass number=0.29. Comparison of free surface and acceleration results for experiment and added mass theory.

4.6.5. Flat1 Results

The entry of model Flat1 is shown in Figure 4.6.11 for normalised drop height 0.85 and mass number 0.29. The calculation of the free surface is in error on the outside of the demi-hull. This is apparently due to the separation that occurs from the chine near the bottom of these demi-hulls. The pile up of water on the inside of the demi-hull is approximately equal to that observed in experiment. There is significant error in the calculated acceleration record. The peak acceleration which occurs when the flat wet deck impacts the water surface is predicted to occur at 94.3ms which is some 15ms prior to the to the peak acceleration experienced by the hull section in experiments. This is due to the onset of arch closure process condition being satisfied too early. The magnitude of the theoretical acceleration spike ($200m/s^2$) is similar to that observed in experiments ($233.5m/s^2$), as too is the time period over which the spike occurs. Prior to the acceleration spike the theoretical and experimental accelerations are essentially equal.

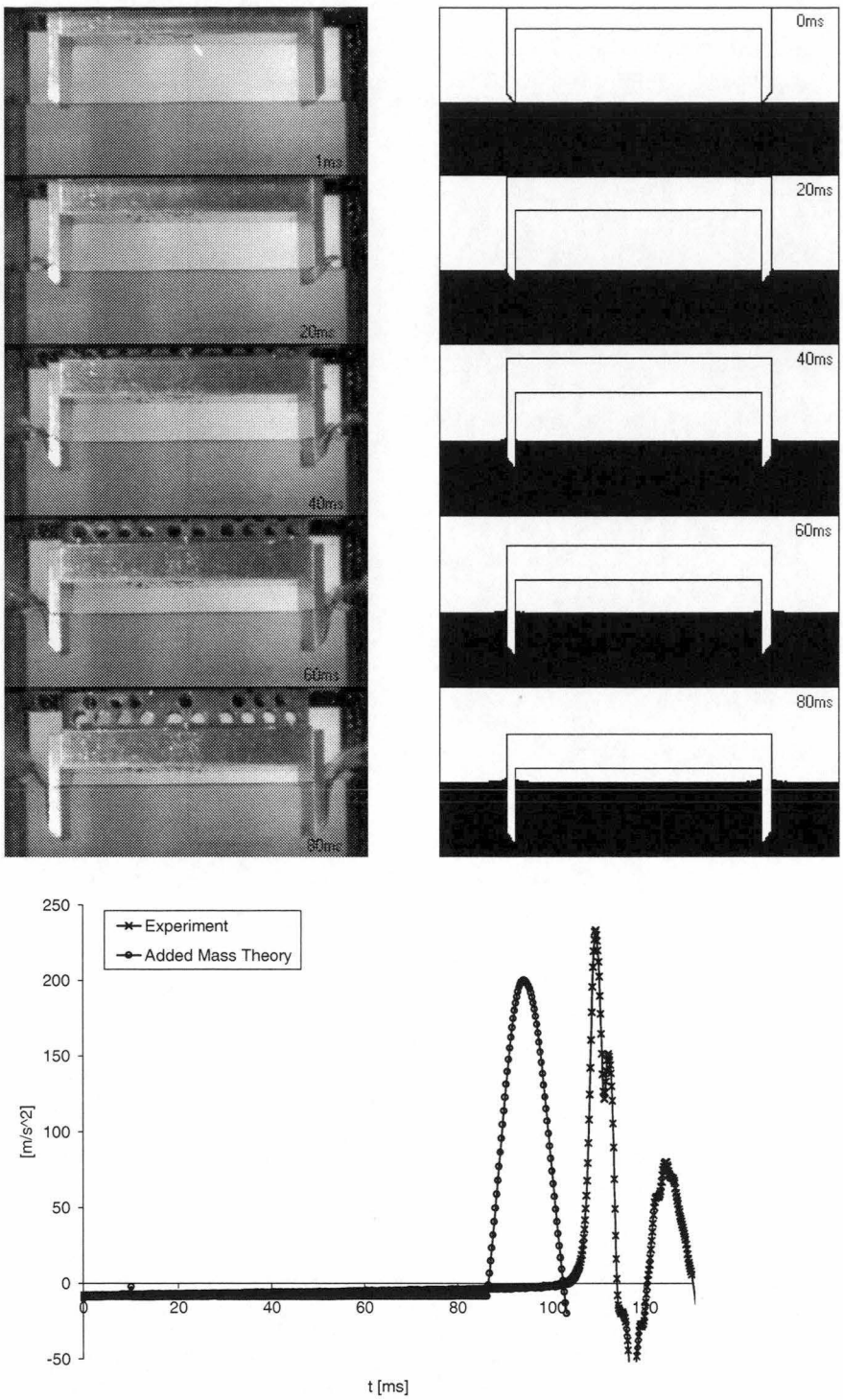

Figure 4.6.11 Flat1. Normalised drop Height=0.85, Mass number=0.29. Comparison of free surface and acceleration results for experiment and added mass theory.

4.6.6. Peak Acceleration Results

The relationships between peak acceleration and normalised drop height are shown in Figure 4.6.12 to Figure 4.6.20 for each of the nine hull section geometries.

The results for hull section wedge25 and wedge12 are shown in Figure 4.6.12 and Figure 4.6.13 respectively. The peak accelerations are predicted well for both hull sections at mass number 0.29. For mass number 0.58 the added mass theory under predicts the peak acceleration. The rate of increase of peak acceleration with normalised drop height is however similar to that measured in experiments. The simple wedge hull sections do not have an arch geometry and thus these two solutions are found using only the pre-arch closure added mass theory.

The theoretical acceleration of the wedge25 with sideplates is seen to be significantly less than the peak acceleration measured during experiments (Figure 4.6.14). This is attributed to the causes discussed in section 4.6.2. It is interesting to note that the theoretical peak acceleration increases for normalised drop heights less than 0.87. A similar feature and perhaps related feature is observed for the J-series and Incat1 experimental results. However given the significant error associated with this the application of this theory to this particular hull section the significance of this observation is difficult to quantify.

The peak accelerations experienced by the wedge15 with sideplates are shown in Figure 4.6.15. There is generally quite good agreement between the experimental and theoretical peak accelerations. However it should be noted that the form of the acceleration time theoretical record for these results is significantly different from the experimental record. Thus the accurate prediction of the peak acceleration may indeed be merely fortuitous.

The calculated and theoretical peak acceleration results for the J-series hull sections are shown in Figure 4.6.16 to Figure 4.6.18. The theoretical results for hull section J1 (Figure 4.6.16) displays, for both mass number 0.29 and 0.58, a monotonic increase in peak acceleration. For mass number 0.29 the experimental peak acceleration is initially greater than the theoretical peak acceleration until normalised drop height 0.89 when the theoretical peak acceleration becomes greater. The theoretical result uncertainty bounds, results for the three onset of arch closure conditions, are observed to over lap with the experimental error bounds for all normalised drop heights greater than 0.80. For mass number 0.58 the theoretical J1 peak acceleration values are less than the experimental peak acceleration value for all normalised drop heights, however for normalised drop heights greater than 0.95 the uncertainty bounds of the theoretical and experimental results overlap. Also for normalised drop heights greater than 0.95 the rate of increase of peak acceleration values with normalised drop height is slightly greater than that of the experimental data values.

The results for hull section J2 are shown in Figure 4.6.17. For mass number 0.29 the theoretical peak acceleration results do not display the non-monotonic curve characteristics of the experimental results. The order of magnitude of the predicted peak acceleration is similar to that of the experimental results. The theoretical and experimental results display the same values at normalised drop height 1.05. The agreement between theoretical and experimental results at mass number 0.58 is not good. The theoretical peak accelerations are significantly less than the experimental results. The theoretical values are calculated to be lower at mass number 0.58 compared with the theoretical results at mass number 0.29. The experimental results display the reverse trend, that is the peak accelerations are generally greater at mass number 0.58 compared with mass number 0.29.

In Figure 4.6.18 are shown the theoretical and experimental peak acceleration results for hull section J3. For mass number 0.29 there is generally reasonable agreement in magnitude of the theoretical and experimental results. The rate of increase of the theoretical results is greater than that of the experimental results for normalised drop heights greater than 0.90. For mass number 0.58 the peak acceleration is under predicted by the theory, however the trend of peak acceleration to increase with normalised drop height is generally adequately predicted.

The Incat1 hull section experimental and theoretical peak accelerations (Figure 4.6.19) are generally similar for normalised drop heights less than 0.90 for mass number 0.29. Above normalised drop height 0.90, the theoretical peak acceleration becomes progressively larger than the corresponding experimental peak acceleration

The peak accelerations for the Flat1 hull section (Figure 4.6.20) at both mass numbers display similar trends, that is to monotonically to increase with normalised drop height, and this is moderately well predicted by theory. Initially the theoretical peak acceleration is less than the experimental peak acceleration, however the difference between the theoretical and experimental values reduces as the normalised drop height increases. The theoretical peak acceleration are generally less at mass number 0.58 compared with mass number 0.29 and this trend is reflected in the experimental results also.

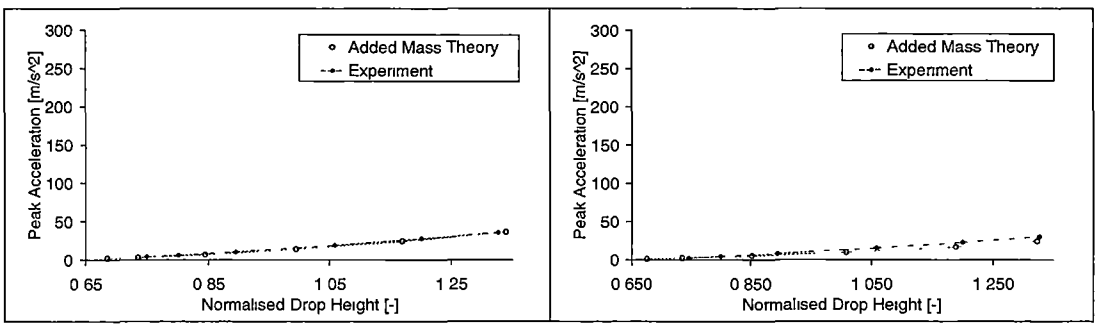

Figure 4.6.12 Peak Acceleration for Wedge 25. Mass No.=0.29 (left), Mass No.=0.58 (right)

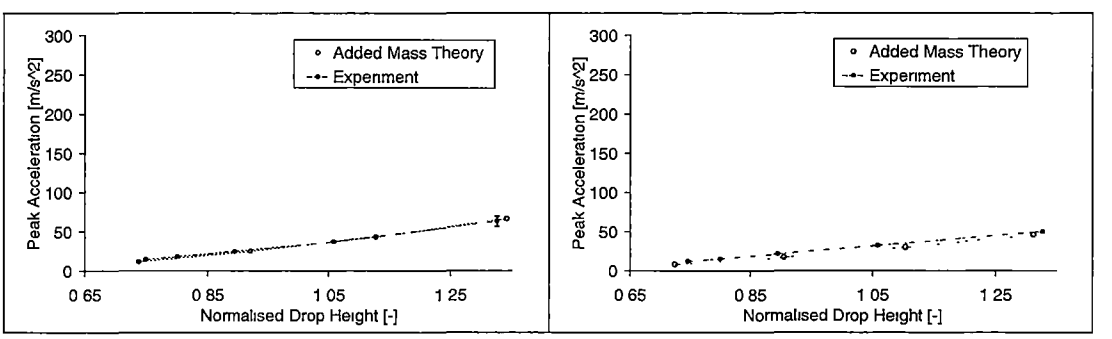

Figure 4.6.13 Peak Acceleration for Wedge 15. Mass No.=0.29 (left), Mass No.=0.58 (right)

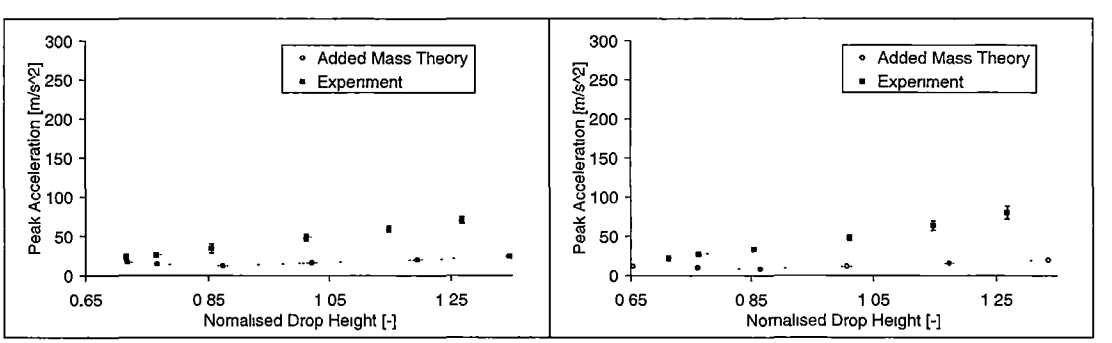

Figure 4.6.14 Peak Acceleration for Wedge25 with sideplates. Mass No.=0.29 (left), Mass No.=0.58 (right).

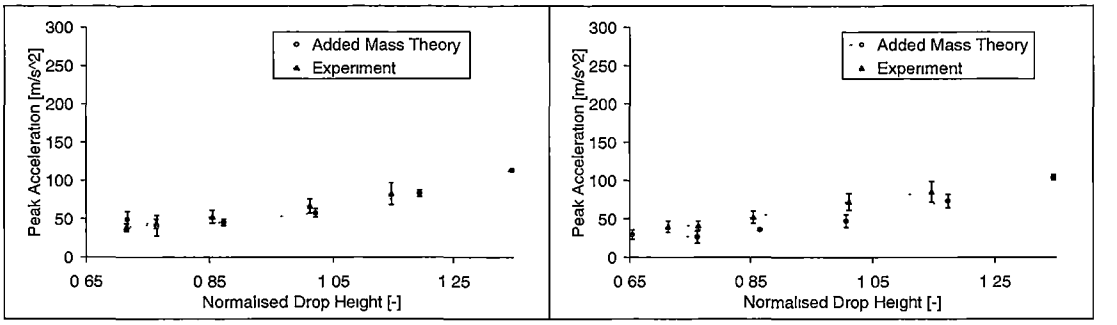

Figure 4.6.15 Peak Acceleration for Wedge15 with sjdeplates. Mass No.=0.29 (left), Mass No.=0.58 (right).

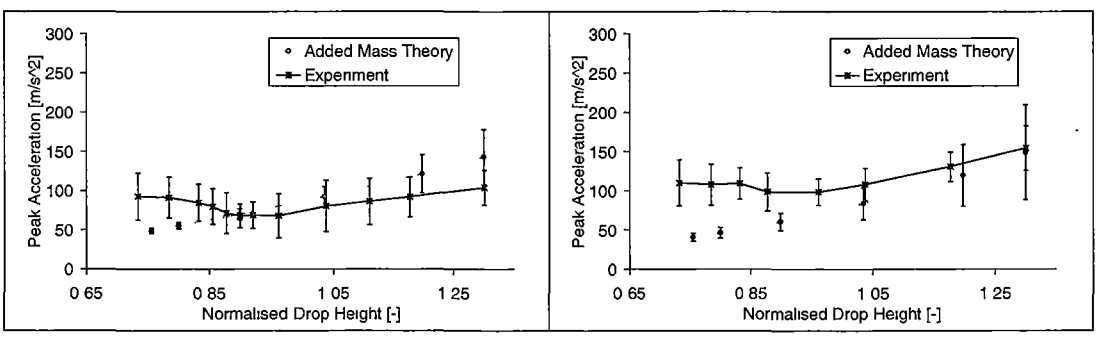

Figure 4.6.16 Peak Acceleration for Model J1. Mass No.=0.29 (left), Mass No.=0.58 (right)

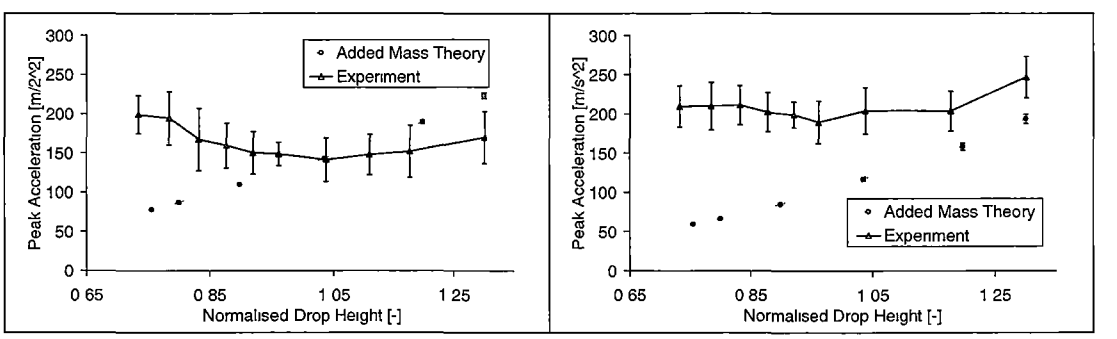

Figure 4.6.17 Peak Acceleration for Model J2. Mass No.=0.29 (left), Mass No.=0.58 (right)

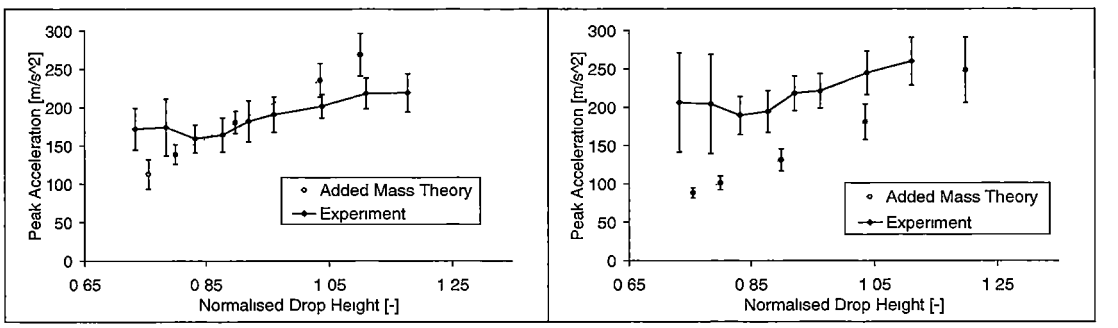

Figure 4.6.18 Peak Acceleration for Model J3. Mass No.=0.29 (left), Mass No.=0.58 (right)

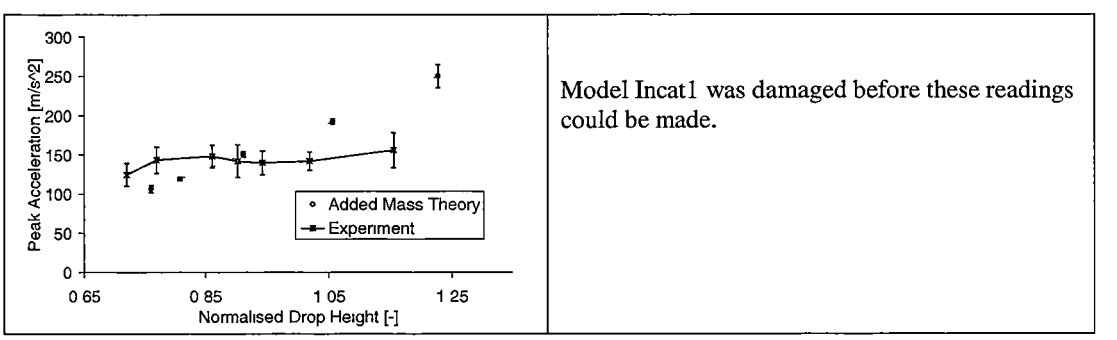

Figure 4.6.19 Peak acceleration for Incat1. Mass No.=0.29 (left), Mass No.=0.58 (right)

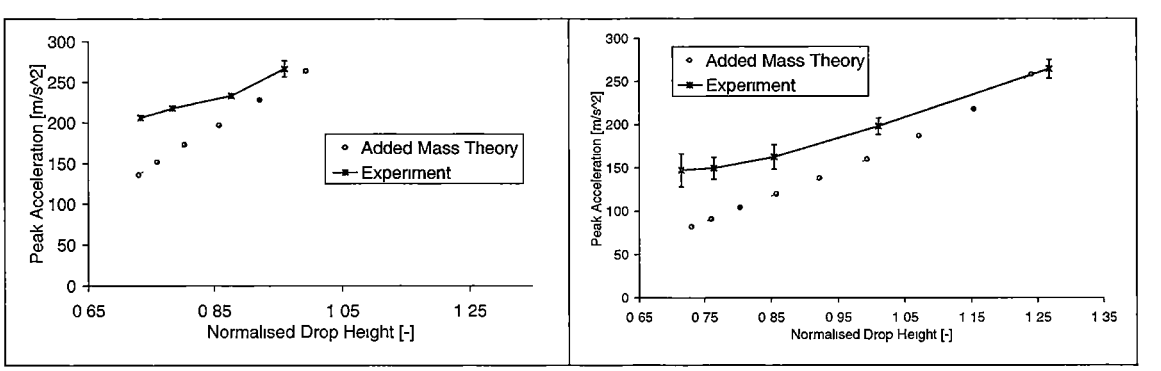

Figure 4.6.20: Peak acceleration for Flat1. Mass No.=0.29 (left), Mass No.=0.58 (right)

4.6.7. Velocity Ratio Results

The ratio of hull section velocity at the instant of peak acceleration and the initial impact velocity against normalised drop height are shown in Figure 4.6.21 to Figure 4.6.29. The theoretical solutions for the velocity ratio displayed adequate agreement with experiment for all hull sections except model wedge15 with sideplates (Figure 4.6.24) for which the velocity ratio was over predicted and model J3 at a mass number of 0.29 for which the velocity ratio was under predicted. The agreement between theory and experiment at normalised drop heights below 0.85 is generally not as good as for larger normalised drop heights (for example Figure 4.6.25). This is because the initial impact velocity at lower normalised drop heights approaches zero and this has the effect of exaggerating any error there is between the experimental and theoretical absolute velocities at the instant of peak acceleration.

The velocity ratios of the 25° and 15° simple wedge hull sections are plotted in Figure 4.6.21 and Figure 4.6.22 respectively. The added mass theory slightly under predicts the velocity ratio for the 25° wedge and over predicts the velocity ratio for the 15° wedge. The 15° wedge results display little increase with decreasing normalised drop height. This is because the initial impact velocity of the hull section is always relatively large compared with the velocity at the time of peak acceleration.

The velocity ratios of the hull section wedge25 with sideplates show very good agreement between theory and experiment (Figure 4.6.23). The theoretical results for wedge15 with sideplates are however over predicted by theory by a significant margin (Figure 4.6.24). Despite the systematic error bias, the shapes of the theoretical and experimental lines are quite similar. For both the 25° and 15° wedge with sideplates hull section it must be noted that the form of the theoretical acceleration against time records were both significantly different to the experimental records and thus any comparison of derivative measures comparing theory and experiment are possibly in error.

The agreement between the added mass theory and the experimental results for the J-series hull sections is generally good as shown in Figure 4.6.25 to Figure 4.6.27, except for hull section J3 mass number 0.29 where the theory under predicts the velocity ratio. For each of the J-series hull sections for a particular normalised drop height the velocity ratio is higher at mass number 0.58 compared with mass number 0.29 and this is attributed to the higher mass of the model.

The velocity ration of the Incat1 and flat1 hull sections, Figure 4.6.28 and Figure 4.6.29 respectively, are observed to display the typical form of the velocity ratio against normalised drop height curves. That is as the normalised drop height increases the velocity ratio decreases. For both these hull sections the theoretical velocity ratio is seen to be slightly less than the experimental acceleration, except for flat1 mass number 0.58 for normalised drop height greater than 1.01. The experimental data set for flat1 is quite limited because the accelerometer saturated for the higher normalised drop

heights and thus it is not possible to compare the theoretical and experimental velocity ratios for this hull section for normalised drop heights greater than 1.00 and mass number 0.29.

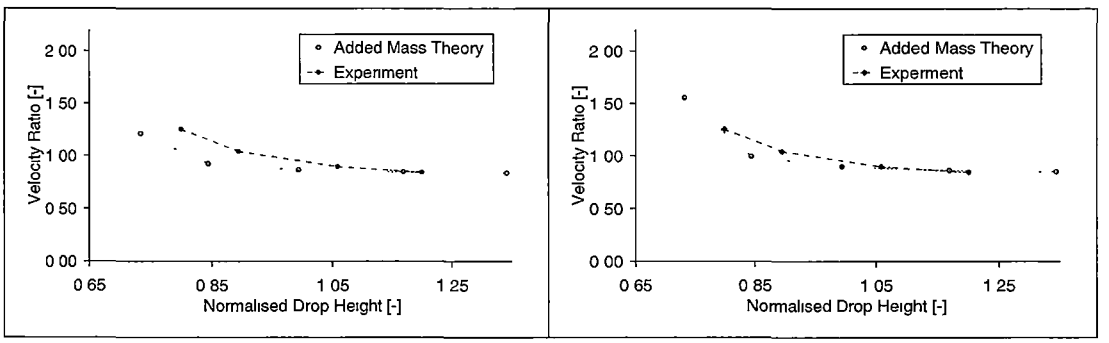

Figure 4.6.21 Velocity ratio for Wedge 25. Mass No.=0.29 (left), Mass No.=0.58 (right)

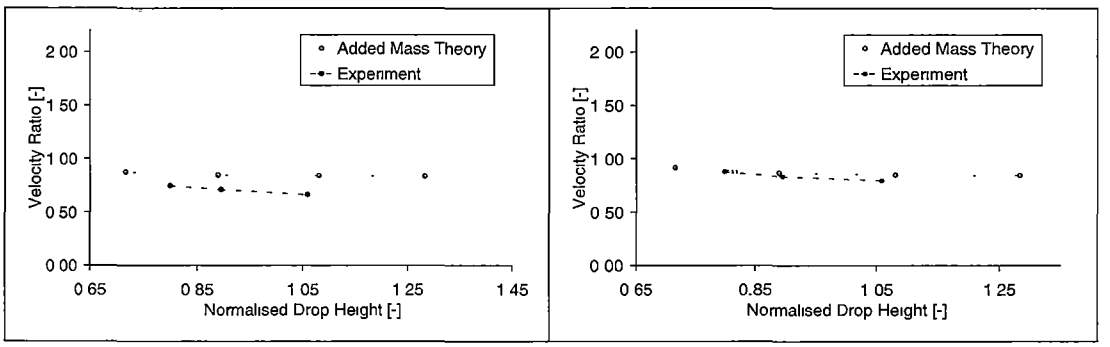

Figure 4.6.22 Velocity ratio for Wedge 15. Mass No.=0.29 (left), Mass No.=0.58 (right).

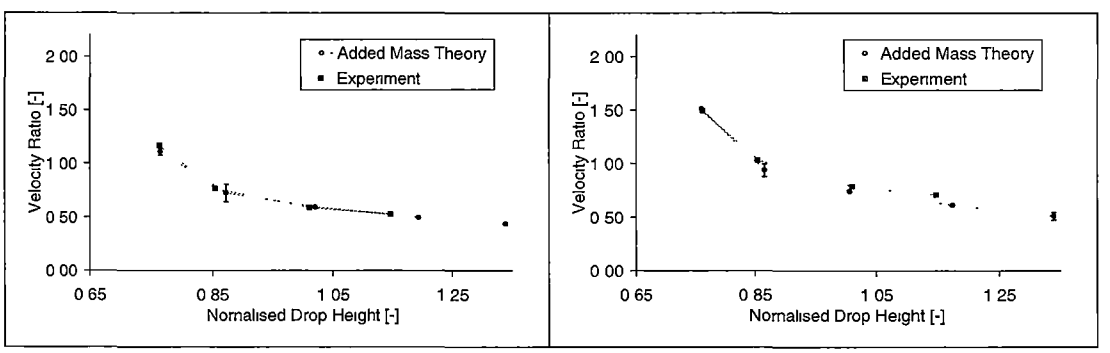

Figure 4.6.23 Velocity ratio for Wedge25 with sideplates. Mass No.=0.29 (left), Mass No.=0.58 (right).

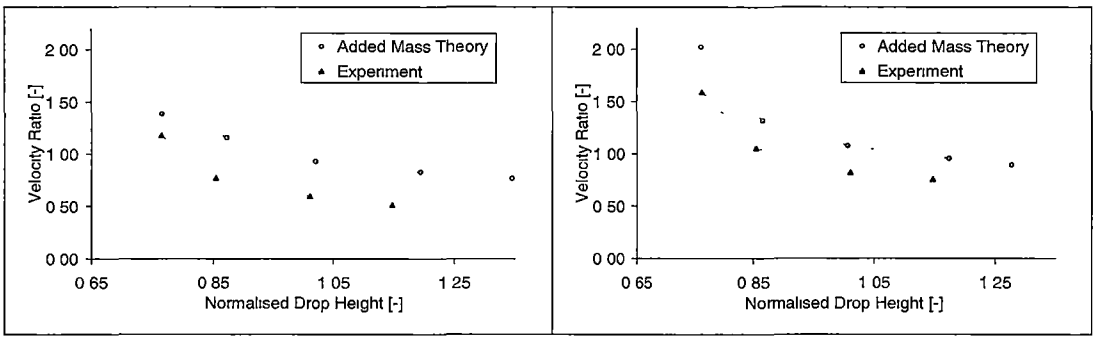

Figure 4.6.24 Velocity ratio for Wedge15 with sideplates. Mass No.=0.29(left), Mass No.=0.58(right)

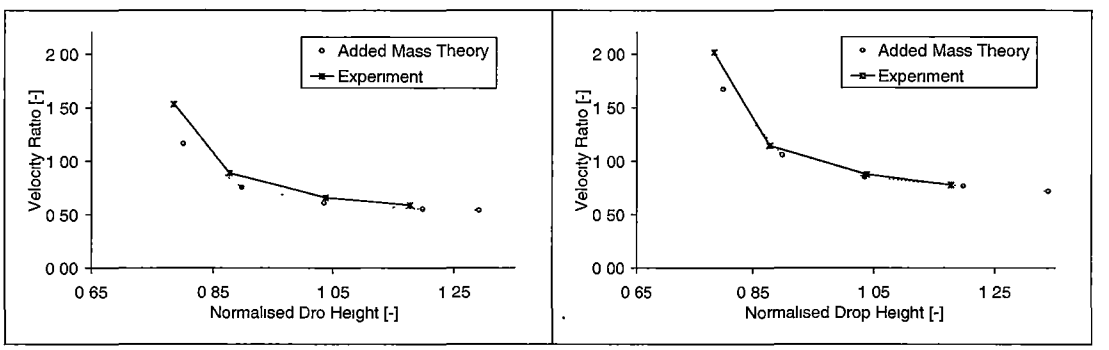

Figure 4.6.25 Velocity ratio for Model J1. Mass No.=0.29(left), Mass No.=0.58(right)

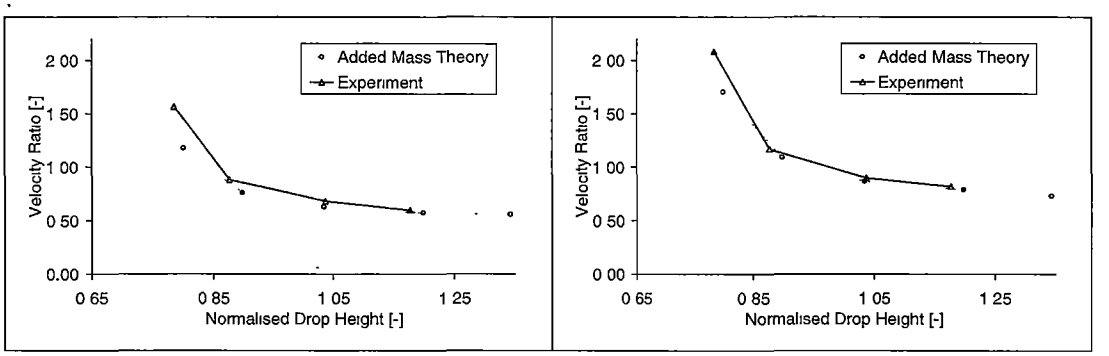

Figure 4.6.26 Velocity ratio for Model J2. Mass No.=0.29(left). Mass No.=0.58(right)

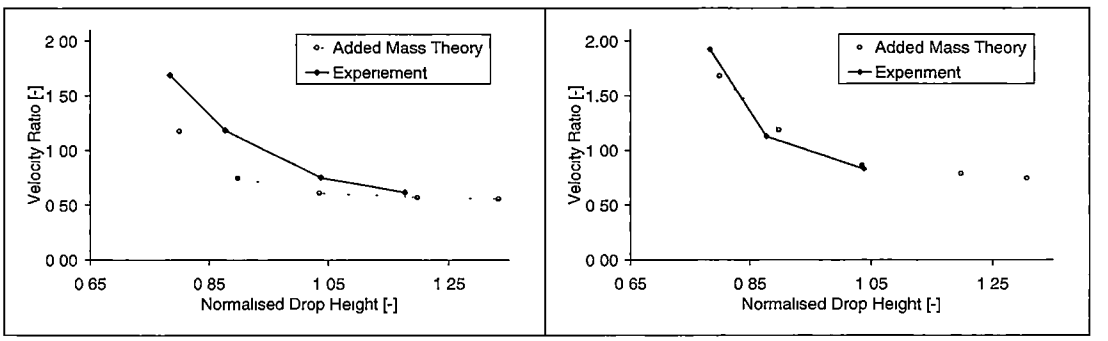

Figure 4.6.27 Velocity ratio for Model J3. Mass No.=0.29(left), Mass No.=0.58(right)

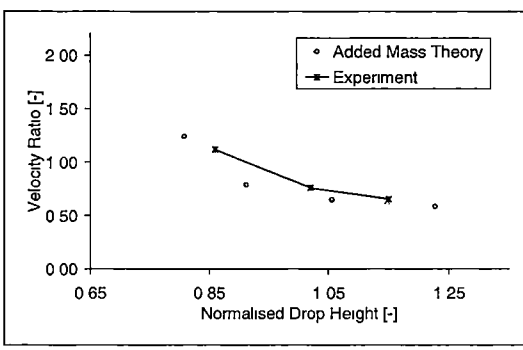

The Model Incat1 was damaged before these readings could be made.

Figure 4.6.28 Velocity ratio for Model Incat1. Mass No.=0.29(left), Mass No.=0.58(right)

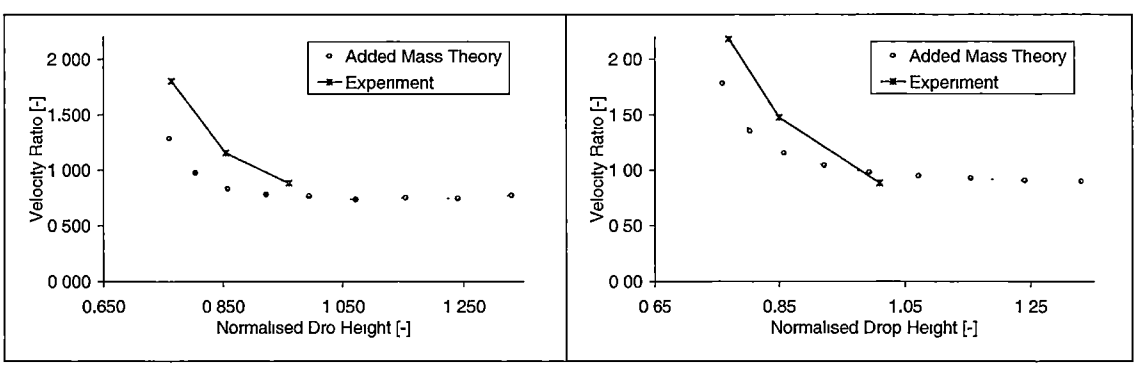

Figure 4.6.29 Velocity ratio for Model Flat1. Mass No.=0.29(left), Mass No.=0.58(right)

4.6.8. Penetration Results

The penetration of the initial water surface by the seven catamaran hull sections at the time instant when they experience peak acceleration (penetration number) was plotted against hull section area ratio (Figure 4.6.30 and Figure 4.6.31). The area ratio is the ratio of the cross sectional area of the hull section beneath the highest point in the arch divided by the product of hull section beam and height ($L \times B$). The results have been plotted for a range of normalised drop heights. However, the normalised drop height corresponding to each point has not been identified because these two graphs are principally to illustrate that the experimental trend of penetration number to decrease with increasing area ratio is correctly predicted by the modified added mass theory. To this end an experimental trend line and an added mass trend line, calculated using a least square linear fit to the experimental data and the theoretical data are plotted on the two graphs. As can be seen, for both mass numbers, the modified added mass trend line and the experimental trend line both decrease with increasing area ratio. The added mass theory trend line at both mass numbers display a lower rate of decrease of penetration number with increasing area ratio than the experimental trend line. A linear fit to both the experimental and theoretical data was considered to be appropriate as the rate of filling of the arch void is dominated by the continuity of fluid volume. Thus if the arch void is smaller, it requires less fluid to fill it. Also the pile up of water around the centre bow and the inside demi-hull will be relatively greater for the hull section with a small arch void and this causes a decrease in penetration number.

The experimental penetration number of the hull section flat1 is seen to be higher than the theoretical prediction. For mass number 0.29 the average theoretical penetration number is 0.96 and the average experimental penetration number is 1.06, and for mass number 0.58 the average theoretical value is 0.99 and the average experimental value is 1.11. The theoretical and experimental penetration number of models J1, J2, and J3 show adequate agreement for both mass numbers as does the incat1 hull section for mass number 0.29. For the two wedge with sideplate hull sections the theoretical penetration number is consistently less than the experimental penetration number and this is particularly the case for hull section wedge15 with sideplates.

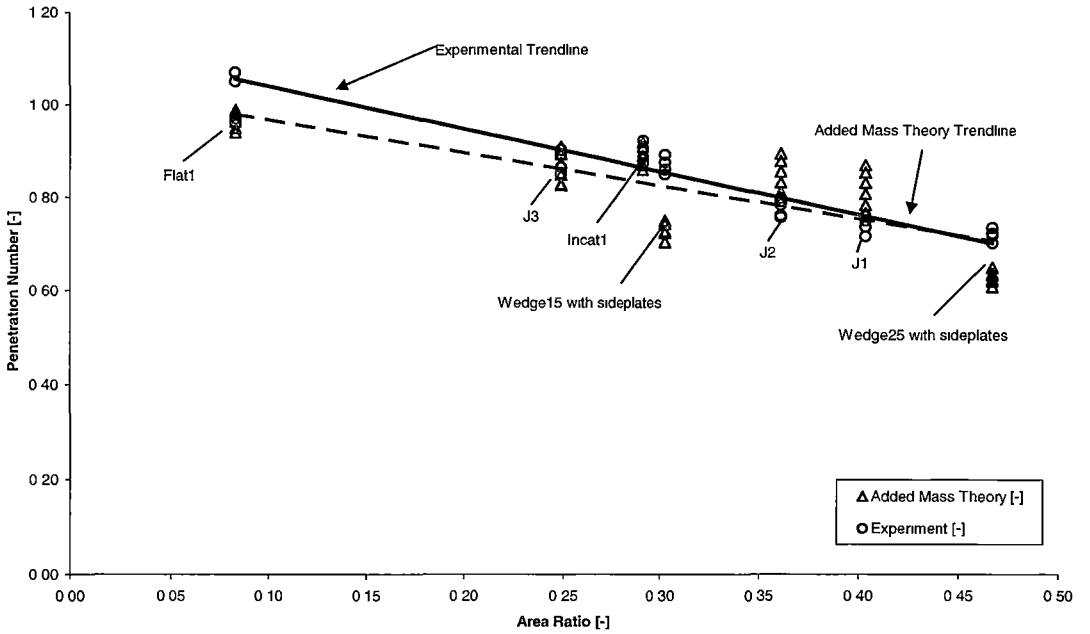

Figure 4.6.30 Penetration number against area ratio for a range of normalised drop heights. Mass Number 0.29

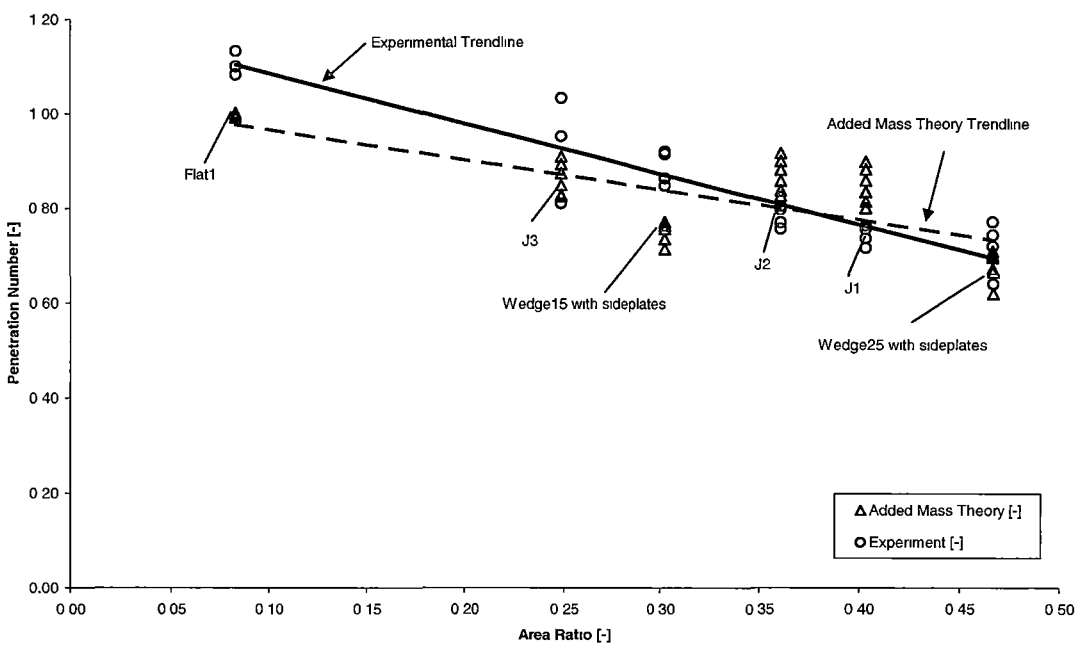

Figure 4.6.31 Penetration number against area ratio for a range of normalised drop heights. Mass Number 0.58

4.7. The Importance of the Highest Point in the Arch

In this section the relationship between the lateral location of the highest point in the arch and the normalised peak acceleration experienced by a hull section of catamaran with centre bow geometry is examined with a simplified added mass analysis. The purpose of this analysis is to identify the effect of the change in added mass between pre and post the arch closure process. This is done by considering the gross change in added mass from that time when a free surface exists at the top of the arch void (pre-arch closure process) to when the arch void is completely filled with fluid (post arch closure process).

In the earlier part of this chapter (section 4.2) the transition from pre-arch closure to post arch closure was modelled with the arch closure process theory. This theory included the effects of a trapped air bubble, the time variation of the added mass associated with the hull section and gravitational, buoyancy and frictional forces. These force components were used to calculate the acceleration against time profile for the hull section during arch closure. In the simplified added mass analysis presented in this section all these forces except those associated with the time variation of the added mass are neglected. The effect of the change in added mass associated with the hull section from pre-arch closure to post arch closure is modelled by considering the impulse that is experienced by the hull section during this process. A normalised mean acceleration during the arch closure process is then calculated by dividing the impulse experienced by a particular hull section by the impulse by the hull section with the highest point in the arch located so that it experiences the maximum impulse. It is assumed that the time scale (Δt_C) for the arch closure process to occur is constant regardless of the lateral location of the highest point in the arch or any other geometric feature of the hull section. This analysis neglects the effects of the normalised drop height, which are subsumed into the arch closure constant time scale assumption.

4.7.1. Theoretical Formulation

During arch closure process the added mass associated with the model changes due to the complete filling of the arch void with fluid. It was assumed that the added mass associated with each separate part of the model that penetrated the still water surface was represented by a von Karman added mass term as in section 4.2. The pre-arch closure added mass was the sum of three added mass terms, one associated with the centre bow and two associated with the demi-hulls. These three distinct added masses were summed because a free surface exists between each demi-hull and the centre bow. Post arch closure the added mass was a single von Karman added mass term with diameter L (see Figure 4.7.1 and equation 4-34)

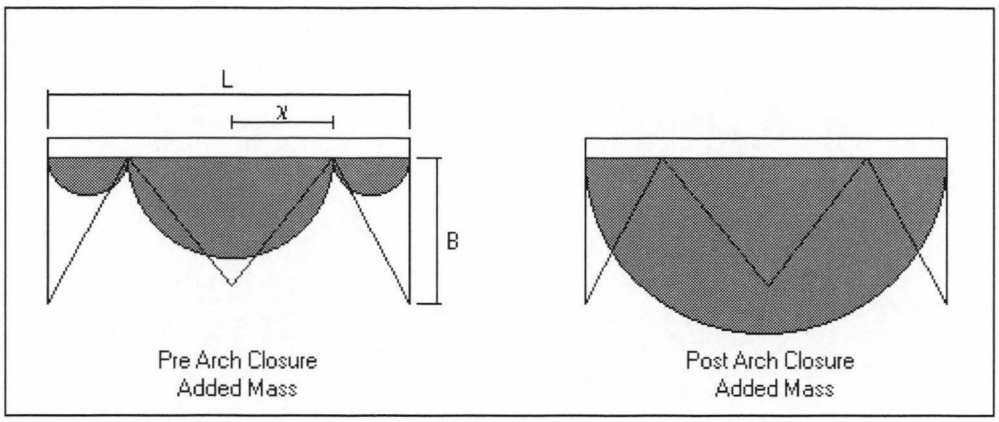

Figure 4.7.1 Highest point in arch added mass definitions.

$$\begin{aligned} m_{a\,\text{pre arch closure}} &= \tfrac{1}{4}\left(\tfrac{L}{2}-\chi\right)^2 \pi\rho + \tfrac{1}{2}\chi^2\pi\rho \\ m_{a\,\text{post arch closure}} &= \tfrac{1}{8}L^2\pi\rho \end{aligned} \tag{4-34}$$

A relationship between the pre and post arch closure hull section velocities was developed by neglecting gravitational, frictional and buoyancy forces and by assuming conservation of linear momentum.

$$\dot{y}_{\text{post arch closure}} = \dot{y}_{\text{pre arch closure}}\left(\frac{m_m + m_{a\,\text{pre arch closure}}}{m_m + m_{a\,\text{post arch closure}}}\right) \tag{4-35}$$

The impulse experienced by the hull section during the arch closure process (I_m) can now be evaluated

$$I_m = m_m\left(\dot{y}_{\text{pre arch closure}} - \dot{y}_{\text{post arch closure}}\right). \tag{4-36}$$

Thus,

$$I_m = m_m \ddot{y}_{\text{mean}}\Delta t_C = m_m \dot{y}_{\text{pre arch closure}}\left(\frac{m_m + m_{a\,\text{pre arch closure}}}{m_m + m_{a\,\text{post arch closure}}} - 1\right). \tag{4-37}$$

Substituting the expression for the added mass,

$$I_m = m_m \ddot{y}_{\text{mean}}\Delta t_C = m_m \dot{y}_{\text{pre arch closure}}\left(\frac{m_m + \frac{1}{4}\left(\frac{L}{2}-\chi\right)^2\pi\rho + \frac{1}{2}\chi^2\pi\rho}{m_m + \frac{1}{8}L^2\pi\rho} - 1\right). \tag{4-38}$$

It assumed that the time scale (Δt_C) over which the arch closure process occurs is constant for a particular normalised drop height regardless of the lateral location of the highest point in the arch. Thus the normalised mean acceleration as a function of the lateral location of the highest point in the arch may be calculated. This is done by normalising (or dividing) the impulse (I_m) experienced by a particular hull section with the impulse experienced by that hull section which has its highest point in the arch located so that it experiences the maximum impulse during the arch closure process. To

determine the lateral location of the highest point in the arch (χ) which causes the maximum impulse during the arch closure process ($I_{m\max}$). The expression for $I_m(\chi)$ is differentiated and the zeroes of the equation found. That is the equation $\frac{dI_m}{d\chi}=0$ is solved. This yields the result

$$\frac{\chi}{L}=\frac{1}{6}. \tag{4-39}$$

That is, when the highest point in the arch is located 1/3 of the distance between the centre line and the side of the hull section, then this hull section will experience a higher impulse than a hull section with any other highest point in the arch location. I_m was then normalised by division by $I_{m\max}$ and substitution of equation 4-34

$$\frac{I_m}{I_{m\max}}=\frac{\ddot{y}_{\text{mean}}}{\ddot{y}_{\text{mean max}}}=\frac{3}{4}+\left(\frac{3\chi}{L}\right)-\left(\frac{3\chi}{L}\right)^2. \tag{4-40}$$

This normalisation process allowed the model mass (m_m) and the time scale (Δt_C) to be cancelled. This was done so that the experimental trends in peak acceleration with the lateral location of the highest point in the arch measured in chapter 3 for the drop tests could be compared with the trend determined from the above simplified added mass analysis.

4.7.2. Highest Point in Arch Results

The relationship between the lateral location of the highest point in the arch and the normalised acceleration experienced by hull sections during the arch closure process (equation 4-40) is plotted in Figure 4.7.2. Also plotted in Figure 4.7.2 are the normalised experimental peak accelerations for models J1, J2, Incat1, wedge15 with sideplates and wedge25 with sideplates. The normalisation process for each experimental hull section is conducted by dividing the peak acceleration experienced by each experimental hull section at a particular normalised drop height by the peak acceleration experienced by hull section J2 at the same normalised drop height. These normalised experimental accelerations are then multiplied by a constant so that the J2 results are made to coincide with the theoretical curve. Experimental results for hull sections J3 and flat1 could not be plotted as it is not possible to define a highest point in the arch for these hull sections as the top of the arch was flat for these two hull sections. The experimental normalised acceleration data points were obtained from a range of normalised drop heights. However no normalised drop height information is given in Figure 4.7.2. This is because the theoretical normalised acceleration equation is derived in such a way that it is only a function of the lateral location of the highest point in the arch. Similarly the method used to normalised the experimental peak accelerations is done so as to cancel the effects of changes in normalised drop height.

Examination of Figure 4.7.2 reveals that as the theoretical normalised arch closure process acceleration reduces as too does the normalised experimental peak accelerations experienced by the drop test hull sections. That is hull section J2 for which the highest point in the arch is located at

$2\chi/L = 0.384$ has the highest normalised peak acceleration. Hull section Incat1 ($2\chi/L = 0.547$) experiences an average normalised peak acceleration over a range of normalised drop heights of 0.91 which compares with the a normalised theoretical acceleration of 0.89 from the added mass theory. Also, the hull section J1 average experimental normalised acceleration of 0.54 that is similar to the value of 0.61 predicted by theory. The results for hull sections wedge25 with sideplates and wedge15 with sideplates reveal that despite having the same location for the highest point in the arch ($2\chi/L = 0.912$), model wedge15 with sideplates experiences a higher normalised peak acceleration. Wedge15 with sideplates experiences an average normalised acceleration of 0.33 that is greater than that experienced by wedge25 with sideplates of 0.24. These two results are comparable to the theoretical normalised acceleration of 0.27.

For each hull section, except hull section J2, the experimental data points display a scatter about the theoretical curve. There is no scatter in experimental normalised acceleration for hull section J2 because it was the peak acceleration values for model J2 which were used to normalised the experimental peak acceleration results. For the other hull sections the scatter in the experimental normalised acceleration for these four hull sections is attributed to two principal factors. Firstly the trend of experimental peak acceleration with normalised drop height was not always monotonic for all models (chapter 3). Hull sections J1, J2 and Incat1 all displayed significantly non-monotonic trends with normalised drop height. Thus when the J2 peak acceleration values are used to normalise the peak accelerations results of the other hull sections this introduces some scatter due to the non-monotonic nature of the J2 peak acceleration results. Also the non-monotonic effects are not consistent for all hull sections, for example the minimum peak acceleration does not always occur at the same normalised drop height for all models. One probable cause of the non-monotonic peak acceleration against normalised drop height trend was that arch closure did not always occur at the same location in the top of the arch void (chapter 3). Thus the geometric highest point in the arch may not necessarily be the actual location where arch closure occurs. The experimental normalised accelerations are for each hull sections plotted at the $2\chi/L$ ratio that corresponds to the location of highest point in arch. If the $2\chi/L$ ratio at which the arch closure actually occurred at a particular normalised drop height then the experimental normalised acceleration data points of each hull section may fit the theoretical curve more closely. Secondly, as identified for hull sections wedge25 with sideplates and wedge15 with sideplates, geometric factors other than the lateral location of the highest point in the arch do effect the peak acceleration experienced by a hull section.

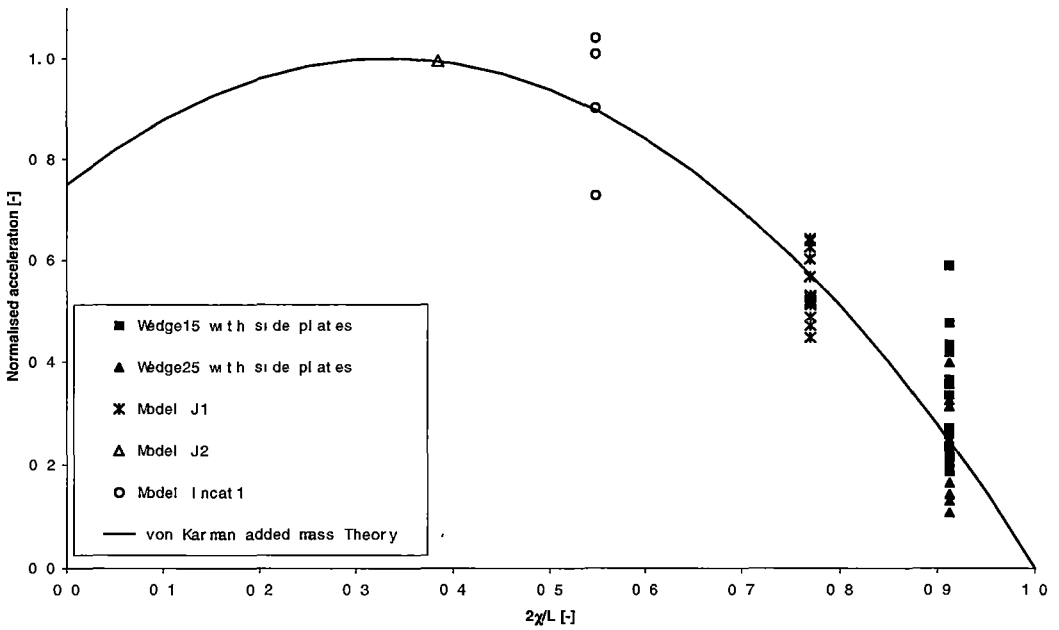

Figure 4.7.2 Theoretical and experimental results for highest point in arch model.

The purpose of this simplified added mass analysis was to theoretically model the trend observed in the experimental drop tests with respect to the lateral location of the highest point in the arch. It was demonstrated that the substantial change in the added mass associated with the arch closure process is a significant cause of the high peak accelerations experienced by hull sections during this process. The lateral location of the highest point in the arch evidently has a significant influence on the relative magnitudes of the acceleration experienced by various hull sections. The intent of this analysis was as first order approximation only.

4.8. Constant Acceleration Ogees

For single hull forms without arch it is possible to control the acceleration history during entry for a specified initial conditions by choice of geometry. In particular acceleration peaks can be reduced. An optimal form would enter with constant acceleration, thus achieving the maximum impulse with minium peak acceleration. Such a hull has an S-shape or ogee form, which can be determined for a given mass number using the von Karman added mass theory as outlined below. The constant acceleration theory is developed because it maybe of interest when designing the centre bow cross section.

4.8.1. Equation of Motion

The motion of a body entering initially still water can be calculated by assuming conservation of linear momentum (L_m). This approach was used in section 4.3.1 in the development of the pre-arch closure modified added mass theory to develop an equation of motion as a function of time (t). In this section an equation of motion is developed as a function of displacement (y). The gravitational,

frictional and buoyancy forces are neglected, thus the time rate change of the vertical linear momentum of the body is,

$$\frac{dL_m}{dt} = \frac{dL_m}{dy}\frac{dy}{dt} = \Sigma F = 0 \tag{4-41}$$

As discussed in section 4.2, the transfer of linear momentum between a body entering an initially still body of water can be modelled using the von Karman added mass expression. Thus the linear momentum of a body and the associated added mass when the body has entered the water to some amount y then,

$$L_m = \dot{y}(m_m + m_a). \tag{4-42}$$

Where the added mass is a function of half the wetted width of the body (C),

$$m_a = \frac{C^2 \pi \rho}{2}. \tag{4-43}$$

And hence differentiating L_m with respect to y and then t and rearranging,

$$\dot{y}\frac{dm_a}{dy} + m_a\frac{d\dot{y}}{dy} + m_m\frac{d\dot{y}}{dy} = \frac{\Sigma F}{\dot{y}} = 0 \tag{4-44}$$

Equation 4-44 was solved numerically by discretisation in y and application of a Taylor series expansion about the j th y position.

$$\begin{aligned}
y_{J+1} &= y_J + \Delta y \\
\dot{y}_{J+1} &= \dot{y}_J + \left.\frac{d\dot{y}}{dy}\right|_J \Delta y \\
C_{J+1} &= C(y_{J+1}) \\
\left.\frac{dm_a}{dy}\right|_{J+1} &= \frac{(C_{J+1}^2 - C_j^2)\pi\rho}{2\Delta y} \\
m_{a\,J+1} &= \frac{C_{J+1}^2 \pi \rho}{2} \\
\left.\frac{d\dot{y}}{dy}\right|_{J+1} &= \frac{-\dot{y}_{J+1}\left.\frac{dm_a}{dy}\right|_{J+1}}{m_m + m_{a\,J+1}} \\
\ddot{y} &= \dot{y}_{J+1}\left.\frac{d\dot{y}}{dy}\right|_{J+1}
\end{aligned} \tag{4-45}$$

4.8.2. Equation of Ogee Geometry

Equation 4-44 gives $\dot{y}$ as a function of m_a which is a function of $C(y)$, the wetted half width of the body. From conservation of linear momentum the relationship between initial and final model velocities is found. Noting also that B is the vertical distance between the keel of the hull section and top of the hull section. $C(B)$ is half the beam of the top of the hull section, thus,

$$m_m \dot{y}(0) = (m_m + m_a)\dot{y}(B). \tag{4-46}$$

Rearranging and substituting the expression for the added mass of the hull section when it is submerged by an amount of B,

$$\dot{y}(B) = \frac{1}{\left(1 + \frac{\pi\rho c(B)^2}{2m_m}\right)} \dot{y}(0). \tag{4-47}$$

Equating work done on the model and the change in energy and requiring that the model undergoes a constant acceleration (a) during impact with the water, then

$$\dot{y}\frac{d\dot{y}}{dy} = a = \frac{\dot{y}(B)^2 - \dot{y}(0)^2}{2B} \tag{4-48}$$

Substituting the discretised expressions for equation 4-44 into equation 4-48

$$\ddot{y} = a = \frac{-\dot{y}_{j+1}^2 \left.\frac{dm_a}{dy}\right|_{j+1}}{m_m + m_{a\,j+1}}. \tag{4-49}$$

Thus,

$$a = \frac{-\dot{y}_{j+1}^2 \frac{\left(C_{j+1}^2 - C_j^2\right)\pi\rho}{2\Delta y}}{m_m + \frac{C_{j+1}^2 \pi\rho}{2}}. \tag{4-50}$$

Rearranging to solve for c_{j+1},

$$C_{j+1} = C\left(y_{j+1}\right) = \sqrt{\frac{\frac{\dot{y}_{j+1}^2 \pi\rho}{2\Delta y} C_j^2 - am_m}{\frac{a\pi\rho}{2} + \frac{\dot{y}_j^2 \pi\rho}{2\Delta y}}} \tag{4-51}$$

For a given mass number, simultaneous solution of equation 4-44 and equation 4-51 will yield a hull section geometry that will experience a constant acceleration during impact with an initially still body of water.

4.8.3. Constant Acceleration Ogee Geometries

The geometries of the constant acceleration ogee hull sections for a range of mass numbers are shown in Figure 4.8.1. These hull sections have been calculated using the method developed in section 4.8. The geometries have been normalised by B (vertical axis) and $L/2$ (horizontal axis) so as to have a scaled height of 1.0 and scaled half beam of 1.0. It is noted that as the mass number tends to infinity the profile of the ogee approaches a parabolic form, as predicted by Arai et al (1995). It is observed that the lower the mass number the finer the hull section initially is. The upper portions of the lower mass number hull sections are bluffer than the corresponding portion of the higher mass number hull sections.

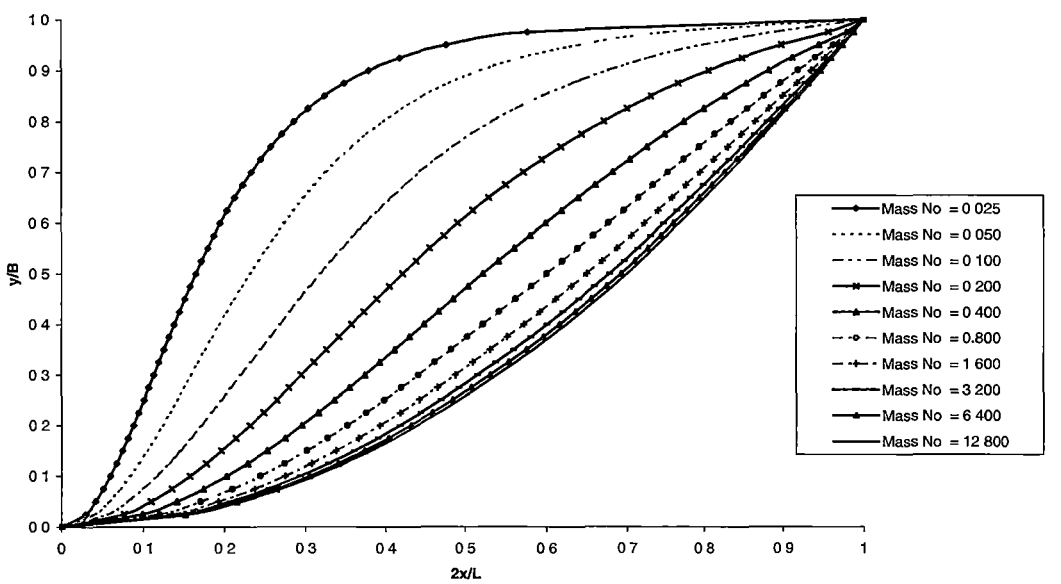

Figure 4.8.1 Constant acceleration ogee geometries for various mass numbers.

4.8.4. Ogee Acceleration against Displacement Records

Acceleration against displacement graphs for four different constant acceleration ogees are calculated for a normalised drop height of 0.7192 in Figure 4.8.3 and Figure 4.8.4. The geometries of these four ogees were obtained by calculation using mass numbers 0.025, 0.100, 0.400 and 12.800 and they are plotted in Figure 4.8.2. As can be seen in this figure these geometries have been scaled to have the same L/B ratio as a 25° wedge. This has been done to allow the comparison of the performance of constant acceleration ogee forms with the performance of a simple vee wedge geometry. When calculating the acceleration against displacement graph for each of the four ogees the mass number used in each calculation corresponded to the mass number for which each constant acceleration ogee was optimised. For example the acceleration against displacement graph for the ogee geometry determined for mass number 0.025 was calculated using a mass number of 0.025. As can be seen in Figure 4.8.3 and Figure 4.8.4 the acceleration against displacement graph for each of the ogees

(denoted by a line with open triangles) is in each case a horizontal line. This of course represents a constant acceleration which is what the constant acceleration ogees were contrived to experience.

Also shown in Figure 4.8.3 and Figure 4.8.4, for comparative purposes are the acceleration against displacement records for 25° wedge hull sections. For each of the four records 25° wedge impacts the water from a normalised drop height of 0.7192. The mass number for each of the four records however changes so that it is the same in each case as the mass number of the ogee with which it is being compared. That is, when the performance of the 25° wedge is being compared with the ogee calculated for mass number 0.025, then the 25° wedge acceleration record is calculated with a mass number of 0.025. The 25° wedge acceleration records are calculated using the modified added mass theory developed previously in this chapter. Examination of Figure 4.8.3 and Figure 4.8.4 reveals that is each case the 25° wedge experiences a higher peak acceleration than the corresponding ogee. For mass number 0.025 the 25° wedge experiences a peak acceleration at $y = 0.05$ m that is 6 times larger the ogee peak acceleration. However once the 25° wedge has penetrated the initial water surface by $y = 0.135$ m its acceleration becomes less than that experienced by the ogee, and after $y = 0.25$ m the acceleration of the wedge becomes very small indeed. A similar trend is displayed for mass number 0.100. For this mass number the wedge experiences a peak acceleration which is 3 times larger than that of the 0.100 mass number ogee and occurs when $y = 0.1$ m. Once the wedge has penetrated the undisturbed free surface by 0.20m its acceleration becomes less than that experienced by the ogee. When the mass number is increased to 0.400 the peak acceleration experienced by the wedge becomes 1.5 times greater than that experienced by the mass number 0.400 ogee. The acceleration of the wedge is initially less than that of the wedge until the wedge has penetrated the undisturbed free surface by 0.06m. The acceleration of the wedge remains larger than the ogee until a displacement of 0.34m is reached. At mass number 12.8 the acceleration experienced by the wedge is initially less than the ogee until y=0.14. The acceleration of the wedge then continues to increase until a maximum is obtained.

In each of the four acceleration against displacement results it can be observed that the 25° wedge records terminate before the ogee records terminate. This is because the pile up of water around the wedge is included in the modified added mass theory, but this is not the case in constant acceleration ogee theory. It is this pile up of water that causes the earlier termination of the acceleration against displacement record for the wedge. To quantify this pile up of water acceleration against displacement result for each of the four ogee geometries, at appropriate mass numbers, were calculated which included the effect of the pile up of water. This was done using the modified added mass theory. These results are shown in Figure 4.8.3 and Figure 4.8.4 (dark solid line). For each ogee geometry including the effects of the pile up of water around the ogee causes an increase in the peak acceleration experienced by the ogee compared with the constant acceleration ogee calculation alone. The peak acceleration remains, in all four cases, less than that experienced by the wedge. The acceleration record for the ogees calculated with the modified added mass theory is seen to terminate

earlier than the acceleration record calculated using the constant acceleration ogee theory. This is attributed to the pile up of water around the ogee.

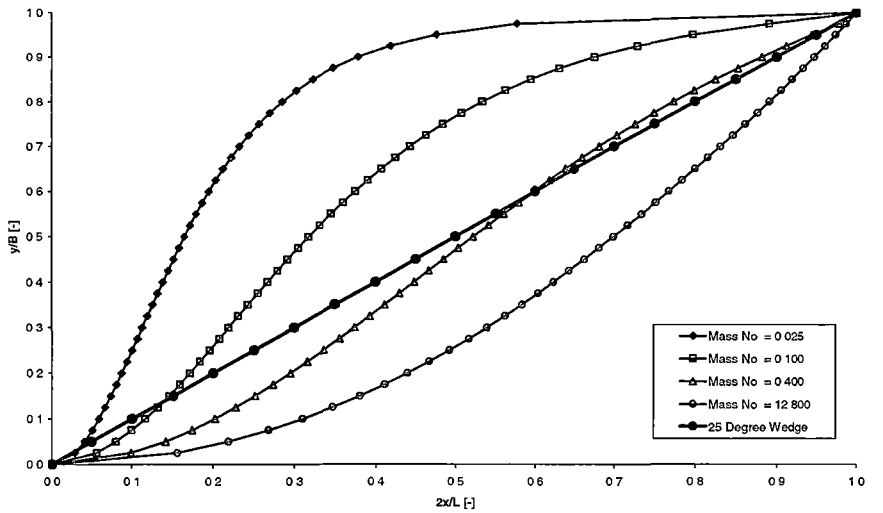

Figure 4.8.2 Four different constant acceleration ogee geometries for the comparison of acceleration profiles with a 25 degree vee wedge geometry.

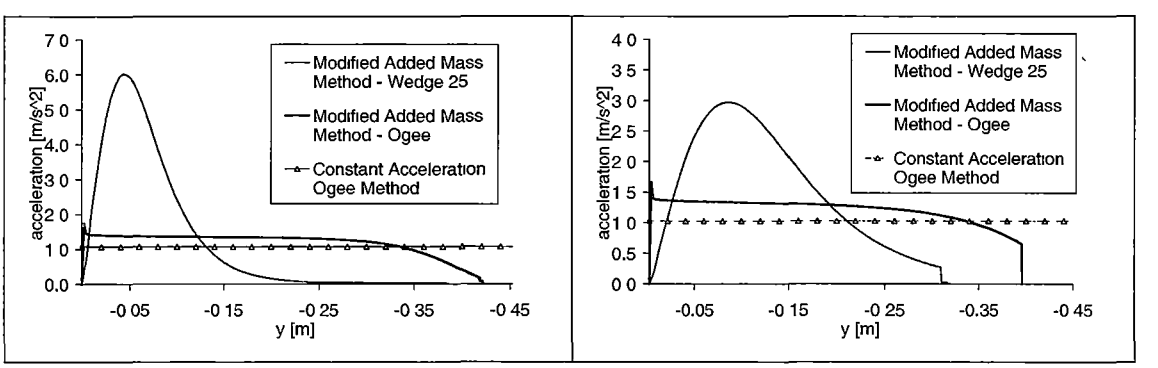

Figure 4.8.3: Optimised ogees acceleration against displacement records. Mass number 0.025 (left), Mass Number 0.100 (right)

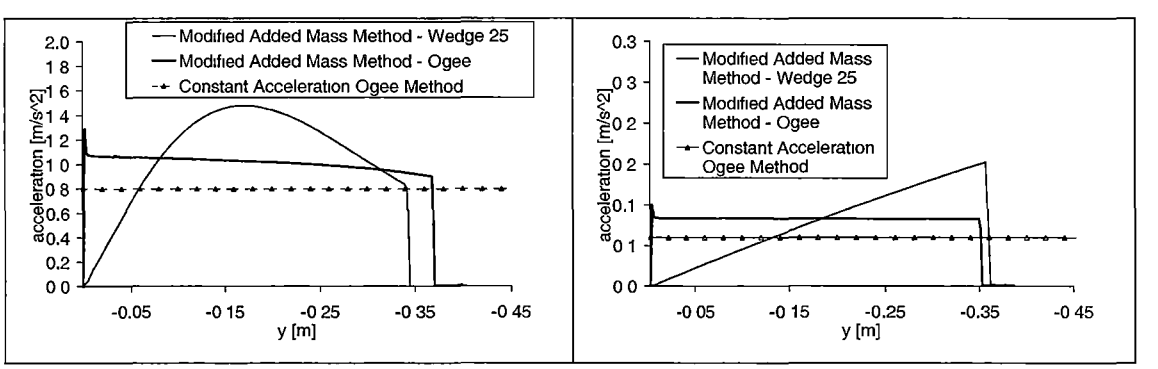

Figure 4.8.4: Optimised ogee acceleration against displacement records. Mass number 0.400 (left), Mass Number 12.800 (right)

4.8.5. Comparison of 25° Wedge and Ogee Peak Acceleration

In section 4.8.3 10 different constant acceleration ogee geometries were calculated for 10 mass numbers. These geometries are shown in Figure 4.8.1. In section 4.8.4 it was observed that four ogee geometries (calculated for four different mass numbers) experienced lower peak accelerations than the 25° wedge hull section tested a mass numbers corresponding to the mass number for which each ogee was optimised. In this section the reduction in peak acceleration that an optimised ogee will experience compared with a 25° wedge is quantified. The basis for comparison is that the ogee geometries are tested at the mass numbers for which they are individually optimised for and a peak acceleration is calculated. This peak acceleration is then compared with the peak acceleration calculated for the 25° wedge being tested at the same mass number. The results of this analysis are shown in Figure 4.8.5. The peak accelerations experienced by the 25° wedge at a particular mass number are normalised by the peak acceleration of the corresponding constant acceleration ogee at the same mass number.

As observed in Figure 4.8.5 the normalised peak acceleration of the constant acceleration ogee over all mass numbers is of course 1.0 as each of these peak accelerations is divided by itself during normalisation. The normalised peak acceleration of the 25° wedge is observed to be initially high (greater than 5) and then reduces with increasing mass number until a minimum of 1.77 is obtained at mass number 0.8. The normalised peak acceleration than increases gradually until mass number 12.400.

Also plotted in Figure 4.8.5 are the normalised peak accelerations of the 10 ogees calculated using the modified added mass theory. Thus theory incorporates the pile up of the water around the ogees. As can be observed including the effects of the pile up of water increases the normalised peak acceleration experienced by the ogee by approximately 50% regardless of mass number. However the maximum normalised peak accelerations remain less than those experienced by the 25° wedge.

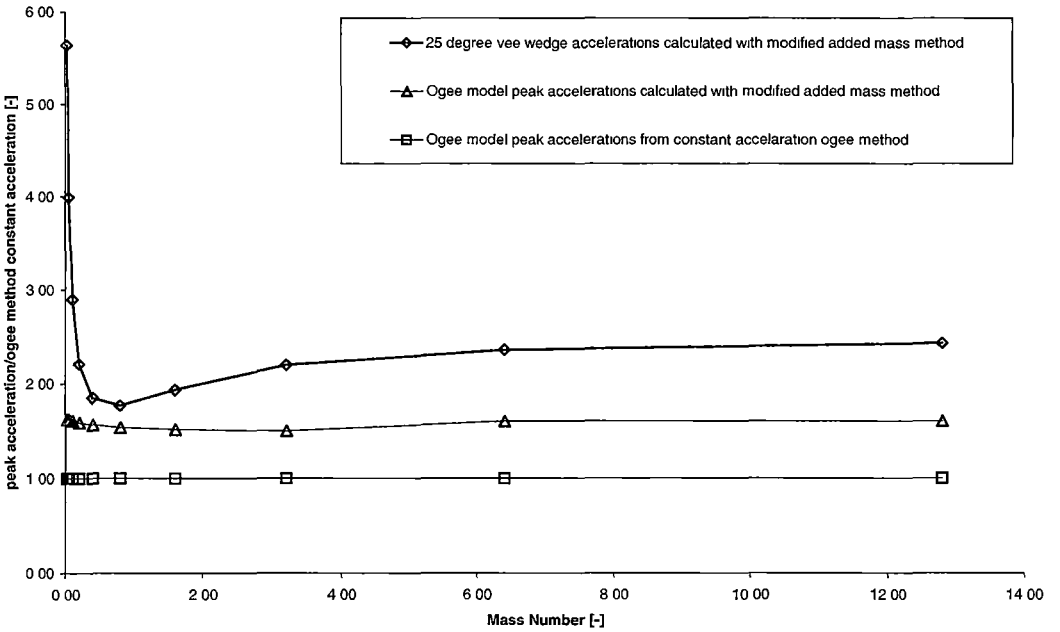

Figure 4.8.5 Comparison of peak accelerations for 25-degree wedge, ogee acceleration calculated with modified von Karman method and constant acceleration ogee method.

4.9. Summary

Added mass theory was used to investigate the impact of various two-dimensional geometric hull sections on initially calm fluid. The theory included the effects of the pile up of fluid around the hull section during entry. A special theory was developed to model the situation that occurs when a catamaran with centre bow hull section penetrates the fluid sufficiently deeply that the arch void completely fills with fluid. This arch closure theory included the effects of the trapped compressible air. The added mass theory predicted the correct trends in the peak acceleration and velocity ratios with normalised drop height for eight of the nine model hull sections tested. The penetration number with hull section area ratio for the catamaran hull sections was also predicted moderately well. The transient acceleration against time records and the free surface deformation with time records were predicted moderately well for seven of the nine hull sections tested.

Added mass theory was also used to identify the importance of the highest point in the arch for catamaran with centre bow hull sections and to develop a low acceleration 'ogee' hull geometry. It was found that the highest point in the arch should be located as far from the centre line of the model as possible. Hull sections with this geometric feature experienced significantly lower peak accelerations.

5. Volume of Fluid Model

5.1. Overview

An improved free surface tracking method (micro-VOF) is presented in this chapter for use in numerical solutions of unsteady, inviscid, incompressible free surface flow problems involving fluid-structure interaction. Problems of this sort are governed by the Euler and continuity equations. These equations may be solved numerically using an Eulerian grid and the porosity finite difference scheme of Hirt and Sicilian (1985). The evolution of the free surface is solved for using the micro-VOF method of Whelan, Davis and Holloway (2002). This numeric scheme is validated against two test problems, these being the collapsing column of water problem and the run up of a Laitone solitary wave on a vertical wall. The numeric model is then used to model the free surface flow about 15° and 25° vee wedges impacting water at a constant velocity. Results of these test problems compare adequately with experimental and other numerical results for these problems.

The content of this chapter is of interest within the context of the current study as it demonstrates that the finite difference volume of fluid class of solutions is an appropriate, promising and flexible solution method of investigating water entry events.

5.2. Governing Equations

Two-dimensional, unsteady, inviscid, incompressible free surface flow problems are governed by the continuity (5-1) and Euler (5-2) equations

$$\nabla\cdot(\rho\vec{u})=0 \tag{5-1}$$

$$\frac{\partial\rho\vec{u}}{\partial t}+(\rho\vec{u}\cdot\nabla)\vec{u}=-\nabla P+\rho(\vec{g}+\vec{a}). \tag{5-2}$$

The Euler and continuity equations can be solved numerically on a rectangular grid with appropriate finite difference approximations to for the terms of the equations. Such numerical schemes have been presented for example by Harlow and Welch (1965), Chan and Street (1970), Hirt and Nichols (1981), Miyata (1986), and Chen, Johnson, Raad and Fadda (1997). When the flow about rigid bodies of arbitrary geometry is required to be solved modifications to the basic rectangular grid finite difference scheme is required. One approach to enable the solution of flow about arbitrary shaped bodies on a rectangular grid is the porosity method of Hirt and Sicilian (1985). This approach has been used previously by Arai (1989) to examine two-dimensional water entry problems and for this reason the porosity method is adopted for the current study. The details of the porosity method are presented here for completeness.

5.3. The Porosity Method

Consider a small region (R) with boundary (S) (Figure 5.3.1).

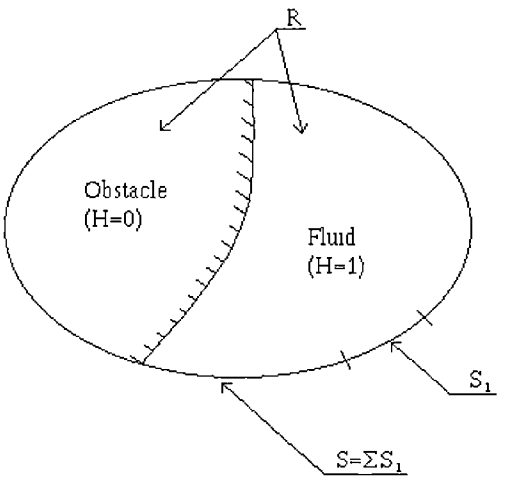

Figure 5.3.1 Small region (R) with boundary (S) showing porosity.

Introducing the notion of porosity ($H(x,y)$) which takes the value $H(x,y)=1$ when the point (x,y) is located in the fluid and $H(x,y)=0$ when (x,y) is located within an obstacle. The porosity can be incorporated into equations (5-1) and (5-2) to yield

$$\nabla\cdot(\rho H\vec{u})=0 \tag{5-3}$$

$$\frac{\partial\rho H\vec{u}}{\partial t}+(\rho H\vec{u}\cdot\nabla)\vec{u}=-H\nabla P+\rho H(\vec{g}+\vec{a}) \tag{5-4}$$

Equations (5-3) and (5-4) can be integrated over some region R with boundary S

$$\frac{1}{R}\int_S \rho H\vec{u}\cdot\hat{n}dS=0 \tag{5-5}$$

$$\frac{1}{R}\int_R\frac{\partial\rho H\vec{u}}{\partial t}dR+\frac{1}{R}\int_S\rho H\vec{u}(\vec{u}\cdot\hat{n})dS=\frac{1}{R}\int_R(-H\nabla P+\rho H(\vec{g}+\vec{a}))dR \tag{5-6}$$

Let $A=\frac{1}{R}\int_R HdR$ and $L_t=\frac{1}{S_t}\int_{S_t}HdS$.

5.3.1. Boundary Conditions

Consider now the boundary conditions that are required to be satisfied to model the wedge entry problem. These boundary conditions are shown in Figure 5.3.2.

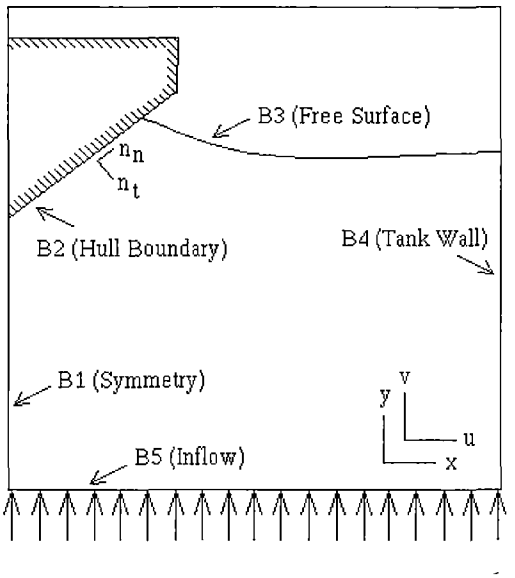

Figure 5.3.2 The boundary conditions and the computational domain.

The boundary condition on boundary B1 is a symmetry condition along the centre line of the wedge thus

$$u = 0 \tag{5-7}$$

$$\frac{\partial v}{\partial x} = 0. \tag{5-8}$$

Boundary B2 represents the rigid side of the wedge. In this formulation the wedge is fixed in the finite difference grid and the fluid is made to flow around it with constant velocity, thus

$$\bar{u}_n = 0 \tag{5-9}$$

$$\frac{\partial \bar{u}_t}{\partial \hat{n}} = 0. \tag{5-10}$$

Free Surface of the fluid is boundary B3. The position of this surface will vary throughout the simulation. The free surface is exposed to atmospheric pressure

$$p = p_a. \tag{5-11}$$

Boundary B4 is modelled as a tank wall, thus

$$u = 0 \tag{5-12}$$

$$\frac{\partial v}{\partial x} = 0. \tag{5-13}$$

Finally boundary B5 is an inflow boundary at which an inflow at a constant velocity is applied,

$$u = 0 \tag{5-14}$$

$$v = V . \tag{5-15}$$

5.3.2. Numerical Implementation

The equations (5-3) and (5-4) are solved by discretisation of the partial derivative terms in these two equations on a rectangular grid as shown in Figure 5.3.3.

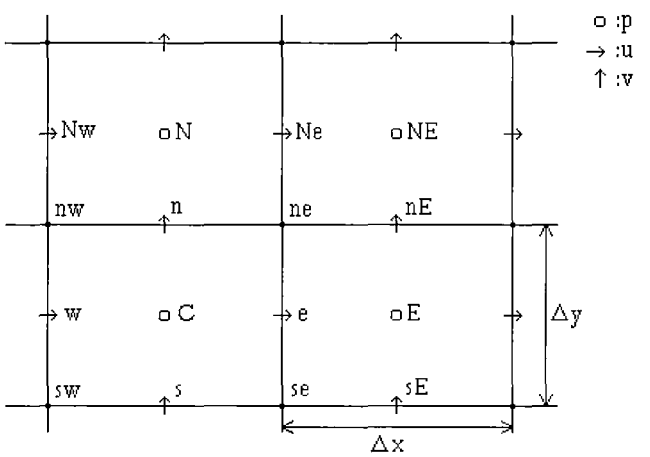

Figure 5.3.3 A rectangular computational grid and the location of primary variables.

Thus the continuity equation (5-3) becomes

$$\frac{\langle Hu \rangle_e - \langle Hu \rangle_w}{\Delta x} + \frac{\langle Hv \rangle_n - \langle Hv \rangle_s}{\Delta y} = 0 . \tag{5-16}$$

The Euler equation in the x direction is expanded to

$$\frac{A_e u_e^{n+1} - A_e u_e^n}{\Delta t} + \frac{\langle Huu \rangle_E - \langle Huu \rangle_C}{\Delta x} + \frac{\langle Hvu \rangle_{ne} - \langle Hvu \rangle_{se}}{\Delta y} = -A_e \frac{(p_E - p_C)}{\Delta x} . \tag{5-17}$$

Substituting

$$\varsigma_e = u_e^n - \frac{\Delta t}{A_e}\left(\frac{\langle Huu \rangle_E - \langle Huu \rangle_C}{\Delta x} + \frac{\langle Hvu \rangle_{ne} - \langle Hvu \rangle_{se}}{\Delta y} \right) \tag{5-18}$$

equation (5-17) can be re-arrange to allow the calculation of u_e^{n+1}. Thus

$$u_e^{n+1} = \varsigma_e - \Delta t \frac{(p_E - p_C)}{\Delta x} \tag{5-19}$$

Similarly the Euler equation in the y direction expands to

$$\frac{A_n v_n^{n+1} - A_n v_n^n}{\Delta t} + \frac{\langle Huv \rangle_{ne} - \langle Huv \rangle_{nw}}{\Delta x} + \frac{\langle Hvv \rangle_n - \langle Hvv \rangle_s}{\Delta y} = -A_n \frac{(p_N - p_C)}{\Delta y} + A_n (g_y + a_y).$$

(5-20)

Substituting

$$\xi_n = v_n^n - \frac{\Delta t}{A_n}\left(\frac{\langle Huv \rangle_{ne} - \langle Huv \rangle_{nw}}{\Delta x} + \frac{\langle Hvv \rangle_n - \langle Hvv \rangle_s}{\Delta y} - A_n (g_y + a_y) \right), \tag{5-21}$$

equation (5-20) is similarly re-arranged to allow the time stepping of v_n^{n+1}. Thus

$$v_n^{n+1} = \xi_n - \Delta t \frac{(p_N - p_C)}{\Delta y}. \tag{5-22}$$

The discretisation scheme used for the calculation of the advection terms in (5-17) and (5-20) is as follows

$$\langle Hu \rangle_e = L_e u_e \tag{5-23}$$

$$\langle Hv \rangle_n = L_n v_n \tag{5-24}$$

$$\begin{aligned} \langle Huu \rangle_C &= \langle Hu \rangle_C u_C^* \\ &= \frac{\langle Hu \rangle_e + \langle Hu \rangle_w}{2} u_C^* \end{aligned} \tag{5-25}$$

$$\begin{aligned} u_C^* &= u_w \text{ if } u_e + u_w \geq 0.0 \\ &= u_e \text{ if } u_e + u_w < 0.0 \end{aligned}. \tag{5-26}$$

The values of A_e and A_n are calculated by linear averaging

$$A_e = \frac{A_C + A_E}{2}, \tag{5-27}$$

$$A_n = \frac{A_C + A_N}{2}. \tag{5-28}$$

The pressure field is required for calculation of (5-19) and (5-22). Three different numeric schemes are used to solve for the pressure field: one scheme for grid cells in which $H = 1$ and are completely full of fluid, a second scheme for cells which contain a free surface and a third scheme for grid cells which contain a segment of the hull boundary ($H < 1$).

The pressure field in grid cells in which the porosity is unity and which are completely full of fluid are solved by ensuring that the continuity equation is satisfied at the n+1 time step, thus

$$\frac{\langle Hu\rangle_e^{n+1}-\langle Hu\rangle_w^{n+1}}{\Delta x}+\frac{\langle Hv\rangle_n^{n+1}-\langle Hv\rangle_s^{n+1}}{\Delta y}=0. \tag{5-29}$$

Substituting equations (5-19) and (5-21) in to (5-29)

$$\frac{L_e\left(\varsigma_e-\Delta t\dfrac{(p_E-p_C)}{\Delta x}\right)-L_w\left(\varsigma_w-\Delta t\dfrac{(p_C-p_W)}{\Delta x}\right)}{\Delta x}+\frac{L_n\left(\xi_n-\Delta t\dfrac{(p_N-p_C)}{\Delta y}\right)-L_s\left(\xi_s-\Delta t\dfrac{(p_C-p_S)}{\Delta y}\right)}{\Delta y}=0 \tag{5-30}$$

Letting

$$S_C=\frac{L_e\varsigma_e-L_w\varsigma_w}{\Delta x}+\frac{L_n\xi_n-L_s\xi_s}{\Delta y} \tag{5-31}$$

then

$$p_C=\frac{\dfrac{(L_wp_W+L_ep_E)}{\Delta x^2}+\dfrac{(L_np_N+L_sp_S)}{\Delta y^2}-\dfrac{S_C}{\Delta t}}{\dfrac{(L_w+L_e)}{\Delta x^2}+\dfrac{(L_n+L_s)}{\Delta y^2}}. \tag{5-32}$$

Equation (5-32) is solved using a successive over relaxation method

$$p_C^{k+1}=p_C^k+\omega_f\left(p_C^{\text{computed}}-p_C^k\right). \tag{5-33}$$

The pressure field in grid cells in which a free surface exists is solved using a modified version of the irregular star method of Chan and Street (1970). Equation (5-32) can be written in the form -

$$S_C=\Delta t\frac{\partial}{\partial x}\left(L\frac{\partial p}{\partial x}\right)+\Delta t\frac{\partial}{\partial y}\left(L\frac{\partial p}{\partial y}\right). \tag{5-34}$$

Approximating the derivatives using first order centred differencing, then (for example)

$$\left(\frac{\partial p}{\partial x}\right)_e=\frac{p_E-p_C}{\eta_1}. \tag{5-35}$$

where η_1 is defined in Figure 5.3.4.

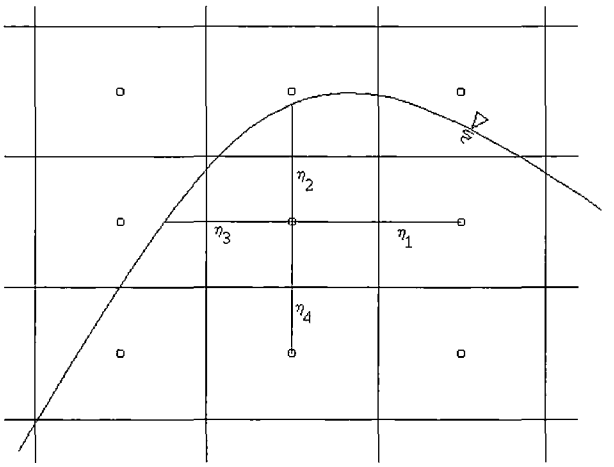

Figure 5.3.4 Irregular star leg lengths used in the computation of pressure in grid cells containing a free surface.

Thus by substitution into equation (5-34)

$$p_C = \frac{\dfrac{\eta_3 L_e p_E + \eta_1 L_w p_W}{\eta_1\eta_3\left(\dfrac{\eta_1+\eta_3}{2}\right)} + \dfrac{\eta_4 L_n p_N + \eta_2 L_s p_S}{\eta_2\eta_4\left(\dfrac{\eta_2+\eta_4}{2}\right)} - \dfrac{S_C}{\Delta t}}{\dfrac{\eta_3 L_e + \eta_1 L_w}{\eta_1\eta_3\left(\dfrac{\eta_1+\eta_3}{2}\right)} + \dfrac{\eta_4 L_n + \eta_2 L_s}{\eta_2\eta_4\left(\dfrac{\eta_2+\eta_4}{2}\right)}}. \tag{5-36}$$

Equation (5-36) is solved using successive over relaxation

$$p_C^{k+1} = p_C^k + \omega_f\left(p_C^{\text{computed}} - p_C^k\right). \tag{5-37}$$

The pressure field in grid cells containing a segment of the hull is solved using the method of Viecelli (1971) in which the requirement that the normal fluid velocity to the hull boundary is zero is satisfied. This is done by varying the pressure in the grid cell until the fluid flux across the hull boundary is zero. Adopting an over relaxation formulation the pressure is solved for using iteration, thus

$$p_C^{k+1} = p_C^k - \frac{\omega_h}{2\left(\dfrac{1}{\Delta x}+\dfrac{1}{\Delta y}\right)\Delta t}\vec{u}_p^{\,k}\cdot\hat{n}_p. \tag{5-38}$$

$\vec{u}_p^{\,k}\cdot\hat{n}_p$ is the normal velocity of the fluid at the centre point of the line segment defining the hull boundary. The bilinear velocity interpolation scheme of Harlow and Welch (1965) is used to calculate this velocity value. This velocity is required to be recalculated at each successive relaxation iteration step (k^{th} iteration).

To ensure the convergence of the pressure field relaxation parameters in the successive over relaxation solution algorithm are selected to have the values $\omega_f = 1.4$ and $\omega_h = 0.8$.

5.4. Micro-VOF Surface Tracking

In unsteady fluid flow problems involving a free surface the evolution of the free surface must be solved for as its spatial and temporal location is not known a priori. There are five major methods of solving for the evolution of the free surface. These include marker particles (Harlow and Welch 1965, Amsden and Harlow 1970) a method that tracks the location of the fluid by the use of marker particles that move with the fluid. The drawback of this method is the large memory and computational requirements to store and flux the marker particles. Also it is difficult to reconstruct the exact location of the free surface. Height functions (Nichols and Hirt 1976, Lardner and Song 1992) track the height of the free surface above some reference line as a function of location and time. This method is limited to problems in which the free surface is single valued. Line segment methods (Chan and Street 1970) use an ordered list of line segments to identify the free surface. These methods experience difficulties when two surfaces interact in an arbitrary manner and the list needs to be reordered. The surface marker and micro cell method (Raad, Chen and Johnson 1995) combines the ideas of marker particles and area flagging. Marker particles are placed on the free surface and are used to flag grid cells (micro cells) that are finer than the computational mesh used for the solution of the pressure and velocity fields. This method only allows for the free surface pressure boundary condition to be applied to within the accuracy of the micro cells. The volume of fluid method (Hirt and Nichols 1981, Varyani, Gatiganti and Gerigk 2000) uses a scalar function F that represents the fractional volume of fluid in a mesh cell. A grid cell with F=1.0 is considered full, with F=0.0 is considered empty and if 0.0<F<1.0 the grid cell may contain a free surface. The scalar variable F moves with the fluid:

$$\frac{\partial F}{\partial t} + u\frac{\partial F}{\partial x} + v\frac{\partial F}{\partial y} = 0 \qquad (5\text{-}39)$$

The volume of fluid method has the advantages that the memory storage requirements are not excessive, the interaction of free surfaces is easily dealt with, and the method can be generalised to three dimensions. However considerable numerical diffusion occurs when standard finite difference schemes are used to model the spatial convection terms in equation (5-39). This leads to inaccurate results (Varyani, Gatiganti and Gerigk 2000).

A method of solving equation (5-39) which uses either third order upwind differencing (Miyata 1986) or a modified SOLA/VOF donor-acceptor formulation as developed by Arai (1989) to approximate the convection terms in (5-39) is used to integrated this equation. Either of these numeric integration techniques are carried out on a grid that is three times finer than the grid used to solve for the pressure and velocity fields Figure 5.4.1. The numeric diffusion of the free surface is thus limited to one pressure and velocity grid cell in total. The free surface is located by linear interpolation within the

micro grid. Correct application of the free surface pressure boundary condition is thus possible and this adds to the accuracy of the solution method (Chan and Street 1970). Velocity values are required at the centre of each micro-cell and these are calculated using bilinear velocity interpolation.

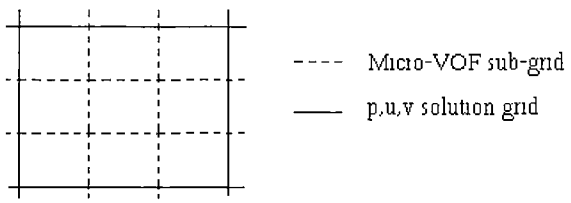

Figure 5.4.1 Definition of the micro sub grid for solution of the VOF flux equation.

The third order upwind differencing operator applied to the flux of F in the x direction has the form

$$u\frac{\partial F}{\partial x}_{i,J} = u_{i,J}\frac{\left(F_{i-2,J} - 2F_{i-1,J} + 9F_{i,J} - 10F_{i+1,J} + 2F_{i+2,J}\right)}{6(\Delta x/3)}, \text{if } u_{i,J} \geq 0$$
$$= u_{i,J}\frac{\left(-2F_{i-2,J} + 10F_{i-1,J} - 9F_{i,J} + 2F_{i+1,J} - F_{i+2,J}\right)}{6(\Delta x/3)}, \text{if } u_{i,J} < 0 \qquad (5\text{-}40)$$

thus

$$F_{i,J}^{n+1} = F_{i,J}^{n} - \Delta t\left(u\frac{\partial F}{\partial x}_{i,J} + v\frac{\partial F}{\partial y}_{i,J}\right). \qquad (5\text{-}41)$$

This numerical solution to (5-39) is used for the problems involving only straight horizontal and vertical tank walls.

The modified SOLA/VOF donor-acceptor method solves equation (5-39) by calculating the flux across each micro cell face. Details of this formulation are given in Arai (1989) and this formulation is slightly adapted for use in a micro grid. Problems involving bodies of arbitrary shape (for example the water entry of a wedge) make use of the modified SOLA/VOF donor-acceptor method.

5.5. Results

The micro-VOF free surface tracking method was validated against two test problems, the collapsing column of water problem (Hirt and Nichols 1981) and the run up of a Laitone solitary wave on a vertical wall (Chan and Street 1970). The water entry of both a 15° and a 25° wedge was also examined.

The collapsing column of water problem entails positioning a rectangular column of water that is initially one unit wide and two units in height adjacent to the one wall of a rectangular tank. The column of water is then allowed to collapse under the influence of gravity. The free surface shape of

the column of water as it collapses is plotted in Figure 5.5.1 for four different non-dimensional times. As can be observed the fluid is initially rectangular in form and then as column collapses a surge front develops. A comparison of the location of this surge front is made with that measured experimentally and also calculated by Hirt and Nichols (1981). It is evident that the micro-VOF algorithm surface tracking algorithm adequately tracks the location of the surge front.

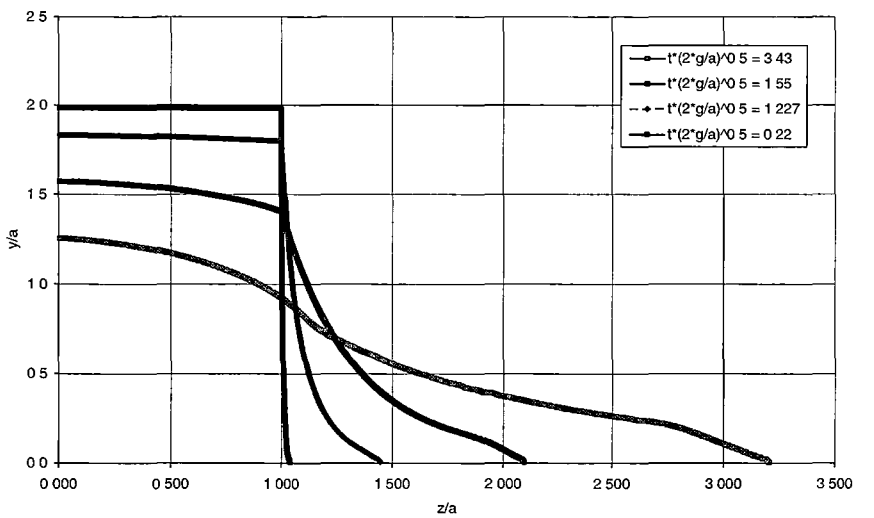

Figure 5.5.1 Free surface configurations at different non-dimensional times for the collapsing column of water problem.

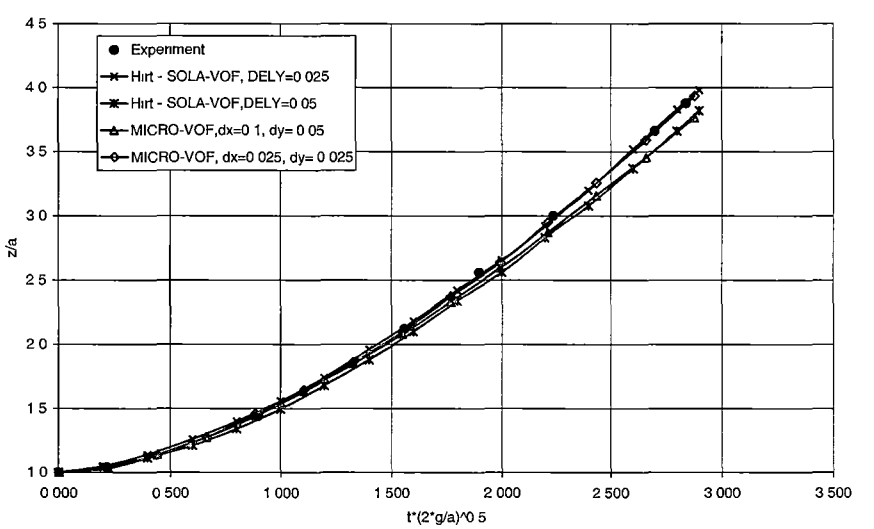

Figure 5.5.2 Comparison of experimental and computer generated data for location of the surge front of a collapsing column of water.

The second test problem examined to validate of the micro-VOF method is that of the run up of a Laitone solitary wave on a vertical wall. This simulation entailed a Laitone solitary wave being located in a long rectangular tank (tank length was fifteen times the still water depth). The Laitone solitary wave then travelled along the tank and collided with the end wall where the water surface became elevated. The still water depth in this simulation was d, the wave crest height H and the run up height R. The shape of the free surface at three non-dimensional times for a H/d ratio of 0.35 is shown in Figure 5.5.3. The maximum run up height (R/d) of the Laitone wave for a range of H/d values is plotted in Figure 5.5.4. As can be observed the run up height (R/d) is adequately predicted by the micro-VOF surface tracking scheme for the range of H/d values considered.

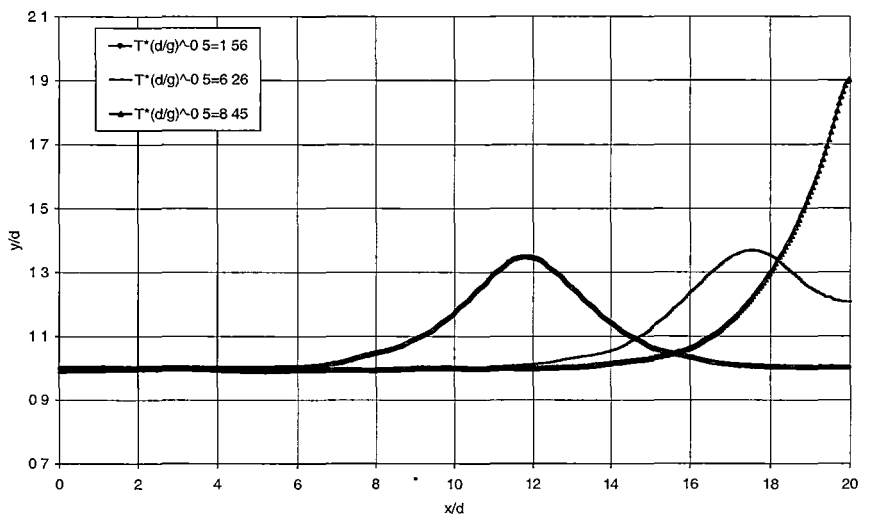

Figure 5.5.3 Free surface configuration for the run up of a Laitone solidary wave on a vertical wall. (H/d=0.35)

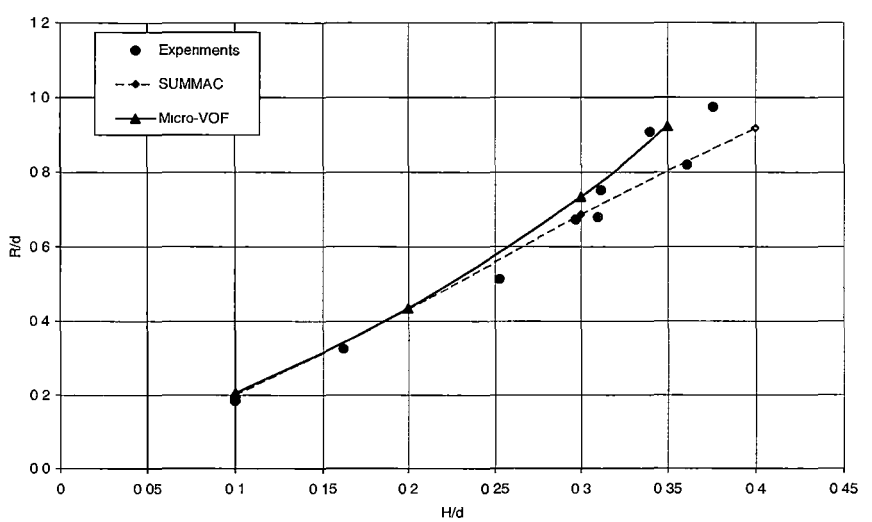

Figure 5.5.4 The maximum run up height (R/d) of a Laitone wave on a vertical wall for a range of H/d ratios.

The evolution of the free surface resulting from the water entry of both a 15° and a 25° wedge is plotted in Figure 5.5.5 and Figure 5.5.6 respectively. Both wedges enter the water at a constant velocity of −1.0m/s. As can be observed the micro-VOF method adequately captures the initial deformation of the free surface in both entry process. The separation of the free surface from the corner of the two wedges is also clearly evident. A similar separation was observed in the experimental flow visualisation presented in chapter 3 for the wedge entry process.

These results are of interest within in the context of the current study as they demonstrate that the VOF class of solutions provide good theoretical solutions to water entry problem. In particular highly non-linear free surface effects such as separation can be accurately predicted with this type of solution. Clearly the current study is limited only to the water entry of vee wedges and the more complex entry of the profiles with arch geometry would provide a good starting point for future study.

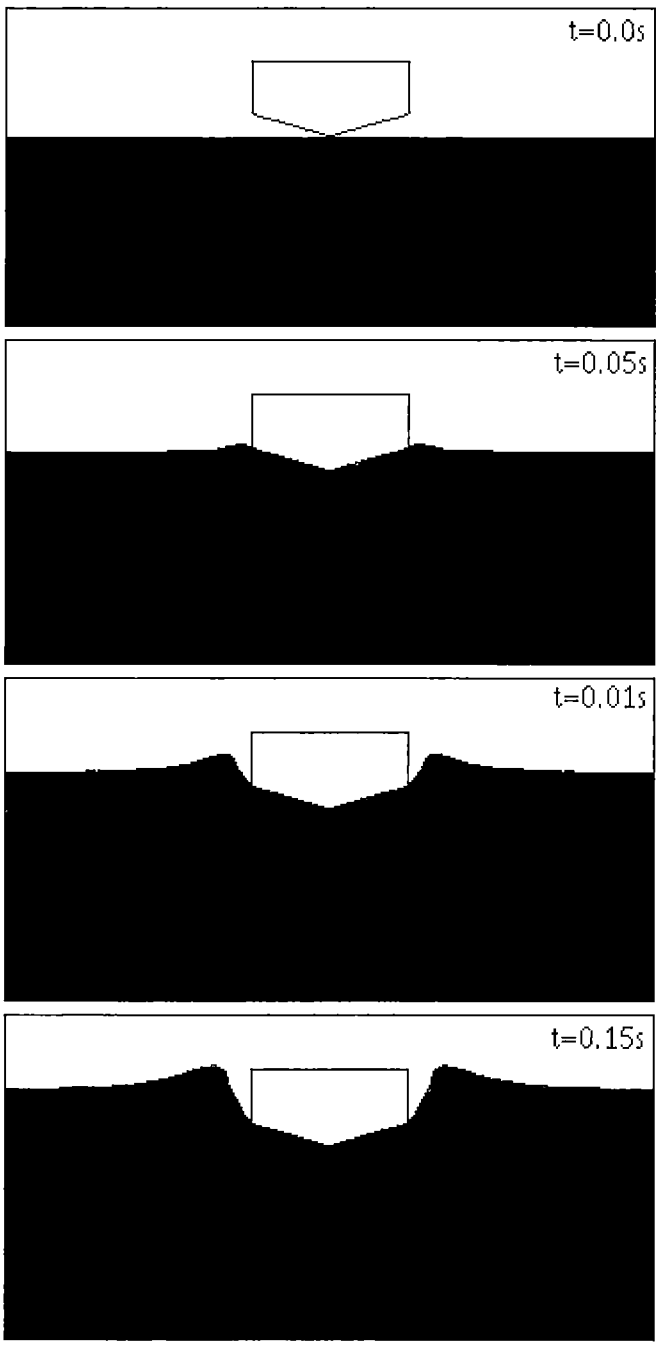

Figure 5.5.5 15° wedge entering water at a constant velocity of –1.0m/s.

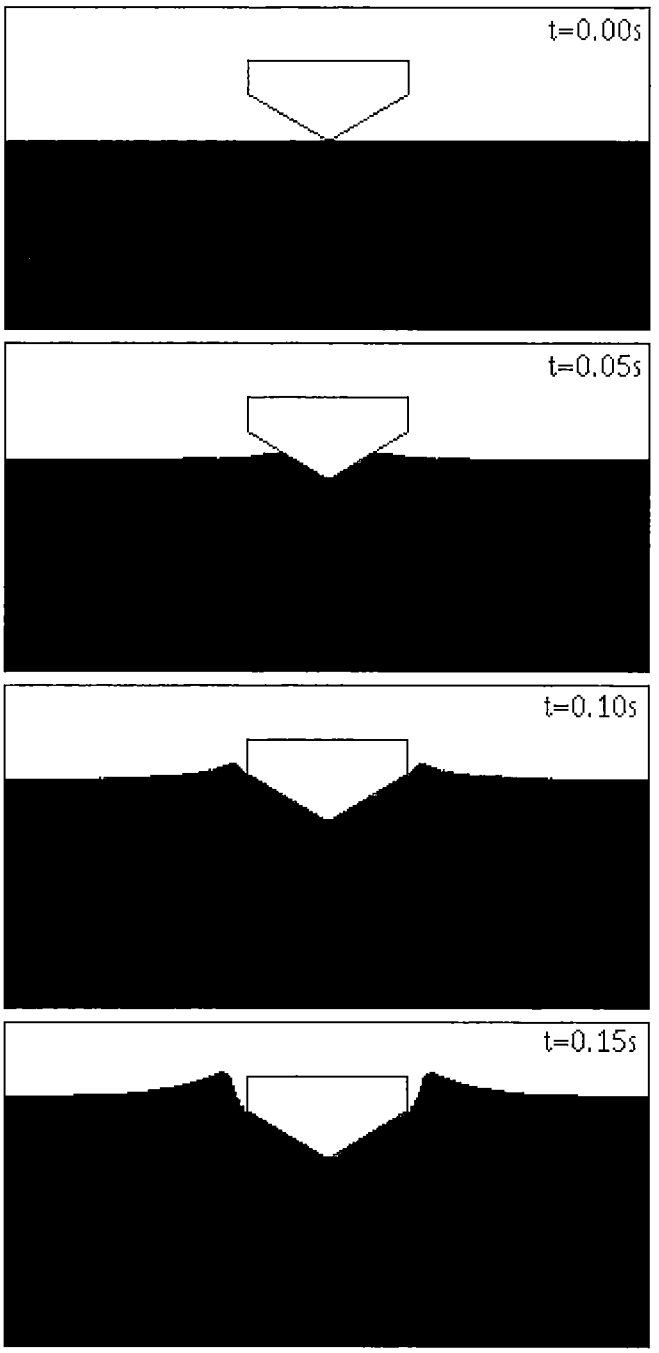

Figure 5.5.6 25° wedge entering water at a constant velocity of –1.0m/s.

5.6. Summary

An improved free surface tracking method (micro-VOF) was presented in this chapter for use in numerical solutions of unsteady, inviscid, incompressible free surface flow problems involving fluid-structure interaction. The micro-VOF surface tracking method was applied to three tests cases, these being the collapsing column of water problem, the run up of a Laitone solitary wave on a vertical wall and the constant velocity water entry of both a 15° and a 25° vee wedge. For each of these test cases the surface tracking algorithm proved to be able to track the spatial and temporal evolution of the free surface. The volume of fluid method was also shown to be a robust method of modelling water entry events and thus this may provide a good area in which to conduct future research.

6. Conclusion

6.1. Summary

The objectives of this project were to investigate the effect of a centre bow on the slamming behaviour of large high-speed catamaran passenger ferries such as those constructed by INCAT Tasmania Pty Ltd and to examine the influence of different centre bow geometries on the slamming performance of this type of catamaran. These problems were investigated by conducting a review of the published literature, by full-scale ship trials, two-dimensional scale model drop tests of realistic catamaran cross-sections and by development of an added mass theory. The water entry of wedges was also modelled using a volume of fluid numeric scheme which used a novel free surface tracking algorithm.

A review of published literature concerning the slamming of ships and in particular catamarans was presented. Based on this review the principal physical features and consequences of slamming were identified. It was noted that slamming takes place in rough seas when the relative motions between the water surface and the ship causes violent impact to occur. Slamming induces substantial loads in vessel structures. Catamarans experience a form of slamming known as wetdeck slamming which is unique to multi-hull vessels. Wetdeck slamming occurs when the cross structure between the demi-hulls comes into contact with the water surface. The loads which wetdeck slamming generates can be particularly severe.

A number of previous reports on full-scale ship trials of displacement mono-hulls, planing mono-hulls and catamarans were reviewed. As a result of this review the state of the art for conducting full-scale ship trials was identified. Previous full-scale trials have usually consisted of undertaking vessel motion and sea state measurements, structural stain measurements and also in some cases hull surface pressure measurements. These previous full-scale trial reports were used to plan the full-scale trials presented in chapter 2. This literature review also identified that there existed a lack of full-scale measurements of the relative velocity profile between a catamaran wetdeck and instantaneous water surface during slamming. This deficiency was addressed in chapter 2.

Drop tests of two- and three-dimensional scale models into water is the principal experimental method of examining the water entry process. A review of previous drop test experiments was undertaken. It was found that drop tests had previously been made with rigid and non-rigid vee wedges, three-dimensional vee wedges, rigid and elastic flat plates, cylinder models, a range of realistic hull forms, cones, spheres, highly elastic models, flying boat floats and parabolic panels. However no reports on drop tests of the general double arch geometric form examined in chapter 3 could be found and it is for this reason that the drop tests presented in chapter 3 were conducted.

Theoretical investigations of the slamming problem were also reviewed. The water entry of two-dimensional wedges, three-dimensional prismatic wedges, cylinder entry, flat plate impact, sphere, cone and curved panel impact and also the water entry of arbitrary shaped bodies have all been modelled theoretically. The use of these theoretical models in calculating the loads on ship structures was also reviewed. This review revealed that added mass based theories had been used to model the water entry of a substantial range of geometries. For this reason an added mass formulation was adopted to model the water entry of a catamaran with a centre bow cross section and this is presented in chapter 4. The use of finite difference based numerical solutions were also found to be a successful method of modelling water entry events in which non-linear effects such as flow separation occur. A finite difference scheme was developed (chapter 5) and used to model the free surface deformation during the water entry of two vee wedges.

6.1.1. Full-scale ship trials closure

Full-scale ship trials (chapter 2) were used to investigate the objectives of this project. The trials were conducted on INCAT vessel 050 during commercial operations in the Cook Strait, New Zealand. Ship motion, sea state and vessel structural stress measurements were made. A definition of a slam event based solely on the magnitude of the structural stresses induced in the structure was developed to allow for the identification and classification of slam events. 38 severe slam events were identified in 10 months of data. Slam loading events were observed to induce a high rate of change stress response in the vessel structure in which the peak stress was significantly greater than the underlaying wave load stresses. All severe slam events recorded were observed to result from wetdeck slamming. The relative motion between the instantaneous water surface and the wetdeck during slamming was calculated and it was found to be approximately parabolic. . Slam entry velocity profiles of this form have not previously been described for catamarans. The average slam velocity profile was used as a basis for scaling the experimental drop tests (chapter 3).

The performance of INCAT vessel 050 during slamming was influenced by a number of parameters including slam wave height, vessel Froude number and the operating policies of the vessel's master. It was found that the master reduced speed as the slam wave height increased. The severity of the slams was found to increase with slam wave height and that the most severe slams occurred when the slam wave height was relatively high and the vessel Froude number was in the mid range of vessel Froude numbers. Also, severe slam events were found to result from the impact of the forward portion of the wetdeck with the trough of the encountered wave.

6.1.2. Experimental methods and results closure

Experimental two-dimensional drop tests of seven realistic catamaran with centre bow cross sections and two vee wedge cross-sections were conducted. Drop tests of catamaran profiles of this form are novel. The drop tests were conducted by allowing the models to fall, under the influence of gravity,

into initially still water. Transient acceleration and pressure data readings were made. The transient pressure readings were made at several locations on each model. Flow visualisation using a high-speed digital camera was also undertaken. The scaling of these experiments was based on the full-scale trials results presented in chapter 2. These drop tests allowed the geometric features which significantly influence the slamming behaviour of catamarans with a centre bow to be identified. These geometric features had previously not been identified.

It was found that cross section geometry significantly effected the accelerations and pressures experienced by the models during water entry. The peak accelerations experienced by the catamaran with centre bow cross sections were significantly (as much as a factor of 10) greater than the peak accelerations experienced by the simple vee wedges for a given normalised drop height. The peak accelerations measured on the catamaran with centre bow cross sections coincided with the complete filling of the arch void with water. This is consistent with the observation made in chapter 2 that severe full-scale ship slams result principally from wetdeck slamming. The pressure transients measured on the catamaran with centre bow cross sections during water entry displayed two pressure spikes. The first spike occurred when the pressure transducer initially came into contact with the water and the second pressure spike coincided with the complete filling of the arch void. For all catamaran models, except the two wedge with sideplate models, the first transient pressure spike was of lower magnitude than the second transient pressure spike. Also, the closer the pressure transducer was located to the top of the arch the greater the second pressure spike for a given model. The pressure transients recorded on the two simple wedge models display a single pressure spike associated with the initial contact of the transducer with water.

The variation of peak acceleration and peak pressure with normalised drop height was found to be complex. The peak accelerations experienced by the vee wedge models with and without sideplates and also the flat plate with sideplates model was found to increase monotonically with normalised drop height. The peak accelerations of the J-series and INCAT models were however found to initially decrease with normalised drop height before increasing with normalised drop height once a minimum had been obtained. This unexpected experimental result was attributed to the detail of the water flow during the final stages of complete filling of the arch void. The peak pressure readings were found to display similar trends to the peak acceleration readings.

The effect of the lateral displacement of the top of the arch from the centre line of the catamaran hull sections was found have a significant influence on the peak accelerations experienced by the models. It was found that models with the highest point in the arch displaced as far as possible from the centre line of the hull experienced significantly lower peak accelerations than hull sections with this point located closer to the centre line of the model. Also, the volume of the centre bow was observed to significantly influence the still water level penetration depth required by the model before it obtained peak acceleration. Models with voluminous centre bows were found to experience peak acceleration at lower still water level penetration depths than models with relatively less voluminous centre bows.

This effect was attributed to the piling up of water around the centre and demi-hulls and the requirement to satisfy continuity of fluid.

A number of slam load cases based on the full-scale trials presented in chapter 2 have been developed by Thomas et al (2001, 2002a, 2003) for INCAT vessel 050. When the peak loads experienced by the drop tests models were scaled to full-scale the scaled loads were found to be substantially greater than the slam load cases developed by Thomas et al (2001, 2002a, 2003). The dissimilarity in the magnitude of the load cases of Thomas et al (2001, 2002a, 2003) and the scale model load cases was attributed to extreme nature of the drop test experiments in which the water surface was precisely aligned with the model underside and also the inherent dissimilarity of a two-dimensional drop test and a three-dimensional ship slam. Despite this, the drop test experiments are of value for comparative purposes when considering the likely effect of various centre bow geometries.

6.1.3. Theoretical investigations of slamming closure

An added mass theory was developed to model the drop test experiments. This theory captured the trends observed in the drop tests. An added mass approach has not previously been used to model the water entry of a catamaran with centre bow geometry. The theory was a two part theory. The first part of the theory modelled the initial entry of a hull section into water by considering the variation of the added mass associated with the hull section. The effects of the piling up of fluid around the hull section was included in the model. A secondary theory was developed to model the special case of the complete filling of the arch void by fluid which occurs during the final stages of the entry of a catamaran with centre hull section. This arch closure theory incorporated the effects of trapped air in the top of the arch. This added mass theory correctly predicted the trends observed in the experiments (chapter 3). The importance of the location of the highest point in the arch and also the effect of the relative volume of the centre bow on the penetration depth required for a model to experience peak acceleration was correctly predicted by the added mass theory. Added mass theory was also used to develop a set of optimised ogee forms which experienced constant acceleration during impact with water.

The water entry a 15° and a 25° wedge including effect of separation from a chine was modelled using a finite difference volume of fluid numeric scheme which used the micro-VOF free surface tracking algorithm. The micro-VOF free surface tracking algorithm correctly captured the evolution of the free surface of both these wedges during the water entry process.

6.2. Implications of Research

High-speed catamaran ferries are a significant segment of the sea transport industry. Design innovations which reduce the capital cost and improve the serviceability of a catamaran ferry allow a competitive advantage to be gained by both the ship builder and the ferry operator. The incorporation

of a centre bow into a catamaran design is potentially such an innovation. The results of both the scale model drop tests and the added mass theoretical analysis indicated that a carefully designed centre bow fitted to a catamaran is likely to reduce the severity of a wetdeck slam event compared with a corresponding slam on a flat wetdeck. The slam load is one of the most substantial loads that a catamaran may experience during its design life. If a catamaran experiences a reduced slam load then the vessel structure may be constructed more efficiently and this reduces the capital cost of the vessel. By reducing the slam loading the likelihood of structural damage is reduced, as too is the likelihood of fatigue damage and these effects improve the serviceability of the vessel. Reducing severe slam events may improve passenger comfort which will provide an additional commercial advantage to the ferry operator. The findings presented in this thesis enable a rational analysis of the likely effect of different centre bow geometries on the slam performance of a catamaran to be undertaken.

A centre bow designed to reduce the severity of wetdeck slamming should display the following geometric features. The centre bow should have the highest point in the arch located as far out board as possible as this configuration minimises the peak load experienced by the vessel when a wetdeck slam occurs. Also the centre bow must not be excessively voluminous as hull cross-sections with substantial centre bows were found to experienced peak loading at a lower relative water surface penetration depth than cross-sections with smaller centre bows. Hence catamarans with voluminous centre bows are likely to experience wetdeck slams more frequently than catamarans with a smaller centre bow for a given seaway. A centre bow geometry which experiences less frequent slamming is of course desirable. The profile of the lower portion of the centre bow was found not to have a substantial effect on the peak loads experienced by a particular hull cross section as the highest loads experienced by the cross-section coincided with the complete filling of the arch void with water (that is when wetdeck slamming occurred). Despite this, it was observed that centre bows with a bluff profile experienced a moderate load spike when the bluff centre bow keel initially impacted the water surface. This load spike was substantially less than the load spike associated with the complete filling of the arch void with water. However as the keel of the centre bow is located close to the water surface it is probable that a substantial number of centre bow keel slams will occur. The magnitude of these centre bow entry slams can be minimised by ensuring that the keel of the centre bow is not excessively bluff.

6.3. Recommendations for Future Study

A substantial amount of additional research is required to completely understand the slamming of a catamaran with a centre bow. Additional research could be undertaken in three general areas. These being additional full-scale trials, scale model testing and more theoretical investigation.

Additional full-scale trials would provide more basic data and hence a better understanding of real world slam events. It would be interesting to place strain gauges on some panels on the wetdeck and centre bow of the vessel. This would allow the local pressures experienced by this region of the

vessel to be estimated. It would also allow the distribution of pressure, both spatially and temporally, to be much better understood. Obtaining better measurements of the encountered sea surface during slamming would also be of interest. This is because the confluence of the sea surface and the wetdeck is critical in determining the severity of a slam event.

Future experimental research which may provide additional insight into this problem includes conducting drop tests of hull sections at a range of roll angles so that the effect of a non-parallel impact may be examined. Water entry tests in which the entry velocity profile is controlled would also be of significant interest as the slam load is a strong function of the entry velocity profile. Model tests of this nature may mitigate the extreme nature of the drop test events as compared with the method of drop tests conducted in this investigation. Experiments in which the venting of air from the top of the arch void is modified may be of interest to better understand the role that trapped air plays in the entry process. The venting of the air could be modified by drilling holes in the model hull sections through which the trapped air could escape. A jet of water would also be forced through such a venting hole when the arch void completely filled with water and the effect water venting in this manner would have on the slam loads experienced by a hull section may also be interesting. The drop test models used in this thesis were inelastic and the effect of model elasticity on slamming loads experienced by catamaran with centre bow cross-sections may provide further insight into the hydroelastic aspects of the problem. Slam panel gauges such as those described by Kapsenberg and Brizzolara (1999) could be used to investigate this feature of slamming. The method used to scale between full-scale and model scale could be examined and a different method could be used for this calculation. For example the model velocity when the arch void completely fills with water could be matched with some appropriate relative velocity at full-scale.

Three-dimensional scale model tests in either a towing tank or wave basin, free running model tests or tests of realistic ship models pivoted at the transom and dropped into still water could provide understanding of the three-dimensional effects which occur during catamaran with centre bow slamming. Model tests of this nature may also allow experiments which are not extreme in nature to be undertaken. Tests of this nature would also allow the validity and limitations of the conclusions based on the two-dimensional drop test experiments and theoretical analysis to be quantified. Of particular interest would be examining whether the conclusions relating penetration number to area ratio and also the relationship between location of the highest point in the arch and peak acceleration are valid for three-dimensional geometries..

Additional theoretical study of the catamaran with centre bow slamming problem could involve the use of a volume of fluid method to model the water entry of a catamaran with centre bow geometry. Potential exists for additional theoretical examination of the role of the trapped air during the final stage of the arch closure process. The effect of compressibility of the water could also be examined theoretically as too could hydroelastic structural response effects. Commercially available software programs would be useful for this research. Also the added mass approach to modelling water entry

problem could be modified. For example a more sophisticated method could be used to calculate the added mass associated with the section as it impacts with the water rather than merely assuming the von Karman (1929) added mass terms.

References

G. Aertssen. An estimate of whipping vibration stress based on slamming data of four ships. *International Shipbuilding Progress*, 26(294): 23-31, 1979.

S. Aksu, W. G. Price, K. R. Suhrbier and P. Temarel. A comparative study of the dynamic behaviour of a fast patrol boat travelling in rough seas. *Marine Structures,* 6: 421-441, 1993.

S. Aksu, W. G. Price and P. Temarel. A comparison of two-dimensional and three-dimensional hydroelasticity theories including the effects of slamming. In *Proceedings of Institute of Mechanical Engineers*, 205(C1): 3-16, 1991.

A. A. Amsden and F. H. Harlow. A simplified MAC technique for incompressible fluid flow calculations. *Journal of Computational Physics,* 6:322-325, 1970.

S. Ando. Cushioning of slamming impact by elastomeric layers. *Journal of Ship Research,* 33(3):169-175, September, 1989.

M. Arai and R. Tasaki. A numerical study of water entrance of two-dimensional wedges --- effect of gravity, spray generation and vertical load. In *Proceedings of PRADS '87*, pages 377-385, 1985.

M. Arai and K. Matsunaga. A numerical and experimental study of bow flare slamming. *Journal of the Society of Naval Architects of Japan*, 165: 343-353, 1989. (In Japanese)

M. Arai, L-Y. Cheng, Y. Inoue. A computing method for the analysis of water impact of arbitrary shaped bodies. *Journal of the Society of Naval Architects of Japan*, 176: 233-240, 1994.

M. Arai, L-Y. Cheng, and Y. Inoue. A computing method for the analysis of water impacting of arbitrary shaped bodies (2nd report). *Journal of the Society of Naval Architects of Japan*, 177:91-99, 1995.

M. Arai, L-Y. Cheng, Y. Inoue, T. Miyauchi and M. Ishikawa. A study on slamming characteristics and optimisation of bow forms of ships. In *Proceedings of PRADS'95,* pages 1.672-1.683, September, 1995.

M. Arai, L-Y. Cheng, Y. Inoue and T. Miyauchi. Numerical study of water impact loads on catamarans with asymmetric hulls. In *Proceedings of Fast'95*, pages 221-232, 1995.

J. Armand and R. Cointe. Hydrodynamic analysis impact analysis of a cylinder. *ASME Journal of Offshore Mechanics and Arctic Engineering*, 109: 237-243, 1987.

S. A. Batterson. The NACA impact basin and water landing tests of a float model at various velocities and weights. Technical Report No. 795, National Advisory Committee for Aeronautics, 1944.

R. F. Beck. Time-domain computations for floating bodies. *Applied Ocean Research*, 16:267-282, 1994.

Ö. Belik, R. Bishop and W. Price. Influence of bottom and flare slamming on structural responses. *Transactions of Royal Institution of Naval Architects*, pages 261-275, 1987.

V. Bertram. *Practical Ship Hydrodynamics.* Butterworth-Heinemann, 2000.

W. Beukelman. Bottom impact pressures due to forced oscillation. *Shipbuilding Marine Technology Monthly,* pages 107-125, May, 1980.

R. E. D. Bishop, J. D. Clarke and W. G. Price. Comparison of full scale and predicted responses of two frigates in severe weather trial. *Transactions of the Royal Institution of Naval Architects,* 126: 153-166, 1983.

R. L. Bisplinghoff and C. S. Doherty. Some studies of the impact of vee wedges on a water surface. *J F I,* pages 547-561, 1952.

S. F. Borg. Some contributions to the wedge-water entry problem. *Journal of the Engineering Mechanics Division*, paper 1214, April, 1957.

S. F. Borg. The maximum pressures and total force on straight-sided wedges with small deadrise. *Journal of the American Society of Naval Engineers*, 71(3): 559-561, 1959.

R. Børresen and F. Tellsgård. Time history simulation of vertical motions and loads on ships in regular, head waves of large amplitude. *Norwegian Maritime Research,* 2: 1-12, 1980.

J. C. Brown, J. D. Clarke, R. S. Dow, F. L. Jones and C. S. Smith. Measurement of wave-induced loads in ships at sea. *Philosophical Transactions of Royal Society of London A*, 334: 293-306, 1991.

K. C. Brown, R. G. Wraith and P. N. Joubert. Local pressure on hull plating due to slamming. In *Proceedings Fast'99*, pages 947-956, 1999.

R. K.-C Chan and R. L. Street. A computer study of finite-amplitude water waves. *Journal of Computational Physics*, 6: 68-94, 1970.

S. Chen, D. B. Johnson, P. E. Raad and D. Fadda. The surface marker and micro cell method. *International Journal for Numerical Methods in Fluids*, 25: 749-778, 1997.

L. Chihua and H. Yousheng. Ship hull slamming analysis with nonlinear boundary element method. *China Ocean Engineering*, 11(4): 411-418, 1997.

S-L. Chuang. Experiments on flat-bottom slamming. *Journal of Ship Research,* pages 10-17, March, 1966.

S-L. Chuang. Experiments on slamming of wedge-shaped bodies. *Journal of Ship Research*, pages 190-198, September, 1967.

S-L. Chuang. Investigation of impact of rigid and elastic bodies with water. *Technical Report Subproject S46-06X, Task 1707 (Hydrofoil Hull), Catholic University of America*, June, 1969.

S-L. Chuang. Theoretical investigations on slamming of cone-shaped bodies. *Journal of Ship Research*, 13: 276-283, December, 1969a.

S. L. Chuang. Investigations of impact of rigid and elastic bodies with water. DTNSRDC, Report Number 3248, 1970.

S-L. Chuang and D. T. Milne. Drop tests of cones to investigate the three dimensional effects of slamming. Technical Report 3543, Naval Ship Research and Development Center, April, 1971.

R. Clevenger and L. Melberg. Slamming of a Ship Structural Model. *M.I.T. Engineer's Thesis*, May 1963.

R. Cointe. Two-Dimensional Water-Solid Impact, *Journal of Offshore Mechanics and Arctic Engineering*, 111: 109-114, May, 1989.

S. Cook. Investigation into wave loads on catamarans. In *proceedings AME'98*, 1998.

R. Dambra, M. G. Hoogeland and A. W. Vredeveldt. Drop test analysis of flat panels using a finite element hydro-code. In *Proceedings Nav 2000*, pages 5.7.1-5.7.12, 2000

Z. Dobrovol'skaya. On Some Problems of Similarity Flow of Fluid with a Free Surface, *Journal of Fluid Mechanics,* 36(4): 805-825, 1969.

A. Fabula. Ellipse-fitting approximation of two-dimensional normal symmetric impact of rigid bodies on water. In *Proceedings 5th Mid-Western Conference Fluid Mechanics*, pages 299-315, 1957.

S. Falch. Slamming of flat-bottomed bodies calculated with exact free surface boundary conditions, *International Conference on Numerical Ship Hydrodynamics, Hiroshima,* 5: 180-195, 1989.

O. Faltinsen, O. Kjaerland, A. Nøttveit and T. Vinje. Water Impact Loads and the Dynamic Response of Horizontal Circular Cylinders in Offshore Structures. In *Proceedings Ninth Annual Offshore Technology Conference, Houston Texas, May 2-5*, paper number OTC 2741, pages 119-123, 1977

O. Faltinsen. Hydrodynamics of high speed vehicles. *Advances in Fluid Mechanics,* 5: 133-176, 1996.

O. Faltinsen. The effect of hydroelasticity on ship slamming. *Philosophical Transactions of Royal Society of London A.,* 355: 575-591, 1997.

O. Faltinsen and R. Zhao. Water entry of a wedge into a channel. In *13th International Workshop on Water Waves and Floating Bodies*, Delft, the Netherlands, 1998.

O. Faltinsen. Water entry of a wedge with finite deadrise angle. *Journal of Ship Research,* 46(1): 39-51, 2002.

W. Frank. Oscillation of cylinders in or below the free surface of deep fluids. Report number 2375, NSRDC, 1967.

W. Frank and N. Salvesen. The Frank close-fit motion computer program. Report number 3289, NRSDC, June 1970.

P. Gallagher. A finite difference, time marching solution of the slamming problem (water entry problem). In *Proceedings Third International Conference on Methods in Lamina and Turbulent Flows*, Pineridge Press, pages 463-474, 1983.

P. Gallagher and R. McGregor. Slamming simulations: an application of computational fluid mechanics. In *Proceedings Fourth International conference on Numerical Ship Hydrodynamics, Washington DC, USA*, pages 117-136, 1985.

P. Garabedian. Oblique water entry of a wedge. *Communications on pure and applied mathematics*, 6: 157-165, 1953.

T. Geers. A Boundary Element Method for Slamming Analysis. *Journal of Ship Research*, 26(2): 117-124, June, 1982.

J. Giannotti. Prediction of slamming loads for catamarans, *Seventh Annual Offshore Technology Conference, Houston, Texas,* May 5-8, paper number OTC 2281: 348-357, 1975.

M. Greenhow. Wedge entry into initially calm water. *Applied Ocean Research*, 9(4): 214-223, 1987.

M. Greenhow and L. Yanbao. Added massed for circular cylinders near or penetrating fluid boundaries – review, extension and application to water –entry, -exit and slamming. *Ocean Engineering*, 14(4): 325-348, 1987.

L. Grossi and M. Dogliani. Load and seakeeping assessment of HSC based on full scale monitoring. In *Proceeding s NAV 2000*, 2000.

K. Hagiwara and T. Yuhara. Fundamental study of wave impact loads on ship bow (2nd report) – effect of the scale of the model on maximum impact pressure and equivalent static pressure. *Journal of the Society of Naval Architects of Japan*, 140: 115-119, December, 1976.

P. Hansen. On combination of slamming- and wave-induced responses. *Journal of Ship Research*, 38(2): 104-114, June, 1994.

F. H. Harlow and E. J Welch. Numerical calculation of time dependent viscous incompressible flow of fluid with free surface. *The Physics of Fluids*, 8(12): 2182-2189, 1965.

E. M. Haugen, O. Faltinsen and J. V. Aarsnes. Application of theoretical and experimental studies of wave impact to wetdeck slamming. In *Proceedings Fast '97,* pages 423-431, 1997.

E. M. Haugen and O. Faltinsen. Theoretical studies of wetdeck slamming and comparisons with fullscale measurements. In *Proceedings Fast'99*, pages 577-591, 1999.

B. Hay, J. Bourne, A. Engle and R. Rubel. Characteristics of hydrodynamic loads data for a naval combatant. In *Proceedings International Conference on Hydroelasticity in Marine Technology*, pages 169-188, 1994.

B. Hayman, T. Haug and S. Valsgård. Response of fast craft hull structures to slamming loads. In *Proceedings Fast'91*, pages 381-398, 1991.

S. R. Heller and N. M. Jasper. On the structural design of planing craft. *Transactions of the Royal Institution of Naval Architects*, 103: 49-65, 1961.

C. W. Hirt and B. D. Nichols. Volume of fluid (VOF) method for dynamics of free boundaries. *Journal of Computational Physics*, 39: 201-225, 1981.

C. W. Hirt and J. M. Sicilian. A porosity technique for the definition of obstacles in rectangular cell meshes, In P*roceedings 4th International conference on Numerical Hydrodynamics*, 1985.

S. Howison, J. Ockendon, and S. Wilson. Incompressible Water-Entry problems at Small Deadrise Angles, *Journal of Fluid Mechanics,* 222: 215-230, 1991

F. Hughes. Solution of the Wedge Entry Problem by Numerical Conformal Mapping, *Journal of Fluid Mechanics,* 56(1): 173-192,1972.

R. Iaccarino, S. Monti and L. Sebastiani. Evaluation of hull loads and motions of a fast vessel based on computations and full scale experiments. In *Proceedings NAV 2000*, pages 5.9.1-5.9.10, 1999.

E. Johnstone and A. Mackie. The Use of Lagrangian Coordinates in the water Entry and Related Problems. In *Proceedings of the Cambridge Philosophical Society (Mathematics and Physical Sciences),* 74, 529-538, 1973.

R. Johnstone. The effect of air compressibility in a first approximation to the ship slamming problem. *Journal of Ship Research,* pages 57-68, March, 1968.

N. Jones. Slamming Damage. *Journal of Ship Research*, pages 80-86, June, 1973.

P. Kannari, P. Klinge, S. Rintala, T. Karppinen, T. P. J. Mikkola and A. Rantanen. Comparison of simulated global stresses with full-scale measurements an aluminium fast patrol vessel. In *Proceedings International Conference on Hydroelasticity in Marine Technology*, pages 477-484, 1998.

P. Kaplan. Analysis and prediction of flat bottom slamming impact of advanced marine vehicles in waves. *International Shipbuilding Progress, Marine Technology Monthly*, 34(391): 44-53, March, 1987.

P. Kaplan and M. Silbert. Impact Forces on Platform Horizontal members in the Splash Zone, *Eighth Annual Offshore Technology Conference, Houston, Texas, May 3-6,* paper Number OTC 2498, pages 749-761, 1976.

G. K. Kapsenberg and S. Brizzolara. Hydro-elastic effects of bow flare slamming on a fast monohull, *Fifth International Conference on Fast Sea Transportation, Seattle, Washington USA, August 31-September 2,* pages 699-708, 1999.

G. M. Katsaounis and M. Samuelides. Comparison of structural behavior of wet deck panels made of different materials under slamming loads. In *Proceedings Fast'99*, pages 35-47, 1999

B. Koehler and C. Kettleborough. Hydrodynamic impact of a falling body upon a viscous incompressible fluid, *Journal of Ship Research*, 21(3) 165-181, September, 1977.

A. Korobkin and V. Pukhnachov. Initial stage of water impact. *Ann. Rev. Fluid Mech.*, 20: 159-185, 1988.

A. Korobkin. Blunt-Body Impact on a Compressible Liquid Surface. *Journal of Fluid Mechanics,* 244: 437-453, 1992.

A. Korobkin. Wave impact on the bow end of a catamaran wet deck. *Journal of Ship Research,* 39(4): 321-327, 1995.

A. Korobkin. Water impact problems in ship hydrodynamics. *Advances in Fluid Mechanics,* 5: 323-365, 1996.

A. Korobkin. Acoustic approximation in the slamming problem. *Journal of Fluid Mechanics,* 318: 165-188, 1996a.

A. Korobkin. Elastic response of catamaran wetdeck to liquid impact. *Ocean Engineering,* 25(8): 687-714, 1998.

R. L. Kreps. Experimental investigation of impact in landing on water. Technical Report NACA Technical Memorandum 1046, National Advisory Committee for Aeronautics, 1943.

J. Kvålsvold and O. Faltinsen. Hydroelastic modelling of slamming against the wetdeck of a catamaran. *Fast'93*, pages 681-697, 1993.

J. Kvålsvold. Hydroelastic modelling of wetdeck slamming on multi-hull vessels. Ph.D. Thesis, Department of Marine Hydrodynamics, The Norwegian Institute of Technology, Norway. MTA report 1994:100, 1994.

J. Kvålsvold and O. Faltinsen. Hydroelastic modelling of wet deck slamming on multi-hull vessels. *Journal of Ship Research,* 39(3): 225-239, September, 1995.

R. W. Lardner and Y. Song. A comparison of spatial grids for numerical modelling of flows in near-coastal seas. *International Journal of Numerical Methods in Fluids*, 14: 109-124, 1992

G. Lewison and W. M. Maclean. On the cushioning of water impact by entrapped air. *Journal of Ship Research*, pages 116-130, June, 1968

G. R. G. Lewison. On the reduction of slamming pressures. *Transactions of the Royal Institution of Naval Architects*, 112: 285-306, 1970

A. Mackie. A linearized theory of the water entry problem. *The Quarterly Journal of Mechanics and Applied Mathematics,* 15(2): 137-151, 1962.

A. Mackie. The Water Entry Problem. *The Quarterly Journal of Mechanics and Applied Mathematics,* 22: 1-17, 1969.

A. Magee and E. Fontaine. A coupled approach for the evaluation of slamming loads on ships. . Practical Design of Ships and Mobiles Units, publishers Elsevier Sciences, editors M. Oosterveld and S. Tan, pages 589-595, 1998.

J. Marco. Hull slamming using non linear finite element methods. Defence Science and Technology Organisation, Aeronautical and Marine Research Laboratory, 2002.

W. L. Mayo. Analysis and modification of theory for impact of seaplanes on water. Technical Report No. 810, National Advisory Committee for Aeronautics, 1945.

W. L. Mayo. Hydrodynamic impact of a system with a single elastic mode I-theory and generalised solution with an application to an elastic airframe. Technical Report No. 1074, National Advisory Committee for Aeronautics, 1952.

R. W. Miller and K. F. Merten. Hydrodynamic impact of a system with a single elastic mode II – Comparison of experimental force and response with theory. Technical Report No. 1075, National Advisory Committee for Aeronautics, 1952.

B. L. Miller. Wave Slamming Loads on Horizontal Circular Elements of Offshore Structures, *Transactions of the Royal Institution of Naval Architects*, 120: 81-95, 1978.

T. Miloh. On the Oblique Water-Entry Problem of a Rigid Sphere, *Journal of Engineering Mathematics*, 25: 77-92, 1991.

B. Milwitzky. Generalised theory for seaplane impact. Technical Report No. 1103, National Advisory Committee for Aeronautics, 1952.

H. Miyata. Finite-difference simulation of breaking waves. *Journal of Computational Physics*, 65: 179-214, 1986.

M. Moghisi and P. T. Squire. An experimental investigation of the initial force of impact on a sphere striking a liquid surface. *Journal of Fluid Mechanics*, 108: 133-146, 1981.

M. Monaghan. Theoretical examination of effect of deadrise in seaplane water impact. Royal Aircraft Establishment, T. N. No. Aero1989, 1949.

B. D. Nichols and C. W. Hirt. Calculating three-dimensional free surface flows in the vicinity of submerged and exposed structures. *Journal of Computational Physics*, 12: 234-246, 1976.

M. Ochi. A method to estimate slamming characteristics for ship design. *Marine Technology*, pages 219-232, April, 1971.

M. Ochi and L. Motter. Prediction of slamming characteristics and hull responses for ship design, *Trans. SNAME,* pages 144-176, 1973.

O. Okland, T. Moan and J. Aarsnes. Structural response in large twin hull vessels exposed to severe wet deck slamming. Practical Design of Ships and Mobile Units, publishers Elsevier Sciences, editors M. Oosterveld and S. Tan, pages 69-78, 1998.

P. Olkinuora, E. Knuuttila, M. K. Hakala, S. Rintala and J. Vuorio. Structural design of an aluminium missile boat. In *Proceedings Fast'91*, pages 727-764, 1991.

P. Payne. Recent developments in 'added mass' planing theory. *Ocean Engineering*, 21(3), 1994.

P. Payne. The vertical impact of a wedge on a fluid. *Ocean Engineering, 8(4):* 421-436, 1981.

J. Pierson. The penetration of a fluid surface by a wedge. Experimental towing tank, Stevens Institute of Technology, Report No. 381, July, 1950.

J. Pierson. On the virtual mass of water associated with an immersing wedge. *Journal of the Aeronautical Sciences*, pages 430-431, 1951.

H. Pinsent. On the entry problem for a compressible liquid. *Journal Fluid Mechanics*, 25(3): 577-587, 1966.

P. E. Raad, S. Chen and D. B Johnson. The introduction of micro cells to treat pressure in free surface fluid flow problems. *Journal Fluids Engineering*, 117: 683-690, 1995.

D. Radev and W. Beukelman. Slamming on forced oscillating wedges at forward speed part 1 – test results. *International Shipbuilding Progress*, 39(420): 399-422, 1992.

P. Rassinot and A. Mansour. Ship hull bottom slamming. *Journal of Offshore Mechanics and Artic Engineering*, 117:252-260, 1995.

RINA's Rules for the design and construction of HSC, 1999

T. J. Roberts, N. L. Watson, M. R. Davis. Evaluation of sea loads in high speed catamarans. In *Proceedings FAST'97*, pages 311-316, 1997.

T. Roberts and P. Yakimoff. Adequate global design loads for fast ferry vessels. *In Proceedings 14th Fast Ferry International Conference*, 1998.

T. Roberts. Personal correspondence. T. Roberts was head of research and development at INCAT Tasmania Pty Ltd and is now head of research and development at Revolution Design Pty Ltd (principal design consultants for INCAT Tasmania Pty Ltd). 2003.

A. Rosén and K. Garme. Slamming studies on high-speed planning craft through full-scale trials and simulations. In *Proceedings Fast'99*, pages 683-697, 1999.

T. Sarpkaya. Wave impact loads on cylinders. In *Proceedings Tenth Annual Offshore Technology Conference*, volume 1, paper number OTC 3065, pages 169-176, 1978.

R. Saucer. Anwendung eines neuen differenzenverfahrens auf die ausbreitung nichlinearer druckwellen. *Publications de l'Institut Mathematique de Béograde, Yugoslavia, Nouvellr serie*: 2 (16), 43-52, 1962.

R. Saucer. Differenzenverfahren fürhyperbolische anfangswertprobleme bei mehr als zwei un abhängigen veränderlichen mit hilfe von nebencharak teristiken. *Numer. Math.*: 5, 55-67, 1963

E. Schnitzer. Theory and procedure for determining loads and motions in chine-immersed hydrodynamic impacts for prismatic bodies. Technical Report No. 1152, National Advisory Committee for Aeronautics, 1953.

T. Shibue, A. Ito and E. Nakayama. Structural response analysis of cylinders under water impact. *Hydroelasticity in Marine Technology,* pages 221-228, 1994

M. Shiffman and D. Spencer. The force of impact on a sphere striking a water surface. AMP rep. 42. 2R, AMG-NYU No. 105, 1945a.

M. Shiffman and D. Spencer. The force of impact on a sphere striking a water surface. AMP rep. 42. 2R, AMG-NYU No. 133, 1945b.

R. Smiley. A semi-empirical procedure for computing water pressure distribution on flat and V-bottom planing surfaces during impact or planing. NACA TN 2583, December 1951.

N. J. Smith, P. K. Stansby and J. R. Wright. The slam force on a flat plate in free flight due to impact on a wave crest. *Journal of Fluids and Structures,* 12: 183-196, 1998

C. Soares. Transient response of ship hull to wave impact. *International Shipbuilding Progress,* 36(406): 137-156, 1989.

B. Stavovy and S-L Chuang. Analytical determination of slamming pressures for high-speed vehicles in waves. *Journal of Ship Research,* 20(4): 190-196, December, 1976.

P. Steinmann, K. Fach and B. Menon. Global and slamming sea loads acting on an 86m high speed catamaran ferry. In *Proceedings Fast'99,* pages 709-718, 1999.

J. Sydow. Über den einfluss von lederung und kislung auf den landestoss. *Jahrbuch der deutschen luftfahrtforschung,* 1938.

J. Talvia and R. Wiefelspütt. Offshore measurements on large scale model and investigation of structural response aspects of slamming loads for high speed monohulls. In *Proceedings Fast'91,* pages 797-809, 1991.

T. Takahashi and Y. Kaneko. Experimental study on wave loads acting on a semi-displacement type high-speed craft by means of elastic model. In *Proceedings High-Speed Surface Craft Conference,* pages 160-169, 1983.

H. Takemoto, T. Miyamoto, Y. Hashizume, S. Oka and N. Ohsawa. Slamming impact loads and hull girder response of a large high-speed craft in waves. In *Proceedings Fast'93*, pages 723-731, 1993.

J. Taylor. Some hydrodynamical inertia coefficients. *Phil. Mag.* 9(55), 1930.

G. Thomas, M. Davis, J. Whelan and T. Roberts. Slamming response of large high speed catamarans. In *Proceedings Fast 2001*, 2001

G. Thomas, M. Davis, D. Holloway and T. Roberts. Extreme asymmetric slam loads on large high-speed catamarans, In *Proceedings of HSMV 2002, 6th Symposium on High-speed Marine Vechicles*, ed: Claudio Pensa, pages 15-23, Naples 18-20 September 2002.

G. Thomas, M. Davis, D. Holloway and T. Roberts. Transient dynamic slam response of large high-speed catamarans, In *Proceedings of FAST'03, 7th International Conference on Fast Sea Transportation*, 2(B1):1-8, Naples, 7-10 October, 2003a.

G. Thomas, M. Davis, D. Holloway, N. Watson and T. Roberts. The slamming response of a large high speed catamaran, *Marine Technology*, 40(2):126-140,2003

G. Thomas. Influence of slamming and whipping on fatigue life of large high speed catamarans. *School of Engineering Research Report SERR 16/03,* University of Tasmania School of Engineering, February, 2003.

F. L. Thompson. Water pressure distribution on a flying boat hull. Technical Report No. 346, National Advisory Committee for Aeronautics, 1930.

L. Trilling. The impact of a body on a water surface at an arbitrary angle. *Journal of Applied Physics*, 21: 161-170, February, 1950.

K. Varyani, R. Gatiganti and M. Gerigk. Motion and slamming impact and catamaran hull. Internal Report University of Glasgow, Report Number NAOE-98-24, 1998.

K. Varyani, R. Gatiganti and M. Gerigk. Motion and slamming impact and catamaran. *Ocean Engineering*, 27:729-747, 2000.

J. H. G. Verhagen. The impact of a flat plate on a water surface. *Journal of Ship Research*, 9:211-223, December, 1967.

J. A. Viecelli. A computing method for incompressible flows bounded by moving walls. *Journal of Computational Physics*, 8: 199-143, 1971.

T. Vinje and P. Brevig. Nonlinear two-dimensional ship motions. In *Proceedings 3rd International conference numerical ship hydrodynamics*, Paris, June pages 257-266, 1980.

T. von Karman. The impact on seaplane floats during landing. Technical Report TN 321, NACA, October, 1929.

W. Vorus. A flat cylinder theory for vessel impact and steady planing resistance. *Journal of Ship Research*, 40(2): 89-106, June, 1996.

R. Vulovich, T. Hirayama, N. Toki and H. Mizuna. Characteristics of hull stresses measured on a large containership in rough seas. *SNAME transactions*, 97: 397-428, 1989.

H. Wagner. The phenomena of impact and planning on water. NACA translation 1366, National Advisory Committee for Aeronautics, Washington, D.C. ZAMM, 1932.

M. Wang, A. Troesch and B. Maskew. Comparison of two different mixed eulerian-lagrangian schemes based on a study of flare-slamming hydrodynamics. *Transactions of the ASME,* 118: 174-183, August, 1996.

I. Watanabe. Effects of the three-dimensionality of ship hull on the wave impact pressure. *Journal of The Society of Naval Architects of Japan*, 163: 163-174, 1987.

N. L. Watson, M. R. Davis, T. J. Roberts. Shipborne measurement of sea conditions and seakeeping response of high speed ferries. In *Proceedings FAST'97*, pages 713-718, 1997.

K. Weem, S. Zhang, W. Lin, J. Bennett and Y. Shin. Structural dynamic loadings due to impact and whipping. Practical Design of Ships and Mobiles Units, publishers Elsevier Sciences, editors M. Oosterveld and S. Tan, pages 79-85, 1998.

J. V. Wehausen and E. V. Laitone, Surface Waves, Encyclopedia of Physics, Volume 9, Fluid Dynamics III, edited by S. Flügge, pages 446-778, 1960

J. R. Whelan, M. R. Davis and D. S. Holloway. Micro-VOF: An improved free surface tracking algorithm for unsteady free surface flow problems, In *Proceedings 2nd International Conference on Computational Fluid Dynamics, ICCFD*, Sydney, Australia, 15-19 July, pages 791-792, 2002

J. R. Whelan, D. S Holloway, T. Roberts and M. R. Davis, MR. Wetdeck slamming of high-speed catamarans with a centre bow. In *Proceedings FAST 2003, The7th International Conference on FAST SEA TRANSPORTATION*, Ischia (Italy), pages B33-B40, 2003.

R.G. Wraith, K. C. Brown, P. N. Joubert and P. Yan. The response of various ships hull plating materials to pressure loads caused by slamming.. In *Proceedings FAST'93*, pages 461-472, 1993.

M. Wu, M. Tulin and E. Fontaine. On the simulation of amplified bow waves induced by motion in head seas. *Journal of Ship Research*, 44(4):290-299, December, 2000.

L. Xu, A. Troesch and W. Vorus. Asymmetric vessel impact and planing hydrodynamics. *Journal of Ship Research*, 42(3): 187-198, September, 1998.

P. Yakimoff. State-of-the-art computer simulation for structural analysis of high speed catamarans. In *Proceedings FAST'97*, pages 107-113, 1997.

Y. Yamamoto, M. Fujino, T. Fukasawa and H. Ohtsubo. Slamming and whipping of ships among rough seas. In *Proceedings Eurotech Colloq.* 122:19-33, 1979.

Y. Yamamoto, M. Fujino, H. Ohtsubo, T. Fukasawa, Y. Iwai, G. Aoki, I. Watanabe, H. Ikeda, A. Kumano and T. Kuroiwa. Disastrous damage of a bulk carrier due to slamming. *J.S.N.A*, 154: 159-169, December, 1983.

Y. Yamamoto, K. Iida, T. Fukasawa, T. Murakami, M. Arai and A. Ando. Structural damage analysis of fast ships due to bow flare slamming. *International Shipbuilding Progress*, 32(369): 124-136, 1985

R. Zhao, O. Faltinsen and J. Aarsnes. Water entry of arbitrary two-dimensional sections with and without flow separation. *Twenty-First Symposium on Naval Hydrodynamics*, pages 408-423, 1997

R. Zhao and O. Faltinsen. Water entry of two-dimensional bodies. *Journal of Fluid Mechanics*, 246: 593-612, 1993.

L. Zhu and D. Faulkner. Slamming drop tests for small scale SWATH characteristic model. Technical Report NAOE-94-34, University of Glasgow, 1994a.

L. Zhu and D. Faulkner. Slamming on the wet-deck of twin-hull vessels. In *Proceedings International conference on New Ship Technology*, Shanghai, China, pages 283-290, 22-25 November, 1994.

L. Zhu and D. Faulkner. Design pressure for the wet-deck structure of twin-hull ships. In *Proceedings Fast'95*, pages 257-268, 1995.